Air Pollution Dispersion within the Tamar Valley (Volume One)

by

Michael Power, BSc. (hons.)

Submitted in fulfilment of the requirements

for the Degree of

Doctor of Philosophy

University of Tasmania (July, 2001)

This thesis contains no material which has been accepted for a degree or diploma by the University or any other institution, except by way of background information and duly acknowledged in the thesis, and to the best of the candidate's knowledge and belief no material previously published or written by another person except where due acknowledgement is made in the text of the thesis.

Michael Power
19 July, 2001

This thesis may be made available for loan and limited copying in accordance with the *Copyright Act 1968*.

Michael Power
19 July, 2001

Abstract

The Tamar Valley is a well-defined coastal valley, located in northern Tasmania (Australia). The valley has significant air pollution problems. At Bell Bay, approximately 5 km inland, there is a heavy industrial estate containing an aluminium smelter, a ferroalloy smelter, a medium density fibreboard plant and a thermal power station. The city of Launceston (pop. 72 000) is located 65 km inland, at the head of the valley. Launceston has a significant winter woodsmoke problem, regularly exceeding the 24-hour *National Environment Protection Council* (*NEPC*) goal for PM_{10} particles.

Data from a network of 16 meteorological stations were combined to produce a climatology of the Tamar Valley, with many variables being mapped on a seasonal basis. The most important climatological parameters were amalgamated into an index of air pollution potential.

A diagnostic wind field model, *NUATMOS* was used to model hourly wind fields for two-day periods each season under poor dispersion conditions. The modelled wind fields clearly showed the dominant flows occurring in the valley under anticyclonic conditions. Coastal westerlies and sea breezes are channelled inland along the northwest-southeast aligned valley. At night, there is a transition to down-slope and down-valley winds, which drain out of the valley.

The *CITPUFF* Gaussian puff dispersion model was used to simulate dispersion of current winter woodsmoke emissions throughout the valley under poor-dispersion conditions. This model was used to help devise woodsmoke reduction strategies. The findings show that a 72 % reduction in woodheater numbers in Launceston is required to meet the *NEPC* particle goal. This goal is exceeded only in the

Launceston region, and is chiefly caused by local sources, with only 4% of the particles modelled within Launceston originating outside of the city. Measured particle concentrations in Launceston have declined over the past few years, however additional measures are required if the *NEPC* goal is to be met. The introduction of reticulated natural gas to Launceston will allow the *NEPC* goal to be met if the city experiences an uptake to gas heating similar to that experienced by Canberra when gas was introduced. A more realistic scenario, with an uptake half that of Canberra's, would provide a significant reduction in PM_{10} concentrations, however this alone would not meet the *NEPC* goal. Banning open fires and non-certified woodheaters would come close meeting the goal. The goal is most likely to be met using a combination of reduction measures.

Dispersion of SO_2 from the combined Bell Bay industrial sources was modelled for each season, showing frequent exceedences of the *NEPC* hourly goal for SO_2. The Bell Bay thermal power station was the dominant source, however this will shortly be converted from oil-fired to gas-fired operation. Modelled NO_x emissions from the gas-fired power station reveal a significant reduction in the number of exceedences.

Acknowledgments

This thesis wouldn't have eventuated if it wasn't for the help, support and encouragement of a lot of people and organisations...

Chief among these is my wife Phillipa, who has supported me throughout the whole process, who has willingly given me time to disappear into the study, who didn't get too upset each time the submission date changed, and who a year ago presented me with a wonderful son Liam. I love and appreciate you both. You have me back now!

To my supervisors Manuel Nunez, Kelvin Michael and Peter Manins. You've all helped and encouraged me enormously along the way. This thesis couldn't have been produced without you. Kelvin and Manuel also proof-read the thesis, dramatically improving it along the way. Thanks also to my other "expert advisors" Frank Carnovale, John Todd and Bill Wood. Whenever I talk to any of the six of you I'm reminded how little I know about climatology and air pollution.

Thanks for the support of my parents and family, who I know had my best interests at heart when they kept on asking me how the thesis was going. You can ask me now (please!). Thanks Mum and Dad for buying me a replacement computer when mine suddenly and catastrophically died.

Many organisations provided funding to the *TVAS*. The *Tasmanian Development Authority* provided core study funding, with the *George Town Council*, *Launceston City Council, West Tamar Council, Comalco Aluminium (Bell Bay) Ltd.*, *Port of Launceston Authority*, and *BHP Temco* providing additional funding.

Daily running of the *TVAS* was undertaken by Steve Carter, then of *Stevenson EMF,* with the overall project being instigated and managed by Bill Wood of *DELM.* Richard Hammond, who took over from Bill Wood, sited the met stations, kept them running and provided me with a very high quality meteorological dataset.

Thanks to everyone who went on the *IOPs*. You've helped to create a fantastic dataset! Thanks also to the land owners and managers who consented to the long term establishment of met stations on their land, and use of their land for *IOPs*.

DPIWE/DELM have helped this project enormously, firstly by overseeing the *TVAS*, but also by providing me with a scholarship and a computer, and eventually with full time employment. *Stevenson EMF* and *CSIRO DAR* provided additional scholarship funding. Working within *DPIWE* has given me access to a lot of information and resources that I otherwise wouldn't have had. In particular many people have

showed considerable interest in the study, and provided me with advice and encouragement and help in numerous ways.

Thanks to Mike Wall, ex-*NPI* Officer, *DPIWE* for providing me with encouragement and laughter, the woodsmoke emissions methodology, various reports and data. Thanks for your frequent computer advice and for persistence and generosity in fixing my computers. Thanks also Martyn Summers for your frequent advice, concern, encouragement and friendship, and for freely providing me with a computer to cannibalise when mine died.

Graeme Ross and Andrew Lewis, of *CAMM*, developed and supplied *NUATMOS/CITPUFF*, created the *NUATMOS* input files for each *IOP* and provided general modelling advice. I hope you approve of the way I've applied your models.

CSIRO DAR, especially Dr Peter Manins, ran *LADM* to help site the anemometer network, lent us the theodolites and provided invaluable advice along the way.

Darren Turner wrote the software which calculated the integral measures and atmospheric stability classes. Wind rose software was written by Tim Freeman. Mark Fowler wrote software to unpack the *NUATMOS* and *CITPUFF* output files. Richard Mount suggested that the *TVAS* dataset could best be stored within an *ACCESS* database, and helped me to implement it. Thank you to all of you, for cheerfully helping me in an area that I'm weak in.

The staff and postgrad students of *Geography and Environmental Studies* provided me with a stimulating environment to learn and work in, and with teaching opportunities and support. Thank you Les Wood for supporting and encouraging me as deadlines loomed.

The *Bureau of Meteorology* provided frequent advice, data and updated forecasts prior to each *IOP*.

Vagn Jensen designed and built the differential temperature sensors. Paul Waller kept the tethersonde functioning, and provided electronic advice throughout the project.

Bill Wood took the daily photos of Launceston that appear in the introduction, and gave permission for their use.

Thank you Carey Denholm, Dean of Science, for listening to me, giving me support and for giving me an extension when no one else seemed interested. I'm looking forward to shaking your hand too!!

And finally my nephew Cameron Utting must be acknowledged. He didn't actually help me in any way but still insisted that he got mentioned in the acknowledgements.

Table of Contents

Volume 1 Chapters One to Six

Table of Contents

Volume 2 Chapters Seven to Ten Appendices One to Three

List of Figures

List of Tables

Abbreviations

Abbreviation	*Description*
ABS	Australian Bureau of Statistics
ACT	Australian Capital Territory
AIR	Association of Independent Research— a group of retired scientists who opposed the Environment Canterbury proposal to ban the use of coal in the New Zealand city of Christchurch.
AIR	Atmospheric Instrumentation Research Company, Inc.
Airsonde	*AIR* Radiosonde
ALC	Aerated Lightweight Concrete – A lightweight concrete made with aluminium pastes and powders produced at the Eckart plant located at Bell Bay.
AMG	Australian Map Grid. All *AMG* co-ordinates quoted in this thesis are given relative to the *Universal Transverse Mercator Grid, Zone 55* using the *Australian Geodetic Datum 1966*.
ASCOT	Atmospheric Studies in Complex Terrain
AWS	Automatic Weather Station – Normally used to refer to the 10-m masts and monitoring equipment located at Sites 1 to 16 or the *BOM* site located at the Launceston Airport.
BASIC	Beginner's All-Purpose Symbolic Instructional Code. An interpreter-driven programming language.
BOM	Bureau of Meteorology— Hobart and Antarctica Office, Hobart; or the Launceston Regional Office, Launceston Airport.
CAMM	Centre for Applied Mathematical Modelling. The organisation that developed *NUATMOS* and *CITPUFF*, and produced the *NUATMOS* input files for each *IOP*. Located at Monash University, Victoria.
CAR	CSIRO Atmospheric Research located at Aspendale, Victoria. Formally known as CSIRO Division of Atmospheric Research (CSIRO DAR).
CD	ABS Census Collection District— These change with every census, and represent the most detailed level at which census data is aggregated and released to the public.
CITPUFF	A gaussian puff dispersion model developed by *CAMM* for estimating pollutant concentrations in complex terrain.
CO	Carbon monoxide
CSIRO	Commonwealth Scientific and Industrial Research Organisation
CTIs	Critical Transport Indices
DEI	*Duke Energy International*— the company chosen to provide reticulated natural gas to Tasmania.
DELM	*Department of Environment and Land Management* — Tasmanian State Government Department that commissioned and oversaw the *TVAS* (Recently renamed to *DPIWE*)
DEM	Digital Elevation Model— a raster-based model showing the dominant topography of a region. The *TVAS DEM* was covers the entire *NUATMOS* computational domain at a 1x1km resolution, with cell values representing the mean elevation of each cell.
DPIWE	*Department of Primary Industries, Water and Environment*— Tasmanian State Government Department (Known as *DELM* during the *TVAS*)
DST	Daylight Savings Time— Equals UTC plus 11 hours (or EST plus 1 hour)
EPAV	Environment Protection Authority, State Government of Victoria
EST	Eastern Standard Time— Equals UTC plus 10 hours
GIS	Geographic Information System— Computer software designed to facilitate the display and analysis of spatial data. The *NUATMOS* and *CITPUFF* output files were displayed in map form using the *ESRI ArcView GIS* package.
GLC	Ground Level Concentration
IDS	Inverse Distance Squared— One of three *NUATMOS* interpolation schemes, which interpolate winds along computational sigma levels. The *IDS* scheme was used exclusively throughout the *TVAS*.
ISC	Industrial Source Complex model. This is a gaussian plume model used by the *EPAV* for regulatory purposes.
IOP	Intensive Observation Period
LADM	Lagrangian Atmospheric Dispersion Model— Prognostic mesoscale wind field model and Lagrangian particle dispersion model developed by *CSIRO DAR*.
LGA	ABS Census Local Government Area— a broad seale level at which census data is aggregated.
LVAS	Latrobe Valley Airshed Study
LVAS PTE	Latrobe Valley Airshed Study Plume Tracking Experiment
MASL	Metres Above Sea Level
MDF	Medium Density Fibreboard – produced at the *Starwood MDF* plant at Bell Bay
MS	*Microsoft*

Abbreviation	*Description*
NEPC	National Environment Protection Council
NEPM	National Environment Protection Measure
NO_x	Oxides of Nitrogen, comprising NO and NO_2
NPI	National Pollutant Inventory - generally referring to either the Hobart or Launceston air pollution inventories.
NUATMOS	3D Diagnostic wind field model developed by *CAMM*. Originally based on the *ATMOS1* model.
Piball	Pilot Balloon
PLA	Port of Launceston Authority
PM_{10}	Particulate matter with an aerodynamic diameter less than 10 μm
ppb	Parts per billion, a unit of contaminant concentration. To convert ppb to ppm, divide by 1000.
ppm	Parts per million, a unit of contaminant concentration. To convert ppm to ppb, multiply by 1000.
RMA	Resources Management Act 1991 (New Zealand)
STP	Sewage Treatment Plant. The Site 16 meteorological station is located at the Ti Tree Bend STP.
TAPAS	*Topographic Air Pollution Analysis System* produced by *CAMM*, composed of *NUATMOS* and *CITPUFF*.
Tethersonde	*AIR* Tethered Balloon Sounding System
TVAS	Tamar Valley Airshed Study
VOC	Volatile Organic Compounds

This research was performed, and the thesis written, largely on a part-time basis. During this time the author was consecutively:

- a research assistant and PhD student with the *Tamar Valley Airshed Study*,
- a part-time lecturer and tutor within the *Department of Geography and Environmental Studies*, *University of Tasmania*, and
- a full-time scientific officer with the *Department of Primary Industries, Water and Environment*.

1 Introduction

1.1 Introduction

The Tamar Valley is one of the most polluted regions in Australia, with a severe wintertime woodsmoke problem, and significant emissions from industrial sources at Bell Bay. This thesis will describe and model the winds occurring throughout the valley, using a diagnostic wind field model. A Gaussian puff dispersion model will be used to simulate current dispersion of industrial and residential emissions throughout the valley. A series of pollution reduction scenarios will be also be modelled.

This chapter will provide an introduction to the thesis. It will describe the Tamar Valley and surrounding areas, revealing its location, topography, population distribution and climate. Air pollution sources within the area are then described, focussing on urban diffuse sources and the Bell Bay industrial point sources. Current national air pollution standards are then listed. Past concentrations of respirable particles, measured at Launceston, are briefly described. The *Tamar Valley Airshed Study*, which sponsored this research, is then described. The chapter concludes by posing a series of specific research questions and providing an outline of the thesis.

1.2 Site Description

1.2.1 Location

The Tamar Valley is a coastal valley located in the northeast of Tasmania, Australia. Tasmania is an island state, situated to the south of the Australian mainland (see inset map in Figure 1.1). The City of Launceston (population 72,000) lies 55 km inland on the headwaters of the Tamar River. Other major towns in the region include Devonport and Ulverstone on the northwest coast (Figure 1.1).

A heavy industrial park is located at Bell Bay, some 10 km inland, on the eastern banks of the Tamar.

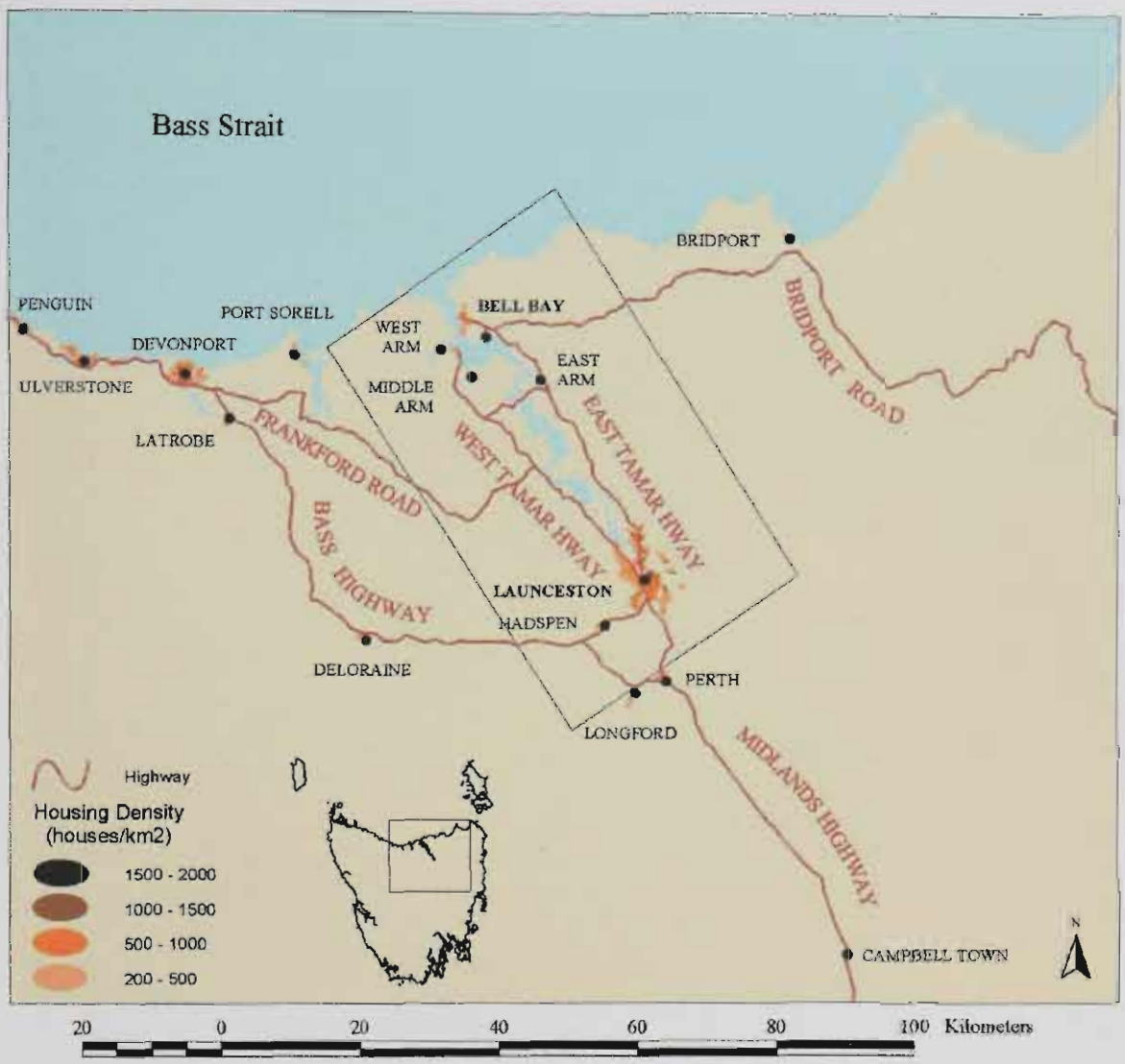

Figure 1.1 Major population centres and highways within the Tamar Valley region. The northwest/southeast-aligned rectangle shows the extent of the *TVAS* study area. Launceston and Bell Bay are highlighted in bold type. The inset map places the region within the state of Tasmania. Housing densities were obtained from the Australian Bureau of Statistics Census '96 data.

1.2.2 Topography

Figure 1.2 shows the topographic features defining the northwest/southeast-aligned Tamar Valley. The Asbestos and Dazzler Ranges, Bald Tier, Foresters Hill, Grassy Hut Tier and Mt. Arnon form the southwest wall. To the far southwest are the Great Western Tiers. The northeast wall of the valley comprises the Tippogoree Hills, the Den and Dismal ranges, and Mts. Arthur and Barrow. The highest elevation in the valley occurs at the summit of Ben Lomond (1574 m.a.s.l.) located in the southeast.

The Tamar River runs through the centre of the valley, dividing the West-Tamar region from the East-Tamar. Table 1.1 lists the major topographic features forming the Tamar Valley, and provides their elevations.

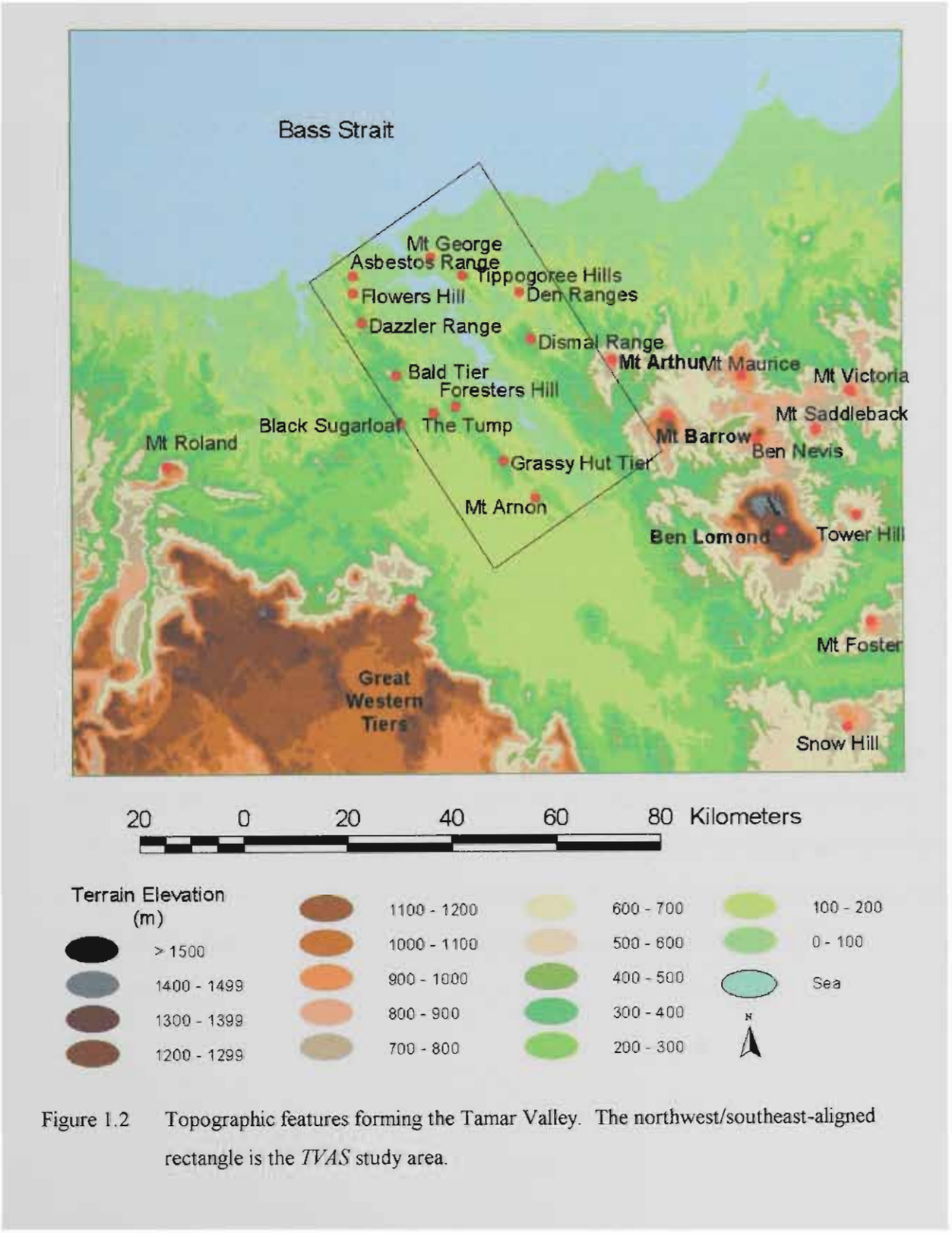

Figure 1.2 Topographic features forming the Tamar Valley. The northwest/southeast-aligned rectangle is the *TVAS* study area.

Table 1.1 The main topographic features forming the Tamar Valley

Topographic Feature	*Elevation (m.a.s.l.)*
Southwest wall	
Asbestos Range	392
Dazzler Range	508
Bald Tier	310
Foresters Hill	390
Grassy Hut Tier	410
Mt. Arnon	315
Great Western Tiers	1298
Northeast wall	
Mt. George	242
Tippogoree Hills	360
Den Ranges	210
Dismal Range	520
Mt. Arthur	1187
Mt. Barrow	1414
Ben Lomond	1574
Mt. Foster	1012
Snow Hill	971

The northwest/southeast-aligned rectangle, shown in both Figures 1.1 and 1.2, represents the *Tamar Valley Airshed Study (TVAS)* study area. This region will be investigated in detail within this thesis. The *TVAS* study area is aligned with, and centred over, the valley axis. It is 65 km long and 40 km wide. The study area contains Bell Bay in the northwest and Launceston in the southeast.

1.2.3 Population Distribution

Figure 1.3 shows the housing density and locations of towns in and near the study area. Launceston is by far the greatest population centre in the region, containing approximately 72 % of the total population of the study area. The main Launceston suburbs are shown in Figure 1.4. These are mainly concentrated to the southeast of the Tamar River, however ribbon developments follow the banks of the river towards the coast. The town of George Town (population 5600) is located at the opposite end of the valley. George Town is the main dormitory suburb for the Bell Bay workforce.

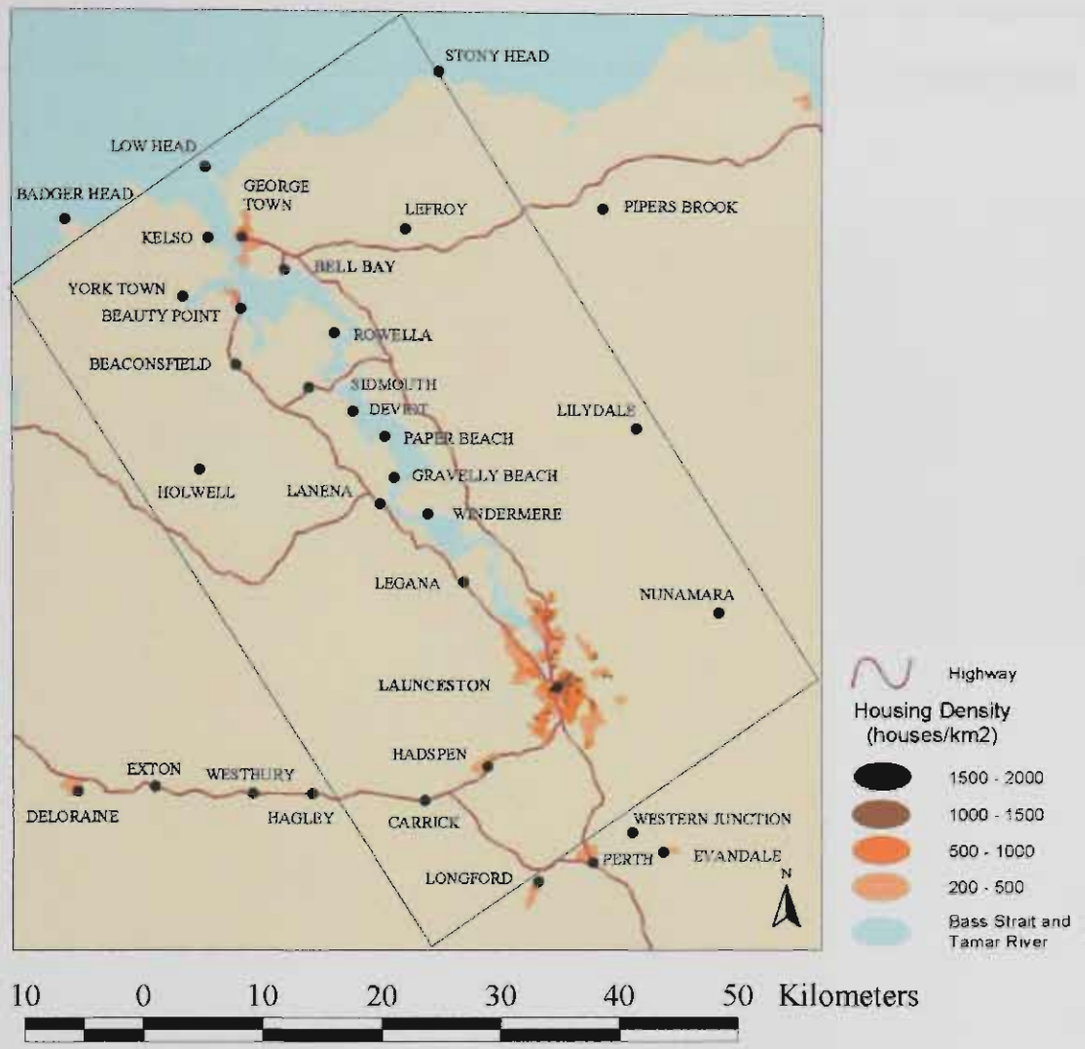

Figure 1.3 Towns and townships in the vicinity of the *TVAS* study area. Launceston and Bell Bay are highlighted in bold type. Housing densities were obtained from the Australian Bureau of Statistics Census '96 data.

1.2.4 General Climate

The island state of Tasmania experiences a temperate maritime climate, with temperatures being moderated by the sea. Prevailing winds are from the west, reflecting Tasmania's latitudinal position in the mid-latitude westerlies, otherwise known as the 'roaring forties'.

Winds are strongest and most persistent during late winter and early spring, and are controlled by the passage of cyclones and anticyclones across the state. The westerlies tend to weaken during the summer, as the subtropical ridge migrates south, allowing afternoon sea breezes to develop.

Cold fronts are often embedded within the westerlies, crossing the state from west to east. These bring cold weather and rain to the state, and during winter may bring snow to low levels. (Anon., 1999)

Figure 1.4 Launceston suburbs and housing densities (obtained from the Australian Bureau of Statistics Census '96 data)

Table 1.2 summarises some of the more important climatic variables for Launceston. The mean daily-minimum temperature varies between 2.0 °C in July (winter) and 12.1 °C in January (summer). Mean daily-maximum temperatures are also lowest in winter and highest in summer, ranging between 12.4 °C (July) and 24.3 °C (February) respectively. Temperatures outside of these ranges frequently occur, with a lowest recorded temperature of –5.2 °C and a highest recorded temperature of 35.4 °C.

Mean daily-wind-runs vary between 186 km (August) and 361 km (December), corresponding to average speeds of 2.2 ms^{-1} and 4.2 ms^{-1} respectively.

Significant rainfall occurs all year round, with the monthly mean number of rain days varying between 6.3 in February and 14.7 in August. The mean monthly-rainfall follows this pattern with mean falls of 29.7 mm and 81.1 mm in February and August respectively.

Launceston is well known for its frequent winter fogs, and has consequently earned itself the nickname "Fog Hollow". Winter fogs often persist throughout the entire night, and through most of the following morning. An average of 8.3 fog days are recorded every July by the *Bureau of Meteorology*. This figure probably underestimates the true number of fog days as manual observations only occur at 09:00 and 15:00 daily. If the fog has dissipated by 09:00 then it will not be recorded.

1.3 Air Pollution Sources

1.3.1 Launceston Urban Diffuse Sources

Air pollution emissions in Launceston mainly occur from diffuse sources. The two major diffuse sources are woodheaters and motor vehicles.

Approximately 58 % of houses in Launceston are heated by wood combustion, with most burning occurring in controlled combustion heaters. A small percentage (4 %) of households use open fires for space heating purposes. Particles are the dominant contaminant associated with wood combustion, however significant carbon monoxide (CO) emissions also occur. The locations and strengths of the woodsmoke sources within the Tamar Valley will be described in detail in Chapter Eight.

The second major diffuse source in the Tamar Valley is from motor vehicles, which emit CO, nitrogen oxides (NO_x), volatile organic compounds (VOC) and particles. No sustained measurements of CO, NO_x or VOC have been made in Launceston, however significant concentrations are likely to occur.

Table 1.2 The climate of Launceston. All data was recorded at the Ti Tree Bend Sewage Treatment Plant, Launceston, between 7/5/1980 and 20/4/2001.

Season	*Month*	*Lowest Recorded Temperature* (°C)	*Mean Daily Minimum Temperature* (°C)	*Mean Daily Maximum Temperature* (°C)	*Highest Recorded Temperature* (°C)	*Mean Daily Wind Run* (km)	*Lowest Recorded Monthly Rainfall* (mm)	*Mean Monthly Rainfall* (mm)	*Highest Recorded Monthly Rainfall* (mm)	*Mean Number of Rain Days*	*Mean* * *Number of Days with Frost*	*Mean* * *Number of Days with Fog*
Summer	January	2.5	12.1	24.1	35.4	333	9.8	46.9	139.4	8.1	0.1	0.1
	February	3.4	11.8	24.3	34.4	296	0.4	29.7	107.4	6.3	0.0	0.1
Autumn	March	0.5	10.0	22.3	32.3	302	2.6	36.6	106.2	7.0	0.4	0.4
	April	-1.5	7.3	18.8	27.7	206	19.0	53.5	124.6	8.7	2.9	2.1
	May	-3.0	5.3	15.8	22.0	265	8.5	70.1	138.8	10.9	6.6	4.5
Winter	June	-4.9	2.6	12.9	18.2	216	21.2	61.5	108.7	11.7	12.8	5.6
	July	-5.2	2.0	12.4	17.6	207	39.8	80.2	157.7	14.2	13.7	8.3
	August	-3.5	3.6	13.7	19.6	186	14.9	81.1	162.1	14.7	11.0	3.9
Spring	September	-2.4	5.1	15.5	24.8	266	8.4	63.3	110.6	13.4	8.2	1.2
	October	-0.6	6.9	18.1	28.7	286	16.8	55.9	121.4	11.8	4.3	0.7
	November	-2.0	8.5	20.1	30.7	309	20.8	51.7	85.2	9.8	2.3	0.2
Summer	December	2.0	10.6	22.4	33.8	361	6.1	47.5	145.1	8.0	0.4	0.0

Data supplied by the *Bureau of Meteorology*

* Note: Manual observations of frost and fog occur at 09:00 and 15:00 daily. Occurrences of frost or fog outside of these hours are not included in these figures.

1.3.2 Bell Bay Industrial Point Sources

1.3.2.1 Comalco Aluminium Smelter

The *Comalco Aluminium Smelter (Bell Bay) Ltd.* commenced operations on 23 September 1955, and is the oldest and smallest aluminium smelter in the Southern Hemisphere. The plant was commissioned in response to Australia's desperate need for aluminium, used in aircraft production, during World War II. It was the first industry located at Bell Bay. Bell Bay was chosen because of the availability of cheap hydro-electric power and deep-water port facilities. (Carroll, 1980; *Comalco*, 1998)

Comalco's operations at Bell Bay are centred around the smelting and casting of primary aluminium and its alloys. The three main process areas are:

- the manufacture of carbon products (used later in the smelting process);
- the conversion of alumina ($2Al_2O_3$) to aluminium (Al); and
- metal alloying and casting.

(*Comalco*, 1998)

Comalco produced approximately 150,000 t of aluminium products at Bell Bay in 2000.

1.3.2.2 TEMCO Manganese Alloy Smelter

TEMCO is a producer of manganese alloys, which are added to steel to improve its rolling and abrasive properties. The plant, which is the only one of its kind in Australia, was set up in 1962 to reduce Australia's reliance on overseas sources of strategic alloys.

The company operates four submerged arc electric smelting furnaces, which they use to produce ferromanganese (FeMn) and silicomanganese (SiMn). *TEMCO* also runs a sinter plant, which produces manganese sinter. This is used as a feed to the *TEMCO* furnaces, and can also be used in direct alloying processes.

The current annual production capacity is 120,000 t of ferromanganese, 120,000 t of silicomanganese and 320,000 t of sinter. *TEMCO* operates on a continuous basis. (Chesterman and Hassell, 2000)

1.3.2.3 Starwood Medium Density Fibreboard Plant

The *Starwood Medium Density Fibreboard (MDF) Plant* is the latest industry to commence operation at Bell Bay, with construction occurring between 1995 and 1998. The plant produces MDF boards varying in thickness between 9 and 32 mm and up to 12.4 m^2 in area.

The production process includes:

- Sourcing and stockpiling of radiata pine and eucalypt wood chips;
- Washing and sorting the raw wood chips;
- Digesting the wood chips using pressurised steam, and refining them to a fibre material;
- Drying the wet fibre to a desired moisture content, and adding resin and wax;
- Forming the fibre into partially compressed mats;
- Pressing the mats into boards;
- Cooling the boards; and
- Conditioning the boards in a warehouse prior to finishing, grading and packing.

Approximately 29,000 t of marketable products were produced in 1999, approximately a quarter of that allowed under their operating permit (120,000 t per annum). Annual production is expected to rapidly rise to 80 to 90 % of licensed output once the plant reaches full production capacity. (e-systems, 2001)

1.3.2.4 Eckart Aluminium Powder and Paste Plant

The *Eckart Aluminium Powder and Paste Plant* manufactures aluminium powders and pigments for use in the chemical, metallurgical, printing and paint industries. The plant was developed and operated by *Comalco* in 1968, however it was sold to *Eckart Australia Pty. Ltd.* in January 1998.

Operations use approximately 10 % of *Comalco's* aluminium output with molten aluminium being transported directly from *Comalco* to the plant, via a private roadway, for immediate use in production processes. Table 1.3 shows the major products and annual output of the *Eckart* plant.

Table 1.3 Annual Output and Use of Products from the *Eckart Aluminium Powder and Paste Plant*

Product	*Product Usage*	*1998 Output (t per annum)*	*Estimated 2000 Output (t per annum)*
Atomised powder	Refractories, chemicals, brake linings, de-oxidants	5,500	7,000
Granules	Alloy additions	4,500	5,000
Pigment paste	Pigment for paints and plastics	316	600
Aerated Lightweight Concrete (ALC) paste and powder	Aerating agent for lightweight concrete	120	200

Source: Eckart Australia (1999)

Emissions to air are dominated by hydrocarbons (white spirits), which are discharged from the paste and Aerated Lightweight Concrete (ALC) plants. Fugitive emissions occur and are mainly due to evaporation, occurring most frequently during the milling process. It is estimated that in 2002 the total emission of white spirits, from all sources, will be 31 t.

Particulate emissions are discharged from four stacks. These are the powder plant cyclone stack, the furnace exhaust, the atomising air heater exhaust and the hot oil heater stack in the ALC plant. Modelling studies, prior to extensive modifications, suggest that current particulate emissions will be very low. (*Eckart Australia*, 1999)

1.3.2.5 Bell Bay Thermal Power Station

The *Bell Bay Thermal Power Station* is located at Donovans Bay, 3 km to the southeast of Bell Bay. The power station operates two 120 MW generators, the first installed in 1971 and the second in 1974. The oil-fired station burn approximately 1250 t of fuel oil a day when operating at full capacity. The station is infrequently used however, only being fired up when water storage levels in Tasmania's hydroelectric dams are low. The dominant emission is SO_2, however the station also emits significant quantities of SO_3, CO, CO_2, NO_x and hydrocarbons.

1.3.2.6 Other Minor Sources

Other industrial operations in the Bell Bay region include:

- The *Comalco Research and Technical Development Centre*;
- The *Bell Bay Wharf* complex;
- The *Mobil Oil* Storage facility;
- The *George Town Waste Water Treatment Plant*; and
- The *North Forest Products* and *Boral* woodchip mills located 7 km to the southeast at Longreach.

Emissions from these sources are minor, and hence will be ignored in this thesis.

1.4 Air Pollution Standards and Concentrations

1.4.1 National Air Pollution Standards and the Air NEPM

Australia has recently developed national standards for six major pollutants occurring in ambient air. These are:

- Carbon Monoxide (CO)
- Nitrogen Dioxide (NO_2)
- Photochemical Oxidants, as Ozone (O_3)
- Sulfur Dioxide (SO_2)
- Lead (Pb)
- Particles, as PM_{10}

The standards were developed to ensure that all Australians experience equivalent levels of protection from air pollution, and that business decisions are not distorted by variations in environmental standards.

The National Environment Protection Council (*NEPC*), a statutory body made up of ministers from each state and territory in Australia, developed the standards. The standards are contained within the "*Air NEPM*" (National Environmental Protection Measure), which was "made" on 26 June 1998. This requires each state and territory to achieve specific air pollution goals within 10 years and, where necessary, to monitor and report on concentrations of the six major pollutants listed above.

Table 1.4 summarises the *NEPM* standards, and the goals to be achieved by June 2008. The standard that is most relevant to Launceston is that for particles, which are mainly emitted from diffuse woodheater sources. The *Air NEPM* allows 24-hour average PM_{10} concentrations to exceed 50 μgm^{-3} on only five occasions a year. The PM_{10} class of particles, otherwise known as 'respirable particles', is defined as those particles having aerodynamic diameters less than 10 μm. These are important as they are small enough to be breathed deeply into the lung, and have hence been associated with a wide range of respiratory problems.

Table 1.4 *National Environment Protection Council* Ambient Air Quality Standards and Goals

Pollutant	*Averaging Period*	*Maximum Concentration*	*Goal by 26 June 2008, Maximum allowable exceedences*
Carbon Monoxide (CO)	8 hours *	9.0 ppm	1 day a year
Nitrogen Dioxide (NO_2)	1 hour	0.12 ppm	1 day a year
	1 year	0.03 ppm	none
Photochemical Oxidants, as Ozone (O_3)	1 hour	0.10 ppm	1 day a year
	4 hours *	0.08 ppm	1 day a year
Sulfur Dioxide (SO_2)	1 hour	0.20 ppm	1 day a year
	1 day	0.08 ppm	1 day a year
	1 year	0.02 ppm	none
Lead (Pb)	1 year	0.50 μgm^{-3}	none
Particles, as PM_{10}	1 day	50 μgm^{-3}	5 days a year

Source: Modified from *NEPC*, (1998), Schedule 2.
* Calculated using rolling averages based on 1-hour averages. For the purpose of calculating and reporting 4 and 8 hour averages, the first rolling average period in a calendar day ends at 01:00 and includes hours from the previous day.

Carbon monoxide may also be an important contaminant in Launceston, mainly emitted by vehicular sources. There have been no formal monitoring programs for CO in Launceston, so representative concentrations are unknown. The *NEPM* standard is couched in terms of an 8-hour rolling average, calculated from successive 1-hour averages. The goal is 9.0 ppm, with one allowable exceedence a year.

At Bell Bay, industrial emissions of nitrogen dioxide and SO_2 are also important, with hourly standards of 0.12 and 0.20 ppm respectively. Both standards may only be exceeded during one day a year. (*NEPC*, 1997; 1998)

1.4.2 Respirable Particle Concentrations in Launceston

DPIWE measures 24-hour mean PM_{10} concentrations at the Ti Tree Bend sewage treatment plant in Launceston. Samples are collected daily, during the period between 1 May and 30 September, using a pair of co-located high volume samplers. Outside of this period, samples are collected every sixth day.

Particles have been monitored at Ti Tree Bend since 1991. Only limited data are publicly available. During winters 1991 to 1993, concentrations exceeded the then acceptable 24-hour level of 120 μgm^{-3} on 2, 7 and 1 occasions respectively. The maximum concentration recorded during winter 1992 was 189 μgm^{-3} (Working Party, 1996, Graph 13, p. 23D). Since this time, PM_{10} concentrations have been gradually falling at Ti Tree Bend.

Table 1.5 summarises the recent PM_{10} history at Ti Tree Bend for summer and winter. During summer, all measured concentrations were below 50 μgm^{-3}, with a maximum summer concentration of 30 μgm^{-3} occurring in February 2000. The *NEPC* 24-hour goal of 50 μgm^{-3} was exceeded on a third of winter days between 1997 and 1999, with maximum concentrations exceeding 120 μgm^{-3} in 1997 and 1998. The *NEPC* 24-hour goal was exceeded on 32 occasions during winter 1999, with a maximum concentration of 92 μgm^{-3}.

Table 1.5 Ti Tree Bend 24-hour Average PM_{10} Concentrations: Summer (1997 to 2000) and Winter (1997 to 1999)

	1997		*1998*		*1999*		*2000*
	Summer	*Winter*	*Summer*	*Winter*	*Summer*	*Winter*	*Summer*
Number of Samples Collected	15	90	13	91	14	92	10
Number of Exceedences of 50 μgm^{-3}	0	32	0	37	0	32	0
Highest Concentration (μgm^{-3})	17	121	20	122	14	92	30
Second Highest Concentration (μgm^{-3})	14	110	18	121	12	85	29
Third Highest Concentration (μgm^{-3})	11	109	16	112	12	83	24
Fourth Highest Concentration (μgm^{-3})	11	98	14	109	11	81	21
Mean Concentration (μgm^{-3})	8	40	12	45	9	41	17
Median Concentration (μgm^{-3})	6	38	12	39	9	42	15
Lowest Concentration (μgm^{-3})	2	0	7	3	5	4	6

Source: *DPIWE* Note: Samples are collected daily during winter (1 June to 31 August) and every sixth day during summer (1 December to 29 February)

Figure 1.5 illustrates Launceston's woodsmoke problem by presenting a series of photos, each taken in 1992 from the same location, under increasing PM_{10} loadings. Visibility clearly decreases with increasing particle loadings. These photos are provided for illustrative purposes only, and cannot be used as a means of visually estimating PM_{10} concentrations.

1.5 The Tamar Valley Airshed Study

The Government of Tasmania initiated the *Tamar Valley Airshed Study* (*TVAS*) in response to concern about air pollution concentrations within the Tamar Valley, from Bell Bay industrial sources at the coast and urban sources inland at Launceston. The study commenced in 1993 and concluded in 1995.

One of the major aims of the *TVAS* was to develop a wind field and pollution-dispersion modelling system covering the entire Tamar Valley airshed. The modelling system was required to be capable of simulating dispersion of emissions from multiple sources located throughout the region. The *NUATMOS* diagnostic

wind field model, and the *CITPUFF* multiple-source Gaussian puff dispersion model were found to be the most suitable models for use in the Tamar Valley.

9 μgm^{-3} (26/6)

31 μgm^{-3} (15/5)

67 μgm^{-3} (18/6)

91 μgm^{-3} (18/5)

110 μgm^{-3} (15/6)

144 μgm^{-3} (23/5)

Figure 1.5 The City of Launceston under different 24-hour average PM_{10} loadings. These pictures are indicative only. They cannot be used as a basis for visually estimating mean daily particle concentrations. Dr. Bill Wood (*DELM*) took all of the photos in 1992.

The *Centre for Mathematical Modelling* (*CAMM*), located at Monash University (Melbourne), developed both models and provided advice throughout the study. Other members of the consulting team included *CSIRO Atmospheric Research* (*CSIRO AR*, then known as *CSIRO Division of Atmospheric Research- CSIRO DAR*), and the University of Tasmania.

A network of 10-m masts, supporting meteorological instrumentation, was established throughout the study area. Intensive campaign measurements of wind and temperature profiles were also made under poor dispersion conditions. These data were collected for use within the modelling system and to facilitate research into the air pollution climatology of the airshed.

The author was attached to the *TVAS* as a PhD student and research assistant. As a result he was closely involved in every aspect of the *TVAS*, from initial selection of meteorological station locations, the design and implementation of the measurement program, data entry and analysis, and the subsequent modelling program. *CAMM* used the digital data supplied by the author to create configuration files for the *NUATMOS* wind field model. *SEMF Consultants*, a Hobart consultancy firm, managed the day-to-day running of the *TVAS*.

This thesis represents the major, and final, report of the *TVAS*.

1.6 Research Questions and Thesis Outline

The following questions were developed to guide research progress into air pollution dispersion throughout the Tamar Valley:

1. *Spatial and temporal variation of climatic variables...*

   How do readily available climatic variables, affecting air pollution concentrations, vary throughout the Tamar Valley in space and time? Can these variables be combined to form a measure of air pollution potential? If so, what is the air pollution potential of Bell Bay and Launceston?

2. *Spatial and temporal variation of winds under anticyclonic conditions...*

   How do the mean winds in the Tamar Valley vary spatially, diurnally and seasonally under anticyclonic (poor dispersion) conditions?

3. *Modelled wind fields for each season...*

   Model representative, three-dimensional, time-varying, transport fields for contaminants during poor dispersion events in each season. What are the dominant mechanisms causing or inhibiting air pollution transport within the Tamar Valley at such times?

4. *Winter woodsmoke dispersion...*

   How is winter woodsmoke dispersed throughout the Tamar Valley? How many woodheaters can Launceston support before the *NEPC* 24-hour goal for particles is exceeded? Will the current woodsmoke reduction measures achieve the *NEPC* goal by June 2008? What effect will the introduction of reticulated natural gas have on PM_{10} concentrations? Would banning open fires and non-certified woodheaters achieve the *NEPC* goal by June 2008? Can economic incentives be focussed on a small area, or do they have to include the entire Tamar Valley?

5. *Dispersion of Bell Bay industrial emissions...*

   How are the Bell Bay industrial emissions dispersed throughout the Tamar Valley during each season under poor dispersion conditions? Will the conversion of the Bell Bay power station from oil-fired to gas-fired operation improve the air quality of the region?

This thesis will answer the research questions posed above.

Chapter Two will provide a detailed literature review. It commences with an overview of past air pollution studies within the Tamar Valley. These include a previous PhD study centred on the Bell Bay region, an investigation into Launceston's air quality, and a pilot study by *CSIRO AR* focussing on fine particles. The review then summarises the major methods of measuring and calculating atmospheric stability, and describes some integral measures of ventilation, recirculation and stagnation. Finally air pollution modelling systems will be discussed, with a detailed review of wind field modelling and Gaussian puff dispersion modelling.

Chapter Three documents the data acquisition and storage phase of the study. The 10-m mast measurements are described, with mast locations, instrumentation and performance history being provided. Descriptions of the relational database, used to store measurements and derived parameters, then follow. The chapter concludes with a detailed description of the campaign measurements, of wind and temperature profiles, collected under poor dispersion conditions.

The *NUATMOS/CITPUFF* modelling system is described in Chapter Four. Model histories, technical descriptions, validation studies and model configurations for the *TVAS* will be provided for each model.

Chapter Five analyses the three years of data collected during the *TVAS*. Data is summarised at each measurement site using wind and stability roses, and a new form of rose called a 'transport rose'. The major parameters affecting air pollution dispersion are mapped on a seasonal basis, and are combined to form an index of air pollution potential.

Vector averaged winds are calculated in Chapter Six, for all measurement intervals where the surface pressure exceeds 1020 hPa. This allows the wind variations to be described and mapped for the "average anticyclonic day" in each season.

The wind field modelling results are presented in Chapter Seven. Hourly surface wind fields are presented for two-day periods, under anticyclonic conditions, for each season. Wind fields are described and the dominant atmospheric flows highlighted. The chapter also summarises the measured vertical temperature structure of the atmosphere throughout each intensive measurement program.

Chapters Eight and Nine present the results of the *CITPUFF* modelling programme. In Chapter Eight the Launceston woodsmoke problem is modelled, with a 'Base Scenario' characterising current woodsmoke dispersion under poor dispersion conditions in winter. This is varied in a series of scenarios to determine the woodheater carrying capacity of the Tamar Valley, the effect of continuing current woodsmoke reduction policies, and the effect of the planned introduction of reticulated natural gas to the State. Further scenarios investigate the effect of a ban on the use of open fires and non-certified woodheaters, and the extent of advected woodsmoke emissions into Launceston. This final scenario shows that financial incentives to remove woodheaters can be cost effectively applied to the Launceston area only.

Chapter Nine presents modelling results for the Bell Bay industrial sources. Dispersion of SO_2 is modelled and described for each season, and results compared

with *NEPC* standards. The effect of converting the Bell Bay power station from oil-fired to gas-fired operation is then modelled.

The final chapter, Chapter Ten, discusses the results of Chapters Five to Nine, and answers the research questions posed above. It concludes with recommendations for further research.

1.7 Conclusions

This chapter has provided an introduction to the thesis. It began with a description of the Tamar Valley and surrounding areas, describing the location, topography, population distribution and climate. Air pollution sources within the area were then described, focussing on urban diffuse sources, mainly centred around Launceston, and the industrial point sources located at Bell Bay. Current national air pollution standards were then provided, along with a brief description of PM_{10} concentrations in Launceston, and the Tamar Valley Airshed Study. The chapter concludes by posing a series of specific research questions and providing an outline of the thesis.

2 Literature Review

2.1 Introduction

Chapter two provides a brief literature review of topics relevant to this study. The chapter commences with a summary of the seven air pollution studies that have occurred in the Tamar Valley since 1982. It then summarises various turbulence typing methodologies that have been developed to categorise atmospheric stability. The third section describes a methodology developed by Allwine and Whiteman (1994) to identify stagnation, ventilation and recirculation events, and regions prone to these conditions. Air pollution modelling systems are then described, with subsequent sections focussing on diagnostic and prognostic wind field models, and on Gaussian puff dispersion models.

2.2 Air Pollution Studies within the Tamar Valley

Prior to 1982 there had been no studies into air pollution levels and dispersion within the Tamar Valley, despite growing concern over air pollution issues within the airshed. Vegetation damage, as a result of emissions from the Bell Bay sources, had been reported in the area since the early 1960s. Woodsmoke was also an issue, following the growth in the use of woodheaters in Australia from 1978. This date corresponds to the government decision to adopt world parity prices for oil products. This step resulted in a dramatic price increase for heating oil, and the subsequent large-scale adoption of woodheaters throughout Australia. (Low *et al.*, 1989; Todd, 1996)

Since 1982 there have been seven studies investigating various aspects of the air pollution problem within the Tamar Valley. These are:

- the *Air Quality Study in the Lower Tamar Valley* (1982 to 1986);
- the *Investigation into Air Pollution, Environmental Health and Respiratory Diseases, Launceston and Upper Tamar Valley* (1991 to 1994);
- the *Tamar Valley Airshed Study* (1993 to 1995);
- the *Comalco Local Airshed Study* (1993 to 1997);
- the *Air Emissions Trials for the National Pollutant Inventory* (1995 to 1996);
- the *Australian Fine Particles Pilot Study* (1997); and
- the *National Pollutant Inventory (Tamar Valley Region)* (2000 to -).

2.2.1 The Air Quality Study in the Lower Tamar Valley

The first air pollution study in the Tamar Valley commenced in 1982, and was conducted as part of a PhD program. The study was focussed on industrial emissions from the Bell Bay region and included meteorological and chemical measurements at a number of sites in the area. In addition to the thesis (Low, 1986), three papers were published based on findings of the study (Low, 1988; Low and Bloom, 1988; Low *et al.*, 1989).

Low (1988) and Low and Bloom (1988) monitored bulk atmospheric deposition at 17 locations, each within 10 km of Comalco, in the lower Tamar Valley. Monthly samples were collected in glass deposit gauges, mounted on wooden stands 3 m above the ground. The sampling program commenced in July 1982 and concluded in August 1983. The pH of each sample was measured, normally within two days of collection. Soluble fluoride (F^-) originating from the Comalco emissions was then measured using an ion-selective electrode.

Acidic samples were largely attributed to the oil-fired thermal power station. Acidity was greatest (i.e. pHs were lowest) at sampling locations close to the power station, especially at locations to the northwest or southeast of the station. This was attributed to the effects of the frequent sea breezes and down-valley drainage flows. Acidic samples were collected at even the most distant sampling location from the power station, indicating that Bell Bay emissions could penetrate significant distances inland. (Low, 1988)

The site with the highest frequency of acidic samples was located 1 km to the northwest of the power station, indicating the importance of the drainage flows. The second highest frequency was experienced 7 km to the east of the power station, at a site on the opposite side of the Tippogoree Hills. This occurred as a result of the prevailing westerlies, which frequently transported emissions from the 107-m power station stack out of the valley to the east. (Low, 1988)

The greatest mean fluoride deposition rate (approximately 150 times that of the background) occurred at a site located 800 m to the east-southeast of Comalco. However, elevated rates were measured at many sites within 3 km of the smelter. Fluoride distribution was largely dependent on the meteorological conditions experienced during each monthly sampling period. Sea breezes, down-valley drainage flows and local katabatic flows resulted in greater deposition occurring at sites located along the valley axis, and to a lesser extent to the southwest of the plant. The Comalco plume was also noted to penetrate inland over significant distances. A mean monthly deposition rate 3.3 times the background rate was recorded at the most distant site, 9.7 km east-southeast of the plant. (Low and Bloom, 1988)

Comalco no longer emits significant levels of fluoride. In 1997 the wet-scrubbing technology was replaced by a more modern dry-scrubbing system. The six potroom fume scrubbers were replaced by a single dry-scrubbing stack.

The third paper published from the *Air quality study in the lower Tamar Valley* (Low *et al.*, 1989) was concerned with atmospheric flows. Tethered balloon wind and temperature soundings were collected at Bell Bay on two separate spring nights (23 September, 1982 and 5-6 October, 1982). A network of six Lambrecht Woelfle type anemometers, each mounted on poles at a height of 10 m, was also established in the Bell Bay region.

Both sets of soundings showed a surface stable layer, which developed overnight, extending to heights between 200 m and 300 m. An elevated temperature inversion, present between 425 m and 530 m above the ground, was also noted during the second of the two spring nights. Both sounding programs revealed the presence of

local drainage flows in the lower levels, with northerly or northeasterly synoptic flows above.

An elevated stagnant layer (Froude number 1.39) was observed, between heights of 60 and 80 m, in the profile collected at 23:10 on 5 October, 1982. The layer was attributed to either of two causes. The first was upstream blocking of the persistent northeasterly synoptic winds by the Asbestos and Dazzler Ranges, which form the southwestern wall of the valley. The second possible cause, which Low *et al.* considered the more probable, was the development of a lee wave initiated by the flow of the synoptic winds over the northeastern wall of the valley (Mt. George and the Tippogoree Hills). Regardless of the cause, the stagnant layer resulted in a gentle (0.2 ms^{-1}) southwesterly katabatic flow, from the Asbestos and Dazzler Ranges, draining out of West Arm. This reached Bell Bay as a westerly to west-northwesterly flow. The southwesterly flow was detected by measurements from the 10-m anemometer network. Another katabatic flow was identified as draining out of the saddle between Mt. George and the Tippogoree hills to the northeast of Bell Bay. Figure 2.1 shows the possible katabatic flows identified by Low *et al.* (1989).

2.2.2 Investigation into Air Pollution, Environmental Health and Respiratory Diseases

A multi-disciplinary study of air pollution in the Launceston region was conducted between 1991 and 1994 (Working Party, 1996). The expert working party, consisting of academics, environmental officers at both state and local government level, and medical specialists, made the following measurements:

- TSP, PM_{10} or $PM_{2.5}$ samples with subsequent filter analysis for lead at five sites located within Launceston or the Upper Tamar Valley (Glen Dhu, Ti Tree Bend, Newnham, East Launceston and Newstead);
- Ambient ozone measurements (Glen Dhu only);
- Surface meteorological measurements including air temperature, wind speed and direction, sigma-theta, relative humidity, solar radiation, and barometric pressure (Glen Dhu, Ti Tree Bend, Hobler's Bridge); and

Two overnight tethered-balloon sounding programs (September 1991) at Glen Dhu and Ti Tree Bend;

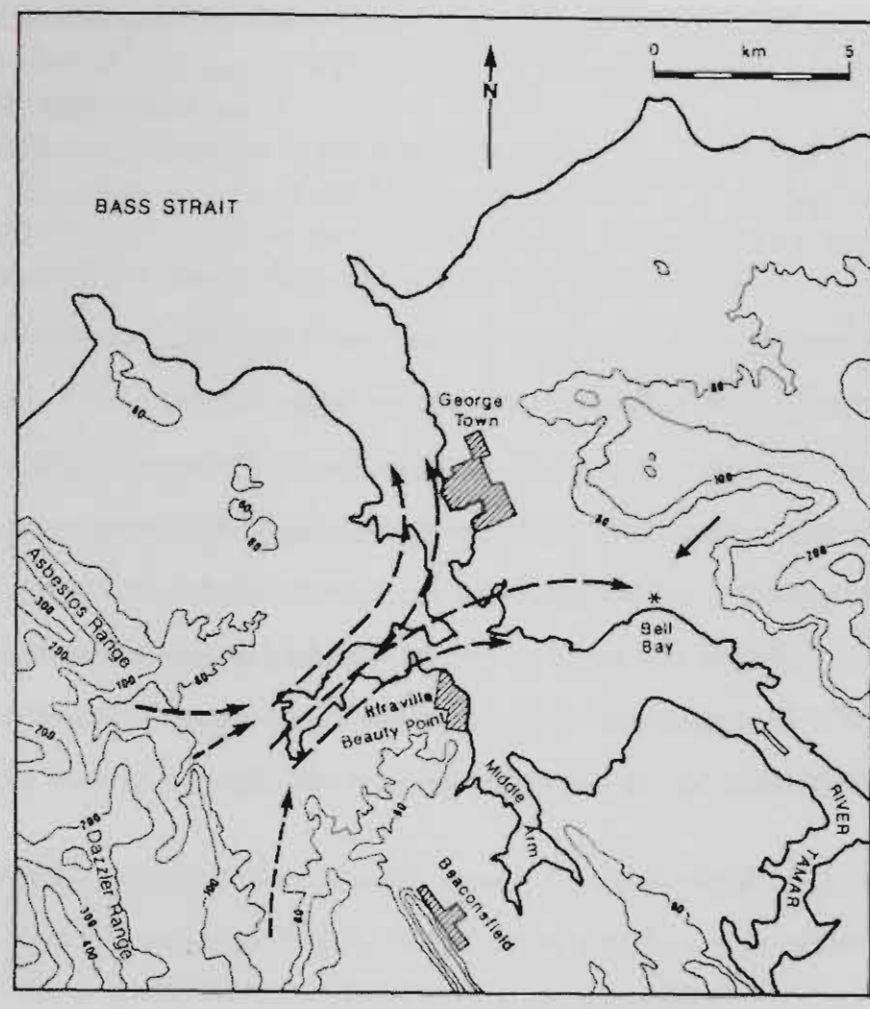

Figure 2. 1 Possible katabatic flows identified by Low *et al.* (1989) occurring when a northeasterly synoptic wind interacts with the valley walls to produce stagnation in the lower Tamar Valley. The dashed streamlines represent katabatic flows draining off the Asbestos /Dazzler Ranges and out of West Arm. The solid arrow represents a katabatic flow from the northeastern wall of the valley, whereas the hollow arrow represents the large-scale southeasterly down-valley flow. The tethered-balloon launching site is identified by a star. (Source: Low *et al.*, 1989, Figure 5, p. 1933)

In addition, medical records from the Launceston General Hospital were studied for the period 1980 to 1993 to identify pattern in:

- In patient admissions for bronchial asthma;
- In patient admissions for total respiratory illness;
- Presentations at the Department of Emergency Medicine with respiratory causes; and
- Upper and lower respiratory effects.

The following major conclusions were reached by the study:

- Launceston has a significant, and potentially serious, winter air pollution problem which is exacerbated by the local topography and meteorology;
- The principal source is particulates, mainly derived from wood combustion, however this is supplemented by vehicle and industrial sources;

- Particulate concentrations in winter frequently exceeded the then proposed 24-hour standard of 120 μgm^{-3}, with 19 exceedences occurring during winter 1992 and 4 the subsequent year;
- Photochemical pollution was not a problem in the Launceston airshed; and
- The investigations into local medical records failed to find conclusive cause and effect relationships between particulate pollution and some respiratory diseases. This was probably due to the small population of the region.

The tethered-balloon soundings were reported in an appendix attached to the main report (Nunez, 1991). Soundings in both locations revealed the presence of light shallow katabatic winds draining off the local topography during the early evening. As the nights progressed the main down-valley flow developed, extending throughout the entire vertical extent of the soundings (600 m). The surface-based temperature inversion reached a height of 140 m on the first night (12-13 September, Ti Tree Bend) and 240 m on the second night (23-24 September, Glen Dhu). Nunez theorised that inversion height was strongly controlled by the upper level winds.

Nunez also produced a conceptual model describing the physical processes causing worst-case air pollution dispersion in the Launceston region. This worst-case scenario operates during winter, under anticyclonic conditions.

Figure 2.2 shows that at nighttime, the presence of the anticyclone causes clear skies and subsequent radiative cooling at the surface, in conjunction with light winds aloft (at approximately 850 hPa, i.e. 1500 m). These conditions facilitate the development of a strong radiative temperature inversion at the surface. A gentle, stable down-valley drainage flow results. Woodsmoke emissions, prompted by the cold temperatures, are entrained into this down-valley flow and gently drift out of the valley following its axis.

The temperature inversion is eroded the next morning by solar radiative warming of the surface, resulting in a surface-based layer of neutral stability, which increases the mixing depth. A gentle anabatic flow develops, which transport contaminants further inland, recirculating emissions from the previous night. These conditions can last for several days in winter, resulting in emissions building up as contaminants are recycled in the diurnal anabatic and katabatic flows.

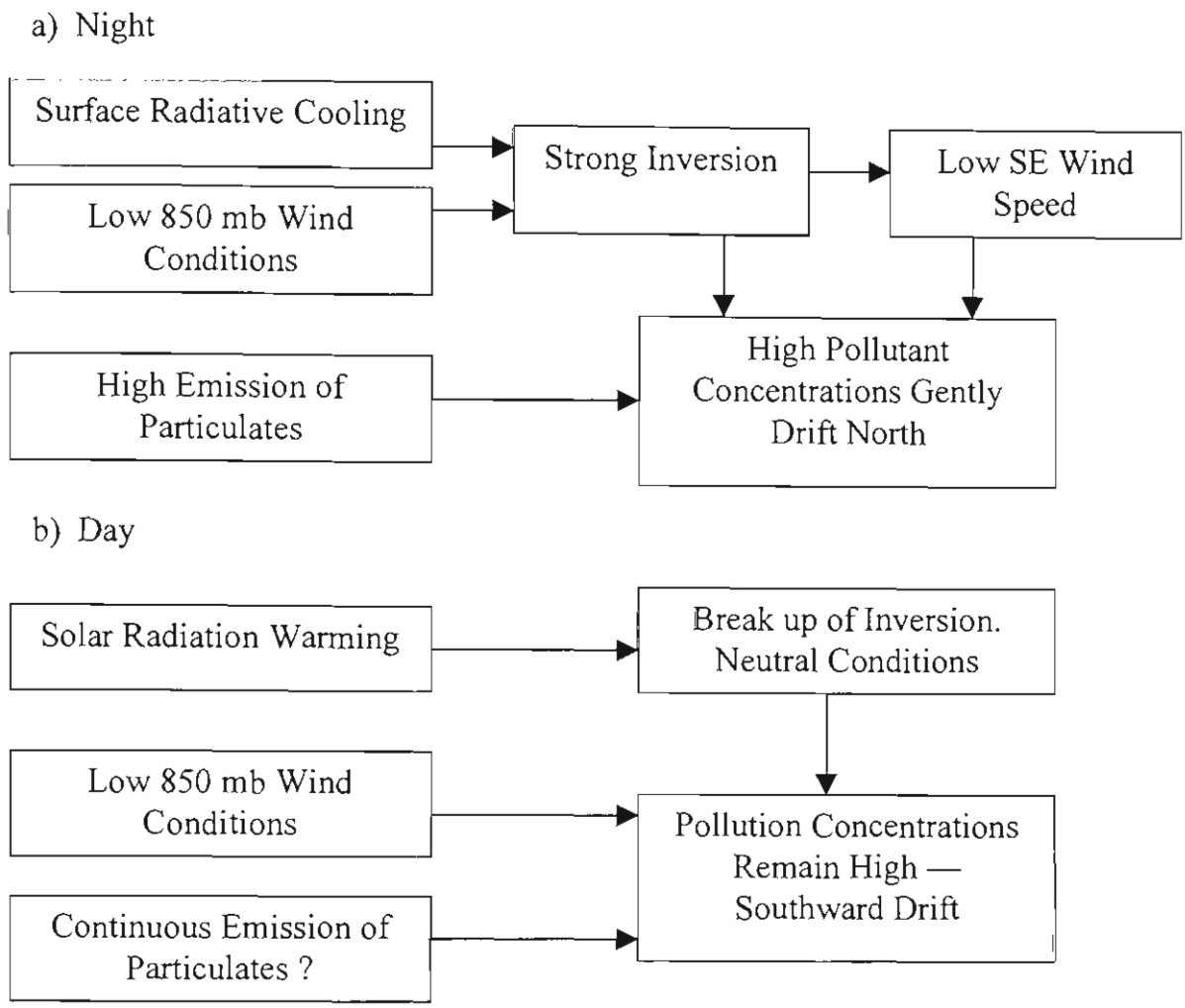

Figure 2.2 Conceptual model of the processes resulting in worst case pollution dispersion in the Tamar Valley. These processes occur during winter, under anticyclonic conditions. (Redrawn from Nunez, 1991, Figure 12)

2.2.3 The Tamar Valley Airshed Study

The Tamar Valley Airshed Study (*TVAS*) was initiated by the state government, running between 1993 and 1995. Its major aim was the development of an airshed management system, consisting of the *NUATMOS/CITPUFF* wind field and dispersion modelling system, and the collection of field data required to support the models. Results from *NUATMOS/CITPUFF* were displayed using the *IDRISI* raster-based *GIS* system.

The author was attached to the *TVAS* as a PhD student. He helped to design and run the measurement program, utilizing both continuous and campaign measurements.

He was directly involved in the collection of temperature and wind profile measurements. The author was responsible for entering the data into spreadsheets and providing an initial analysis of the results. *CAMM* used the digital data supplied by the author to create configuration files for the *NUATMOS* wind field model. The author created and ran the *CITPUFF* scenario used to demonstrate the *NUATMOS/CITPUFF* modelling system. The *TVAS* concluded with the production of a final report (Carter *et al.*, 1995), which the author helped to write. It included a brief analysis of the air pollution climatology of the Tamar Valley, also produced by the author.

This thesis represents the final report for the study, and presents and analyses the results in far greater detail than were originally presented in Carter *et al.* (1995). The thesis also extends the work by the production of a detailed climatology and modelling program.

2.2.4 The Comalco Local Airshed Study

The Comalco Aluminium Smelter at Bell Bay has also conducted a study into the dispersion of its atmospheric emissions. This has resulted in the development of a tailored version of the *AUSMET* diagnostic wind field model and the *AUSPUFF* Gaussian puff dispersion model (Ross *et al.*, 2000).

The author was involved in the preliminary studies, and helped to plan and execute the field program. Wind profiles were measured for each season, under anticyclonic conditions, at three sites in the lower Tamar Valley. Temperature profiles were measured at one of these sites, located at Bell Bay. A limited number of 10-m weather stations were established, however this data were supplemented using data from the *TVAS* network.

The model system was validated using measurements of SO_2 and dry deposition of gaseous hydrofluoric acid (HF). Unfortunately the results of the entire airshed study are unavailable, as they are considered "commercial in confidence".

Ross *et al.* (2000) did however, publish a brief description and evaluation of the site-specific modelling system. The *AUSMET/AUSPUFF* system is slightly more

advanced than the *NUATMOS/CITPUFF* system, used in the *TVAS* and presented in this thesis, however the general operating principles are the same.

Figure 2.3 shows the predicted 24-hour average ground-level gaseous HF concentrations for 19 June 1997, prior to Comalco's changeover to dry scrubbing. A southeasterly drainage flow was present for the entire 26-hour modelling period, directing emissions out of the valley towards the northwest. The plume passed to the northeast of George Town, and was constrained by Mt. George further to the northeast. The figure also provides the locations of the monitoring sites.

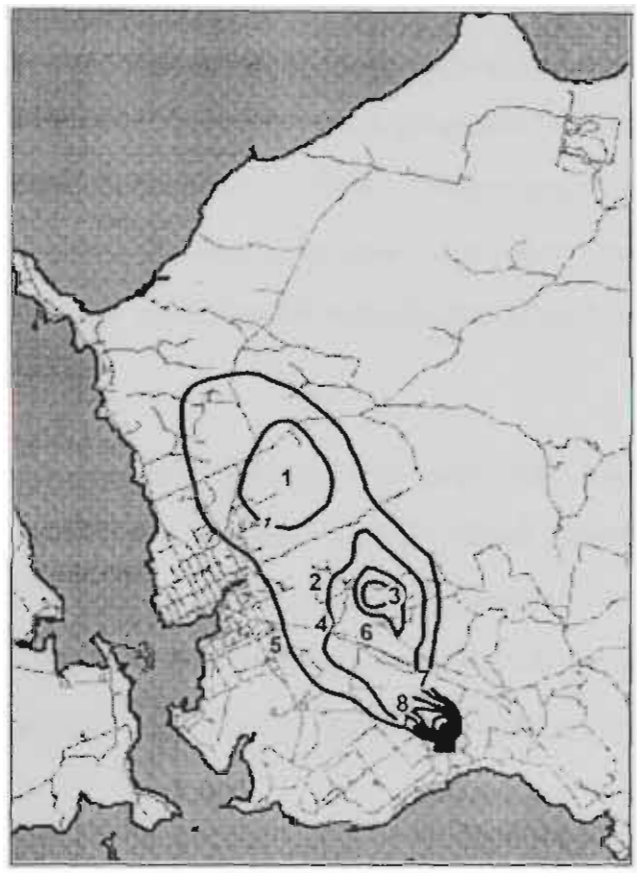

Figure 2.3 Predicted winter 24-hour average ground-level HF concentrations, modelled using Comalco's *AUSMET/AUSPUFF* dispersion modelling system. Gaseous HF emissions from the Comalco plant were modelled prior to the smelter's conversion to dry scrubbing. The concentration contour levels are: 0.5, 1, 2, 2.9, 5, 7.5 and 10 μgm^{-3}. The numbers mark the position of the monitoring sites. (Source: Ross *et al.*, 2000, Figure 4.1, p. 181)

The model was found to show very good agreement between observed and predicted concentrations at the "far-field" (Site 1) and "intermediate-field" (Sites 2, 4 and 5) sites. The "near-field" sites (Sites 7 and 8) and two of the "intermediate-field" sites (Sites 3 and 6) were found to significantly overpredict concentrations. The

overpredictions were attributed to terrain effects at Site 3 (Mt. George) and the difficulties in predicting near-field concentrations due to uncertainties in characterising initial plume rise, vertical dispersion and fumigation.

Ross *et al.* (2000) found that the model predictions were within a factor of two for five of the eight sites, however it had a clear tendency to overpredict. Significant overprediction occurred at the remaining three sites.

2.2.5 The Air Emissions Trials for the National Pollutant Inventory

Methodologies were developed for the estimation and collation of point source and diffuse emissions during the National Pollutant Inventory (NPI) trials. Results from the NPI trials are reported in Boyle *et al.* (1996). Four study regions in Australia were chosen to test the newly developed inventory systems. These were: Dandenong (Victoria), Port Pirie (South Australia), Newcastle (New South Wales) and Launceston.

Major industries in each study region were asked to provide data on their estimated emissions. Diffuse sources, such as motor vehicles, small industrial and commercial services, and domestic sources were also estimated. Emission estimations of the 30 selected air pollutant species were stored on a computerised database. The *AUSPLUME* Gaussian plume model was used for modelling dispersion of selected pollutant species.

The Launceston trial ran between 1995 and 1996, and focussed on a 200 km^2 area, centred over the city, which was defined to incorporate the maximum number of significant point sources.

Figure 2.4 shows the predicted maximum 24-hour PM_{10} concentrations (μgm^{-3}) for the NPI Launceston study region in 1994. Concentrations were high, reaching maximums of greater than 200 μgm^{-3}. The figure shows a strong northeast/southwest gradient, with maximum concentrations occurring in the southwest.

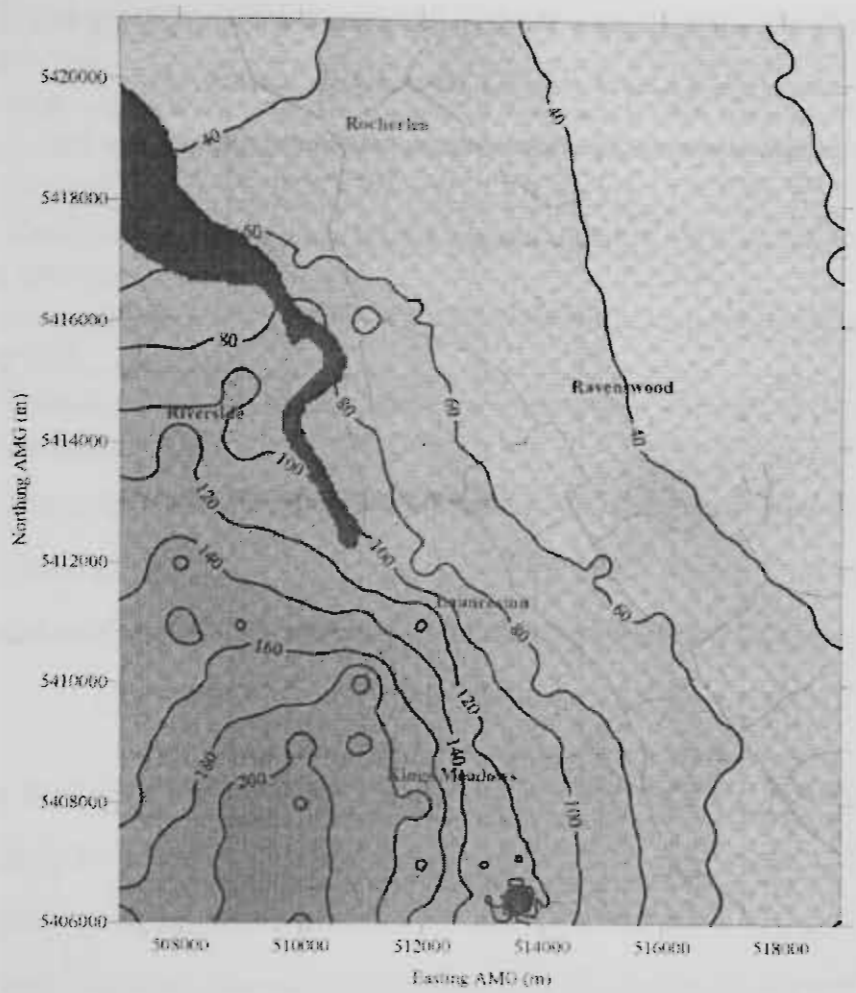

Figure 2.4 Predicted maximum 24-hour PM_{10} concentrations (μgm^{-3}) from the National Pollutant Inventory emission trials, Launceston study region 1994. Concentrations were modelled using the *AUSPLUME* Gaussian plume dispersion model. Source: Boyle *et al.*, 1996, Figure 2.26, p. 2-39.

2.2.6 The Australian Fine Particles Pilot Study

In 1996, Environment Australia commissioned the *Australian Fine Particle* (AFP) Study. CSIRO Atmospheric Research (CAR) was contracted to conduct a pilot study in six cities: Sydney, Brisbane, Melbourne, Canberra, Launceston and Adelaide. Sampling occurred between July 1996 and August 1997, with the Launceston phase commencing on 11 June 1997 and finishing approximately seven weeks later on 28 July 1997.

A wide range of aerosol properties was monitored at Ti Tree Bend in Launceston using many different instruments including:

- a Micro-Orifice Uniform Deposit Impactor (MOUDI), which is effectively a 12-stage cascade impactor. The MOUDI collected 24-hour samples on a series of eleven 47 mm filters (0.4 μm pore size), each sub-sampling a different size range,

with 50 % cut-points ranging between 0.056 μm and 18 μm. The final (residual) sub-sample was collected on a 37 mm teflon-backed Fluoropore filter, having a 1 μm pore size. All filters were weighed to determine concentration within each size range, and were subject to analysis for chemical composition of each sub-sample. In total, seven samples were collected on a six-day cycle.

- a pair of Radiance Research type M903 nephelometers, one heated to 40 °C and the other unheated.
- a Rupprecht and Patashnick TEOM series 1400 continuous mass balance, recording $PM_{2.5}$.
- a Nolan-Pollack ultrafine condensation nuclei counter, measuring ultrafine particle number concentration.

Many papers have been produced, based on the results of either the seven week Launceston phase (Keywood *et al.*, 1998; Keywood *et al.*, 2000a; Gras *et al.*, 2000), or the Australia-wide sampling program (Keywood *et al.*, 1999; Keywood *et al.*, 2000b).

Results from the Launceston measurements indicate that the PM_{10} loading ranged from moderately low levels (35 μgm^{-3}) to very high levels (114 μgm^{-3}). Four of the seven wintertime samples exceeded the *NEPC* PM_{10} standard of 50 μgm^{-3}. As the particle loading increased, the size distribution moved from being a poorly-defined bimodal distribution, to a well-defined unimodal distribution (Figure 2.5). The unimodal distribution showed particulate mass concentrated between 0.6 and 1 μm diameters. (Keywood *et al.*, 1998)

Table 2.1 summarises the particle distributions in terms of the mean mass percentage of the commonly used measures of particulate concentration: TSP, PM_{10}, $PM_{2.5}$ and PM_1. Sample L9 was not included in the means, as it was collected for polycyclic aromatic hydrocarbon (PAH) determination, thus reducing the sample size to six. The table shows that 90 % of total suspended particulates (TSP) are within the respirable particle (PM_{10}) range, with 78 % of these being fine particles ($PM_{2.5}$). Hence it can be seen that the particulates within the Launceston airshed are dominated by fine particles. (Keywood *et al.*, 2000a)

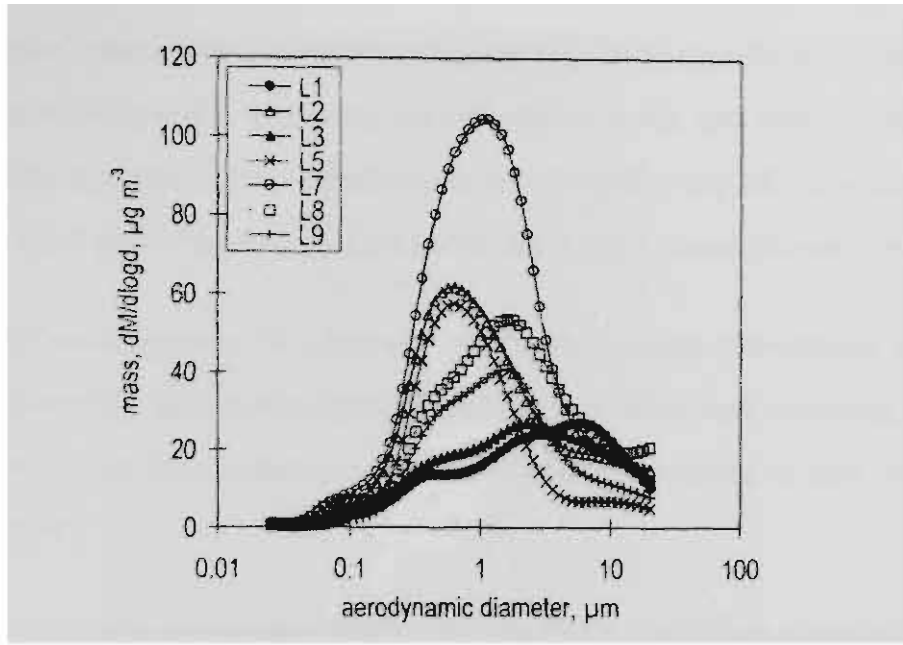

Figure 2.5 Mass size distributions for seven samples collected at Ti Tree Bend by CSIRO AR during June and July 1997. The mass distributions display gradation between poorly-defined bimodal (samples L1 and L3) and unimodal (samples L2, L5 and L7) with increasing particle loading. (Source: Keywood *et al.*, 1998, Figure 1, p. 228)

Table 2.1 Matrix of mean mass percentage of TSP, PM_{10}, $PM_{2.5}$ and PM_1 from the CSIRO deployed MOUDI. The figures are based on six 24-hour average samples collected at Ti Tree Bend during winter 1997.

	TSP	*PM_{10}*	*$PM_{2.5}$*	*PM_1*
TSP	100 %			
PM_{10}	90 %	100 %		
$PM_{2.5}$	70 %	78 %	100 %	
PM_1	46 %	51 %	65 %	100 %

(Source: Keywood *et al.*, 2000a, Table 4, p. 421)

Chemical analyses of the filter contents helped identify the sources of the particles. Ion chromatography was used to determine the concentration of various soluble ions. Among these were "non sea-salt potassium" ($nssK^+$), total potassium (K^+) and chlorine (Cl^-). PAHs and $nssK^+$ were used as biomass burning tracers, whilst K^+ and Cl^- in the coarse range indicated particle origins other than wood-burning, such as seawater and soil dust.

High particle loadings were associated with fine particles and the biomass burning tracers, indicating that increasing particle loadings are heavily influenced by wood-burning. In contrast, low particle loadings were associated with coarse particle sizes and the presence of K^+ and Cl^-, suggesting the dominance of non-woodburning sources in these instances.

The woodsmoke source was also seen to alter the acid-base equilibrium of the aerosol, concentrating acidic species (especially NO_3^-) in the fine particle ranges. Visibility, as determined by the nephelometer aerosol scattering efficiencies, was also strongly affected by the fine particle sizes, showing a strong diurnal cycle.

Motor vehicles were found to be a less significant source than woodsmoke sources. This was displayed by differences in the diurnal cycles of aerosol scattering, continuous $PM_{2.5}$ and CN number concentration, and the presence of lead. (Keywood *et al.*, 1997,1998)

Comparisons with measurements made in the other five Australian cities indicated that Launceston and Canberra were both dominated by unimodal particle size distributions. The chemistry samples collected in Launceston and Canberra indicated that biomass burning processes were dominant. In contrast, Sydney, Brisbane, Melbourne and Adelaide showed bimodal distributions having both coarse and fine particles. In these cases the chemical composition of the samples indicated that both mechanical particle formation processes and combustion were important sources. (Keywood *et al.*, 1999; Keywood *et al.*, 2000b)

2.2.7 The National Pollutant Inventory (Tamar Valley Region)

With the conclusion of the NPI trials in 1996, NPI units were established in each of Australia's states and territories. The Tasmanian NPI unit commenced with estimating point source and diffuse emissions to air and water in the Hobart region. In 2000 it commenced estimating emissions within the Tamar Valley. The Tamar Valley program is currently underway and no results have been released to date.

2.3 Turbulence Typing

"Air [pollution] concentration patterns are controlled by atmospheric diffusion, a process that depends on the state of the atmospheric turbulence at any location and time ..." (Gifford, 1976, p68). Turbulence is therefore an important parameter in air pollution studies, however it is difficult and expensive to directly measure. To overcome this a number of empirically based, qualitative turbulence typing schemes

have been developed. These classify turbulence in terms of atmospheric stability. Atmospheric stability is the tendency of the atmosphere to resist, or enhance, vertical motion and existing turbulence (Gifford, 1976).

The most widely used of these is the *Pasquill-Turner Stability Scheme.* However the *Brookhaven National Laboratory (BNL) Scheme*, which is closely related to that of Pasquill, has also seen wide use.

In 1961 Pasquill (1961; 1962) developed a stability classification with six discrete categories: A to F. This was further modified by Turner (1961; 1964) to include a category, G, corresponding to near calm conditions on clear nights. Table 2.2 summarises the finalised Pasquill-Turner Stability Scheme.

Table 2.2 The Pasquill-Turner stability scheme

Stability Description	*Class Descriptor*
Extremely unstable	A
Moderately unstable	B
Slightly unstable	C
Neutral	D
Slightly stable	E
Moderately stable	F
Near calm	G

Many methods exist for determining Pasquill stability classes, the main ones being compared by Mitchell (1982). These are:

- Vertical Temperature Gradient (DT/DZ);
- U.S. National Weather Service Pasquill-Turner (NWS-PT);
- Sigma-Theta (Sigma); and
- Modified Sigma Theta (MST).

A further technique, the Modified Smith Method (MS), described by Cope *et al.* (1985), will also be discussed.

In all cases stability classes range from A (extremely unstable) through D (neutral) to G (extremely stable).

2.3.1 Vertical Temperature Gradient (DT/DZ)

The stability classes are related to the vertical temperature gradient between two heights, typically 10-m and 60-m (Table 2.3). USNRC (1972) requires the lower measurement to be at 10-m and the subsequent measurement at least 30-m higher. Temperature inversions are associated with poor vertical mixing, and hence stable

conditions, whereas strong lapse conditions are associated with convective turbulence and hence unstable conditions. Routine measurements are normally conducted using instrumented towers, however any accurate method of temperature gradient measurement may be used. Mitchell (1982, p765) states that this method "...is currently the most frequently used for estimating dispersion at nuclear power plant sites in the United States", however Sedefian and Bennett (1980), in their comparison of stability categorisation schemes, found that it performed poorly. Guidelines for this technique appear in USNRC (1972).

Table 2.3 Stability class determination using DT/DZ

Stability Classification	*Pasquill Category*	*Temperature Change with Height (°C/100m)*
Extremely unstable	A	< -1.9
Moderately unstable	B	-1.9 to -1.7
Slightly unstable	C	-1.7 to -1.5
Neutral	D	-1.5 to -0.5
Slightly stable	E	-0.5 to 1.5
Moderately stable	F	1.5 to 4.0
Extremely stable	G	> 4.0

(Extracted from DeMarrais, 1978, p1958)

2.3.2 National Weather Service Pasquill-Turner (NWS-PT)

This technique is based on the work of Turner (1964). It utilises standard observations of wind speed and estimates of a net radiation index, using cloud cover and solar altitude, to classify stability in terms of "Turner Classes". As such this data is ideally suited to routine hourly measurements at airports and meteorological stations, and has frequently been applied to historical data bases and air pollution studies. However it is important to, if at all possible, use on-site data when calculating stability. Off-site meteorological data may poorly represent the conditions at the on-site location due to terrain differences and distance between the two sites.

Turner classes range from one to seven, with one applying to strongly convective, light wind conditions (extremely unstable), four applying to purely mechanical turbulence (neutral), and seven for extremely stable stratification. Table 2.4 describes Turner's system, which is completely objective and so may be calculated using a simple computer program.

The Turner Classes are calculated from Table 2.4 as follows:

1. If total cloud cover = $^{10}/_{10}$ and ceiling < 7000 ft, then the Net Radiation Index (NRI) = 0 (Regardless of whether it is day or night).
2. For night-time (between sunset and sunrise):
    a. If total cloud cover ≤ 4/10, then NRI = -2.
    b. If total cloud cover > 4/10, then NRI = -1.
3. For daytime:
    a. Determine the *Insolation Class Number* (ICN) as a function of solar altitude from Table 2.5
    b. If total cloud cover ≤ $^{5}/_{10}$, then NRI = ICN.
    c. If cloud cover > $^{5}/_{10}$, then modify ICN (MICN) as follows:
        i. If Ceiling < 7,000 ft, then MICN = ICN-2.
        ii. If 7,000 ft ≤ Ceiling < 16,000 ft, then MICN = ICN-1.
        iii. If total cloud cover = $^{10}/_{10}$ (and Ceiling ≥ 7000 ft), then MICN = ICN-1.
        iv. If Steps i. to iii. have not modified ICN, then MICN = ICN.
        v. If MICN < 1 then MICN = 1.
        vi. Use NRI = MICN in Table 2.4

(Panofsky & Dutton, 1984, p140; Turner, 1964, p91)

Table 2.4 Definition of Turner classes

Wind Speed (knots)	*Net Radiation Index (NRI)*						
	4	*3*	*2*	*1*	*0*	*-1*	*-2*
0-1	1	1	2	3	4	6	7
2-3	1	2	2	3	4	6	7
4-5	1	2	3	4	4	5	5
6	2	2	3	4	4	5	6
7	2	2	3	4	4	4	5
8-9	2	3	3	4	4	4	5
10	3	3	4	4	4	4	5
11	3	3	4	4	4	4	4
≥12	3	4	4	4	4	4	4

(Panofsky & Dutton, 1984, p140; Turner, 1964, p91)

Table 2.5 Determination of Insolation Class Number

Solar Altitude (a)	*Insolation*	*Insolation Class Number (ICN)*
60° < a	Strong	4
35° < a ≤ 60°	Moderate	3
15° < a ≤ 35°	Weak	2
a ≤ 15°	Very weak	1

(Panofsky & Dutton, 1984, p140; Turner, 1964, p91)

Turner (1964) notes that since urban areas do not become as stable in the lower layers as non-urban areas, stability classes six and seven should be reclassified as class-5 in urban areas. Gifford (1976) notes that Turner's numerical labelling of classes was fortuitous as the classes (intentionally) corresponded with Pasquill's alphabetic classes. However, Golder (1972), after consideration of a large amount of

data, concluded that Turner classes should be converted to Pasquill classes as follows:

- 1 to A;
- 2 to B;
- 3 to C;
- 4 to D;
- 6 to E; and
- 7 to F.

Pasquill-Turner Stability classes are calculated using Table 2.6.

Table 2.6 Stability class determination using Pasquill-Turner classes

Wind speed at 10-m (ms^{-1})	*Day-time Insolation*			*Night-time Conditions*	
	Strong	*Moderate*	*Slight*	*Thinly Overcast or ≥ 4/8 Low Cloud*	*Clear or ≤ 3/8 Cloud*
<2	A	A-B	B		
2-3	A-B	B	C	E	F
3-5	B	B-C	C	D	E
5-6	C	C-D	D	D	D
>6	C	D	D	D	D

Note: Neutral conditions, class-D, are applicable to heavily overcast skies or to strong winds. The degree of cloudiness is defined as that fraction of the sky above the local apparent horizon that is covered by clouds.
Modified from Panofsky & Dutton (1984, p242); Hanna (1982, p3)

2.3.3 Sigma Theta (Sigma)

The standard deviation of the horizontal wind fluctuations at 10-m elevation, sigma-theta ($\sigma\theta$), can be related to the stability class, based upon the assumption that small standard deviations are associated with stable conditions, and large standard deviations with unstable conditions. Table 2.7 summarises stability class determination using sigma-theta.

Table 2.7 Stability class determination using sigma-theta

Stability Classification	*Pasquill Categories*	*Sigma Theta ($\sigma\theta$)*
Extremely unstable	A	$\sigma\theta \geq 22.5°$
Moderately unstable	B	$22.5° > \sigma\theta \geq 17.5°$
Slightly unstable	C	$17.5° > \sigma\theta \geq 12.5°$
Neutral	D	$12.5° > \sigma\theta \geq 7.5°$
Slightly stable	E	$7.5° > \sigma\theta \geq 3.8°$
Moderately stable	F	$3.8° > \sigma\theta \geq 2.1°$
Extremely stable	G	$\sigma\theta < 2.1°$

(Extracted from Clark, 1983, p67; DeMarrais, 1978, p1958)

The minimum acceptable averaging time period is ten minutes, however the usual averaging time used is one hour. Sigma-theta can be estimated by dividing the range of the horizontal wind fluctuations by six, as originally suggested by Markee (1963) and advocated by Gifford (1976), and more recently used by Low (1986) and Mitchell (1982). Guidelines for using sigma-theta to calculate stability classes appear in USNRC (1972).

2.3.4 Modified Sigma Theta (MST)

This technique, presented by Mitchell and Timbre (1979), is a modification of the sigma-theta technique. It utilises the sigma-theta method by day and a modification to account for horizontal meander at night. This is because horizontal meander increases at night during periods of lower wind speed and stronger vertical thermal stability (Mitchell, 1982). Night time is defined as the period from one hour before sunset to one hour after sunrise. Table 2.8 summarises this technique.

Table 2.8 Stability class determination using the modified sigma-theta technique

Sigma-Theta	*Daytime Stability Class*	*Wind Speed (m/s)*	*Night-time * Stability Class*
$\sigma\theta \geq 22.5°$	A	$u < 2.4$	G
		$2.4 \leq u < 2.9$	F
		$2.9 \leq u < 3.6$	E
		$u \geq 3.6$	D
$22.5° > \sigma\theta \geq 17.5°$	B	$u < 2.4$	F
		$2.4 \leq u < 3.0$	E
		$u \geq 3.0$	D
$17.5° > \sigma\theta \geq 12.5°$	C	$u < 2.4$	E
		$u \geq 2.4$	D
$12.5° > \sigma\theta \geq 7.5°$	D	all wind speeds	D
$7.5° > \sigma\theta \geq 3.8°$	E	all wind speeds	E
$3.8° > \sigma\theta \geq 2.1°$	F	all wind speeds	F
$\sigma\theta < 2.1°$	G	all wind speeds	G

* Night-time is defined as the period from one hour before sunset to one hour after sunrise.
(Mitchell, 1982)

2.3.5 Modified Smith Method (MS)

The modified Smith method (Smith, 1972) has been described in Cope *et al.* (1985). This uses similar parameters to NWS-PT to estimate the Pasquill stability category from surface meteorological data. These are:

- 10-m wind speed (ms^{-1});
- incoming solar radiation (Wm^{-2});
- cloud cover (octas); and
- time of day.

Cope *et al.* (1985) produced a nomogram which is used to determine the Pasquill stability category on the basis of these variables (Figure 2.6).

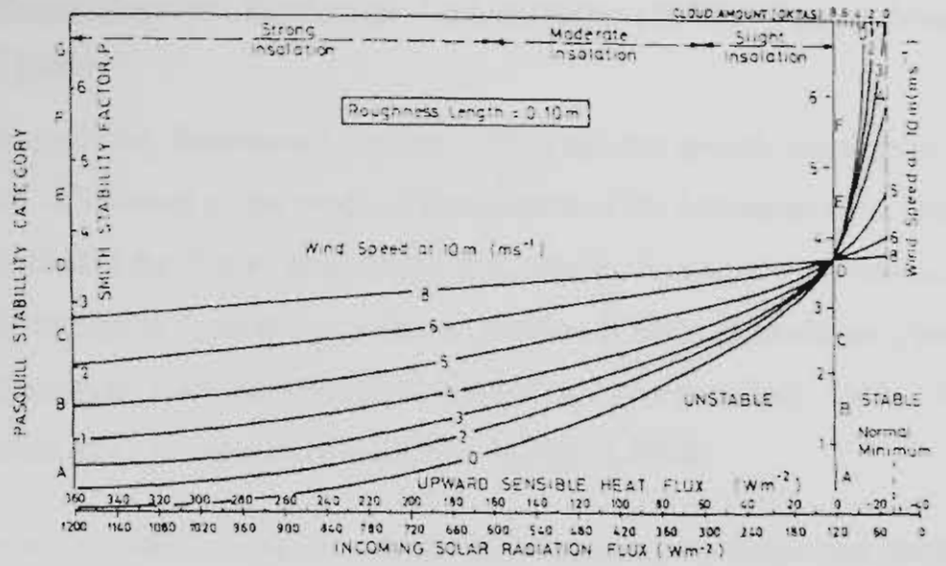

Figure 2.6 Nomogram for the determination of Pasquill stability category from surface meteorological data. (Source: Cope *et al.*, 1985)

2.3.6 Applicability of the Pasquill Stability Classification Techniques.

Mitchell (1982, p772) compared the stability classification schemes mentioned above and concluded that:

In terms of application to practical problems involving low-level sources the following suggestions are offered. At the phase of a siting study or impact analysis where only the magnitude of short-term or long-term dispersion estimates are needed, the use of historical airport-type data and the use of the NWS-PT method to classify the atmospheric stability is reasonable. However, at a study phase where a particular source, site and or receptors are involved, and short-term or long-term dispersion estimates are needed, then the use of on-site wind data (from a properly selected location) and the MST method to classify atmospheric stability is reasonable.

Of course, in the latter case, the use of vertical temperature gradient data from an on-site tower and the employment of the DT/DZ method to classify stability could be used as well. An advantage, however, of the MST approach would be in the use of a smaller tower, less instrumentation, and reduced maintenance calibration, since only a 10-m wind system would be needed.

2.3.7 Brookhaven National Laboratory (BNL) Turbulence Types

This typing scheme, developed by Smith (1951), is a site specific measure of turbulence. It is based on the range of fluctuations of the horizontal wind direction trace, recorded at the 108-m level, of the BNL tower. As such the scheme can only be strictly applied to equivalent conditions to those at BNL. Turbulence types range from A (extremely unstable) through C (neutral) to D (very stable). Table 2.9 describes the BNL turbulence type scheme. (Gifford, 1976)

The scheme has been developed, refined and summarised by Singer and Smith (1953); Smith (1956); Smith *et al.* (1957); Singer and Smith (1966) and Singer *et al.* (1966).

Table 2.9 BNL turbulence type description

BNL Type	*Description of the Horizontal Wind Direction Trace.* *
A	Fluctuations exceeding 90°
B2	Fluctuations ranging from 40° to 90°
B1	Fluctuations ranging from 15° to 45
C	Fluctuations greater than 15° distinguished by the unbroken solid core of the trace
D	Trace approximates a line; Short-term fluctuations do not exceed 15°

* Fluctuations (peak to peak) are recorded over a one hour period.(Gifford, 1976, p69)

2.3.8 Relationships Between Turbulence Typing Schemes

Table 2.10 summarises the relationships between the stability categories given by the Pasquill, Turner, BNL and Sigma turbulence typing schemes.

Table 2.10 Relationships between turbulence typing methods

Stability Description	*Pasquill*	*Turner*	*BNL*	*Sigma Theta*
Very unstable	A	1	B2	25
Moderatcly unstable	B	2	B1	20
Slightly unstable	C	3	B1	15
Neutral	D	4	C	10
Moderately Stable	E	6		5
Very Stable	F	7	D	2.5

(Gifford, 1976)

2.4 Integral Measures of Ventilation, Recirculation and Stagnation

2.4.1 Background

Allwine and Whiteman (1994) defined a series of integral measures which could be used to characterise the stagnation, recirculation and ventilation potential of regions

within an airshed. These measures, which are suitable for use with data from 10-m anemometer masts, may be applied to regions of complex terrain.

Stagnation, ventilation and recirculation events have been defined as follows:

> Stagnations are events where atmospheric flows decrease in speed, or stop altogether, allowing pollutants to build up in stagnant air in the vicinity of the pollutant sources. Recirculations are events in which polluted air is initially carried away from the source but later returns to produce a high pollution episode. Ventilations, on the other hand, are events in which polluted air is replaced or diluted by fresh air. Ventilation can occur by fresh air sweeping in to replace polluted air, or by polluted air being diluted by turbulent mixing with clean air, such as during times of convective boundary layer growth. (Allwine and Whiteman, 1994, p713)

This technique characterises ventilation in terms of horizontal advection only, rather than ventilation occurring during turbulent mixing.

2.4.2 Methodology

Consider a time series of N discrete wind speed and direction pairs, U_i and D_i respectively. These may be expressed as horizontal wind vectors, $\vec{V}_i$ where the direction represents the direction *towards* which the wind is blowing. Each $\vec{V}_i$ is resolved into its north-south (north positive) and east-west (east positive) components as follows:

$$n_i = U_i \cos\left(D_i - 180\right) \qquad 2.1$$

$$e_i = U_i \sin\left(D_i - 180\right) \qquad 2.2$$

This results in a discrete time series of horizontal wind vectors with the notation illustrated in Figure 2.7. The magnitude of each vector is given by:

$$\left|\vec{V}_i\right| = U_i = \sqrt{n_i^2 + e_i^2} \qquad 2.3$$

The time, t_i, of each data point is:

$$t_i = t_0 + (i-1)T \qquad 2.4$$

where t_0 is the time of the first data point and T is the averaging interval of the data. In the case of the *TVAS* meteorological data, an averaging interval of 15 minutes was used.

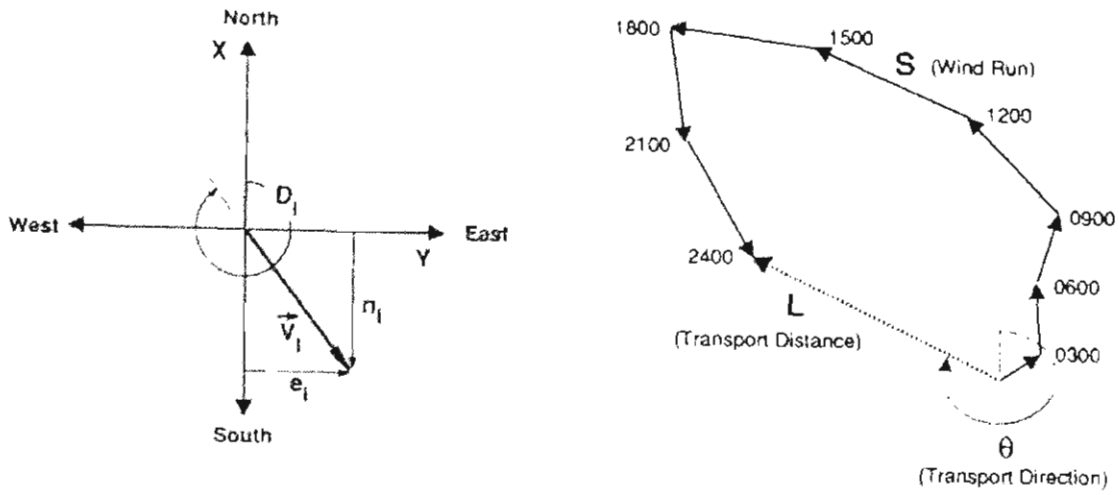

Figure 2.7 The left hand diagram defines the co-ordinate system and notation used to resolve the wind vectors into components. The right hand diagram illustrates the definition of wind run S, transport distance L, and transport direction θ, assuming a 24-hour transport time and 3-hour-average observations (Allwine and Whiteman, 1994, p. 714).

Allwine and Whiteman (1994) defined a series of "running" discrete integral quantities which are computed at each time t_i as follows:

Wind Run $$S_i = T\sum_{j=i}^{i+p}\left|\vec{V}_j\right| \qquad 2.5$$

North-South Transport Distance $$X_i = T\sum_{j=i}^{i+p} n_j \qquad 2.6$$

East-West Transport Distance $$Y_i = T\sum_{j=i}^{i+p} e_j \qquad 2.7$$

Resultant Transport Distance $$L_i = \sqrt{X_i^2 + Y_i^2} \qquad 2.8$$

Resultant Transport Direction $\Theta_i = \arccos\left(\frac{X_i}{L_i}\right) \qquad Y_i \geq 0$ *2.9*

$$\Theta_i = 360 - \arccos\left(\frac{X_i}{L_i}\right) \qquad Y_i < 0$$

and Recirculation Factor $R_i = 1 - \frac{L_i}{S_i} \qquad (0 \leq R_i \leq 1)$ *2.10*

where $i = 1,\ldots,(N-p)$, $p = \frac{\tau}{T} - 1$, $0 \leq p \leq N, [T \leq \tau < NT]$ and τ is the desired transport time, in the *TVAS* case 24 hours.

Figure 2.7 illustrates the definitions of wind run S, transport distance L, and transport direction θ, assuming a 24-hour transport time and 3-hour average observations. Note that θ is the bearing from the origin *towards* the air parcel at the end of the travelling time.

The wind run (S_i) is a measure of the total distance that a parcel of air, originating at the anemometer site, would travel between times t_i and $t_i+\tau$. In a similar manner the resultant transport distance (L_i) and transport direction (θ_i) represent the location of the parcel with respect to the site, at the end of the travelling time.

In a homogenous wind field these quantities would correctly represent the transport of the air parcel. In complex terrain however, they may only be considered as characteristics of the flow at the measurement site. Allwine and Whiteman (1994) intended that the integral quantities would be useful measures of the air pollution transport characteristics of the region surrounding the measurement site.

Stagnation-prone areas are characterised by low mean wind runs (S_i). In the event of total stagnation, there would be no winds occurring and hence S_i would be equal to zero.

The recirculation factor (R_i) indicates the presence of local recirculations occurring over time periods comparable to the transport time (τ). When R_i equals zero, straight

line transport has occurred, with no recirculation. Complete recirculation occurs when R_i equals one. In this case the air parcel would leave the origin at time t_i and would return at time $t_i+\tau$. Recirculation-prone areas are therefore characterised by high mean R_i values.

Ventilation-prone areas are characterised by high mean values of S_i (wind run) and low mean values of R_i (recirculation factor).

Two important points should be noted. The first is that for any site, the sum of the frequencies of stagnation, ventilation and recirculation events does not necessarily total 100 %. This is because other possible flow conditions can occur apart from these. Neither are these mutually exclusive, so that frequencies may total to higher than 100 % in cases where stagnation and recirculation events occur simultaneously.

The second point to note is that there is a mathematical singularity occurring in Equation 2.10 (divide by zero) for cases where S_i (wind run) equals zero. When this occurs however, L_i (transport distance) also equals zero. Clearly in such cases no atmospheric transport has occurred, and hence recirculation can not have occurred either. As such, R_i is defined as zero whenever S_i is zero.

For their three study sites in the Grand Canyon region of Arizona, Allwine and Whiteman (1994) determined *critical transport indices* (CTIs) to characterise stagnation-prone, recirculation-prone and ventilation-prone *areas*. These are applied as in Table 2.11, where, S and R are the 24-hour wind runs and recirculation factors respectively, and their associated means are calculated over the entire period of record. The subscript 'c' denotes the CTIs, whereas the subscript 'v' refers to the ventilation CTIs.

Table 2.11 Application of the critical transport indices to identify sites prone to stagnation, recirculation and ventilation.

Condition	⇒	*Site Prone to ...*
$\overline{S} \le \overline{S}_c$	⇒	Stagnation
$\overline{R} \ge \overline{R}_c$	⇒	Recirculation
$\overline{R} \le \overline{R}_{cv}$ and $\overline{S} \ge \overline{S}_{cv}$	⇒	Ventilation

Allwine and Whiteman (1994) applied the following CTIs to their Arizona sites:

- $\overline{S}_c$ = 170 km (approximately 2 ms^{-1} average daily wind speed);

- $\overline{R}_c = 0.4$;
- $\overline{R}_{cv} = 0.2$ and $\overline{S}_{cv} = 250$ km (approximately 3 ms^{-1} average daily wind speed).

These CTIs were chosen on the basis of mean transport indices calculated for a site known to experience frequent stagnation and recirculations (Bullfrog Basin) and another site that is well exposed to synoptic-scale circulation systems (Desert View).

Allwine and Whiteman (1994) also defined CTIs to identify stagnation, recirculation and ventilation *events*. These were applied according to the definitions in Table 2.12 where:

- $S_c = 130$ km (approximately 1.5 ms^{-1} average daily wind speed);
- $R_c = 0.6$;
- $R_{cv} = 0.2$ and $S_{cv} = 250$ km (approximately 3 ms^{-1} average daily wind speed); and
- the transport time (τ) = 24 hours.

Table 2.12 Application of the critical transport indices to identify stagnation, recirculation and ventilation events occurring on a 24-hour time scale

Condition	⇒	*Event*
$S \leq S_c$	⇒	Stagnation
$R \geq R_c$	⇒	Recirculation
$R \leq R_{cv}$ and $S \geq S_{cv}$	⇒	Ventilation

2.4.3 Studies Using Integral Measures

To date, very few researchers have used Allwine and Whiteman's integral measures. Venegas and Mazzeo (1999) assessed the stagnation, ventilation and recirculation potential of five Argentine cities. These were Resistencia, Córdoba, Buenos Aires, Mar del Plata and Comodoro Rivadavia. Two years of hourly surface wind measurements were used to calculate the wind run and recirculation factor at each city, using a 24-hour transport time. Table 2.13 shows the frequency of stagnation, recirculation and ventilation events, determined for each city using the CTI values proposed by Allwine and Whiteman (1994).

Table 2.13 Relative frequency of stagnation, recirculation and ventilation events in five different Argentine cities.

Site	*Stagnation Events (%)*	*Recirculation Events (%)*	*Ventilation Events (%)*
Resistencia	45	4	18
Córdoba	15	10	35
Buenos Aires	10	6	40
Mar del Plata	4	7	52
Comodoro Rivadavia	2	10	58

Source: Extracted from Venegas and Mazzeo (1999), Tables 4 and 5, pp. 52 and 53.

The frequency of stagnation events varied between 2 % at Comodoro Rivadavia and 45 % in Resistencia. Comodoro Rivadavia is located in a region of strong westerly

winds in the south of the country, whereas Resistencia is in the northeast in an area where winds are weak. Recirculation events were most common, occurring 10 % of the time, in Comodoro Rivadavia and Córdoba. Comodoro Rivadavia is exposed to sea and land breezes, and Córdoba experiences local circulations as a result of its complex terrain. Ventilation events were experienced on 58 % of occasions at Comodoro Rivadavia, falling to 18 % at Resistencia.

Stagnation, ventilation and recirculation events were seen to vary according to season. Stagnations were most frequently experienced during autumn and winter. In contrast good ventilation occurred most often during spring. Recirculation events were most common in spring and summer.

Crescenti (1997), as part of the *Lower Rio Grande Valley Environmental Study*, used the integral parameters to assess the air pollution potential of the Texas city of Brownsville, and the surrounding Lower Rio Grande Valley. The study used 15-minute averaged data collected from the roof of a building, located at the University of Texas (Brownsville Campus), approximately 1 km north of the river. Additional data were obtained from a National Weather Service station situated at the Brownsville International Airport. Data were collected during two short-term measurement periods, the first occurring over 23 days in spring (18 March 1993 to 10 April), and the other over 17 days in summer (18 July 1993 to 4 August).

Crescenti (1997) calculated Allwine and Whiteman's integral measures using a 24-hour transport time, however he failed to relate them to the CTIs. Results from the spring study featured relatively large wind runs, ranging from approximately 300 km day^{-1} to over 600 km day^{-1} for the NWS site and between 50 km day^{-1} and 300 km day^{-1} for the less-exposed university site. These well-ventilated periods were interspersed by short episodes of recirculation. The summer study was also dominated by ventilation, however there was no indication of either stagnation or recirculation.

2.5 Air Pollution Modelling Systems

Zannetti (1990) identified two broad classes of models frequently used in simulating the meteorology and dispersion of contaminants within the atmosphere. These are physical and mathematical models.

Physical models, such as small-scale representations of a landscape or industry, may be placed within wind tunnels or water tanks. Emission sources are modelled by injecting dyes or coloured gases into the modelling system. Xuan (1996) used a wind tunnel to investigate the efficiency of windbreaks in preventing fugitive dust emissions from the surface of coal piles. A wind tunnel was also used by Hutchinson *et al.* (1996) in modelling ground contamination of emissions from the stack of an incinerator building. Hutchinson found that a relatively small increase in the height of the stack, from 10 m to 12 m, would prevent contaminants being entrained within the wake of an adjacent building.

It is also possible to simulate different atmospheric stability and temperature regimes within wind tunnels or water tanks. Mizumoto and Nagai (1996) describe the construction of a thermally-stratified wind tunnel, where up to 36 different layers can be created by either heating or cooling, thus facilitating the simulation of complex vertical temperature structures. In a similar manner, Ohba *et al.* (1996) were able to simulate sea breeze conditions by appropriate heating and cooling of floor panels.

Within a water tank, obstacles are inverted and are towed through the fluid beneath a motorised carriage, which moves along the top of the tank. Atmospheric stratification is simulated using brine-water mixtures. Linear density gradients are normally used, created during the filling of the tank via computer-controlled mixing valves. (Vosper, 2000)

In contrast to physical models, mathematical models describe the physical and chemical aspects of atmospheric dispersion via a series of mathematical algorithms. Mathematical air pollution modelling systems usually comprise some or all of the following components:

- a meteorological data pre-processor;
- a meteorological model;

- an atmospheric dispersion model;
- an atmospheric chemistry module; and
- a deposition module.

The meteorological models generally produce time-varying fields of wind speed and direction, often along with other meteorological parameters such as temperature or humidity. In order to provide input to the models, existing meteorological measurements may have to be interpolated in time or space, or simply converted into a suitable form. This may be done manually, however for complex models a data pre-processor is often used.

Contaminants are released from identified sources, with carefully defined source strengths and initial dispersion parameters, and are advected around the modelling domain by the wind fields. Diffusion of the plume elements also occurs and is governed by the turbulence parameters, which are also defined. Consideration of the combined effects of advection and diffusion allow the calculation of time-averaged ground level concentrations.

Some more complex models (e.g. Nester, 1995; Fung *et al.*, 2000; and Wang *et al.*, 2000) take into account the atmospheric chemistry of the plume, and subsequent transformations that occur as the plume travels from source to receptor. Atmospheric chemistry modules are frequently used to simulate the formation of photochemical smog due to the reaction of ozone, nitrogen oxides and carbon-containing species under sunny conditions.

Many models also consider the effect of contaminant removal from the plume via deposition onto the surface (e.g. Böhm and Ford, 1996; Soon-Ung, 1998). Removal may occur via either dry or wet deposition. Dry deposition occurs when contaminants are deposited directly onto the surface by either advection or diffusion. In contrast, wet deposition occurs when the contaminant is absorbed into water droplets within the atmosphere. Absorbed contaminants may be either precipitated onto the surface as rain, or may impact with the surface as fog.

Near field effects, such as plume rise and plume downwash in the vicinity of buildings, may also be modelled. Fumigation can also be simulated, where for example an elevated plume is brought to the surface as a developing unstable surface

layer grows to reach the plume, or when contaminants from a coastal source interact with a thermal internal boundary layer.

Air pollution modelling systems are often completed by the addition of an interface, which allows modelled results to be imported into a geographic information system. Such systems clearly reveal the spatial variation in ground level concentrations, and greatly aid in the interpretation of results. Consecutive time-averaged images may also be animated in order to display temporal variations.

Each of the above modelling processes may be achieved using many different techniques. As a result modelling systems tend to be produced by combining the most suitable, or best available, modules.

2.6 Wind Field Modelling

Mathematical meteorological models can be classified as either analytical or numerical. Analytical models, which provide exact solutions, are impractical due to the degree of computation resources, and definition of inputs required, and hence numerical models are more frequently used. Numerical models provide approximate solutions, obtained by using numerical integration techniques. Numerical meteorological models can be further classified as either diagnostic or prognostic models. (Zannetti, 1990)

2.6.1 Diagnostic Wind Field Models

Diagnostic wind field models are the simpler of the two classes, being based on available measurements. As a result there is little physics involved in the computations, with the wind fields being derived largely by interpolation and extrapolation of existing measurements. It is therefore important to maximise the number of measurement locations, and to optimise their location (Zack and Minnich, 1991).

Diagnostic wind fields are normally adjusted to conform with conservation of mass and momentum principles. These adjustments ensure that there is no artificial creation or destruction of material mass, and the subsequent wind fields are described

as being 'mass-consistent'. Arena *et al.* (1997) state that mass-consistent models play an important role, as they represent a good compromise between accuracy and computational speed.

There are no time-tendency terms in diagnostic models, and hence each hour of a simulation is based on direct measurements, or interpolations in time and space between measurement pairs. They are referred to as 'diagnostic' or 'steady-state' as they have no ability to forecast the evolution of a meteorological field. They must therefore be considered to produce a best estimate of a steady-state or quasi steady-state condition (Zannetti, 1990).

2.6.2 Prognostic Wind Field Models

In contrast to diagnostic models, *prognostic* models contain full time-dependent equations, and incorporate the physics required to forecast the evolution of meteorological fields over time. The atmospheric system is modelled by integrating the equations of conservation of mass, heat, motion, water (and other substances if required) over time and space. This requires the solution of a set of many simultaneous non-linear partial differential equations. Until recently, prognostic models were too complex to be run on personal computers. (Zannetti, 1990; Kumar and Russell, 1996)

2.6.3 Combined Diagnostic and Prognostic Wind Field Models

Many meteorological models contain both diagnostic and prognostic elements. A prognostic model may incorporate 'nudging' techniques, which allow the use of meteorological measurements to bias the modelled outputs. An example of this occurs in the *MM4* model (Kumar and Russell, 1996), where in order to help control the growth of errors, observations are assimilated at the initial time and throughout the simulation period. *MM4* combines analysis nudging, where nudging occurs at every grid point, and individual observation nudging, where a single observation has a radius of influence of 40 km.

Prognostic elements may also be incorporated into diagnostic models in order to increase accuracy in regions where measurements are sparse. An example of this is the use of a prognostic nocturnal drainage module within a diagnostic wind field model. The prognostic and diagnostic winds are merged, usually using a four-dimensional data assimilation technique such as kriging.

Barna *et al.* (2000) and Barna and Lamb (2000) found that a relatively sparse network of surface and meteorological observations in a region of complex terrain (the Cascadia region of the Pacific Northwest), necessitated the paired use of a prognostic meteorological model (*MM5*) and the *CALMET* diagnostic model. *MM5* modelling, on a 5-km grid, failed to reproduce observed wind features in some parts of the modelling domain. The *MM5* solution was then utilised as an initial-guess wind field for *CALMET*, thus merging the *MM5* wind fields with the available surface observations. This procedure resulted in better wind field predictions than would otherwise occur if *MM5* was used in isolation.

Barna and Gimson (2000) and Gimson (2000) used a similar approach when simulating winds in Christchurch. Observations were sparse within the modelling domain, so a prognostic weather model (RAMS) was used to provide initialising wind fields, firstly on a 32-km grid then on an 8-km grid. Results from the 8-km grid were then used as hourly initial guess fields within *CALMET*.

2.6.4 Wind Field Model Limitations and Comparison Studies

The main limitation of mass-consistent diagnostic wind field models is that their performance strongly depends upon on the density, representativeness and accuracy of the observed winds within the modelling domain (Seaman, 2000). Hernández *et al.* (1997) found that their (un-named) diagnostic wind field model was able to accurately reproduce observed winds, with a maximum difference between observed and predicted winds of less than 1 ms^{-1} in wind speed and 20° in wind direction. The model however failed to accurately reproduce a localised drainage flow from a small valley. They concluded that a strategically-placed mast would have aided the model to accurately reproduce the flow in this region.

Regions dominated by steep orographies can only be accurately simulated, by the incorporation of additional measurement locations. Arena *et al.* (1997) found that, for "gentler slopes", wind fields generated by the mass-consistent *WINDS* code showed good agreement with non-divergent reference wind fields produced in a wind tunnel.

Adding extra observation sites will not necessarily improve the accuracy of a modelled wind field, without careful siting. Desiato *et al.* (1998) found that when applying two different mass-consistent models, *CONDOR* and *MINERVE,* to an area of very complex terrain in Switzerland, the best result was obtained using only three surface sites and one vertical wind profile. This was despite the fact that at least seven surface sites and five vertical profile sites were available. Desiato *et al.* also found that it was important for wind data to extend to the top of the modelling domain. Without at least one detailed wind profile, unrealistic flow features were produced in the upper levels.

Prognostic models are particularly useful in areas where there is limited observational data. They are however very sensitive to initial and boundary conditions. Solving the simultaneous prognostic equations is a difficult task, and hence simplifying assumptions are used. These assumptions, in conjunction with uncertainties in the inputs, can cause errors in the predicted wind fields. (Kumar and Russell, 1996)

Giovannoni and Russell (1995) compared the results of prognostic and diagnostic wind field models when modelling dispersion of photochemical oxidants in Athens. The two models produced very different predictions, however the diagnostic model was able to predict winds more accurately than the prognostic model at five urban measurement sites. The mean wind strength was also more accurately predicted using the diagnostic model. Giovannoni and Russell felt that the diagnostic wind field model would be unlikely to accurately reproduce the wind field outside of the urban area, particularly around the mountains in regions where there were no measurements. The land and sea breeze flows were detected at the measurement locations and hence were realistically modelled by the diagnostic model.

Kumar and Russell (1996) compared the results of a diagnostic wind field model and a prognostic wind field model (*MM4*) with observations. In general they found that the diagnostic meteorological fields (wind speed, temperature and mixing height) agreed well with observed values, whereas the prognostically-derived fields showed poor agreement. Both models performed similarly when predicting upper-level velocities. When used to provide the transportation fields for a photochemical ozone model (*CIT*), once again diagnostically-derived fields resulted in ozone predictions that were closer to observations than those predicted using prognostically-derived fields.

2.6.5 Wind Field Modelling Studies

An early example of a diagnostic wind field model was *MATHEW*, developed by Sherman (1977) to provide wind fields for *ADPIC*, a pollution transport model. The three-dimensional, mass-adjusted model has been applied to many areas within the United States, representing a variety of terrain features and meteorological conditions. Tracer experiments have shown that the *MATHEW/ADPIC* models produce results within a factor of 2 in 50 % of cases, and within an order of magnitude in 90 % of cases. (Sherman, 1977)

King and Bunker (1988) utilised the *ATMOS1* diagnostic wind field model, in conjunction with *ATMOS2* pollution dispersion model, in tracer experiments conducted in different areas of complex terrain. Experiments occurred in complex terrain under nocturnal drainage conditions, and in flat terrain under stable conditions. Wind observations were provided using a mixture of surface wind stations and profiling stations (tethersonde balloons and theodolite-tracked piballs). The models performed most accurately under stable conditions. The major source of error was identified as slight inaccuracies in predicted wind speed (between 0.3 ms^{-1} and 0.8 ms^{-1}) becoming compounded over large distances (50 km) and times (2 days). Despite this, King and Bunker concluded that diagnostic wind fields can provide valuable information, even with sparse meteorological data. In all three simulations results were found to be in reasonable agreement with observations.

Melas *et al.* (1998) were able to resolve the main features of the land and sea breezes in a region of complex terrain (Thessaloniki, Greece) using a diagnostic wind field model producing wind fields in real time.

A more recent study (Chen *et al.*, 1999, Lindsey *et al.*, 1999) used the California Air Resources Board (*CARB*) diagnostic mesoscale wind-flow model, in conjunction with the *CARB* trajectory model, to simulate power station emissions in the Grand Canyon National Park.

The *CARB* diagnostic wind field model consists of a pair of models. One model was used to calculate hourly wind fields at the surface, using data from a network of meteorological towers. The other model calculated wind fields above the surface using the results of the surface model and wind profile observations. The modelled wind fields were then adjusted for mass consistency. (Lindsey *et al.*, 1999)

Continuous surface meteorological observations were collected at 15 sites over a three-month period. Four Doppler sodars and three Doppler radar profilers collected continuous profile data during the study. Intensive Observational Periods were scheduled whenever the power station plume was forecast to impact the Grand Canyon National Park. During these periods, additional wind and temperature profiles were collected at five rawinsonde sites, four airsonde sites, and using two tethersondes.

The *CARB* models showed that complex terrain features affected winter wind-flow patterns. The model was used to help generate a conceptual model explaining how power station emissions were transported to the Grand Canyon. The model showed that even though power station emissions became entrained within stable slope and valley flows, their low speed ensured that they were not a significant mechanism in transporting emissions from the power station to the Grand Canyon. The dominant mechanism was found to be synoptic-scale winds, which became channelled by the major terrain features.

The *CARB* model results were not sufficiently detailed to resolve small-scale features such as local channelling, decoupled canyon winds, and slope and valley flows.

Small-scale features were characterised well if they were represented within the observational data network. Chen *et al.* (1999) concluded that a prognostic subroutine would resolve some of these features in the absence of measurements.

A similar problem was noted by Banta *et al.* (1996), with the *MATHEW* diagnostic wind field model failing to represent a small-scale, topographically forced, nocturnal exit jet flowing from Eldorado Canyon in Colorado. The narrow jet, 2 km wide, and extending from a few tens of meters to 800 m above the ground, was poorly sampled by the meteorological network.

The *CALMET* model, slightly modified and known as *AUSMET* in Australia, represents the state-of-the-art in diagnostic wind field modelling. It is paired with a Gaussian puff dispersion model (*CALPUFF* or *AUSPUFF*), which will be discussed later.

CALMET was developed by Earth Tech. It consists of a diagnostic wind field module and modules for simulating overwater and overland boundary layers. The *AUSMET* model offers the choice of using either the diagnostic wind field model developed by Earth Tech, or the *NUATMOS* model used in this thesis. *AUSMET* produces gridded mass-consistent fields of the u, v and w wind components, along with gridded fields of:

- Surface friction velocity,
- Convective velocity scale,
- Monin-Obukhov length,
- Mixing height,
- Pasquill Gifford Turner atmospheric stability class,
- Air temperature, and
- Precipitation rate.

(Ross *et al.*, 1995c).

CALMET has been used in a number of recent studies. Barna and Gimson (2000) were able to successfully simulate the merging of drainage flows in Christchurch under winter anticyclonic conditions using *CALMET*. The model was also used in Auckland, in conjunction with the *CALGRID* photochemical Eulerian 3-D model, to simulate summer ozone formation and transport over a two day period (Adeeb and Shooter, 2000). A similar modelling program, using *CALMET* and *CALGRID*, was

used to evaluate various emission control strategies in the Milano metropolitan area (Silibello *et al.*, 1998; Finzi *et al.*, 2000). An adjusted version of *CALMET* has been incorporated into an emergency response system (*TAMOS*) for a nuclear power station near Austria (Pechinger *et al.*, 2001).

2.7 Gaussian Puff Dispersion Modelling

Gaussian plume models, often referred to as steady-state models, are the most commonly used of the air pollution models, being widely used for regulatory applications. They are conceptually simple, easy to apply and have been evaluated using many different datasets. Despite their conceptual elegance, Gaussian plume models are limited in their application. They may only be used to simulate continuous plumes emitted in homogenous terrain, under steady state meteorological conditions. In particular, they may only be used when the wind speed is constant and non-zero. (Zanetti, 1990)

Gaussian puff dispersion models have been developed to overcome some of the limitations inherent in the steady-state approach, whilst retaining the benefits of the approach. These models account for time-varying emissions, from multiple sources, occurring under non-homogeneous dispersion conditions, in regions of complex terrain. In particular they are able to simulate dispersion in low wind or calm conditions.

2.7.1 Model Formulation

Puff models, as their name implies, simulate emissions from sources as a series of puffs, each having duration Δt. The mass of each puff, ΔM, is given by $\Delta M = Q\,\Delta t$, where Q is the time-varying emission rate. The puff centre is advected around the modelling domain according to local, time-varying wind vectors. If a point $p(t) = (x_p, y_p, z_p)$ represents the position of the puff centroid at time t, then the concentration due to that puff (Δc) at a receptor point $r = (x_r, y_r, z_r)$ can be determined using Equation 2.11, where σ_h and σ_z represent the horizontal and vertical dynamics of each puff's growth. The total concentration at any receptor point is obtained by

summing the contributions, Δc, at that point from all existing puffs, generated by all existing sources.

$$\Delta c = \frac{\Delta M}{(2\pi)^{3/2}\sigma_h^2\sigma_z}\exp\left[-\frac{1}{2}\left(\frac{x_p - x_r}{\sigma_h}\right)^2\right]\exp\left[-\frac{1}{2}\left(\frac{y_p - y_r}{\sigma_h}\right)^2\right] \cdot \exp\left[-\frac{1}{2}\left(\frac{z_p - z_r}{\sigma_z}\right)^2\right] \qquad 2.11$$

Equation 2.11 is often expanded to include reflection and atmospheric deposition or decay terms. Under stationary, homogeneous transport conditions, the equation is reduced to that of the Gaussian plume formula.

The wind speed is not explicitly represented in Equation 2.11, however puff models use wind speed to control the puff density in any given region. Low wind speeds result in a succession of puffs which are spatially close to each other. As wind speeds increase, successive puffs become separated by greater distances. This approach allows puff models to simulate the effects of low or zero wind speeds. (Zanetti, 1990; Sandu, 1995)

2.7.2 Model Comparisons

Godfrey and Scire (2000) discussed some of the advantages of using puff models as opposed to plume models. They considered a complex terrain site in the Colombia River Valley in Central Washington. The region contained a sharply curving main valley, with deep side canyons. A fictitious odour source was located within a side valley, in an area where pollutant transport and dispersion would be dominated by terrain influences. A single surface meteorological station was located several kilometres distant from the source, in a region outside of the main valley. Upper air measurements were obtained from a site located over 200 km away. Results from the puff dispersion model *CALPUFF* were compared with those generated by the *AUSPLUME* steady-state model.

The first advantage of puff models is that they utilise non-steady-state conditions in complex terrain. Steady-state models assume horizontally-uniform wind fields,

which are not adjusted to account for terrain effects. They are also unable to handle curved flows, caused by terrain-induced channelling. As a result, plume models may incorrectly represent the spatial area of plume impact, and the magnitude of peak ground level concentrations. In contrast, Godfrey and Scire (2000) found that the *CALMET*-derived wind field was consistent with observations of the nocturnal drainage flow, showing strong channelling of the flow by the terrain.

Puff models allow the mean position of a puff to remain unchanged during periods of calm or light winds, whilst still allowing the puff to grow in size due to dispersion. In contrast, *AUSPLUME* has a wind speed cut-off of 0.5 ms^{-1}. Speeds lower than this are adjusted to equal 0.5 ms^{-1}. In their low-wind case study, Godfrey and Scire (2000) found that the *CALPUFF* plume was constrained within the valley walls, and was consistent with the *CALMET* wind field. In contrast, the *AUSPLUME* plume was forced to cross several terrain contours in an unrealistic manner.

A major limitation of plume models is that they are unable to account for causality effects. The Gaussian plume equation has no time term, assuming that contaminants are instantly transported throughout the modelling domain. Plume models therefore do not take into account the time taken for transport to occur. This is explicitly accounted for within puff models, along with changes in dispersion conditions and transport directions. These effects have been found to be important when modelling dispersion over distances of only a few kilometres (Godfrey and Scire, 2000).

Dispersion of emissions from tall stacks under convective conditions is also poorly handled by plume models, which assume a Gaussian distribution along an elevated plume centreline. *CALPUFF* specifically implements a probability density function, which more accurately simulates vertical dispersion within the convective boundary layer.

Inversion breakup fumigation is also handled well by puff models. Nocturnal emissions into a surface-based inversion are allowed to accumulate throughout the night. Previously released emissions are brought to the surface when inversion breakup allows convective mixing to reach the plume. In contrast, plume models

consider each hour to be unrelated to previous hours, and hence do not take previous emissions into account.

Accurate modelling of coastal effects, such as the diurnal reversal of land and sea breezes, also requires previous emissions to be accounted for, along with recognition of the large changes in meteorological conditions occurring over small distance and time scales. These are accounted for in puff models, and ignored in plume models.

Hamilton (1999) found that *AUSPLUME* and *AUSPUFF* predicted similar near-field SO_2 concentrations from four industries in Altona, Melbourne with a high degree of accuracy. In the near-field, *AUSPUFF* behaved as if it was a plume model, and hence the potential advantages of the puff dispersion approach were not demonstrated.

Bluett (2000) compared modelled SO_2 concentrations, generated using *AUSPLUME* and *CALPUFF,* for a flat industrial estate in Christchurch, New Zealand. The estate contained approximately 20 buoyant sources with relatively low release heights. *AUSPLUME* was found to overpredict the 99.9 percentile observation by 75 %, whereas the *CALPUFF* overprediction was 45 %.

Hibberd (2000) compared the peak concentrations predicted by *AUSPLUME*, *AUSPUFF* and a prognostic dispersion model, *TAPM,* for tall stacks located in flat terrain under highly convective conditions. He found that *AUSPUFF* and *TAPM* predicted similar peak ground level concentrations during highly convective conditions, and these were two to three times larger than levels predicted by *AUSPLUME*. The spatial pattern of ground level concentrations predicted by *AUSPUFF* and *TAPM* were found to be quite different. The greatest difference between all three models occurred close to the stacks. With stack heights less than 150 m, model predictions for all three models were similar at distances greater than 3 km from the source.

2.7.3 Gaussian Puff Modelling Studies

The Gaussian puff dispersion model, *VALPUFF*, was applied to simulate nocturnal drainage flow within a deep valley in Western Colorado (Tangirala *et al.*, 1992).

Surface concentration and meteorological data were obtained from two 1984 tracer experiments, conducted as part of the *ASCOT* (*Atmospheric Studies in Complex Terrain*) program. An elevated release and a surface release occurred. Model simulations were compared with observations collected by a network of 51 samplers.

The coefficient of variation (standard deviation/mean) was similar for both predicted and observed concentrations. Approximately 85 % of the predictions for the elevated release were within a factor of 5 of the observed values. The surface release was modelled less well, with 53 % of predictions within a factor of 5 of the observations.

California's Pacific Gas and Electric Company developed a diagnostic wind field model, coupled with a Gaussian puff dispersion model. The *PGEMS* model was developed to simulate dispersion of emissions from their many power stations located in regions of complex terrain (Thuillier, 1992).

The *PGEMS* model was tested in the San Luis Obispo region of California, using a field gas-tracer experiment. The wind field model utilised measurements from 18 surface sites, and profiles from 3 Doppler sites. Temperature profiles were collected at 4 aircraft sites. Tracers were released at three sites over the eight-day experimental period, with sampling occurring over a network of 150 air samplers. Samplers were carefully positioned to cover terrain gaps, the entrance and exit of the inland valley, and the coastal boundary, as these were expected to provide the main transport paths.

The modelling period featured many modified flow patterns, such as sea breeze circulations, terrain wake eddies, thermally-induced slope flows and inertial wind direction rotations. On the whole these were well represented by the model. There were however three regions where the model lacked sufficient data to provide a proper simulation. In these regions the model failed to simulate an eddy circulation into a valley, the bifurcation of a plume and a flow along a coastline.

Thuillier (1992) found that with the addition of a building-wake algorithm, near-field biases were well within a factor of two. The model tended to over-predict near-field concentrations, however at higher concentrations there was a tendency to under-predict. The model also performed well in the far-field, simulating the gross

transportation features. Far-field concentrations were positively biased (i.e. the model over-predicted concentrations), but were generally within a factor of two of observations in regions where the wind field was adequately resolved.

In contrast, Sandu (1995) found that the Gaussian puff model *INPUFF,* applied to Lillestrøm, Copenhagen and Kincaid, tended to under-estimate concentrations for plumes emitted from elevated sources. At low source heights, using the Pasquill-Gifford-Turner dispersion parameters, the model performed well.

The *MINERVE* mass consistent diagnostic wind field model and the *SCIPUFF* puff dispersion model were used by Cox *et al.* (1998) to simulate atmospheric dispersion during an early morning radiation inversion, inversion dissipation and afternoon mixed convection. Trace amounts of sulfur hexafluoride (SF_6) and indium oxide (InO_x) were released at the White Sands Missile Range, New Mexico. A network of 11-15 surface stations and one to three upper-air sites provided input to *MINERVE.* Tracer gas was sampled from a large number of samplers, arranged in 90° arcs spaced 278 m, 912 m, 28 km and 60 km from the release point.

MINERVE produced wind fields that were consistent with observations as well as with the terrain. Compared with observations, the mean deviation in wind speed was 0.4 ms^{-1}, and less than 10° for wind direction. Deviations were greatest during inversion dissipation. *SCIPUFF* also performed well. Measurements of the plume centroid, 2.5 hours after release, showed less than 10 % difference in location, with concentrations of the same order of magnitude. Agreement between observed and modelled concentrations was maintained six hours after release, with *SCIPUFF* accurately determining suitable monitoring sites 60 km down wind of the release point.

More recently, Barna and Gimson (2000) used the *CALMET/CALPUFF* model to predict wintertime PM_{10} concentrations, from domestic wood and coal fires in Christchurch, under anticyclonic conditions. Throughout the early to mid-afternoon, PM_{10} concentrations were low within the region. Concentrations began to rise between 16:00 and 18:00, coinciding with the establishment of the nocturnal surface inversion and increased emissions from domestic heating sources. PM_{10}

concentrations reached a peak of approximately 400 μgm^{-3} at 22:00, coinciding with wind speeds below 1 ms^{-1}. Concentrations began to fall after 22:00, and by 06:00 the following morning PM_{10} concentrations were less than 50 μgm^{-3}. At times strong concentration gradients were noted between adjacent suburbs, with predicted PM_{10} concentrations varying by as much as 100 μgm^{-3} within the space of a kilometre.

Table 2.14 compares modelled 24-hour average PM_{10} concentrations with observations recorded at four surface monitoring sites. *CALPUFF* is seen to slightly underpredict concentrations, with biases ranging between +14 μgm^{-3} (overprediction) at Beckenham to -21 μgm^{-3} (underprediction) at St. Albans.

Table 2.14 Observed and predicted 24-hour average PM_{10} concentrations during wintertime in Christchurch.

PM_{10} monitoring site	*Observed 24-hour average PM_{10} concentration (μgm^{-3})*	*Predicted 24-hour average PM_{10} concentration (μgm^{-3})*	*Bias (μgm^{-3})*
Beckenham	33	45	+13.6
Hornby	48	42	-5.5
Opawa	62	56	-5.0
St. Albans	101	78	-21.2

Source: Barna and Gimson (2000), Table 1, p. 14

Barna and Gimson (2000) are currently refining their modelling system, with the aim of using it to determine the effects of various emission control strategies. Policy options to be modelled include banning the use of coal and open fires, and regulating the emission factors of slow combustion heaters.

Puff dispersion models have also seen use in novel applications. Hargreaves and Baker (1997) applied the technique to modelling motor vehicle emissions within urban street canyons. Vehicles were modelled both as mobile emission sources, and as sources of turbulence. Street level winds were determined by the winds above the urban canyon. Godfrey and Clarkson (1998) modelled dispersion of PM_{10} and SO_2 emissions from Scott Base in Antarctica using *CALMET/CALPUFF*. Dispersion results appeared to be very realistic in both their spatial patterns and concentrations, however they were not verified by comparison with direct measurements. *CALMET/CALPUFF* has also been successfully used to model the dispersion of the pesticide methyl bromide from agricultural fields in the Salinas Valley, California (Honaganahalli and Seiber, 2000).

2.8 Conclusion

This chapter has provided a brief literature review of topics relevant to this study. It commenced by summarising the results of the seven previous air pollution studies that have occurred in the Tamar Valley since 1982. Turbulence typing methodologies were then described. The subsequent section developed a methodology for calculating integral measures of stagnation, ventilation and recirculation, and the use of these to identify events and regions prone to these conditions. The chapter concluded with sections on wind field modelling and Gaussian puff dispersion modelling.

Diagnostic wind field models have been found to perform well, accurately reproducing observed winds. They are heavily dependent on careful selection of measurement locations, and require at least one measured wind profile to accurately characterise winds aloft. Under good siting conditions, typical maximum differences between predictions and observations are below 1 ms^{-1} for wind speed and 20° for wind direction. Diagnostic wind field models have been shown to perform as well as, if not better, than prognostic models.

Puff dispersion models have been shown to provide superior results to steady-state plume models, largely because they can account for spatial and temporal variations in the transport field, for calm conditions and causality effects.

Diagnostic wind field models and Gaussian puff models have been used and validated in many parts of the world, providing satisfactory results in many cases. Agreement to one order of magnitude is quite common.

3 Data Acquisition and Storage

3.1 Introduction

This chapter describes the data collection phase of the *TVAS*, specifically the network of 16 automatic weather stations that was established to provide a continuous data source covering a three-year period. The locations of each site will be discussed, along with the instrumentation attached to each of the 10-m towers. The performance history of the network will be analysed. Data has to be stored in some fashion, so the data loggers which store results in the field, and the database which amalgamates data from the entire network will be described. Discussion will then turn to the derived parameters that were calculated from the measured variables.

Whilst data from the network is an extremely valuable resource, on its own it is not sufficient to support the *NUATMOS/CITPUFF* modelling suite. These models require wind and temperature profile data in order to provide three-dimensional modelling results. These data were collected during a series of five *Intensive Observation Periods* or *IOPs*. The two-day *IOPs* occurred on a seasonal basis, and were timed to coincide with 'worst-case pollution dispersion' periods.

This chapter will conclude with a description of the *IOP* program, the temperature profiling techniques utilised and the measurement locations selected.

3.2 10-m Mast Measurements

3.2.1 Meteorological Station Locations

At the commencement of the *TVAS* a network of 14 meteorological stations was proposed. The *CSIRO Division of Atmospheric Research* (*CSIRO DAR*) was contracted to model the Tamar Valley wind field, under worst-case dispersion conditions, in order to help determine suitable representative measurement locations.

This was achieved using the wind field component of their three-dimensional prognostic model *LADM* (Lagrangian Atmospheric Dispersion Model). *LADM* requires: a gridded digital elevation model; the surface properties of the modelled terrain; a specified large-scale wind field (from a synoptic chart); an early morning temperature profile; and estimates of changing cloud cover over the region to be modelled. The model uses Lagrangian techniques to predict wind speed and direction, temperature, mixing height and turbulence properties at each of the grid points for every five-minute time-step (Physick, 1993).

LADM was used to simulate a 48-hour period commencing at midnight on 12th September, 1991. The synoptic analysis chart was dominated by an extensive anticyclone (central pressure 1020 hPa) centred around latitude 30° S, which ridged to latitudes well south of Tasmania. During the course of the modelled period, the anticyclone slowly passed over the state from west to east (CSIRO DAR, 1993).

Three consecutive nested runs occurred, with the initial modelling run covering the entire state using a coarse 10-km grid. The second run covered a subset of the first run at a 5-km grid resolution, using lateral boundary conditions obtained from the previous run. The final run, at a 2.5-km resolution, covered the *TVAS* study region using predictions from the previous model run.

Progressive wind fields from this final *LADM* simulation were used to identify possible meteorological sites at locations representative of broad flows within the study region. A set of 'typical' field measurements was generated, consisting of hourly surface wind speeds and directions at each potential surface meteorological site, and wind and temperature profiles at each of the proposed upper air sites.

These were input into the diagnostic wind field model *NUATMOS,* which was to be routinely used during the course of the *TVAS.* The resulting wind fields were compared with the original *LADM* wind fields in order to assess the acceptability of each proposed surface and upper air site.

Fourteen broad locations were identified by *CSIRO DAR* as being suitable for possible meteorological sites. These were visited and specific measurement locations were found. Each of the final monitoring sites conformed to AS 2922—1987 (Standards Association of Australia, 1987a) and AS 2923—1987 (Standards Association of Australia, 1987b). All sites were located in the centre of large open areas with no nearby obstructions. With the exception of a site located on a navigation beacon on the banks of the Tamar River (Site 6), and another on a wharf (Site 9), all sites were within large grassed areas.

Once the stations had been established it was decided to include a pre-existing station, located near Launceston at Ti Tree Bend, into the network. The Ti Tree Bend station (Site 16) had been established by *DELM* in early 1992 as part of a separate study (Carter *et al.*,1995). It was considered worthwhile to include this station as *NUATMOS,* the wind field model, is diagnostic in nature, relying heavily on interpolation between existing measurement sites. As such, the addition of another station would improve the accuracy of the modelled wind fields in the Launceston region.

A final change to the network came a year into the study period, when one of the masts (Site 14) was relocated to a coastal site (Site 15). This occurred as it was found to be located within a slight frost hollow, and hence its recorded flows were unrepresentative of the broad region. Table 3.1 summarises the site numbers, locations and AMG co-ordinates of the 16 locations used throughout the *TVAS.* These are mapped as Figure 3.1.

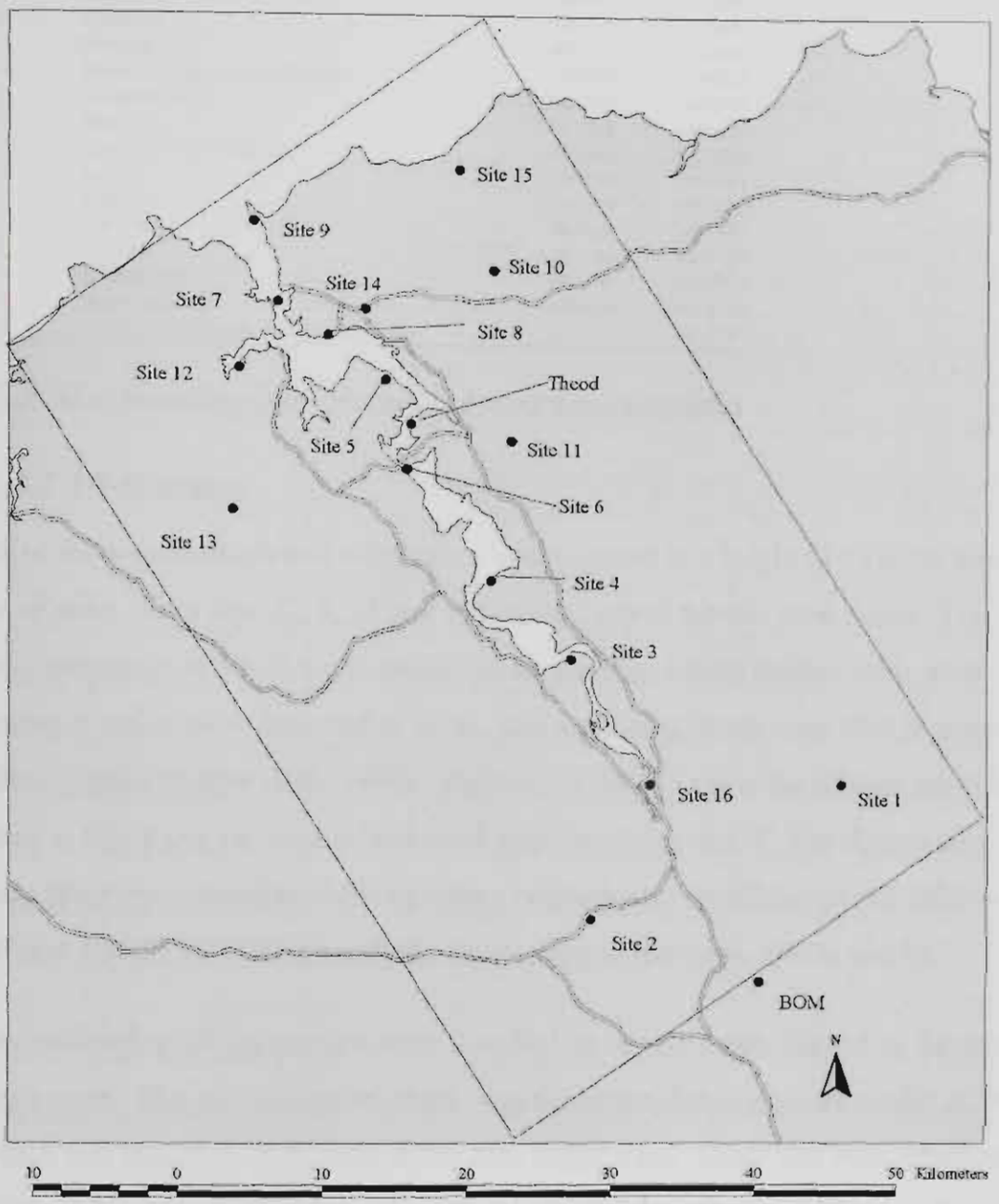

Figure 3.1 Meteorological station locations used in the *TVAS*. The diagonal rectangle represents the *TVAS* study area. 10-m wind speed and direction measurements are recorded at Sites 1 to 16. Wind profiles were measured at Sites 3,7,8 and Theod during the *IOPs*. Temperature profiles were measured at Site 8 during the *IOPs*. *BOM* radar wind profiles and 10-m winds are recorded at 6-hourly intervals at the *BOM* site located at the Launceston Airport.

Table 3.1 *TVAS* meteorological station locations

Site Number	*Site Location*	*AMG Easting (m)*	*AMG Northing (m)*
1	Nunamara	523617	5414497
2	Hadspen	506180	5405023
3	Dog Point	504705	5423305
4	Windermere	499200	5428800
5	Rowella	491775	5442829
6	Barrett's Point Marine Marker	493306	5436587
7	Garden Island	484285	5448236
8	Bell Bay	487745	5445922
9	Low Head Pilot Station	482602	5453800
10	Lefroy	499313	5450481
11	East Arm	500614	5438562
12	West Arm	481619	5443653
13	Holwell	481249	5433751
14	Bridport Rd	490346	5447751
15	Stony Head	496885	5457441
16	Ti Tree Bend Sewage Treatment Plant	510300	5414500

3.2.2 Meteorological Station Instrumentation

3.2.2.1 10-m masts

Each of the anemometers and wind vanes was mounted at a height of 10 m on some form of mast. Four sites (2, 8, 11 and 13) utilised guyed tubular steel masts. The wind instruments at Site 6 were attached to an existing marine marker using steel framework and a boom mounted at 10 m. The remaining masts were 10.4 m treated hardwood poles (Carter *et al.*, 1995). Figures 3.2 and 3.3 show the tubular steel mast located at Site 8 and the treated hardwood pole located at Site 9. The figures also clearly show the compliance with the siting requirements mandated by AS 2922—1987 and AS 2923—1987 (Standards Association of Australia, 1987a and b).

Most meteorological instruments were installed on booms extending out to the side of each mast. The only exception to this was the atmospheric pressure sensor at Site 8, which was mounted on the rear of the data logger case. Cable ties were attached to each boom in an attempt to discourage their use as bird perches (see Figure 3.5). This strategy had mixed success.

All masts and instruments were installed by *DELM*, with assistance from the author in finding suitable sites, and erecting and mounting instruments on the guyed masts. *DELM* staff maintained the masts and instruments, and downloaded the data on a regular basis. A rigorous data screening procedure occurred before the data was presented to the author for analysis.

Figure 3.2 The Bell Bay meteorological site (Site 8), illustrating the tubular steel masts. This photo was taken at the conclusion of the study and shows the mast "telescoped down" to a height of 5 m. Throughout the *TVAS*, all tubular steel masts recorded winds at 10 m.

Figure 3.3 The Low Head meteorological site (Site 9), located at the Low Head Pilot Station, illustrating the treated hardwood pole.

3.2.2.2 Dataloggers

East mast was initially equipped with a *Dataflow Systems* 980 Series datalogger. These eventually proved to be inadequate with the following faults or problems occurring:

- the failure to record data at midnight each day due to a firmware programming fault;
- loggers experiencing short circuits during data download;
- moisture related problems; and
- the inability to determine average wind directions and sigma-theta ($\sigma\theta$) over the 15-minute averaging period.

In April 1994, the loggers were replaced with superior *Unidata 6004B Starloggers* (Figure 3.4). These allowed vector averaged wind directions and sigma-theta to be determined. They also permitted the installation of temperature sensors at nominal heights of 2 m and 10 m (Carter *et al.*,1995).

Figure 3.4 *Unidata* model *6004B Starlogger* data logger (Site 8)

All meteorological parameters were averaged and logged at 15-minute time intervals, using instantaneous measurements calculated every 5 seconds. In addition to the averaged parameters, the *Unidata* loggers also recorded the maximum and

minimum of the instantaneous wind speed measurements during each 15-minute interval. The date and time of each set of measurements was recorded using the time at the *end* of each averaging period.

3.2.2.3 Wind Speed

Synchrotach 480 anemometers were initially chosen for use in the *TVAS*. These were selected because of their low wind speed threshold (less than 0.2 ms^{-1}), which would allow the detection of light katabatic winds. The anemometers were consequently very small, light and had fragile cups.

After numerous failures at the most exposed sites, the manufacturers agreed to modify the anemometers by replacing the solid wire spindles with spindles made from hollow hypodermic syringe stock. This reduced the failure rate, however continued failures resulted in the decision to use more robust instruments.

Environdata WS30 anemometers were tested and installed on each mast in November 1993. These heavier duty, three-cup instruments have an operating range of 0 to 50 ms^{-1}, and a start-up threshold of 0.2 ms^{-1} or better. Output pulses are generated, at a rate of 1250 pulses km^{-1}, by an optical interrupter arrangement providing a stated accuracy of 1 ms^{-1}. The instruments are specifically designed for long-term use in isolated locations and may typically provide five year's operation before requiring overhaul (Environdata, 1993a). After some initial problems caused by the ingress of salt spray, slightly modified *Environdata* anemometers were used for the remainder of the study. Figure 3.5 shows the WS30 installation at Site 9, which is typical of the configuration used throughout the *TVAS* anemometer network.

3.2.2.4 Wind Direction

Wind vane assemblies manufactured by *Dataflow* Systems were used. These were of the single potentiometer type, and had a dead-band of approximately 10°. After some initial problems with water leaking into the casings, resulting in erroneous directions, the subsequently modified vanes reported few problems (Carter *et al.*,1995). The wind vane located at Site 9 is depicted in Figure 3.5. This arrangement was representative of those used throughout the network.

Figure 3.5 *Environdata WS30* anemometer and *Dataflow Systems* wind vane (Site 9). The figure also illustrates the use of cable ties as a bird deterrent.

3.2.2.5 Differential Temperature

In September 1994, differential temperature sensors were installed at Sites 1, 2, 4, 5, 8, 10, 11, 12, 13, and 15 in order to measure low level vertical temperature gradients. These nine units were designed and fabricated by technicians at the *University of Tasmania*. The temperature differential circuit used two analogue *AD590* integrated circuit temperature sensors in a differential configuration. The matched sensor pairs were calibrated to provide a one-volt output when each sensor was at the same temperature. The circuit gain was 300 mV $^{\circ}C^{-1}$, with a positive increase above one volt occurring when the lower sensor was at a greater temperature than the upper sensor. The sensor pairs were housed in plastic radiation shields and were mounted at the end of 1m booms. Paired sensors were installed on the same mast at nominal heights of 2 m and 10 m respectively (Jensen, 1994; Carter *et al.*,1995).

Figure 3.6 shows the installation of the upper differential temperature sensor, whilst the lower sensor is shown in Figure 3.7. Both photographs were taken at Site 8.

Differential temperature data was used throughout the *TVAS* on an operational basis, mainly being used to check atmospheric stabilities. Surface temperatures were also used in the meteorological files required by *CITPUFF*.

Figure 3.6 The upper differential temperature sensor is located inside a plastic radiation shield and a Kipp and Zonen pyranometer measuring global radiation is mounted on the lower boom (Site 8).

3.2.2.6 Barometric Pressure

An *Environdata BP10 Series* barometric pressure sensor was installed at Site 8 (Figure 3.7). This sensor uses a solid state silicon strain gauge as a sensing element, and outputs atmospheric pressure in hectopascals. The sensor has an operating range of 750 to 1050 hPa and a resolution of 1 hPa. It is accurate to within 3 hPa, and typically may operate in the field for five years before requiring overhaul. The unit is designed to operate in temperatures ranging between -10 and 50 °C and in

humidities between 0 and 100 % (Environdata, 1993b). The pressure sensor operated without fault for the duration of the *TVAS*.

Figure 3.7 Lower differential temperature sensor, *Environdata BP10* pressure sensor and rear of the data logger case (Site 8).

3.2.2.7 Solar Radiation

A *Kipp & Zonen CM 11* pyranometer measuring global radiation was installed on a boom, at a height of approximately 7 m, on the Site 8 mast (Figure 3.6). This was interfaced with the datalogger via an amplifier designed and fabricated by *Unidata*. The *CM 11* measures global irradiance on a plane surface in Wm^{-2}. It incorporates a 100-thermocouple thermopile, imprinted on a thick-film substrate which is housed under a K5 glass dome. The pyranometer operated without fault for the duration of the *TVAS*.

3.2.3 Instrument Calibration

All meteorological instruments were calibrated by the manufacturer prior to installation, or after any repair occurring as a result of instrument failure. A brand

new anemometer and wind vane were occasionally paired with existing wind instruments in order to check the field instrument's accuracy. No problems were ever found and the 'calibration' instruments were eventually required to replace damaged instruments.

3.2.4 Performance History

An analysis of the *TVAS* anemometer network performance was conducted by extracting the dates for which midday wind speed measurements existed at each individual site. It was assumed that met station down-time of any significance would result in a missed midday wind speed measurement, which would be apparent in the analysis. Table 3.2 summarises the results of this analysis.

Table 3.2 Performance history of the *TVAS* anemometer network: analysis of midday wind speed measurements.

Site #	*First Measurement*	*Last Measurement*	*Elapsed Time (days)*	*Number of Measurements (days)*	*Data Completeness (%)*
1	26/6/93	17/5/96	1056	745	71
2	29/5/93	17/5/96	1084	840	77
3	26/6/93	17/5/96	1056	832	79
4	5/7/93	17/5/96	1047	639	61
5	9/9/93	18/5/96	982	657	67
6	4/12/94	18/7/95	226	220	97
7	15/7/93	20/4/96	1010	647	64
8	27/5/93	18/5/96	1087	760	70
9	6/6/93	18/5/96	1077	851	79
10	27/6/93	18/5/96	1056	753	71
11	5/6/93	11/5/96	1071	711	66
12	24/6/93	18/5/96	1059	770	73
13	19/5/93	17/5/96	1094	842	77
14	30/6/93	31/12/93	184	126	68
15	6/6/94	18/5/96	712	566	79
16	19/5/94	19/4/96	701	610	87

The first anemometer to start recording was located at Holwell (Site 13). Measurements commenced at this site on 19th May, 1993. The majority of the remaining stations were quickly established, with a further 12 sites producing data within the next three and a half months. It took a while to realise that data from the pre-existing Ti Tree Bend (Site 16) sampler was available, with the first measurements being received a year to the day after the commencement of the measuring period. Site 15 was established on 6th June, 1994 by relocating a meteorological station located in a frost hollow at Site 14. The last useful data recorded at Site 14 were logged on 31st December, 1993.

Site 6 was the most problematic of the meteorological stations. It was located on a navigation beacon owned by the *Port of Launceston Authority* (PLA). The *PLA* installed the station in what was climatologically speaking a perfect location, however there followed a long period of breakdowns and inaccurate data. This was largely a result of the site's location over water, with strong winds and ingress of water and salt spray resulting in a large amount of unusable data. The first useable results were logged on 4th December, 1994. The station performed well for seven and a half months, however the difficulty in accessing the site and eventual instrument failure resulted in the site being decommissioned on 18th July, 1995.

The remainder of the met stations were decommissioned over a one month interval in April/May, 1996, at the end of the study period. The final midday wind speeds were logged at Sites 5, 8, 9, 10, 12 and 15 on 18th May, 1996, three years after the commencement of the measuring period.

Figure 3.8 shows the *TVAS* anemometer network performance in terms of existing and missing midday wind speed data. The horizontal lines represent continuous streams of data, logged at each anemometer site, with the gaps representing missed data largely due to instrument failure. The time series record for each site consists of large periods of continuous data, separated by smaller periods of missing data. Missing data periods ranged in length from 15 minutes (i.e. one measurement) to five months (Sites 4 and 12). Typical missing data periods are of the order of one month, and occurred with breakdowns happening midway between subsequent data downloads.

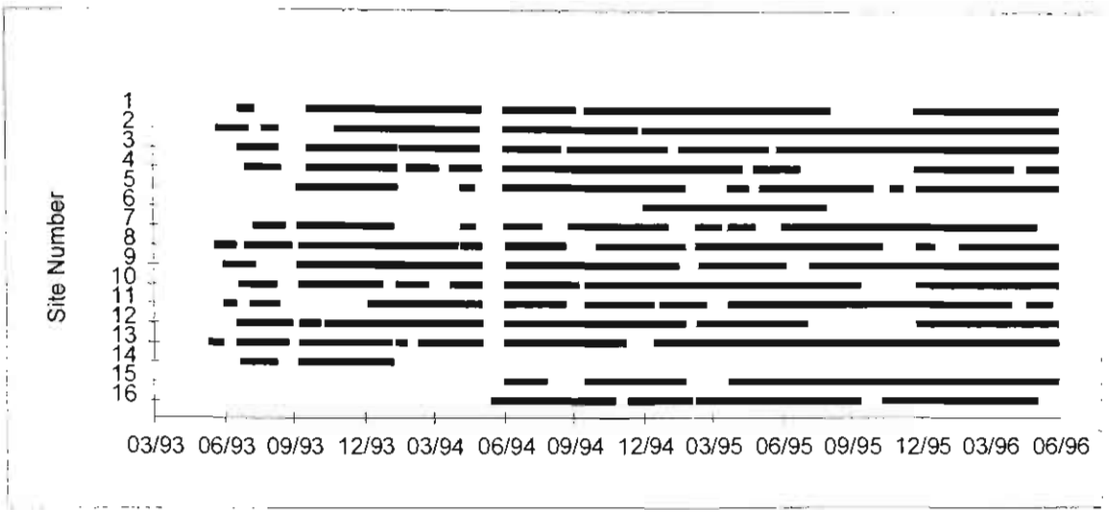

Figure 3.8 Period of record of *TVAS* anemometer network

Figure 3.9 summarises each site's record in terms of percentage completeness, with the available data for each site being expressed as a percentage of the maximum possible amount for that site (based on the dates of each site's first and last midday wind speed readings).

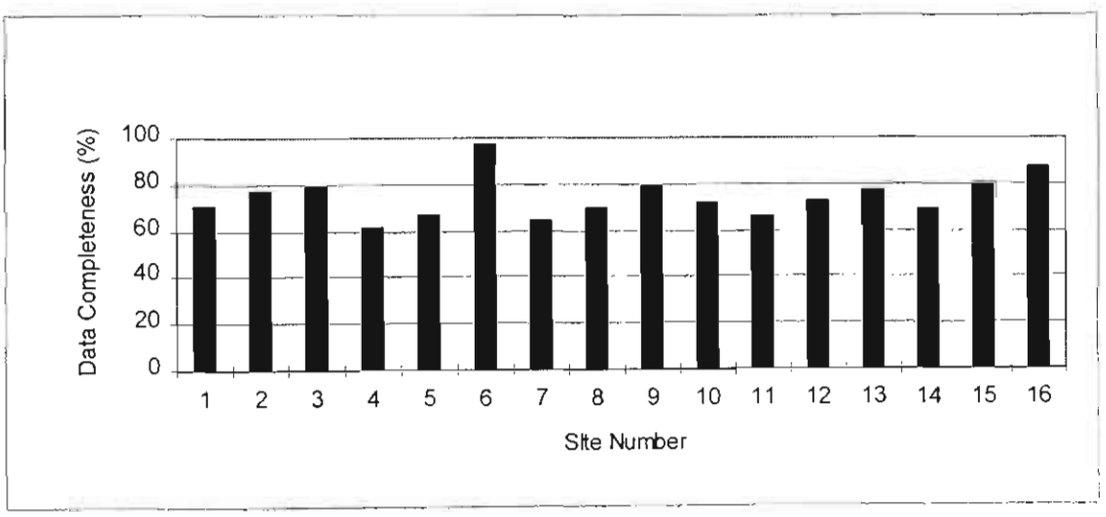

Figure 3.9 Completeness of record of *TVAS* anemometer network

Site 6 logged just over seven months worth of useable data before it was decommissioned, with a completeness of 97%. The next most complete wind record was logged at Site 15 (87%), with the majority of remaining sites being over 70% complete. Five sites, Sites 4, 7, 11, 5 and 14 were less than 70% complete, with the greatest proportion of data loss occurring at Site 4 (61%).

3.2.5 Derived Parameters

A programmer was employed to write software, which appended the following fields to each record of the *TVAS* meteorological dataset where possible:

- Pasquill stability class, using the modified sigma-theta technique;
- wind run (S_i km), where T = 15 minutes and τ = 24 hours;
- transport distance (L_i km), where T = 15 minutes and τ = 24 hours;
- transport direction (θ_i °), where T = 15 minutes and τ = 24 hours; and
- recirculation factor (R_i), where T = 15 minutes and τ = 24 hours.

Table 3.3 shows the estimated sunrise and sunset times used in calculating the atmospheric stability classes. The *Applied Environmetrics Meteorological Tables* software (Beer, 1990) was used to calculate sunrise and sunset times at the latitude of Paper Beach (146° 58'E, 41° 15'S), located midway along the valley on the West Tamar. Times were calculated for the middle of each month and were applied to data from all days in the month at each of the 16 meteorological sites.

Table 3.3 Estimated Tamar Valley sunrise and sunset times used in calculating Pasquill stability via the modified sigma-theta technique

Date	*Sunrise Time [a] (EST)*	*Sunset Time [a] (EST)*
January 16	04:50	19:29
February 16	05:28	19:01
March 16	06:02	18:16
April 16	06:35	17:25
May 16	07:07	16:46
June 16	07:30	16:31
July 16	07:27	16:45
August 16	06:55	17:14
September 16	06:05	17:45
October 16	05:14	18:17
November 16	04:35	18:53
December 16	04:26	19:24

[a] Times calculated using the *Applied Environmetrics Meteorological Tables* software (Beer, 1990) for Paper Beach (*146° 58'E*, 41° 15'S).

3.2.6 TVAS Database

Data from the meteorological station network was originally stored in a series of MS *Excel*™ spreadsheets, with data from each site contained within a separate spreadsheet. With time the datasets grew to such a size that each station's data was stored in a series of separate spreadsheets.

This system eventually grew so cumbersome that the entire dataset was imported into a single relational database. The corresponding MS *Access*™ database characteristics are summarised in Table 3.4.

Of particular interest is the "Allowable Values" column. During the importation process, data were screened against these criteria to ensure that they were of the correct type and were within sensible limits. This checking process highlighted a number of erroneous values and instances of missing data, which would have otherwise placed all further data in incorrect fields. All suspect data were discarded.

3.2.7 Routine Bureau of Meteorology Surface Measurements

In addition to data collected by the *TVAS* meteorological network, data was available from *BOM* measurements collected at the Launceston Airport. The airport is located on the southeast boundary of the study area at Western Junction (Figure 3.1). Observers record three-hourly instantaneous observations of:

- dry bulb temperature (°C);
- wet bulb temperature (°C);
- dew point temperature (°C);
- wind speed (kn);
- wind direction (° from true north; 10° segments);
- MSL pressure (hPa);
- visibility (km);
- precipitation (mm day^{-1});
- cloud type; and
- cloud amount (octas).

Table 3.4 Tamar Valley airshed database characteristics

Field Name	*Description*	*Units*	*Allowable Values*
SiteID	Site Identification Code. Part of Primary Key.	SiteX	X is an integer between 1 and 16
Date(EST)	Date (EST). Part of Primary Key.	dd/mm/yyyy	
Time(EST)	Eastern Standard Time recorded at the END of each 15-minute averaging period. Part of Primary Key.	hh:mm	
Speed(m/s)	15-minute vector average 10-m wind speed	ms^{-1}	Between 0 and 45 or Null
MinSpeed(m/s)	Minimum 10-m wind speed during 15-min averaging period	ms^{-1}	Between 0 and 45 or Null
MaxSpeed(m/s)	Maximum 10-m wind speed during 15-min averaging period	ms^{-1}	Between 0 and 45 or Null
Direction(deg)	15 minute vector averaged 10-m wind direction	° from true N	Between 0 and 360 or Null
SigmaTheta(deg)	Standard deviation of 10-m wind directions during averaging period	°	Between 0 and 103.9 or Null
StabilityClass	Pasquill stability class using the Modified Sigma Theta technique	A-G	A-G or Null
UpperTemp(deg)	Mean air temperature at the top of the mast	°C	Between -10 and 45 or Null
LowerTemp(deg)	Mean air temperature at approx. 1 m above the ground	°C	Between -10 and 45 or Null
TempDiff(deg)	Mean temperature difference between upper and lower sensors (Lower-Upper)	°C	Between -7 and 7 or Null
24hWRun(km)	24 hour Wind Run. (from logged time to time + 24 hours)	km	Between 0 and 2000 or Null
24hTDist(km)	24 hour Resultant Transport Distance (from logged time to time + 24 hours)	km	Between 0 and 2000 or Null
24hTDir(deg)	24 hour Resultant Transport Direction; direction **towards** which transport occurs (from logged time to time + 24 hours)	° from true N	Between 0 and 360 or Null
24hRecirc	24 hour Recirculation Factor where 0=straight line transport, 1=complete recirculation (from logged time to time + 24 hours)		Between 0 and 1 or Null
AtmPress(hPa)	Atmospheric Pressure (Site 8 only)	hPa	Between 950 and 1050 or Null
SolarRad(W/m2)	Solar Radiation Flux (Sites 8 and 16 only)	Wm^{-2}	Between 0 and 1500 or Null

In addition various aviation meteorological parameters are observed, such as CAVOK (used to designate times when visibility exceeds 10km; there is no cloud below 5000 ft and there is no precipitation or thunderstorm).

The *BOM* maintains an automatic weather station at the airport, located at *AMG* co-ordinates 517100 m E; 5401120 m N. This logs 30-minute averages of:

- dry bulb temperature (°C);
- dew point temperature (°C);
- wind speed (m s^{-1});
- maximum gust speed (m s^{-1});
- wind direction (° from true north; 10° segments); and
- MSL pressure (hPa).

Due to cost restraints, *BOM* data was purchased only for days when *Intensive Observation Periods* (*IOPs*) occurred.

3.3 Intensive Observation Periods

3.3.1 The IOP Program

The *TVAS* anemometer network recorded continuous surface meteorological measurements throughout the three-year measurement program. It was not feasible to support this dataset with continuous temperature and wind profile data. Instead a series of seasonal *IOPs* were planned. During each *IOP*, a team of field assistants recorded simultaneous wind and temperature profile measurements at different sites over a two-day period.

Each *IOP* was timed to coincide with worst-case air pollution conditions for the season in question. In practice this corresponded to the slow passage of an anticyclone across the state, bringing light to variable synoptic-scale winds. These typically became decoupled from the surface winds, with thermally-driven wind systems such as katabatic flows and sea breezes occurring at the surface. The stable nature of these flows, coupled with a diurnal reversal in wind direction, ensured that atmospheric contaminants would remain concentrated within the airshed, thus resulting in worst-case dispersion.

Identifying suitable *IOP* conditions in advance was a difficult task. Daily phone calls were made to the duty forecasters at the *BOM*, who provided advance warning of approaching anticyclones. When conditions looked suitable the field team, who had already been put on notice, mobilised and travelled to the study site. Measurements commenced at dawn the next day and continued for two days.

The *Summer IOP* had to be repeated, as the expected sea breeze failed to materialise on the first day. Funds were only available to collect one day's measurements during this *Second Summer IOP*. Table 3.5 summarises the *IOP* program.

Table 3.5 The *TVAS IOP* program

IOP Name	*Date*	*Number of Days*	*Start Time (EST)*	*End Time (EST)*
Summer IOP 1	12-13 December, 1993	2	06:00, 12/12	18:00, 13/12
Summer IOP 2	15 December, 1994	1	05:00, 15/12	18:00, 15/12
Autumn IOP	13-14 April, 1994	2	07:00, 13/4	17:30, 14/4
Winter IOP	27-28 June, 1994	2	07:30, 27/6	17:30, 28/6
Spring IOP	24-25 September, 1993	2	07:00, 24/9	17:30, 24/9

Figures 3.10 a-e show the 10:00 surface analysis charts for each *IOP*.

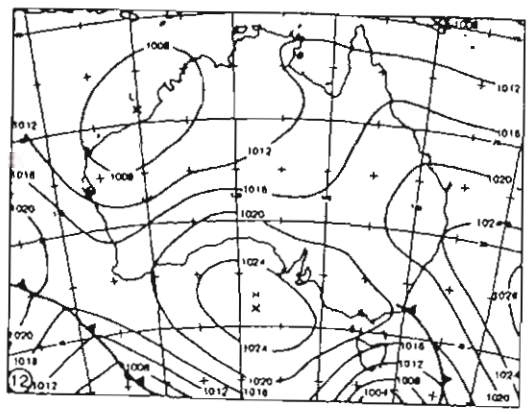

a) *Summer IOP 1*

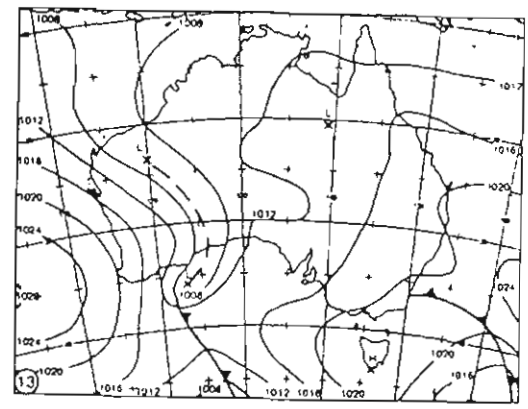

12-13 December, 1993

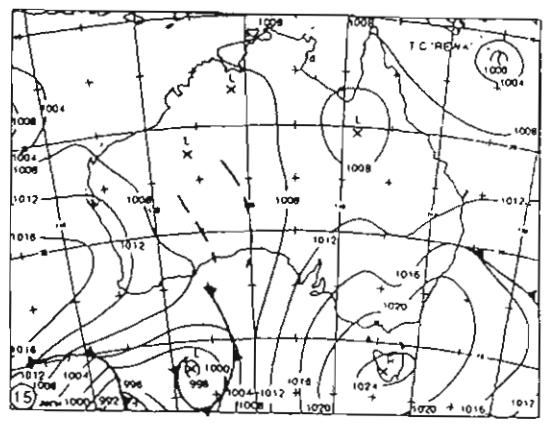

b) *Summer IOP 2* 15 December, 1994

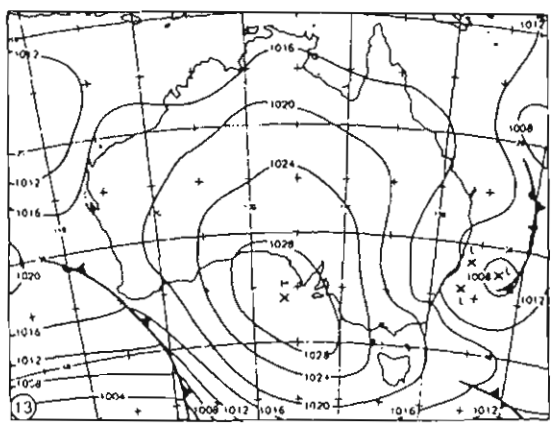

c) *Autumn IOP*

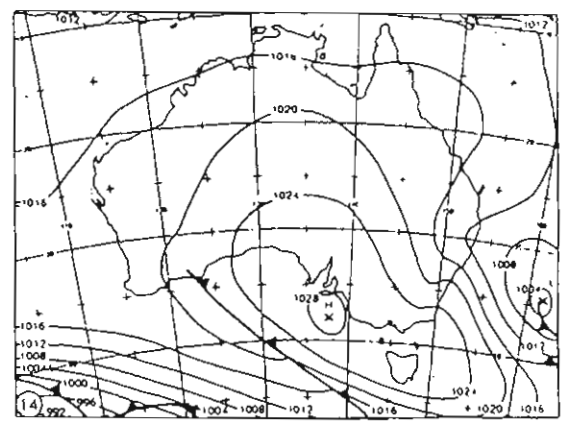

13-14 April, 1994

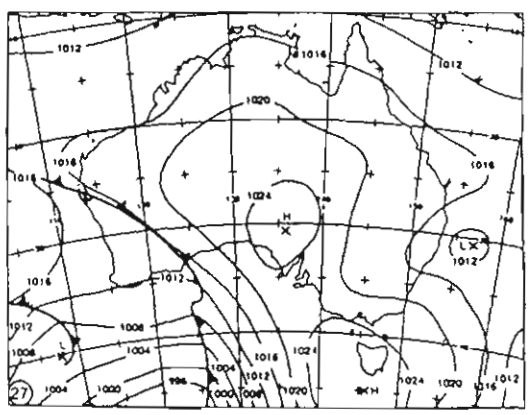

d) *Winter IOP*

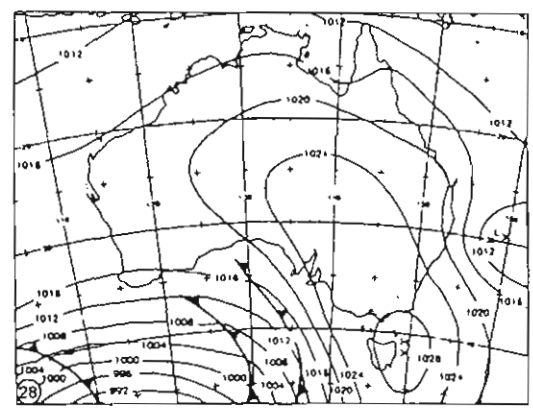

27-28 June, 1994

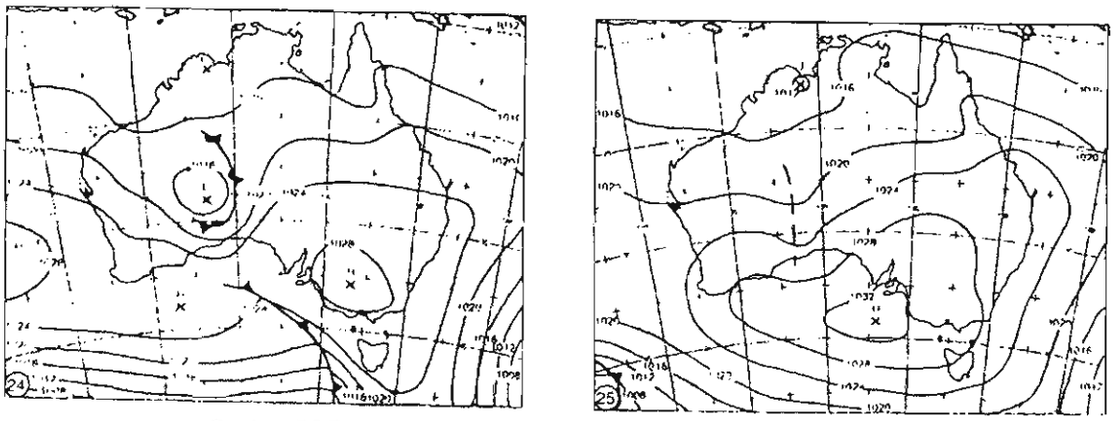

e) *Spring IOP* **24-25 September, 1993**

Figures 3.10 a-e *BOM* surface pressure analyses for each *Intensive Observation Period*

3.3.2 Measurement Locations

Simultaneous wind profiles were measured at Sites 3, 7, 8 and Theod during the *IOPs* (Figure 3.1). In contrast, the more expensive temperature profiles could only be measured at Site 8. The 10-m winds and the (6-hourly) radar wind profiles from Launceston Airport were purchased from the *BOM* for each *IOP*.

3.3.3 Wind and Temperature Profiling Techniques

A number of different techniques were used to measure wind and temperature profiles throughout the *IOPs*. Wind speed and direction profiles were collected using either tethered balloon (*tethersonde*) or pilot balloon (*piball*) soundings. In addition to measuring wind speed and direction, the *tethersonde* system also measured wet and dry bulb temperature, allowing simultaneous profiles of wind speed, wind direction, temperature and humidity to be collected. The *tethersonde* system was limited to wind speeds of 10 ms^{-1}, thus necessitating the use of free flying disposable radiosondes to measure temperature and humidity profiles in strong wind conditions.

3.3.3.1 Tethersonde Balloon Soundings

An *AIR* model *TS-2A tethersonde* was used to measure wind speed and direction soundings throughout the *IOPs*. The system, described by Morris *et al.* (1975), consists of a 3.25 m^3 helium-filled tethered balloon, suspending an airborne sensor package via a torsionally rigid "rope ladder".

The package contains transducers for measuring wet and dry bulb temperature, wind speed and direction, and atmospheric pressure. An eight-parameter multiplexer samples the output from each transducer at regular intervals, typically taking 30 seconds to complete the entire cycle. The measurements are then transmitted to a ground station as an audio-modulated FM signal, transmitted at 403 MHz. The ground station accepts an *ASCII* data stream at a rate of 300 baud. This is transferred to a lap top computer for storage and later analysis.

Wind speed is measured using a cup anemometer driving a DC generator. The anemometer is capable of measuring speeds in the range of 0.5 to 10 ms^{-1} with a precision of ± 0.25 ms^{-1} and a resolution of 0.1 ms^{-1}.

The aerodynamic shape of the balloon (see Figure 3.11a) ensures that it acts as a wind vane, thus keeping the package heading into the wind. Wind direction is measured using a magnetic compass located within the sensor package. The compass needle actuates a circular potentiometer that is fixed relative to the sensor package. This allows wind directions to be measured with a precision of $\pm 5°$ and a resolution of $\pm 2°$.

Wet and dry bulb temperatures are measured using a pair of matched identical bead thermistors, which are mounted coaxially within a radiation shield. A small electric fan aspirates the thermistors with the dry bead mounted in the airstream 2 cm ahead of the wet bead. The wet bead is kept wet by a wick, which sucks distilled water from a small reservoir. Both thermistors have an operating range of -30 to +45 °C, and measure temperatures with a precision of ± 0.5 °C at a resolution of 0.1 °C.

The balloon's altitude is calculated using a small solid-state aneroid capsule. It measures differential barometric pressure in the range 0 to 100 hPa, with a precision of ±1 hPa at a resolution of 0.5 hPa. The altitude of the balloon is calculated using the pressure difference between the surface and that at the balloon's current position.

Figure 3.11a *AIR Instruments* tethersonde balloon used to record wind and temperature profiles: balloon "parked" prior to use (Site 8).

The tether line comprises a bundle of nylon filaments contained in a braided nylon sheath. The 1000-m line, with a mass of 0.9 gm^{-1} and a breaking strength of 445 N, allows typical maximum sounding heights of 750 to 800 m to be attained. Balloon altitude and ascent rate are controlled using an electric winch which is powered by a 9 V heavy duty battery.

Typical soundings take between 20 and 30 minutes to complete. Data are collected only during the ascent phase, with a further 10 minutes being required to retrieve the package using a high-speed descent. Figures 3.11 a-c show a typical tethersonde deployment at Site 8.

Figure 3.11b *AIR Instruments* Tethersonde balloon used to record wind and temperature profiles: attaching instrument package to the balloon prior to launch.

Figure 3.11c *AIR Instruments* tethersonde balloon used to record wind and temperature profiles: a nocturnal sounding

The tethersonde system is limited to conditions where wind speed is below 10 ms^{-1}. In practice, retrieval is commenced whenever speeds exceed 8 ms^{-1}. This means that tethersonde soundings are usually conducted during anticyclonic conditions, and even then are frequently restricted to nocturnal, early morning or evening time periods. Temperature profiles were gathered during high-wind periods using free-flying disposable airsondes.

3.3.3.2 Airsonde Temperature Soundings

Throughout the *TVAS*, temperature profiles were measured using *AIR* model *AS-1A-PTH* airsondes (Figure 3.12). These disposable airsondes measure wet and dry-bulb temperature, and barometric pressure. The radiosonde transducers and FM transmitter are enclosed within a helicoid propeller-shaped housing made of moulded polystyrene. The airsonde is attached to a large free-flying helium-filled weather balloon and released. As the airsonde ascends it is forced to rotate, thus aspirating the wet and dry bulb thermistors mounted within radiation shields on opposite wing tips.

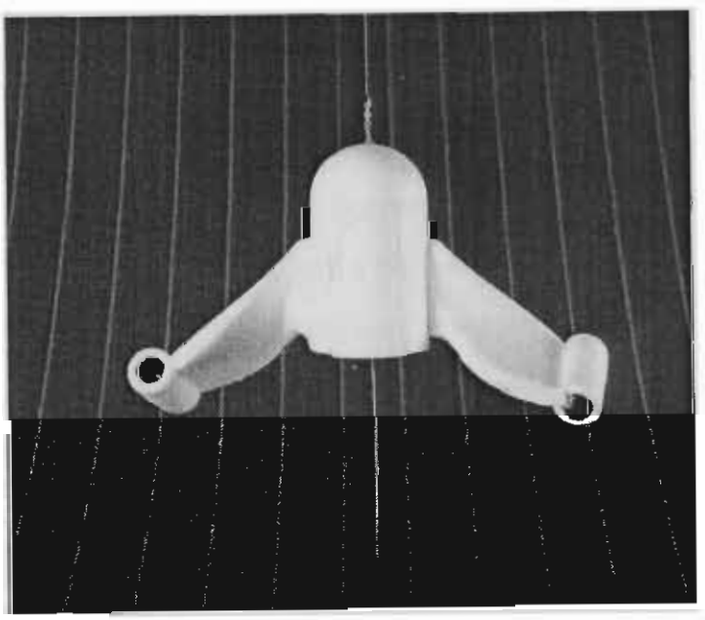

Extracted from Air (1993)

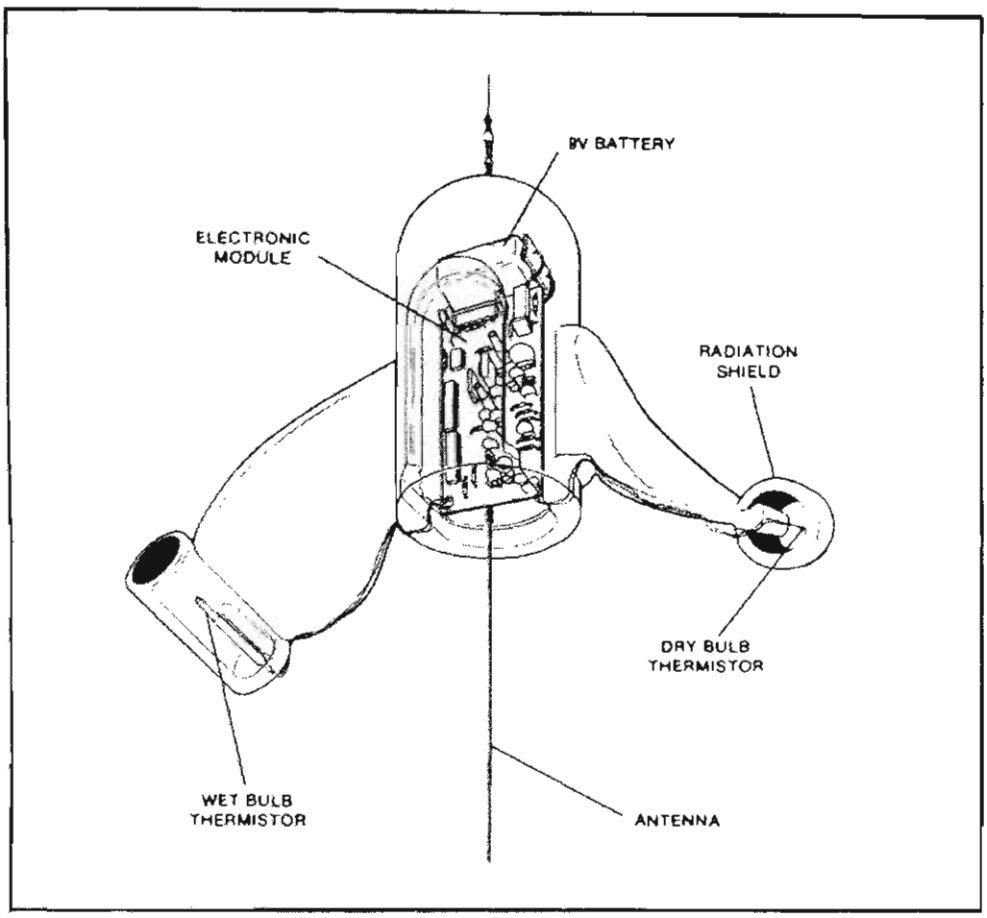

Extracted from Air (1993)

Figure 3.12 The AIR radiosonde ("airsonde")

Wet and dry-bulb temperatures are measured using bead thermistors, matched to within 0.1 °C over the range -20 to +35 °C. This ensures a performance comparable with a good Assman psychrometer. The instrument has a wide operating range (-70 to +50 °C), with a resolution of 0.1 °C and a typical precision of 0.2 °C. Barometric pressure is sensed using an aneroid capacitance pressure sensor located within the housing. Pressure may be measured between 1050 and 250 hPa, with a precision of 3 hPa and a resolution of 0.1 hPa.

The FM transmitter operates on a carrier frequency of 402.25 MHz. The signal is captured and processed by the tethersonde ground station as described earlier. The ground station was typically turned off after a 10-minute flight, when profiles of up to 2000 m were obtained. It was not uncommon however to still receive a clear signal up to 90 minutes after release.

3.3.3.3 Pilot Balloon Wind Soundings

There are two recognised techniques for measuring wind profiles using theodolites and piballs:

- the double theodolite technique; and
- the single theodolite technique.

The double theodolite technique uses a pair of theodolites, aligned along a transect normal to the expected wind direction, with a separation distance of the order of 1000 m. A piball is released at one of the theodolite locations (the 'base' site), and is simultaneously tracked by both theodolites. The piball's elevation and azimuth angles are determined at each theodolite position, using paired reading occurring at regular time intervals. In order to ensure that simultaneous paired readings are recorded, both the base and remote sites are synchronised to the same time signal. This is normally achieved via the use of two-way radios.

With this system it is possible to determine the exact position of the piball in the sky at any reading time. This is because there are four measurements: the base station elevation and azimuth; and the remote station elevation and azimuth, and three unknowns: the piball easting; northing and height. The difference between successive piball positions is a measure of the mean wind speed and direction occurring in the layer that the piball has just traversed, during the time it took to travel from one position to the next. This is of course subject to the accuracy of the theodolites and of the operators using them.

The double theodolite technique, whilst being the more accurate method, is less frequently used than the single theodolite technique. This is because it is 'expensive' in terms of theodolite and personnel use. The single theodolite technique, as its name suggests, uses a single theodolite to track each piball. As a result it halves the number of operators and theodolites required for each sounding, thus releasing them for use in another location.

The single theodolite technique has two measurements and three unknowns. As such it is impossible to determine the position of the piball in the sky without either making a further measurement of some kind or using an assumed piball ascent rate.

The most common solution to this problem is to assume that the piball rises through the atmosphere at a constant rate. If this technique is used then the assumed height of the piball can easily be calculated at any reading time. This assumption provides the third 'measurement', thus allowing the piball's approximate position to be determined.

Another technique uses a long weighted 'tail' attached to the helium filled piball. This normally takes the form of a long streamer of a known length, with an air filled piball attached. The air filled piball is 'dragged' through the sky by the helium filled piball, with both piballs remaining a known distance apart. A measurement of the angular distance between the two piballs at each reading time allows the distance between the theodolite and the piball pair to be determined. This extra measurement thus allows the helium-filled piball's position to be determined.

In the hands of experienced operators the use of a weighted tail provides an acceptable degree of accuracy. Positional accuracy increases with the length of the tail, and with the length of time between successive readings. The technique however is difficult to apply, and may result in errors occurring as the operator attempts to make three simultaneous readings: elevation; azimuth, and angular distance, at the end of each reading interval. Errors may occur under the stress of short reading intervals, and in high wind conditions when the piballs are travelling across the field of view at great speed.

Four model *518/42 Mk II* meteorological theodolites, manufactured by *ER Watts and Son Ltd.*, were made available by *CSIRO DAR*. It is uncertain when these were manufactured however they were painted black with a wartime finish, suggesting that they were manufactured for use in WWII. Despite their age, careful tests proved that each theodolite was in excellent condition and provided accurate elevation and azimuth determinations.

The decision was made to use the single theodolite technique during the *TVAS*. This was because *NUATMOS* is a diagnostic wind field model, relying on interpolations between existing measurement points, and it was considered vital that simultaneous wind profiles occurred at as many locations as possible. The single theodolite

technique allowed the measurement of four simultaneous wind profiles rather than the two possible with the double theodolite technique.

The weighted tail technique was not used, largely due to lack of operator experience. It was felt that the addition of a third reading at the end of each 15-second reading interval could compromise the accuracy of all three readings. It was considered better to accurately record two variables, than to inaccurately record three.

At the commencement of a day's soundings, each theodolite was mounted on a sturdy tripod and carefully levelled. The azimuth scale was then aligned to magnetic north using a hand held compass. These settings were checked prior to each sounding to ensure accuracy.

Helium-filled latex piballs, each weighing 20 g, were inflated to a free lift capacity of 45 g using balloon balances. Piball inflation was conducted inside tents allowing free lift capacity to be carefully controlled in any wind condition. Each piball was inflated immediately prior to use, thus ensuring that helium leakage was minimised and that the piball would be unable to gradually warm or cool in the interval between inflation and launch.

Piballs were released on the hour, and paired elevation and azimuth readings taken every 15 seconds during the 10-minute flight. At the end of each reading interval the operator ceased tracking the piball and read the elevation and azimuth angle. These were spoken into a tape recorder suspended from the theodolite tripod. An assistant directly transcribed the spoken measurements onto a data sheet, allowing the tape to be used as a backup (Figure 3.13a-c).

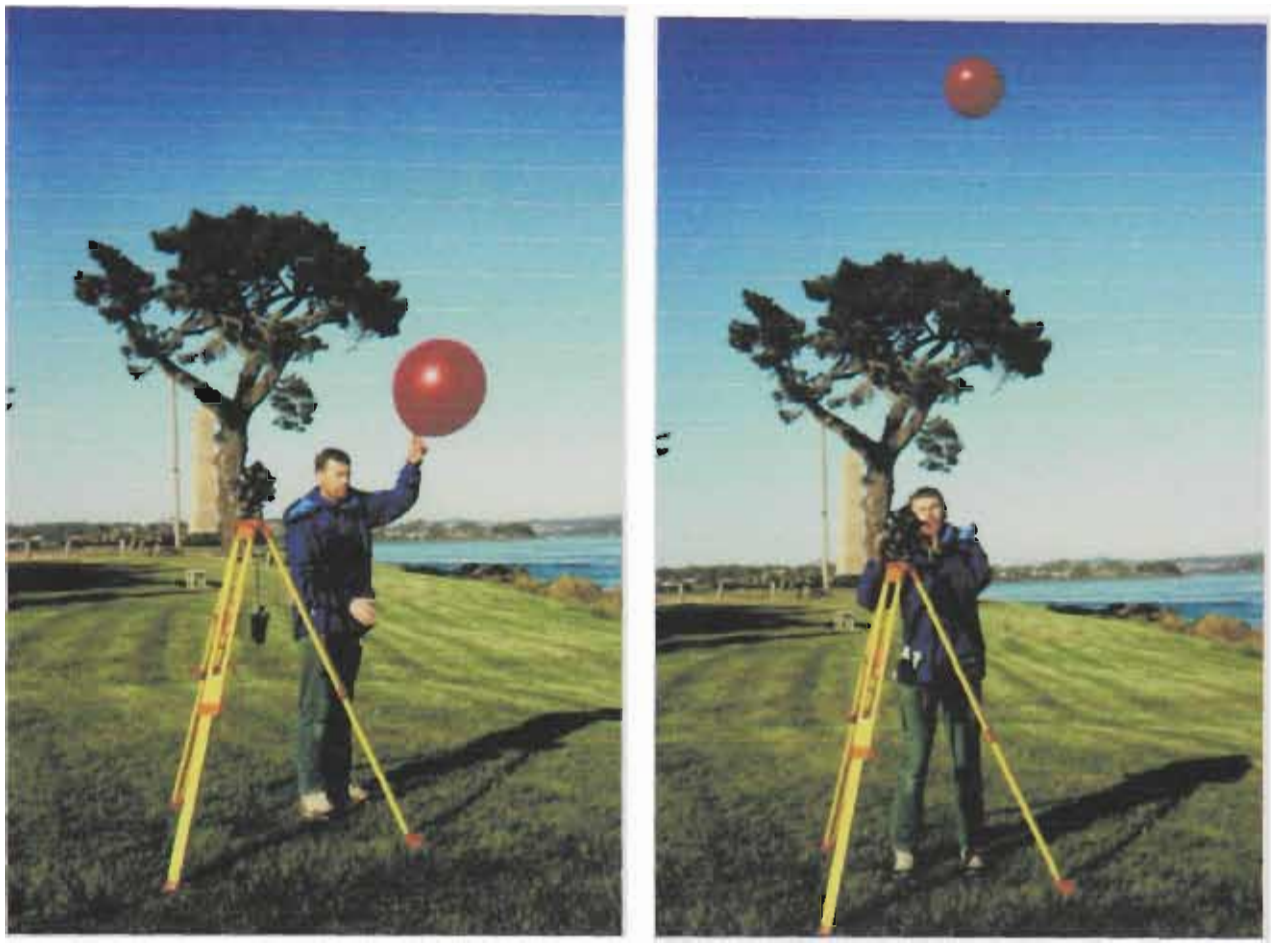

a) b)

Figure 3.13 Wind profile measurements conducted by tracking a pilot balloon using a theodolite: a) prior to release; b) release

Any missed readings were was noted on the tape to ensure that interpolated values could be inserted appropriately. If four sequential missed pairs of readings occurred then the flight was terminated. The operator then repeated the flight if the circumstances warranted it. Typically flights were not repeated if the piball flew into dense fog or cloud.

The reading interval was initially governed by the assistant, who used a stopwatch to count down to the end of each reading interval. This proved to be surprisingly difficult to maintain over a 10-minute period, so use of a pre-recorded timing tape was adopted.

c)

Figure 3.13 Wind profile measurements conducted by tracking a pilot balloon using a theodolite: c) tracking

There was some concern that the reading interval may vary with repeated use of the timing tape. This could occur if the tape gradually slowed down as the tape recorder batteries discharged throughout the course of a day. To combat this the timing tape prompted the user to start a stopwatch at the beginning of the process. A countdown then commenced ending at the word 'release' upon which the user released the piball. Subsequent countdowns occurred at 15-second intervals, with the operator being prompted when to cease tracking and record elevation and azimuth angles. The operator was prompted to stop the stopwatch 30 seconds after the final measurement was made. This time was recorded and was used to calculate the exact timing interval. Timing intervals remained remarkably constant over all piball flights in a day, with typically less than half a second between the longest and shortest intervals.

An assumed constant piball ascent rate of 2.85 ms^{-1} was used when calculating wind speeds and directions. This was determined by averaging the observed ascent rates of several piballs tracked using the double theodolite technique. These test flights were conducted at two Hobart locations, one a large grassed area and the other alongside a sandy beach. In each case theodolite separations of over 800 m were achieved. Flight times were varied throughout the day, with all soundings occurring under anticyclonic conditions. Identical procedures were employed to those used during each *IOP*.

There is some controversy in the literature as to whether the assumption of a constant piball ascent rate is reasonable. Environmental lapse rate was assumed to be the major factor which would act to vary a piball's ascent rate. Reynolds (1966) however found that the effect of lapse rate on the piball ascent rate was relatively small, and may be neglected.

This assumption was questioned by Boatman (1974) who stated that the passage of a piball through an isothermal layer would reduce its ascent rate. He found that

> ... balloon ascent rate is a function of virtual temperature, lapse rate, altitude and balloon diameter in any constant temperature lapse rate environment. Temperature typically decreases with height and balloon diameter increases during the balloon's ascent. These two variables typically decrease the balloon ascent rate... The effect of increasing altitude is to increase balloon ascent rate under constant temperature conditions. Thus, an overall balance of forces affecting balloon ascent rate under normal atmospheric conditions is possible.
>
> If temperature lapse rate were constant but smaller in magnitude than the dry adiabatic lapse rate, ... [then] the balloon ascent rate would be expected to decrease accordingly.
>
> (Boatman, 1974, p961)

Nelson (1975) questioned Boatman's results for isothermal atmospheres, producing his own equations governing piball ascent rates. The final result was inconclusive, however it seems that lapse rate may act to vary piball ascent rates.

The figure of 2.85 ms^{-1} used during the *TVAS* is acknowledged to produce variable quality results, especially in the case of isothermal atmospheres. As a result it is stressed that the single theodolite wind soundings should be viewed as *estimates* of the wind profiles rather than as accurate measurements.

Software was written (in *BASIC*) to convert the paired elevation and azimuth measurements into wind speeds, wind directions and heights using the assumed ascent rate and the accurately determined reading intervals. Each output file produced was stamped with the *IOP* number, the flight date and time, and the name of the site from which the release had occurred.

3.3.3.4 Bureau of Meteorology Radar Wind Profiles

Wind speed and direction profiles are measured by the *BOM* four times daily at the Launceston airport. The 03:00, 09:00, 15:00 and 21:00 soundings are conducted by tracking a large helium-filled weather balloon, with a reflective target attached, using the airport's radar facility. These "radar winds" provide coarse-resolution profiles with measurements commencing at heights of approximately 400 m from the ground and extending to heights well above the *NUATMOS* modelling domain of 2500 m.

3.4 Conclusions

This chapter has detailed the *TVAS* data acquisition process. The network of automatic weather stations, collecting surface data, has been described along with the database containing the complete surface dataset. The *IOP* program, which collected seasonal profiles of temperature and wind, was then outlined. Both the surface and profile datasets were required to provide full input to the *NUATMOS/CITPUFF* models.

4 Description and Use of Models

4.1 Introduction

In this chapter the *NUATMOS/CITPUFF* wind field and pollution dispersion modelling system will be described. A brief history of *NUATMOS* will be given, followed by a detailed technical description of the model. This will include an overview of the model; a summary of the input requirements; a description of the computational grid; details of the interpolation processes used to produce an initial wind field; adjustment of the initial wind field to eliminate divergence; and a description of the drainage flow module.

NUATMOS results will be evaluated using comparisons against ideal and real data. The *NUATMOS* section will end with a description of the configuration used throughout the *TVAS* and during individual *IOPs*.

The *CITPUFF* model will then be introduced, starting with a brief model history and a technical description. Some model validation studies will then be discussed.

The chapter will end with a brief summary of the *GIS* interface developed to display the *NUATMOS* winds and *CITPUFF* concentrations.

4.2 The NUATMOS Diagnostic Wind Field Model

4.2.1 Model History

NUATMOS (Ross *et al.*, 1987b, 1988a, 1988b, 1993a and 1994e) was developed as an improvement of an existing wind field model, *ATMOS1* (Davis *et al.*, 1984). *ATMOS1* was chosen because of its terrain-following co-ordinates and variable

vertical grid spacing, both of which are essential when modelling winds in complex terrain (Ross *et al.*, 1988b).

NUATMOS was evaluated and used as part of the Australian *Latrobe Valley Airshed Study* (*LVAS*). Cook *et al.*, (1988) used *NUATMOS*-generated trajectories to show that high ozone-level events in the Latrobe valley were associated with inter-regional transport of ozone from Melbourne.

In 1987, *NUATMOS* was incorporated into the *Topographic Air Pollution Analysis System* (*TAPAS*). *TAPAS* is a suite of wind field and dispersion models, combined to form a single modelling system, which was jointly developed by the *Centre for Applied Mathematical Modelling* (*CAMM*), the U.S. Department of Agriculture and the U.S. Department of the Interior, Bureau of Land Management. *NUATMOS* was completely rewritten in 1988 as part of its implementation into an emergency response system at the Rocky Flats nuclear facility in Colorado, U.S.A. (Ross *et al.* 1995c).

Current Australian users of *NUATMOS* include the State Electricity Commission of Victoria, The Environmental Protection Authority of Victoria, and *CSIRO* Fossil Fuels. The model has also been incorporated into the state of the art *AUSMET* meteorological model (Ross *et al.*, 1995c), as one of the two available wind field models.

4.2.2 Technical Description

4.2.2.1 Overview

NUATMOS is a diagnostic wind field model, specifically designed for complex terrain. It produces a series of hourly three-dimensional, mass-consistent wind fields, by interpolating arbitrarily located observations on to a regularly spaced grid covering the domain of interest.

Much of the following technical description is directly derived from the Version 6 and 7 *NUATMOS* user manuals (Ross and Lewis, 1993a and Ross *et al.*, 1994e) and

the *AUSMET (NUATMOS)* draft user manual (Ross *et al.*, 1995c). Relevant information has been summarised from a combination of these sources.

NUATMOS wind fields are generated according to a two-stage process. The first stage interpolates the observed wind measurements for any particular hour onto the grid. Measurements are firstly interpolated vertically onto each layer, and then horizontally along the nine terrain-following layers.

The second stage applies minimal adjustments to the gridded wind field to eliminate divergence and to ensure that the final wind field is consistent with conservation of mass, energy and the vertical component of vorticity.

4.2.2.2 Input Requirements

NUATMOS will accept wind measurements from the following variety of sources:

- Surface meteorological stations recording data at a uniform height, typically 10 m; and/or
- Meteorological towers recording winds at a number of different heights; and/or
- Wind soundings collected by tethered balloon sounding systems or by the tracking of free flying pilot balloons.

In addition the model requires the input of a digital elevation model (*DEM*), covering the entire computational domain at the same north-south and west-east resolutions as the computational grid.

4.2.2.3 Computational Grid

Figure 4.1 shows the *NUATMOS* computational domain. Grid cells need not be square, with different resolutions allowed in the west-east and north-south directions. The average terrain elevation is required for every grid cell shown with a central dot. Wind velocity estimates are produced for each of these cells. Velocities can be interpreted as representing either the mean velocity for the entire cell, or the velocity experienced at the cell centre.

The *NUATMOS* modelling domain is vertically divided above each grid cell into a series of terrain following layers (Figure 4.2). The layer boundaries, termed *input*

sigma levels, are defined by surfaces along which the parameter σ is constant. σ is defined as

$$\sigma = \frac{Z_t - z}{Z_t - h}, \qquad 4.1$$

where Z_t is the top of the modelling domain, h is the terrain elevation at position (x,y) and z is the height of the input sigma level. All of these are expressed relative to a common datum level, normally mean sea level.

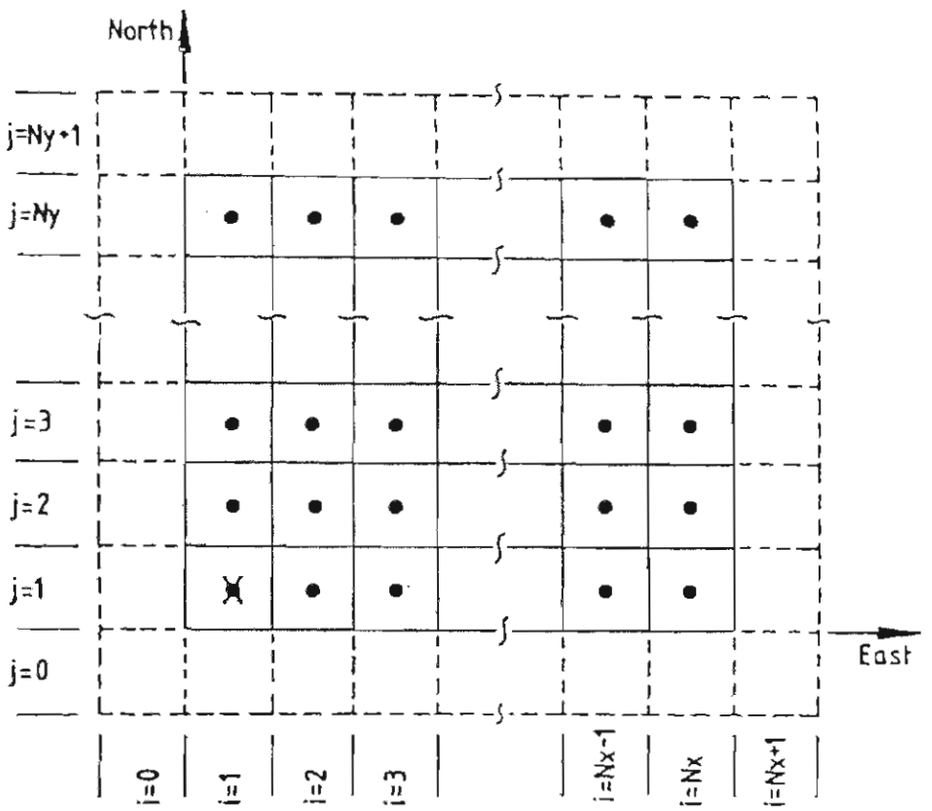

Figure 4.1 Schematic plan view of the *NUATMOS* computational grid. (Source: Ross and Lewis, 1993a, p4)

Wind velocities are modelled at cell mid-heights, along *computational sigma levels*. The top of the modelling domain is defined by the constant sigma level equalling 0.00. This must be above the highest terrain point. Likewise the sigma level at value 1.00 represents the ground level.

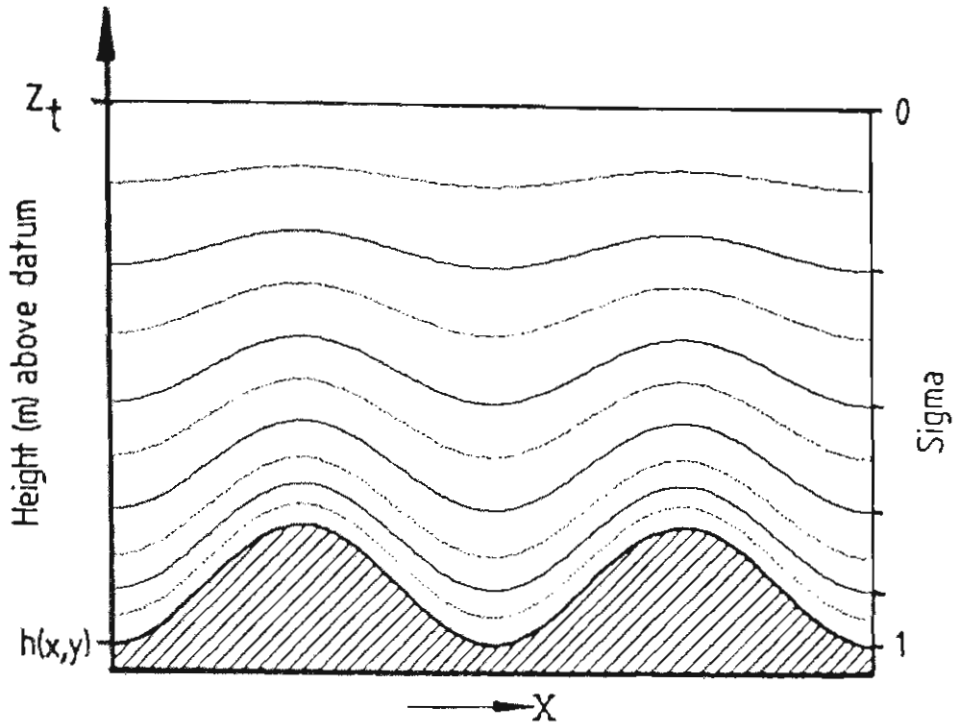

Figure 4.2 Schematic vertical view of the *NUATMOS* computational grid. The solid lines represent the input sigma-levels, whereas the dashed lines are the computational sigma-levels where the wind velocities are determined. (Source: Ross and Lewis, 1993a, p4)

4.2.2.4 *Interpolation of Observations onto the Computational Grid*

A two-stage interpolation process obtains the initial wind field for each hour. Existing measurements are firstly vertically interpolated onto the grid's computational sigma levels. These are then horizontally interpolated onto the grid points *along* the computational sigma levels.

4.2.2.4.1 *Vertical Interpolation Onto the Computational Sigma Levels*

Wind measurements from each observation station are considered in turn. If the station records winds at only one height, such as from a 10-m meteorological site, then *NUATMOS* maps this measurement directly onto the closest computational sigma level. If the observation station records measurements from a number of different heights, such as from large towers or wind sounding equipment, then individual measurements are linearly interpolated onto successive computational sigma levels, extending from the surface to the height of the maximum measurement.

Great care must be taken when defining the sigma levels (Ross *et al.* 1994e). If two or more measurements exist within the vertical extent of a particular grid cell, and there are no other data above and below, then both measurements are ignored. Likewise if there is more than one observation below the lowest computational level and no others above then the measurements are discarded. In both cases the solution lies in a more careful definition of the sigma levels to obtain maximum utility from the available measurements.

4.2.2.4.2 Horizontal Interpolation Along the Computational Sigma Levels

NUATMOS allows the west-east and north-south wind components to be interpolated along the computational sigma levels, using any of three available interpolation schemes. These are:

- the *Inverse Distance Squared* (IDS) weighting scheme;
- the *Variable Radius of Influence* scheme; and
- the *Mean Wind* scheme.

The *IDS* scheme is a simple interpolation scheme, commonly used in diagnostic wind field models. Equation 4.2 (Ross and Lewis, 1993a, p7) illustrates the expression used to interpolate the west-east wind component u_p onto a grid point p,

$$u_p = \frac{\sum_{i=1}^{N} \frac{u_i}{d_i^2}}{\sum_{i=1}^{N} \frac{1}{d_i^2}} \qquad 4.2$$

where d_i represents the horizontal distance between the grid point and an observation u_i. N is the number of observations present on the sigma level in question.

The *Variable Radius of Influence* scheme was incorporated into *NUATMOS* in order to improve initial wind field estimates in locations where grid points were relatively distant from direct observation points. This technique involves characterising the 'mean wind' observed throughout all observation points on the sigma level in question. This is then used to improve upon a first guess, which is based on the *IDS* scheme. Ross and Lewis (1993a) and Ross *et al.* (1994e) note that there are

significant deficiencies in the *Variable Radius of Influence* scheme, and despite many modifications they were not able to significantly improve on the *IDS* scheme.

The *mean wind* scheme sets interpolated wind components to the mean value of all observations along each cell layer. It is therefore not appropriate for use when modelling complex flows, such as those seen in the Tamar Valley.

Ross and Lewis (1993a) and Ross *et al.* (1994e) recommend the simple *IDS* scheme over the more complex *Variable Radius of Influence* scheme. The *IDS* scheme was consequently the scheme used throughout the *TVAS*.

If there are no wind observations assigned to a particular sigma level by the vertical interpolation stage, then the gridded wind field from the computational sigma level below it is copied to this level.

4.2.2.5 Production of a Divergence Free Wind Field

Once the observations have been interpolated and extrapolated onto the computational grid, minimal adjustments are applied to the gridded wind field. This ensures that the final wind field is consistent with conservation of mass, energy and the vertical component of vorticity.

The process involves minimising the function

$$E(u,v,w) = \iiint \left[(u-u_0)^2 + (v-v_0)^2 + \alpha^{-2}(w-w_0)^2 \right] dV \qquad 4.3$$

subject to the constraint

$$\frac{\partial u}{\partial z} + \frac{\partial v}{\partial y} + \frac{\partial w}{\partial z} = 0, \qquad 4.4$$

where x and y are the horizontal co-ordinates and z is the vertical co-ordinate. $V_0=(u_0, v_0, w_0)$ represents the initial interpolated velocity, and $V=(u,v,w)$ represents the final velocity. The parameter α allows the differential adjustment of horizontal and vertical winds, thus supporting the simulation of different atmospheric stability

effects. Throughout the *TVAS*, this parameter was set at its default (and recommended) value of 1, corresponding to a neutral atmosphere.

4.2.2.6 *Drainage Flow Module*

Whilst *NUATMOS* is primarily a diagnostic wind field model, it also contains a prognostic component, which allows it to predict the characteristics of stable drainage flows occurring in measurement-poor regions. This is essential as Smith and Ross (1989) found that diagnostic wind field models consistently fail to capture the features of low-level drainage winds occurring at these times. This may be the result of either poor anemometer performance at low wind speeds or perhaps an indication that the fine scale drainage flows are not being resolved by a widely-spaced anemometer network.

The two-layer vertically integrated model, which was incorporated into *NUATMOS*, was based on a model developed by Garrett and Smith (1984) as part of the *ASCOT* (Atmospheric Studies in Complex Terrain) Project. It utilises a three-step approach (Ross *et al.* 1994f).

The first step initialises the drainage flow module *(DFM)* using a normal *NUATMOS* wind field for the hour corresponding to drainage flow onset. Initial wind fields are produced to characterise both the drainage flow layer and the ambient winds above the layer height. The prognostic model is then used to predict both the surface winds within the drainage layer, and the layer height itself for the next hour.

Step three meshes the *NUATMOS* and the prognostically-derived drainage wind fields for the hour in question, using an appropriate meshing procedure. Throughout the *TVAS*, this was achieved using kriging. The completed wind field is then passed through *NUATMOS* routines, which ensure that conservation constraints are satisfied.

CAMM have evaluated the *DFM* using data from both the *LVAS* (Smith and Ross, 1989) and the *TVAS* (Ross *et al.*, 1994f). In both cases the *DFM* was found to accurately predict drainage flows in the absence of measurements, and to out-perform wind fields created without the use of the *DFM*.

4.2.3 Model Validation Studies

NUATMOS has been extensively evaluated by *CAMM*, using both ideal and real data.

4.2.3.1 Comparisons with Ideal Data

Comparisons of *NUATMOS* wind fields against known potential flow solutions have been made for a number of simple topographic elements. These include flow past a hemisphere (see Figures 4.3 and 4.4), a half-cylindrical ridge, and a variety of three-dimensional hill shapes described by a half-ellipsoid with varying aspect ratios.

These tests simulate the perturbation of a uniform wind caused by various terrain elements. The tests show that for uniform winds, *NUATMOS* yields the correct potential flow as predicted by theory, exhibiting such phenomena as wind speed-up, retardation and channelling.

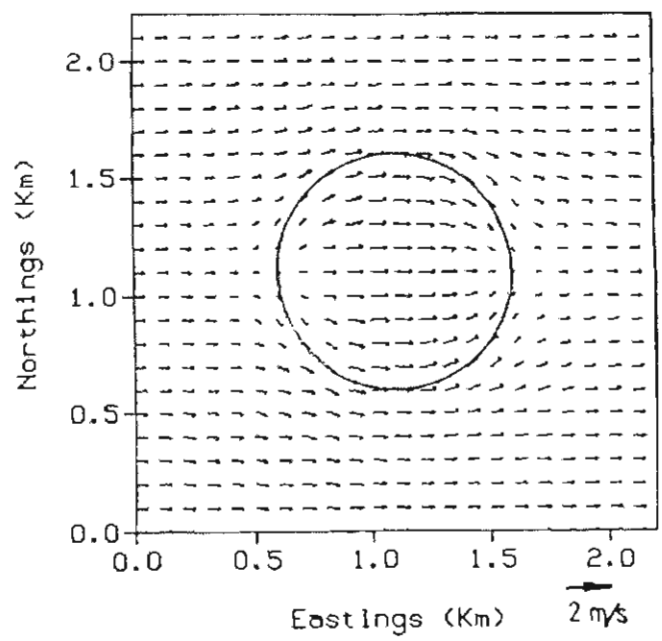

Figure 4.3 Plan view of velocity vectors in the lowest layer of cells (approximately 10 m above ground) as predicted by *NUATMOS* for the hemispherical hill test case. The full modelling domain extends from easting and northing 0 m to 2200 m at 50 m spacing, and vertically to a height of 2500 m above sea level with nine logarithmically-spaced layers. (Source: Ross and Lewis, 1993a, p22)

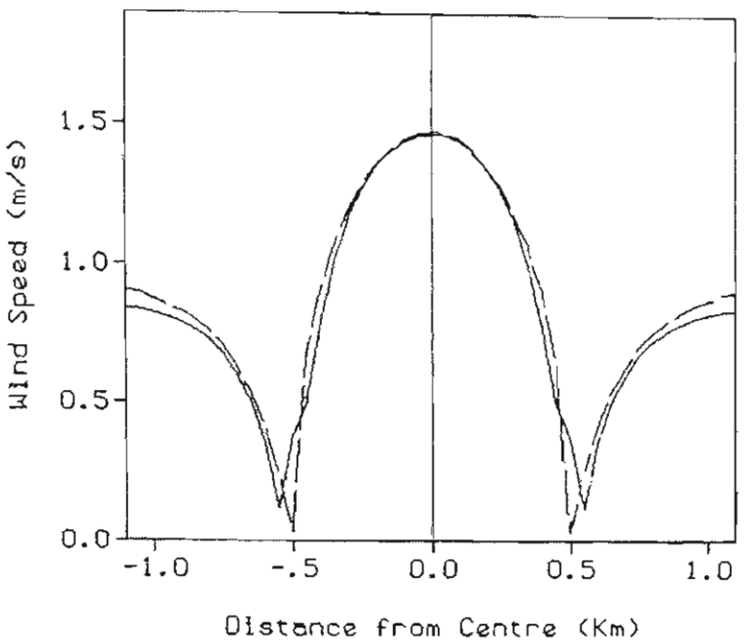

Figure 4.4 East-west wind speed transects across the top of the hemispherical hill for the same model run as in Figure 4.3. The dashed curve illustrates the analytic solution and the unbroken curve is for *NUATMOS*. (Source: Ross and Lewis, 1993a, p22)

4.2.3.2 Comparisons with Real Data

NUATMOS has also been extensively validated against actual meteorological measurements (Ross *et al.*, 1987b, Smith and Ross, 1988). In each case wind vectors were estimated for individual meteorological stations using observations from the remaining stations only, and compared with actual observations made at the same location. Figure 4.5 demonstrates a typical pair of "observed versus predicted" scatterplots for a location in the Latrobe Valley.

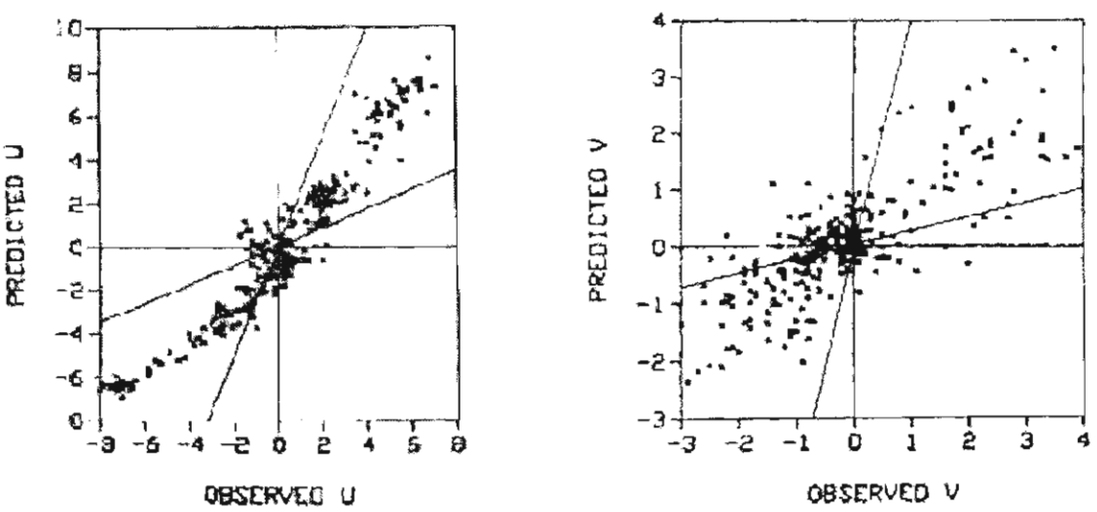

Figure 4.5 Predicted versus observed surface velocity components for the *LVAS* Driffield station for the March 1985 period. (Source: Ross *et al.*, 1987b, pII-154)

Ross *et al.* (1988a, p63) describe the extended model evaluation and validation process, and state that...

> "...reliability was closely allied to observational network density, time of day, time of year, height above the surface and location. It was shown that low wind speeds tended to be associated with low correlations between observing stations which in turn reduced the reliability of interpolated winds. An important feature of the data was found to be the tendency for wind speeds to increase with height while at the same time station density decreases. Thus competing factors appear to determine reliability at any given level."

NUATMOS has also been evaluated using meteorological data collected in the vicinity of the Rocky Flats Nuclear Facility in Colorado (Ross *et al.*,1995c). This dataset contains 300 sets of 15-minute averaged wind observations, covering a wide range of meteorological conditions. Each set is composed of the routinely available data from the region (17 surface stations, and profile data collected from the local airport), augmented by additional data collected for the study (10 surface stations, 6 wind profilers and a 60 m meteorological tower).

The results show that *NUATMOS* was clearly superior to the existing wind field model (*WINDS*), as shown in Figure 4.6. The median difference between *NUATMOS* predicted and observed wind speeds was -1.36 ms^{-1}, showing that *NUATMOS* tended to slightly underpredict wind speed. In comparison, *WINDS* overpredicted wind speeds considerably, with a median difference of 2.09 ms^{-1}. The interquartile range of wind speed difference was 3.35 and 5.63 ms^{-1} for *NUATMOS* and *WINDS* respectively.

In terms of wind direction, *NUATMOS* recorded a mean difference between predicted and observed values of 10.2°, with an interquartile range of 66.5°. In comparison, the values for *WINDS* were -3.5° and 96.7° respectively.

Further validation studies have occurred using data from the San Antonio Mountain region in New Mexico, and the Cinder Cone Butte (CCB) "modellers dataset" (Ross, 1993). CCB, an isolated two-peaked roughly axisymmetrical hill, is located in Idaho. The hill is approximately 100 m in height with a roughly circular base approximately 1 km in diameter.

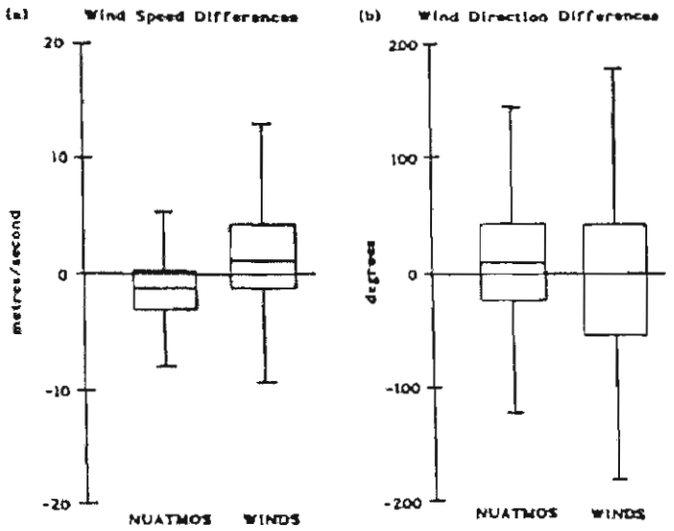

Figure 4.6 Boxplot of difference (predicted-observed) distributions for (a) wind speed and (b) wind direction showing the performance improvements gained by replacing *WINDS* with *NUATMOS*. (Source: Ross *et al.*, 1995c, p19)

A preliminary evaluation of the *DFM* has been conducted for the Latrobe Valley (Smith and Ross, 1989). They found that the model simulated relatively complex drainage flows, with some frequently observed features being correctly resolved. Smith and Ross also found that the *DFM* was not restricted solely to nocturnal flows, allowing the simulation of daytime drainage flows as well.

The *DFM* has also been evaluated in the Tamar Valley during times when drainage flows are evident. Ross *et al.* (1994f) compared *NUATMOS* wind fields, produced with and without the *DFM*, against prognostic wind fields generated by *LADM*, the *Lagrangian Atmospheric Dispersion Model* developed by *CSIRO DAR* (Physick, 1993).

The *LADM* simulation performed to suggest the location of regions requiring *TVAS* meteorological stations (described in Chapter 3, Section 3.2.1), was used to generate a set of pseudo-observations available during a typical *IOP*. These included simulated surface measurements from the anemometer network and profile measurements from simulated pilot balloon releases. *NUATMOS* was then run using two different configurations. *Configuration 1* was the standard *NUATMOS* output, generated without the use of the *DFM*. In contrast, *Configuration 2* used *NUATMOS* and the *DFM* in conjunction with the pseudo-observations to derive its wind fields.

Figure 4.7 shows scatter plots comparing *NUATMOS* winds for each configuration against the "true" winds produced by *LADM*. Ross *et al.*, (1994f), when commenting on this figure, note that the inclusion of the *DFM* results in a reduction in scatter, and a greater proportion of predictions within a factor of two of the observations. This is evident for both the *u* and the *v* components.

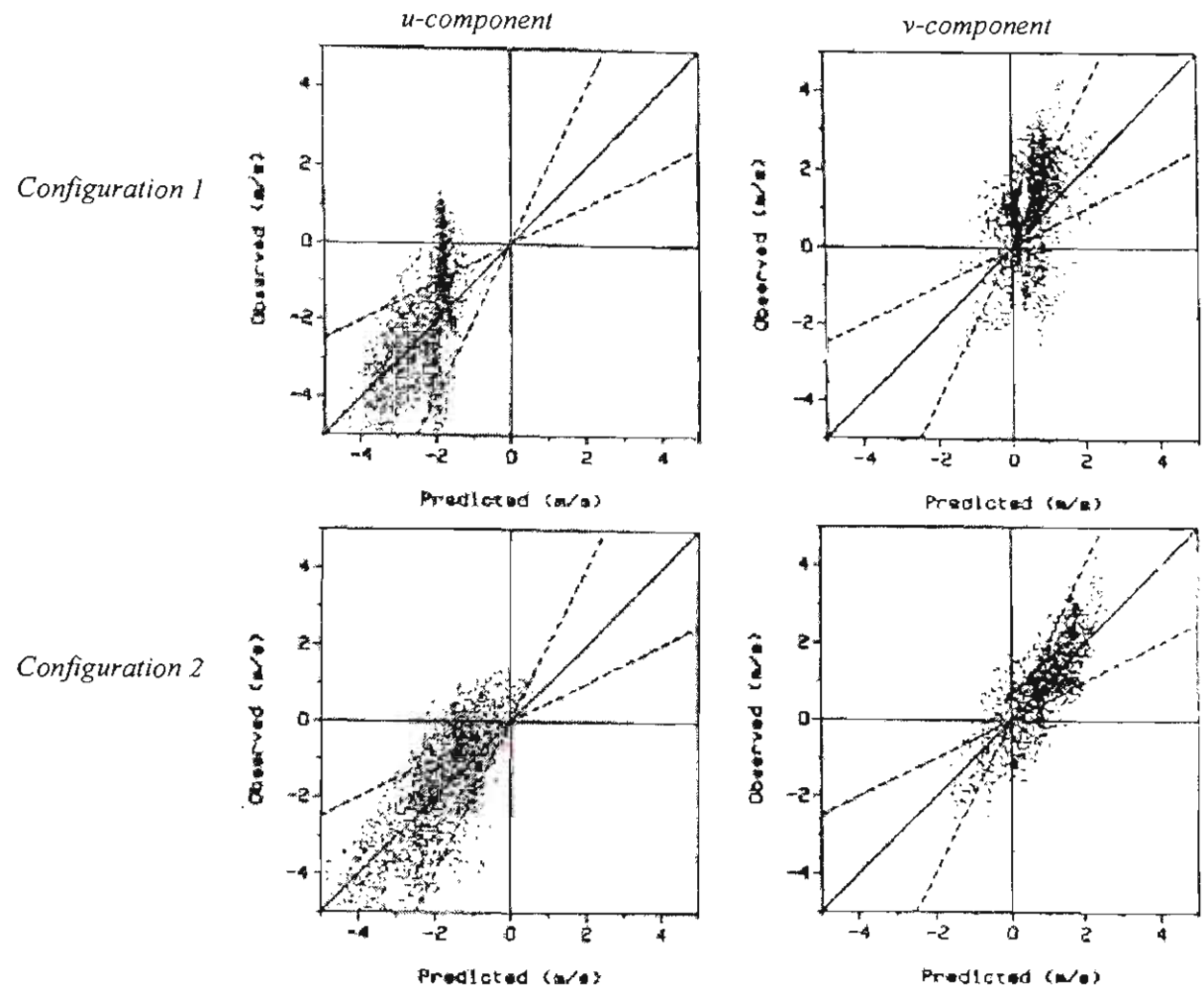

Figure 4.7 Scatter plots of observations versus predictions for 23:00, 12 September, 1991 for the two configurations of the model. The area between the dashed lines contains points that are within a factor of 2 of the solid (perfect fit) line. (Source: Ross *et al.*, 1994f, p320)

Figure 4.8 directly compares the *LADM, Configuration 1* and *Configuration 2* wind fields relating to the scatter diagrams above. Under drainage conditions, the *DFM* clearly produces more detailed and accurate wind fields than those produced in its absence.

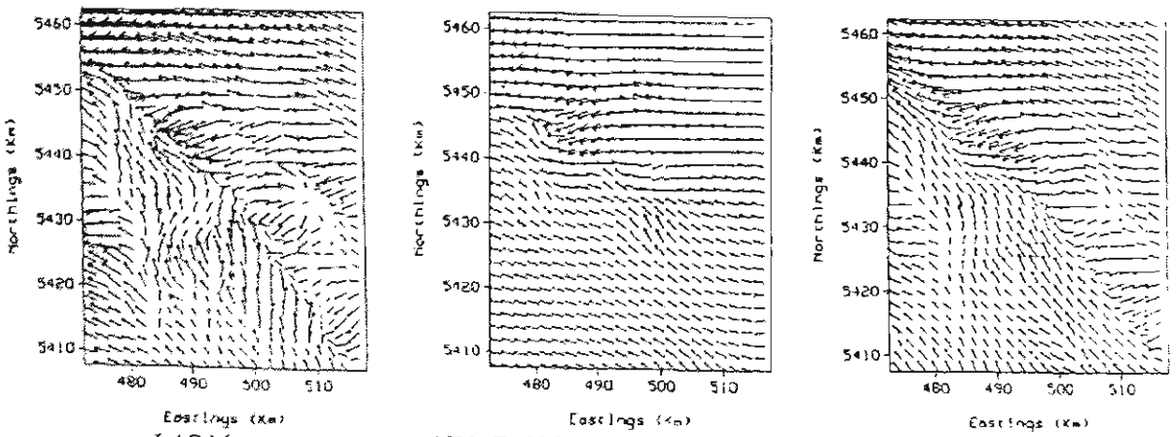

LADM *NUATMOS* Configuration 1 *NUATMOS* Configuration 2

Figure 4.8 Vector plots of the surface (10-m) wind fields from *LADM* and the two configurations of *NUATMOS* for 23:00, 12 September, 1991. (Source: Ross *et al.*, 1994f, p324)

4.2.4 *Model Configuration for the TVAS*

As part of the *TVAS*, *CAMM* were contracted to create the *NUATMOS* configuration and data input files. These were based upon raw meteorological data collected, by the author and others from the University of Tasmania, during each of the *IOPs*.

In this study *NUATMOS* was run using the *CAMM* configuration files, thus generating the same digital three-dimensional wind fields that *CAMM* had originally produced. The author wrote software to extract the appropriate wind vectors and to display them using the *ArcView GIS* system. The entire three-dimensional wind field was used in the modelling program, however only selected surface wind vectors were displayed.

4.2.4.1 *TVAS Modelling and Display Domains*

The *NUATMOS/CITPUFF* models are required to share the same computational domain. The extent of this is shown in Figure 4.9 along with the *DEM* provided by the *DELM* Land Information Bureau. The computational domain covers an east-west distance of 160 km and a north-south distance of 143 km at a 1 km by 1 km grid cell resolution. Table 4.1 provides the *AMG* co-ordinates of each corner of the modelling domain.

The *DEM* was produced from existing 100m contours, mapped at the 1:250,000 scale. This data was supplemented with spot height data. The model, with a grid cell resolution of 1 km by 1 km, has a horizontal accuracy commensurate with the

source data, and a vertical accuracy of ±20 m. The Land Information Bureau created the model using the Intergraph Modeller software. They firstly created a triangulated irregular network model, from which the 1 km *DEM* was then interpolated. The "inferred breakline" option was used, in order to create a better description of the drainage patterns using the input contours.

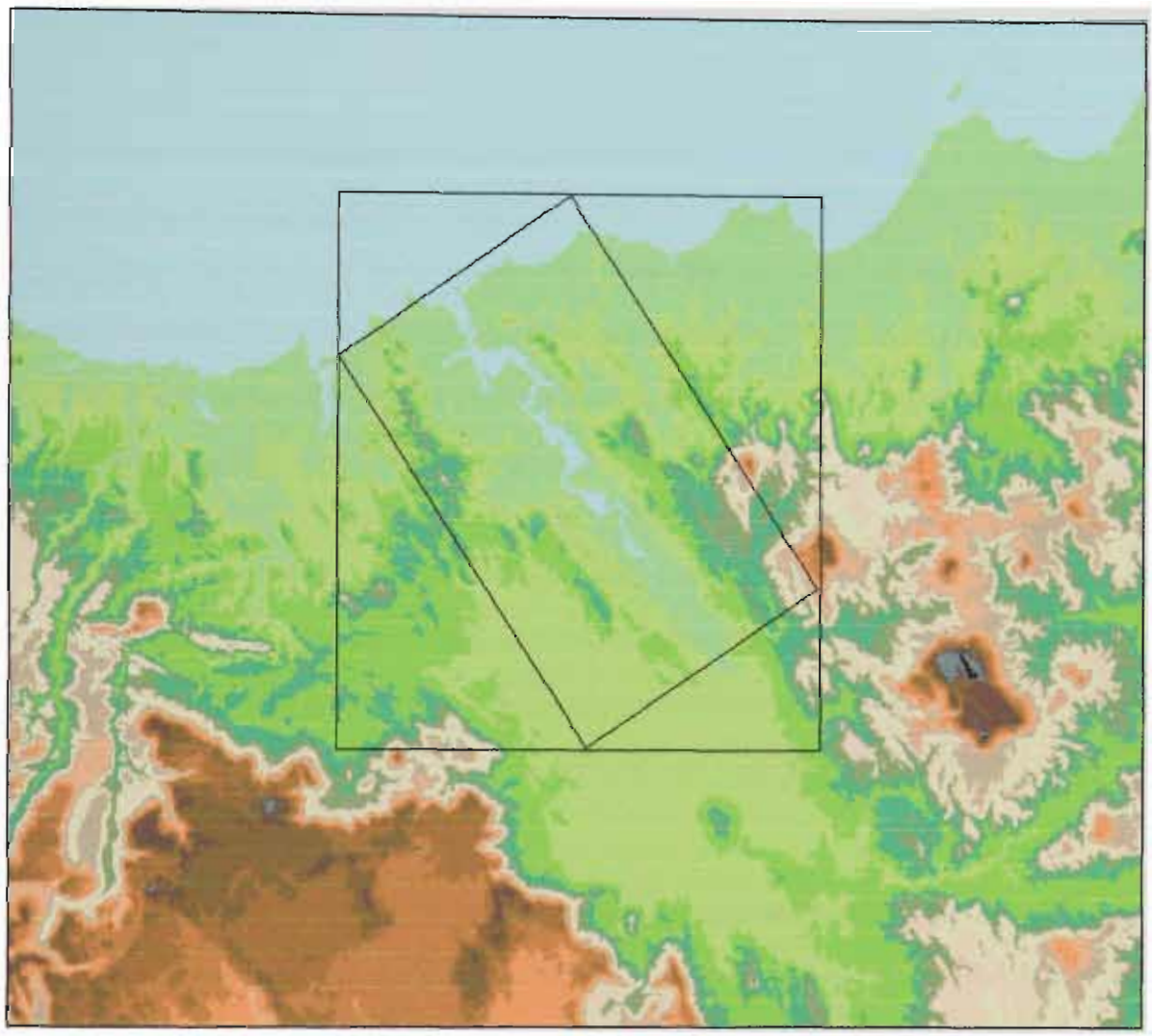

Figure 4.9 The *NUATMOS/CITPUFF* computational domain for the *TVAS*. The NW/SE aligned rectangle represents the *TVAS* study area, and the rectangular box surrounding it is the *NUATMOS* display region which contains the *CITPUFF* receptor grid..

Table 4.1 *NUATMOS/CITPUFF* computational domain boundaries

AMG Easting (m)	*AMG Northing (m)*	*Corner*
420000	5493000	NW Corner
580000	5493000	NE Corner
580000	5350000	SE Corner
420000	5350000	SW Corner

Figure 4.9 also shows the *TVAS* study area and the *NUATMOS* display region. For ease of display the *CITPUFF* receptor grid was set to conform to this region, and was

also at a 1 km by 1 km resolution. The *NUATMOS/CITPUFF* display region is contained within the computational domain, covering an east-west distance of 68 km and a north-south distance of 80 km. The bounding co-ordinates are provided in Table 4.2.

Table 4.2 *NUATMOS/CITPUFF* display domain boundaries

AMG Easting (m)	*AMG Northing (m)*	*Corner*
466000	5468000	NW Corner
534000	5468000	NE Corner
534000	5388000	SE Corner
466000	5388000	SW Corner

The rationale behind the choice of the large computational domain, in comparison with the relatively small display region, can be seen when the dominant topographical features are considered. The Great Western Tiers dominate south and southwest of the study region. To the east and southeast of the region lie Mt. Arthur, Mt. Barrow, Ben Lomond and Snow Hill respectively. These topographical controls exert a large influence on the wind regime of the study area. Firstly they channel the winds in a northwesterly/southeasterly orientation into the Tamar Valley. They also provide a source of drainage flows into the study area. If the *NUATMOS* computational domain was smaller, and failed to take these topographical features into account, then the modelled wind fields within the study region would be of a far lesser quality. Likewise sources located outside the display region will impact on the air quality of the display region itself.

Above the grid, the *NUATMOS* modelling domain was divided into a series of nine terrain-following sigma levels as defined by Table 4.3. The top of the modelling domain was set at 2500 m.a.s.l., with the logarithmically-spaced computational sigma levels below it. The lowest computational sigma level was at 11 m with the highest at 2063 m.

Table 4.3 Terrain-following sigma level structure adopted for the *TVAS* wind fields

Sigma-Level Number	*Lower Input Sigma Level*	*Computational Sigma Level*	*Upper Input Sigma Level*	*Lower * Input Sigma Level Height (m)*	*Computational * Sigma Level Height (m)*	*Upper * Input Sigma Level Height (m)*
1	0.3500	0.1750	0.0000	1625	2063	2500
2	0.6000	0.4750	0.3500	1000	1313	1625
3	0.7500	0.6750	0.6000	625	813	1000
4	0.8400	0.7950	0.7500	400	513	625
5	0.9000	0.8700	0.8400	250	325	400
6	0.9400	0.9200	0.9000	150	200	250
7	0.9738	0.9569	0.9400	66	108	150
8	0.9916	0.9827	0.9738	21	43	66
9	1.0000	0.9958	0.9916	0	11	21

* *Height above ground level given a domain height of 2500 m*

4.2.4.2 TVAS Seasonal Configuration Settings

Whilst the bulk of the *NUATMOS* input parameters were identically configured throughout all *IOPs*, some of necessity were different for each *IOP*. Table 4.4 summarises these differences. In particular it shows the *IOP* start and end times, the *DFM* start and end times, and the timing and location of the wind profile measurements.

CAMM produced a written report for each *IOP*, summarising the configurations used and displaying the modelled wind fields. The reference to each report is also provided in the table.

Table 4.4 *NUATMOS* input data for each *IOP*

	IOP Name				
	Summer 1	*Summer 2*	*Autumn*	*Winter*	*Spring*
Times Relative to...	DST	DST	EST	EST	EST
IOP Start	12/12/93 07:00	15/12/94 06:00	13/4/94 07:00	27/6/94 07:00	24/9/93 07:00
IOP End	13/12/93 19:00	15/12/94 20:00	14/4/94 19:00	28/6/94 18:00	25/9/93 18:00
Simulation Duration (hours)	36	14	35	35	35
Drainage Flow Module Start	12/12/93 20:00	N/A	13/4/94 17:00	27/6/94 16:00	24/9/93 18:00
Drainage Flow Module End	13/12/93 07:00	N/A	14/4/94 07:00	28/6/94 08:00	25/9/93 09:00
DFM Duration (hours)	10	N/A	14	16	14
Surface Wind Sites (10-m)	1-5, 7-14	1-4, 6-10, 12, 16, Launceston Airport AWS	1-5, 7-13	1-5, 7-13, 15-16, Launceston Airport AWS	1, 3-5, 7-10, 12-14
Piball Wind Profile Sites	7, 8, Batman Bridge	3, 7, 8	3, 7, 8	3, 7, 8	7, 8, Batman Bridge
Piball Release Times	Hourly releases, 07:00 to 19:00	Hourly releases, 06:00 to 19:00	Hourly releases, 07:00 to 17:30	Hourly releases, 07:30 to 17:30	Hourly releases, 07:00 to 18:00
Tethered Balloon Site	8	N/A	8	8	8
Tethered Balloon Launch Times	03:22, 04:33, 05:43 13/12	N/A	22:38 13/4; 00:04, 02:32, 04:58, 06:00 14/4	17:56, 21:39, 23:11 27/6; 01:01, 02:58, 08:31, 09:28, 13:04, 14:10, 15:07, 16:05, 17:30 28/6	7:15, 18:00 24/9; 01:24, 03:09, 05:14, 07:02, 08:02, 17:31 25/9
Launceston Airport Radar Wind Schedule	03:00, 09:00, 15:00, 21:00	03:00, 09:00, 15:00, 21:00	03:00, 09:00, 15:00, 21:00	03:00, 09:00, 15:00, 21:00	03:00, 09:00, 15:00, 21:00
CAMM Reports	Ross & Lewis1994d	Ross & Lewis 1995d	Ross & Lewis1995a	Ross & Lewis 1995b	Ross & Lewis1993b, 1994c

4.3 The CITPUFF Gaussian Puff Dispersion Model

4.3.1 Model History

CITPUFF was developed by *CAMM* in 1985, being produced around the same time as *NUATMOS*. Since this time the model has been regularly reviewed and extended where possible (Ross *et al.*, 1987a). It was used extensively in the *Latrobe Valley Airshed Study*, and by the *Environment Protection Authority of Victoria.*

Version 6.0 was used throughout the *TVAS*. *CAMM* are no longer actively developing *CITPUFF*, preferring to concentrate their dispersion modelling efforts on *AUSPUFF*. *AUSPUFF* is a Gaussian puff model, which is rapidly gaining acceptance for regulatory purposes. Although *AUSPUFF* operates on similar principles to *CITPUFF*, it is more versatile and has overcome some of *CITPUFF's* limitations. Chief among these is the *CITPUFF* limitation that puffs cannot impact with the terrain.

4.3.2 Technical Description

4.3.2.1 Overview

CITPUFF is a multi-source Gaussian puff dispersion model, suitable for predicting atmospheric contaminant concentrations in regions of complex terrain. Pollutants are advected using the hourly progressions of three-dimensional wind fields provided by *NUATMOS*.

Sawford and Hearn (1988, p168) describe the general operating principles of Gaussian puff models when they write...

> "In an attempt to take account of temporal and spatial variability in meteorological conditions, while at the same time preserving the simplicity of a Gaussian distribution of material, a range of models known as Gaussian Puff Models have been developed. In these models, continuous emissions are approximated by a series of instantaneous emissions (puffs) separated by a time interval Δt. In the limit $\Delta t \rightarrow 0$, the discrete puffs overlap to form a continuous plume and in practice the separation of puffs is chosen to produce a "smooth" distribution of material. Each puff moves and grows according to conditions at its centre-of-mass. Most of the physical parameterizations used carry over from Gaussian plume modelling, and it is usually assumed that growth in the x-direction is also given by σ_y. Clearly, under steady, spatially uniform conditions a puff model should produce results consistent with a Gaussian plume model using equivalent parameterizations for the transport physics.
>
> In order to realise the potential improvement embodied in puff modelling, it is necessary to provide input data which accurately reflects the temporal and spatial variability of the wind and other meteorological fields and of emissions. This is not possible directly from observation. Instead the wind field is usually derived from a diagnostic model in which observations are first interpolated onto a grid and then minimally adjusted in order to satisfy constraints such as mass consistency."

Gaussian puff models therefore extend the Gaussian approach for use in situations where wind fields are non-uniform in both time and space, and complex terrain exists. Section 2.7 provides a brief overview of Gaussian puff models.

The following technical description is largely derived from the *CITPUFF* Version 5 and 6 manuals (Ross *et al.*, 1987a and 1995e).

Ground level concentrations (GLCs) $\overline{\chi}(x, y, 0)$ are calculated for position (x,y) using equation 4.5 (see equation 2.11)

$$\bar{\chi}(x,y,0) = \frac{2Q}{(2\pi)^{1.5}\,\sigma_y^{\,2}\,\sigma_z}\,\exp\left[\frac{-r^2}{2\sigma_y^{\,2}}\right]\,\exp\left[\frac{-(\Delta z)^2}{2\sigma_z^{\,2}}\right]\,\exp\left[\frac{-kx}{\bar{u}}\right], \qquad 4.5$$

where Q represents the source strength, σ_y and σ_z are the plume spread in the horizontal and vertical respectively, Δz is the puff release height, k the exponential decay constant, $\bar{u}$ is the mean wind speed, and $r^2 = (x - \bar{u}t)^2 + y^2$. It is also assumed that σ_x equals σ_y.

Continuous point source emissions are modelled as a succession of discrete overlapping puffs, which are advected by the *NUATMOS* wind fields using a Lagrangian (puff centred) trajectory algorithm. Multiple sources are simulated using the assumption that the individual concentration fields from each source can be superimposed upon the same receptor grid. This allows the simulation of line, area and volume sources using the placement of virtual point sources with careful specification of the initial Gaussian standard deviations σ_{y0} and σ_{z0}.

During any time step, the pollutant load at a given receptor is calculated as the sum of the contributions from all sources at that point using

$$\psi_s = \int_{t_0}^{t_0+T} \bar{\chi}_s \, dt. \qquad 4.6$$

The parameter T is the dosage time, and ψ_s is known as the dosage. The subscript, s, denotes the fact that the calculation includes all sources and puffs. If ψ_s is divided by T then the average concentration over the time interval T is obtained.

4.3.2.2 The Computational Domain and Receptor Grid

The *CITPUFF* three-dimensional computational domain is required to be the same as that used by *NUATMOS* for any particular scenario. This allows the model to correctly access the *DEM* and the *NUATMOS* winds.

The model produces concentrations on a rectangular ground level "receptor grid". This may be defined at a different resolution to the *NUATMOS* display grid, and may cover a different area within the common computational domain. Throughout the

TVAS however, the *CITPUFF* receptor grid was deliberately chosen to mirror the *NUATMOS* display grid, in location, extent and resolution. In addition to the receptor grid, *CITPUFF* can also output ground level concentrations at discrete, user-selected locations, termed "monitoring sites".

4.3.2.3 Input Requirements

CITPUFF requires the user to provide a number of input parameters prior to a model run. These are set within a series of windows, each detailing a specific feature of the simulation.

The first window specifies general simulation parameters such as a simulation title and output filename. The user must then specify the start date and time for the *NUATMOS* winds; the number of concentration averaging periods, batches of meteorological data, and hours of release from the sources; the averaging period length; and the time delay between commencement of the wind data and the first puff.

The model then requires the computational domain to be defined, by setting the cell resolution in the x and y directions, the number of cells in each direction and the co-ordinates of the origin. The *DEM*, which matches the computational domain, must also be specified along with the receptor grid definition and the location of any discrete receptors.

The third screen lists the *NUATMOS* wind files in the order that they will be accessed during the simulation.

Pollutant sources are then characterised by the following fixed and variable attributes:

Fixed attributes

- Source location relative to the computational grid;
- Elevation of the underlying terrain;
- Release height;
- Initial values of σ_y and σ_z which are used to characterise the initial plume spread; and, where applicable;
- Stack diameter.

Variable attributes

- Hourly varying emission rate; and either
- Exit temperature and velocity, which are used to calculate plume rise; or
- Effective release height.

The model set-up screen, which follows, asks for detailed settings of the different available options. The possible choices vary according to previous selections. These include such parameters as the interval between puff releases; the maximum allowable advection displacement; the decay rate constant; the effective surface roughness height and the dispersion averaging time. The user is asked to identify whether puffs travel along the *NUATMOS* sigma levels or whether they may be transported in the vertical by the *NUATMOS* winds. The puff dispersion type is also chosen in this screen, along with the option to model two layers of different stability. If the latter option is not chosen then the user can specify a lapse rate for an elevated stable layer, and whether partial penetration of this layer is permitted.

The final screen requests the ambient temperature; the mixing depth and the atmospheric stability class (A to F) for both layers during each hourly interval.

4.3.2.4 Puff Dispersion

CITPUFF allows the user to specify one of four different options to be used when calculating puff dispersion. These are:

- Pasquill-Gifford dispersion coefficients;
- Briggs rural dispersion coefficients;
- Lateral spread using sigma-theta data, with vertical spread governed by the Pasquill-Gifford coefficients; and
- Lateral spread using sigma-theta data, with vertical spread governed by the Briggs rural dispersion coefficients.

Each option provides a way of determining the value of σ_y and σ_z as a function of downwind distance. These are calculated for each puff and are used to determine its diffusion relative to the trajectory of its centroid. The σ_y and σ_z values grow with downwind distance, thus enlarging the puff size during its transport.

Throughout the *TVAS*, the Briggs rural dispersion scheme was consistently used, as it was found to provide the best results during the *LVAS* (Ross *et al.*, 1988a). Table 4.5

summarises the formulae this scheme uses, in order to calculate σ_y and σ_z as functions of atmospheric stability and downwind distance.

Table 4.5 Horizontal (σ_y) and vertical (σ_z) rural dispersion coefficients recommended by Briggs, as a function of downwind distance, x (in metres).

Pasquill Stability Category	σy	σz
A (1)	$0.22\,x(1 + 0.0001\,x)^{-1/2}$	$0.20\,x$
B (2)	$0.16\,x(1 + 0.0001\,x)^{-1/2}$	$0.12\,x$
C (3)	$0.11\,x(1 + 0.0001\,x)^{-1/2}$	$0.08\,x(1 + 0.0002\,x)^{-1/2}$
D (4)	$0.08\,x(1 + 0.0001\,x)^{-1/2}$	$0.06\,x(1 + 0.0015\,x)^{-1/2}$
E (5)	$0.06\,x(1 + 0.0001\,x)^{-1/2}$	$0.03\,x(1 + 0.0003\,x)^{-1}$
F (6)	$0.04\,x(1 + 0.0001\,x)^{-1/2}$	$0.016\,x(1 + 0.003\,x)^{-1}$

(Source: Ross *et al.*, 1995e, p14)

4.4 Model Validation

CITPUFF has undergone an extensive evaluation process, both on its own, and in conjunction with *NUATMOS* as a complete modelling system. This has largely been performed using data from the *LVAS* Plume Tracking Experiment (*PTE*) and the CCB modellers dataset.

Initial testing was conducted using four day of data from the *LVAS PTE* (Ross *et al.*, 1988a, 1988c). Modelled SO_2 concentrations from the 13 sources (mainly power stations), were compared with measurements obtained from the *Latrobe Valley Air Monitoring Network.*

Two techniques were used. The first compared measured and modelled concentrations on a point by point basis. The second technique involved a qualitative analysis of the *GLC* contours to see if the modelled plume concentrations were of a correct magnitude, but were possibly incorrectly positioned on the ground.

Non-zero concentrations were predicted at a number of monitoring stations, with all of these sites measuring concentrations above the 'noise' threshold of the instrument. The predictions were described as "qualitatively believable", with predicted concentrations being largely consistent with observations.

A direct comparison between observed and predicted concentrations showed that the order of magnitude was predicted well at all but one station. The likely cause of the

discrepancy was thought to be either a small unmodelled wind direction deviation, or the presence of an unknown local source.

Ross *et al.* (1988a, 1988c) concluded that *CITPUFF* was found to predict the general spatial concentration patterns well. These however were not necessarily located in the correct location or modelled at the exact magnitude. Despite this they stated that the model system had the potential for use in case study work.

Sawford and Hearn (1988) conducted a validation study using winter and spring data drawn from the *LVAS PTE.* In this case two models were evaluated: *CITPUFF* and the *ISC* (*Industrial Source Complex*) model. *ISC* is a Gaussian plume dispersion model, used for regulatory purposes by the *Environment Protection Authority of Victoria (EPAV).*

In general both models performed poorly on a 'point-by-point' comparison of SO_2 observations and predictions. Figure 4.10 shows typical scatter graphs comparing observations and predictions for each model using the June 1984 data. The large degree of scatter, which was considered similar to that seen in overseas tests of both models, was attributed to the inability to correctly prescribe winds at plume height. The combination of narrow plumes and a sparse monitoring network means that a small error in wind direction predictions could easily result in a large error in *GLC* predictions, even if the overall concentrations within the plume were well predicted.

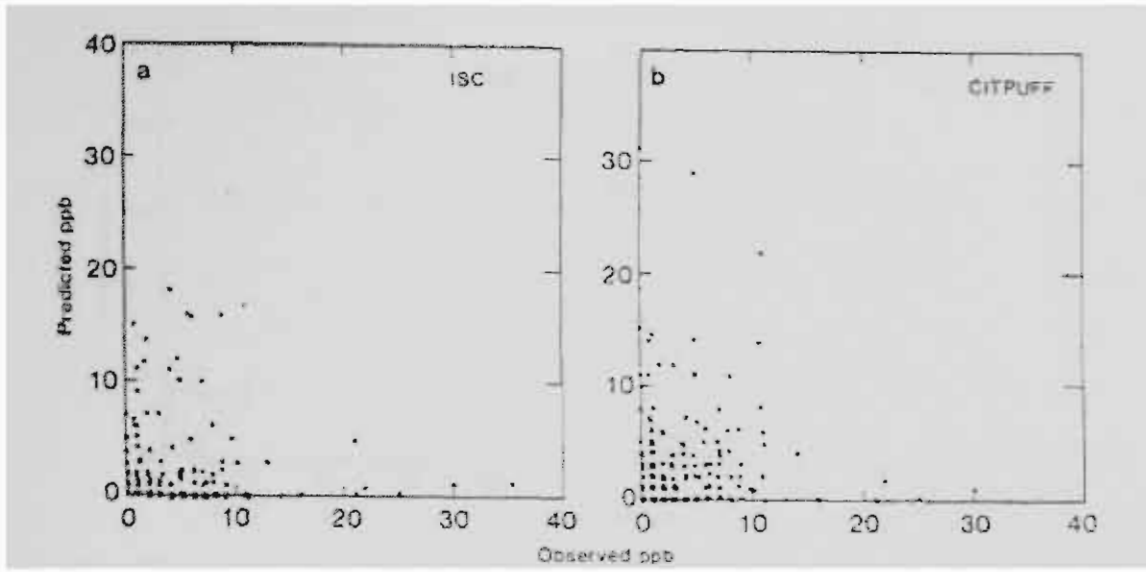

Figure 4.10 Comparison of predicted and observed SO_2 concentration during the June 1984 Plume Tracking Experiment for (a) the *ISC* model and (b) *CITPUFF*. (Source: Sawford and Hearn, 1988, p169)

The points on Figure 4.10 are fairly evenly scattered about the one-to-one line. In addition predictions and observations cover a similar range. This indicates that when using the winter data, neither model exhibited a strong bias. This was not so however, for the spring data. In this case both models showed a tendency to overpredict, with *CITPUFF* performing significantly better than *ICS* (Figure 4.11).

Lorimer *et al.* (1998) and Lorimer (1989) used the June 1984 *LVAS PTE* data to evaluate *CITPUFF* along with *ISC* and a simpler Gaussian plume model called *MAXGLC*. Not surprisingly, similar results were found to those given above.

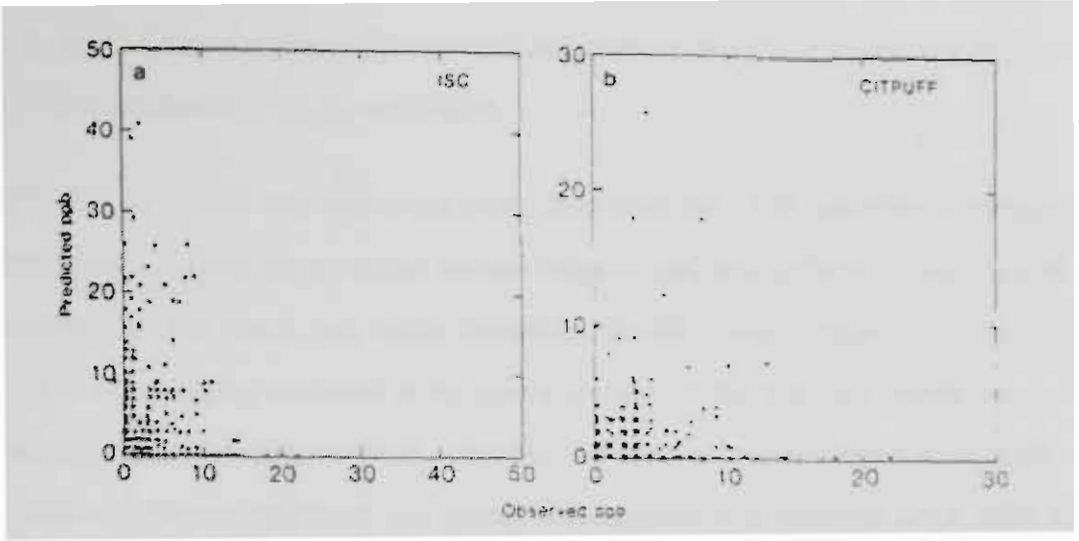

Figure 4.11 Comparison of predicted and observed SO_2 concentration during the March 1985 Plume Tracking Experiment for (a) the ISC model and (b) CITPUFF. (Source: Sawford and Hearn, 1988, p169)

In addition to producing scatter graphs comparing observations and predictions, Lorimer examined the cumulative frequency distribution functions for observations and predictions (Figure 4.12). This analysis served to relax the strict pairing of observations and predictions in both location and time. All three models are seen to poorly simulate the lower percentiles of the distributions. In particular the models grossly overestimate the frequency of occurrence of zero concentrations. *CITPUFF* and *ISC* appear to model data from the upper few percentiles well however.

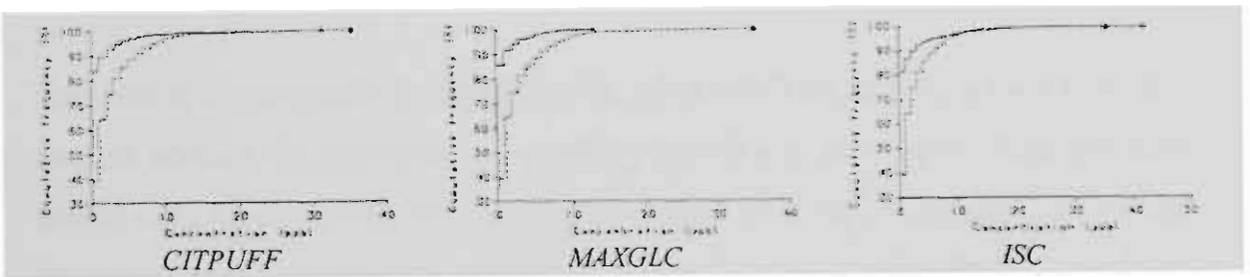

Figure 4.12 Cumulative frequency distribution functions for data collected during the *LVAS Plume Tracking Experiment.* Predictions are designated using continuous lines, whereas dashed lines represent observations. Crosses mark the predicted global maxima, and filled circles the corresponding observations. (Source: Lorimer, 1989, p85)

In his conclusions, Lorimer (1989) states that during periods of light variable winds, all three models greatly underpredicted the area impacted by SO_2. They also had difficulty in predicting GLCs from tall stacks. Two possible reasons were given for these problems. Firstly the emission factors used were only known to a factor of

about 2. In addition the three-dimensional structure of the atmosphere was poorly characterised, especially at plume height.

NUATMOS/CITPUFF was evaluated using data from the CCB modeller's dataset. The modeller's dataset incorporates meteorological and atmospheric concentration measurements. The tracer gas, sulfur hexafluoride (SF_6), was released upwind of CCB. Tracer sampling occurred at receptors located on the hill. An extensive meteorological monitoring network recorded the required parameters during each tracer release. Plume trajectory and spread information was obtained using lidar and photography. (Ross *et al.*, 1990; Ross and Fox, 1991)

Ross and Fox (1991) found that *NUATMOS/CITPUFF* performed better than the existing CCB models for cases when the source release height (h) was greater than the critical streamline height, H_c, and as well as the CCB models when h was below or equal to H_c. The dividing streamline height, H_c, represents a division between two regions of flow which occur around a terrain obstacle under stable stratified flow conditions. At heights less than the critical streamline, the flow does not have sufficient kinetic energy to pass over the top of the terrain feature, and passes around the obstacle in a horizontal plane instead. Above the critical streamline the flow travels over the obstacle.

Two attempts were made at evaluating *NUATMOS/CITPUFF* during the *TVAS*. In the first attempt SF_6, was released at ground level at a location north of George Town during a sea breeze event. One-hour bag samples were collected along a downwind transect aligned normal to the wind direction. Unfortunately analysis of the collected samples failed to find detectable quantities of SF_6 (Carnovale, 2000, pers. comm.).

In the theory that the very narrow level plume passed between two sampling sites, the experiment was repeated. This time the SF_6 was injected into the *Comalco Aluminium* carbon bake furnace stack at Bell Bay. This was done in order to facilitate thorough mixing and dispersion of the tracer by the time it reached ground level. Once again analysis of the collected samples failed to detect significant quantities of SF_6 (Carnovale, 2000, pers. comm.).

It is uncertain exactly what went wrong. The most likely explanation is that the narrow plume missed, or only glanced, the monitoring sites. In the first experiment the separation distance between samplers was large, thus allowing the plume to travel between two widely-spaced samplers. In response to this the second experiment used a narrow spacing between samplers. In this instance it is likely that the plume passed to the side of the entire sampling network.

Another possible explanation lies in the sampling methodology used. Samples were pumped into large thin plastic bags, which were heat sealed after collection. It is possible that either the bags or the seals leaked during the interval between sampling and analysis.

One thing however was certain. Due to lack of finances, the tracer validation experiment could not repeated. In the intervening time the anemometer network has been decommissioned, and trained staff are no longer available to repeat the necessary wind and temperature profile measurements. As a result the *NUATMOS/CITPUFF* modelling system must be considered unvalidated for the Tamar Valley.

One positive factor remains however. The many evaluations of the *NUATMOS/CITPUFF* system during the *LVAS* have resulted in a clearer knowledge of situations and configurations causing poor predictive performance. An example of this lies in the rejection of the *variable radius of influence* scheme, in favour of the simpler *inverse distance squared* weighting scheme, for use in interpolating *NUATMOS* winds along sigma levels. The *Briggs rural dispersion scheme* was also found to provide the best *CITPUFF* results during the *LVAS*. These and other findings have been incorporated into the wind field and pollution dispersion modelling reported on in this thesis. It is hoped that the model system should therefore produce predictions with similar levels of accuracy to those obtained during the *LVAS*.

4.5 The ArcView GIS Display System

NUATMOS and *CITPUFF* results were displayed on maps of the Tamar Valley using the *ArcView™ GIS* package produced by *ESRI*. Software was written which converted the hourly *NUATMOS* and *CITPUFF* output files into *ASCII* form, suitable for input into *ArcView*. The software allowed the user to select the appropriate *NUATMOS* sigma level for display, and to sub-sample the wind vectors so that only each n^{th} vector was selected for viewing. This kept the wind field maps from becoming too cluttered and difficult to interpret.

Point based data, such as the *NUATMOS* wind fields, are easily displayed using *ArcView*. The *CITPUFF* ground level concentrations are presented in a raster form. This required the use of *Spatial Analyst™*, an *ArcView* extension providing a raster functionality to the primarily vector based *ArcView*.

ArcView maps were animated, where necessary, by importing them into the *MS PowerPoint* package.

4.6 Conclusions

This chapter has provided a brief technical description of the *NUATMOS* diagnostic wind field model and the *CITPUFF* Gaussian puff dispersion model. Validation studies for both models have been described. The chapter ends with a description of the *ArcView GIS* system used to display the modelled results.

5 Climatology of the Tamar Valley

5.1 Introduction

In this chapter a climatology will be constructed for the Tamar Valley. It will be largely based on data extracted from the *TVAS* database, specifically the 15-minute averaged time series data collected at the 16 meteorological stations scattered throughout the study area. The period of record nominally spans three years, extending from May '93 to May '96, however some sites, such as Site 14, span shorter time periods.

Data will be summarised on a seasonal basis for each meteorological site using wind roses, stability roses and a new form of rose referred to as the 'transport rose'. Roses will be initially presented in tabular form, however the dominant features for each season will also be mapped, in order to display the spatial distribution of important variables.

The parameters that will be mapped on a seasonal basis are:

- prevailing and second prevailing wind directions;
- mean wind speed;
- frequency of 'calms';
- prevailing Pasquill stability class;
- frequency of stable (class F or G) conditions;
- frequency of unstable (class A or B) conditions;
- mean 24-hour wind run;
- mean 24-hour transport distance;
- frequency of 24-hour transport distances less than 50 km;
- mean 24-hour recirculation factor;
- frequency of 24-hour stagnation events;
- frequency of 24-hour ventilation events; and
- frequency of 24-hour recirculation events.

The chapter will conclude by amalgamating the most important of the meteorological parameters presented into an index of air pollution potential. This will be mapped on a spatial basis and compared with housing densities calculated using data from the 1996 census.

5.2 Wind Frequency Analyses

5.2.1 Seasonal Wind Roses

Wind roses were constructed on a seasonal basis, covering the eight cardinal points of the compass, for six wind speed classes. Calm winds were defined, regardless of wind direction, for all wind speeds less than 0.5 ms^{-1}. The wind speed categories were defined as in Table 5.1.

Table 5.1 Wind speed classes used in the wind rose analysis

Class	*Wind Speed ($m s^{-1}$)*	
	Lower Limit	*Upper Limit*
Calm *		< 0.5
1	≥ 0.5	< 2.0
2	≥ 2.0	< 4.0
3	≥ 4.0	< 6.0
4	≥ 6.0	< 8.0
5	≥ 8.0	

* defined regardless of wind direction

Appendix 1a-e presents wind roses for the entire year, and for each successive season. Roses are tabulated in order of inland distance, with sites located close to the valley axis being clearly marked. Each table is appended with a summary table providing the following details for each anemometer site:

- the frequency of calms (independent of direction);
- the mean velocity (independent of direction);
- the maximum velocity (independent of direction);
- the prevailing direction, and associated mean velocity; and
- the second prevailing direction (i.e. the direction with the second highest frequency of occurrence), and associated mean velocity.

Wind roses are provided as a detailed seasonal summary of winds recorded at each of the sixteen *TVAS* anemometer sites. A brief scan of Appendix 1a-e shows that whilst some roses reveal an evenly-distributed wind regime, throughout all direction and speed classes, many roses are highly skewed.

Site 9 at the coast, for example, is skewed towards strong westerly winds, whereas Site 16 inland is dominated by light northerly winds. In general the skewed roses tend to be aligned with the valley axis, showing frequent up-valley and down-valley flows. This is especially evident at Site 5. The valley-axis skewing is a combination of topographic channelling, the anabatic and katabatic winds occurring in valleys, and the sea and land breeze phenomena occurring near the coast.

The presence of strong westerly winds is often seen, especially at sites located near the coast. This reflects Tasmania's latitudinal position in the 'roaring forties' belt. Another frequent feature is the presence of light winds draining off local hills, and the valley walls. This may be clearly seen in the winter roses, and is exemplified at Site 5.

It would be counter-productive to laboriously detail the features of all 80 roses, covering 16 sites for each of the five seasonal classes. Instead the dominant features listed in each season's summary table will be mapped, in order to reveal the broad spatial pattern existing throughout the entire study area. These include statistics such as the frequency of calms, the prevailing wind direction and mean wind speed.

5.2.2 Prevailing Wind Direction Class by Season

Throughout the wind rose analysis, wind directions were classified into eight classes, each centred on one of the eight main points of the compass. Frequencies were determined for each class. The prevailing wind direction was defined as the direction class with the greatest frequency. Likewise, the second-prevailing wind direction was that with the next highest frequency. This classification was performed on a seasonal basis for each meteorological station.

Figure 5.1 depicts the prevailing wind directions graphically, by plotting wind arrows on a series of maps of the valley. A separate map is used for each season. Wind arrows rather than wind vectors are used, as this analysis involves wind directions only. As a result, all arrows have the same length. Each arrow is centred on the location of the appropriate meteorological station, and is aligned with the mid-point of the direction class that the prevailing wind falls into.

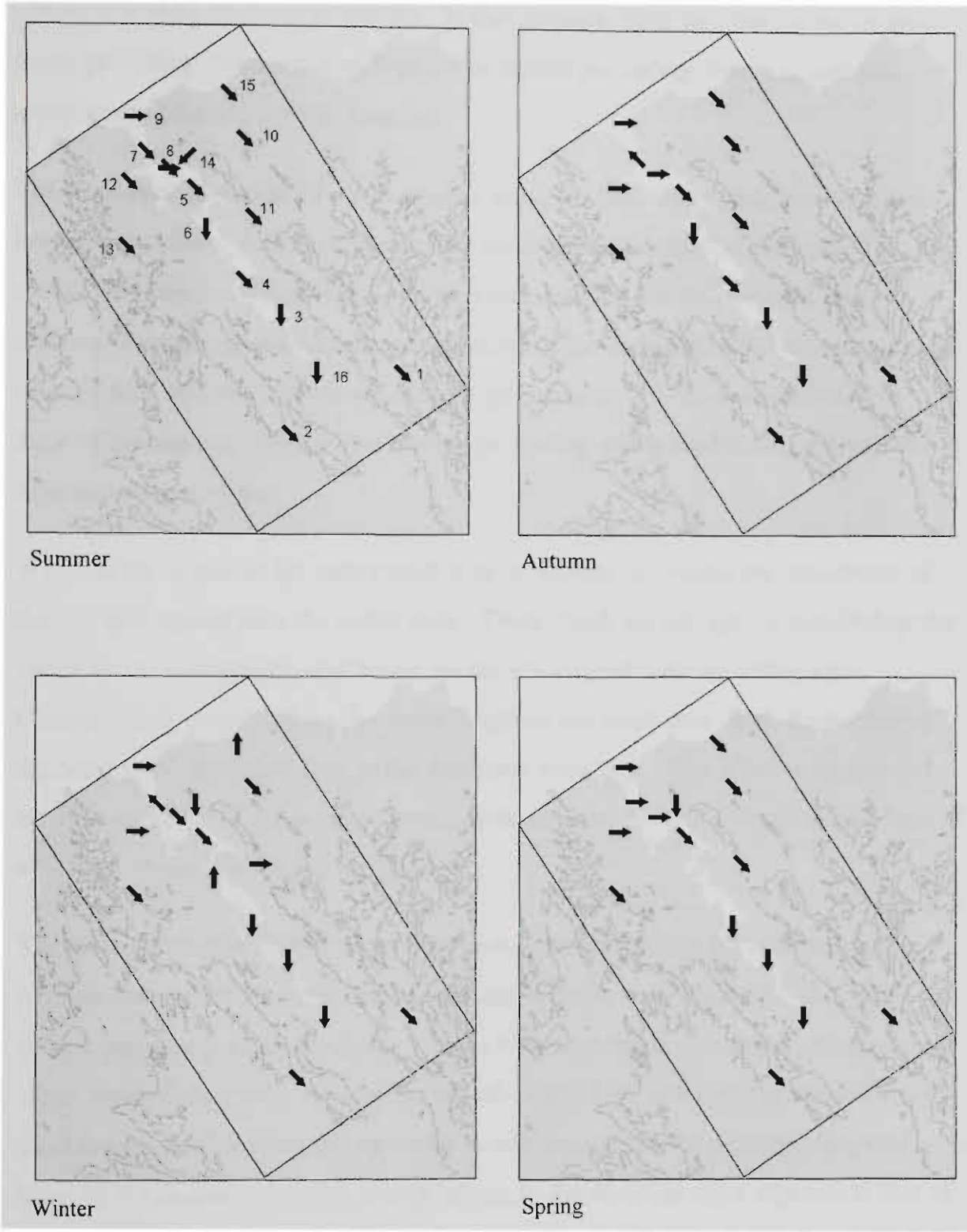

Figure 5.1 Prevailing wind directions by season (May '93 to May '96). The northwest/southeast aligned rectangle shows the extent of the *TVAS* study area. Site numbers are provided on the summer map, and contours are drawn (using a 200 m interval) to provide an indication of topography.

In one case (Summer, Site 8), the maximum frequency occurred for two direction classes simultaneously (NW and W). In this instance, both directions were assigned to the prevailing direction as well as to the second-prevailing direction, and two arrows were plotted over this location.

The maps each show the *TVAS* study area, along with contours on a 200-m contour interval, in order to provide a view of the dominant topographical controls. The most remarkable feature of this diagram is the similarity that occurs across all four seasons. Prevailing wind directions are identical for eight out of the sixteen stations over *all* four seasons. Of the remaining eight stations, four are consistent across three of the seasons. This shows that the prevailing winds tend to be persistent in direction all year round.

Winds at the mouth of the valley tend to be westerlies, reflecting the persistence of the westerly stream over the entire state. These winds are strongly channelled up the valley by the topography, and hence are closely aligned with the valley axis. Channelling is evident along the entire length of the study area, from Low Head at the coast to Western Junction, at the southeast boundary. This effect is augmented by the occurrence of the northwesterly sea-breeze and diurnal anabatic winds, both of which are channelled by the topography.

The second-prevailing wind directions were investigated in order to determine whether drainage flows were also significant in frequency. Figure 5.2 shows the second-prevailing wind directions. Winds with a southerly or easterly component do occur, most often at sites close to the mouth of the river, however the more definite trend is one of reinforcing the up-valley winds depicted in the previous diagram. Many of the second prevailing winds belong to the direction class adjacent to that of the prevailing winds. This is especially noticeable in the spring map.

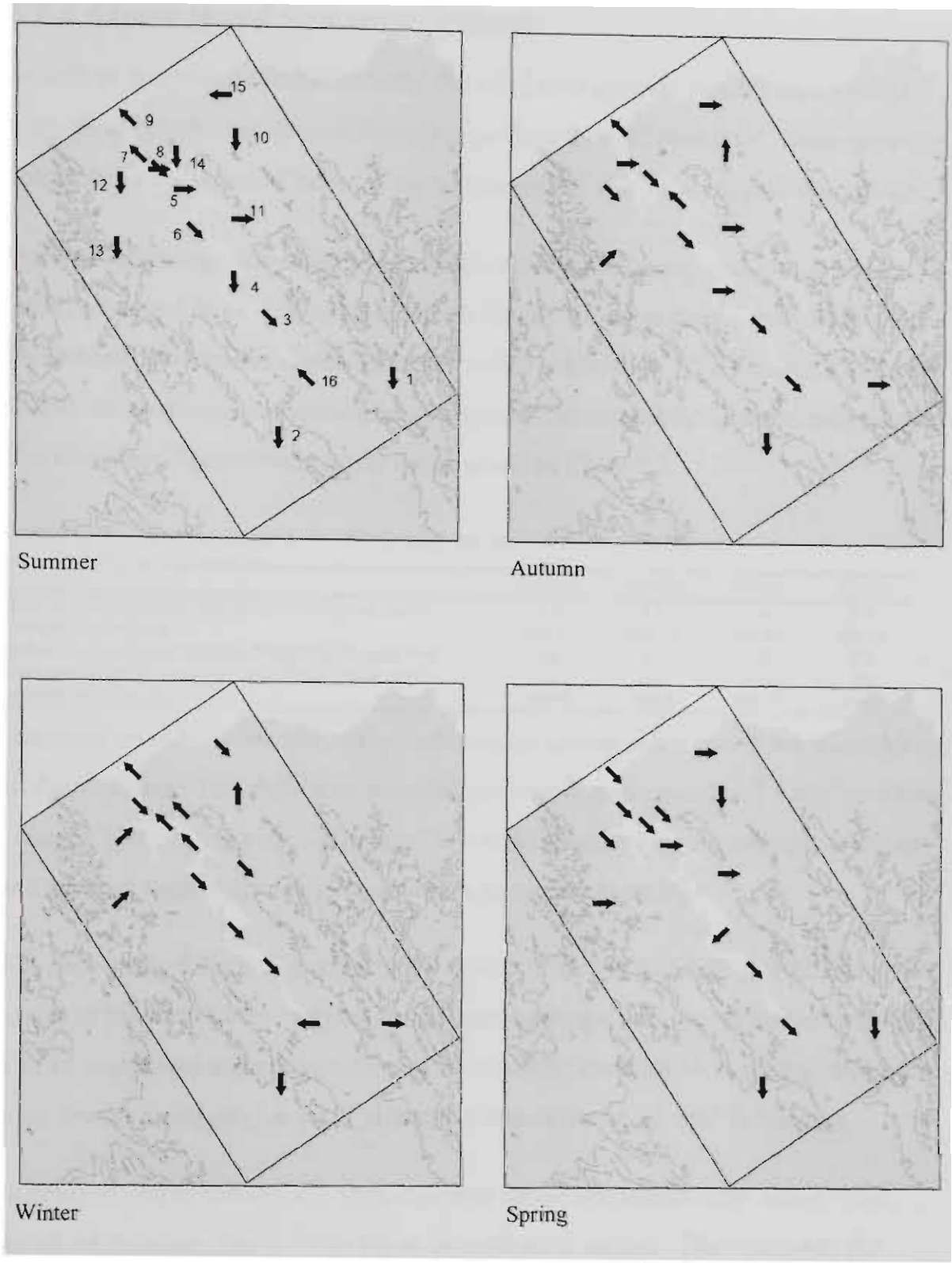

Figure 5.2 Second prevailing wind directions by season (May '93 to May '96). The second prevailing wind direction is the wind direction with the second highest frequency of occurrence. The northwest/southeast aligned rectangle shows the extent of the *TVAS* study area. Site numbers are provided on the summer map, and contours are drawn (using a 200 m interval) to provide an indication of topography.

5.2.3 Mean Wind Speed by Season

As well as prevailing wind directions, the wind rose analysis process also yielded mean wind speeds that were calculated regardless of wind direction. These were determined on a seasonal basis for each anemometer site where data was available.

The sixteen site-specific mean wind speeds, recorded in any given season, were further averaged to provide a spatial-mean speed. This was used as an indication of the seasonal variation in wind speed on a valley-wide basis. The location and value of both the minimum and maximum site-specific mean speeds for each season were also recorded. This information is summarised as Table 5.2.

Table 5.2 Seasonal variation in site-specific and spatial-mean wind speeds

	Summer	*Autumn*	*Winter*	*Spring*
Minimum of the Site-Specific Mean Wind Speeds (ms^{-1})	2.6	1.8	1.6	2.4
Location of Minimum	Site 11	Site 11	Site 16	Site 14
Spatial-Mean of all Site-Specific Mean Wind Speeds (ms^{-1})	3.6	3.1	2.8	3.8
Maximum of the Site-Speeific Mean Wind Speeds (ms^{-1})	5.2	5.4	6.0	5.7
Location of Maximum	Site 9	Site 9	Site 9	Site 9

Examination of the table shows that valley-wide spatial-mean speeds were similar for all four seasons. The study area recorded an overall mean speed of 2.8 ms^{-1} in winter, rising to 3.8 ms^{-1} in spring. In general low wind speeds were experienced in winter and autumn, with slightly higher speeds in summer and spring.

The minimum of the site-specific mean speeds tended to be located within the entire length of the East Tamar, varying as the seasons progressed. Locations ranged from Site 11 in summer and autumn, to Site 16 in winter, and Site 14 in spring. Speeds were lowest in winter (1.6 ms^{-1}), rising to a maximum of 2.6 ms^{-1} in summer.

In contrast, the maximum site-specific mean speed was consistently found at the mouth of the river, Site 9 - Low Head, regardless of season. The maximum site-specific mean speed was lowest in summer (5.2 ms^{-1}), rising to a maximum (6.0 ms^{-1}) in winter.

Mean site-specific speeds, identified by season, AMG easting and AMG northing, were imported into the *Golden Software "Surfer V6.03"* software package. Isolines were drawn through the gridded data, using the kriging option. These were weakly smoothed by the package, and imported into the *ESRI "ArcView V3.1 "* GIS package

for display. This approach was adopted for all of the isoline maps that appear in this chapter.

Figure 5.3 shows the spatial variation in mean seasonal wind speeds experienced throughout the entire study area. Winds are a maximum in speed at the mouth of the valley, and tend to decrease with inland distance along the valley axis. A zone of light winds stretches southeastward along the East Tamar. Light winds are also often associated with sheltered arms of the river, such as at West Arm (Site 12) and East Arm (Site 11). The city of Launceston, located some 50 km inland (Site 16), also experiences relatively low mean speeds throughout the entire year. Mean speeds at Bell Bay tend to be 1.0 to 1.5 ms^{-1} higher than those recorded in Launceston.

5.2.4 Frequency of 'Calms' by Season

'Calm' conditions were defined when the fifteen-minute mean wind speeds were less than 0.5 ms^{-1}. By definition, calms are considered directionless quantities. Table 5.3 summarises the spatial-mean frequency of calms throughout the entire study area on a seasonal basis. It lists the minimum and maximum site-specific frequency of calms and identifies the locations involved.

Table 5.3 Seasonal variation in site-specific and spatial-mean frequency of calms *

	Summer	*Autumn*	*Winter*	*Spring*
Minimum of the Site-Specific Calm Frequencies (%)	0.4	0.6	0.7	0.8
Location of Minimum	Site 9	Site 9	Site 9	Site 15
Spatial-Mean of the Site-Speeific Calm Frequencies (%)	7.6	13.6	16.8	8.9
Maximum of the Site-Specific Calm Frequencies (%)	19.1	36.5	40.8	30.8
Location of Maximum	Site 11	Site 11	Site 11	Site 14

* Calm winds are defined whenever the 15-minute mean speed is less than 0.5 ms^{-1}.

Calms are least likely to be experienced during the summer and spring months (7.6 % and 8.9 % respectively). During autumn calms occurred on 13.6 % of occasions, rising to 16.8 % in winter.

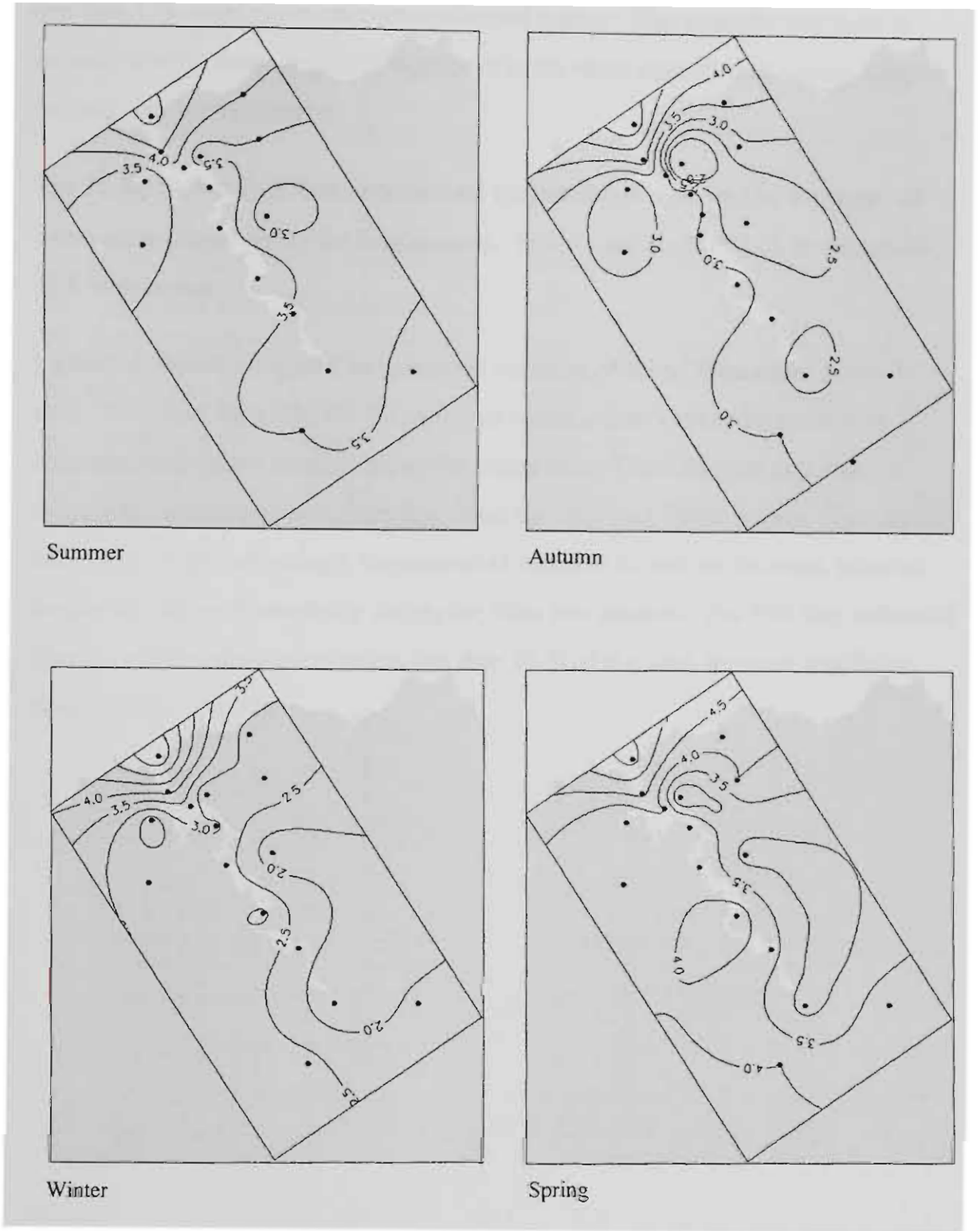

Figure 5.3 Spatial variation in mean wind speed (ms^{-1}) by season (May '93 to May '96). A 0.5 m contour interval is used, with index values oriented towards areas of increasing wind speed. The dots represent the location of each anemometer site. The northwest/ southeast aligned rectangle shows the extent of the *TVAS* study area.

On a spatial basis, the minimum site-specific frequency of calms occurred at either of the two coastal sites, Sites 9 and 15. At both sites frequencies of less than 4 %, often

less than 1 %, were experienced regardless of season. This suggests that there is virtually always some degree of windiness at the coast regardless of season, time of day and weather conditions.

Site 11, located at East Arm, experienced the maximum site-specific frequency of calms during three out of the four seasons. This ranged from 19.1 % in summer to 40.8 % in winter.

Figure 5.4 shows the spatial and seasonal variation of calms throughout the study area. The maps show that the frequency of calms is near zero at the coast, and increases with inland distance along the valley axis. There tends to be a zone of frequently occurring calms extending along the mid-East Tamar region. The city of Launceston experiences high frequencies of calms in winter and summer, however frequencies drop off markedly during the other two seasons. The Bell Bay Industrial Zone generally experiences calms less than 10 % of the time, however this figure rises slightly in spring.

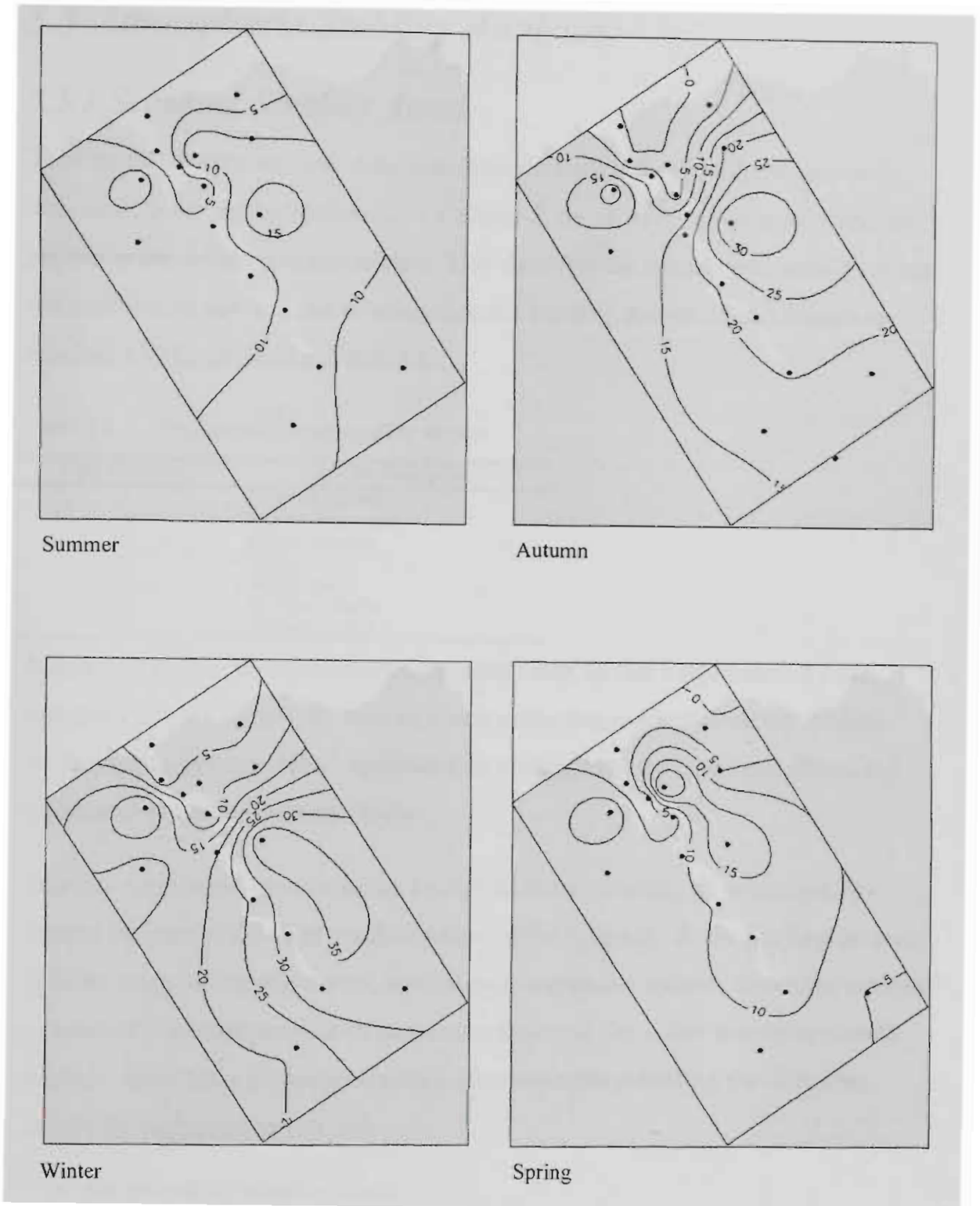

Figure 5.4 Mean frequency (%) of calm conditions by season (May '93 to May '96). Calms are defined as occasions when the wind speed is less than 0.5 ms^{-1}. A 5 % contour interval is used, with index values oriented towards areas of increasing frequency. The dots represent the location of each anemometer site and the northwest/ southeast aligned rectangle shows the extent of the *TVAS* study area.

5.3 Atmospheric Stability Analyses

5.3.1 Seasonal Stability Roses

The Pasquill-Turner stability class was calculated using the modified sigma-theta technique, described in Section 2.3.4, Chapter 2, for all of the 15-minute averaging periods in the meteorological dataset. This classifies the atmospheric stability at any site and time of day into one of seven discrete stability classes. These classes are labelled A to G, as listed in Table 5.4.

Table 5.4 The Pasquill-Turner stability scheme

Class Descriptor	*Stability Description*
A	Extremely unstable
B	Moderately unstable
C	Slightly Unstable
D	Neutral
E	Slightly Stable
F	Moderately Stable
G	Extremely Stable

Stability roses are directly analogous to wind roses, in that frequencies of each stability class are plotted as vanes on a rose according to wind direction. Unlike wind roses there is no 'calm' equivalent, as atmospheric stability must always fall into one of the seven stability classes.

Stability roses were constructed on a seasonal basis, covering all seven stability classes for each of the eight cardinal points of the compass. Appendix 2a-e presents stability roses for the entire year, and for each successive season. Roses are tabulated in order of inland distance, with sites located close to the valley axis being clearly marked. Each table is appended with a summary table providing the following details for each anemometer site:

- the prevailing stability class;
- the frequency of G class stability conditions (%);
- the prevailing direction of winds associated with G class stability;
- the frequency of F class stability conditions (%);
- the prevailing direction of winds associated with F class stability;
- the frequency of B class stability conditions (%);
- the prevailing direction of winds associated with B class stability;
- the frequency of A class stability conditions (%); and
- the prevailing direction of winds associated with A class stability.

In a similar manner to the presentation of wind roses, the stability roses are presented as a detailed seasonal summary of atmospheric stability recorded throughout the study area.

The stability roses tend to be skewed in a similar manner to their corresponding wind roses. This is because each vane is oriented according to the common variable of wind direction. Slight differences may be seen in overall vane length, due to the inclusion of directions associated with calm winds into the stability rose.

The value of the stability rose lies in the fact that, rather than summarising wind speed classes in adjoining vane segments, the stability rose records frequencies of each atmospheric stability class. Thin vanes represent stable conditions, with wider vanes representing increasingly unstable conditions.

Stable flows often drain down the main valley axis, entering Bass Strait at the mouth of the valley. This phenomenon frequently occurs at night, and during the colder winter months. Sites 9 and 7, located at Low Head and Garden Island respectively, frequently display this trait. Stable flows are also seen travelling *up* the valley axis. It is assumed that this less-regularly occurring event is associated with the inland progression of stable sea air from the Bass Strait.

A characteristic common to many of the stability roses is that stable conditions are also associated with flows draining from the valley walls. A clear example of this occurs at Sites 12 at West Arm and 13 at Holwell, where a large-scale stable flow drains off the Dazzler Range situated to the southwest of both sites. Similar localised stable flows regularly drain off Volunteer Hill, south of Site 10 at Lefroy.

Unstable conditions seem to be more evenly distributed throughout the direction classes. This suggests that they are associated with topographically-generated turbulence, and large scale heating effects, both of which tend to be more random in distribution than katabatics.

5.3.2 Prevailing Stability Class

The prevailing stability class at any given site was defined as the stability class with the greatest frequency. When prevailing stability classes were plotted on seasonal maps of the study area, it was noticed that large regions were covered by locations sharing the same prevailing stability class. Dividing lines were drawn through the field of values, forming boundaries between areas of differing prevailing stability. No attempt was made to infer the presence of the full range of stability classes. Thus boundaries were produced separating areas of vastly differing prevailing stability, without including the stability classes that lie in between them on the Pasquill scale.

Figure 5.5 shows the spatial distribution of the prevailing Pasquill stability classes for each season. Winter and autumn are dominated by extremely stable (G class) conditions, with 80 % and 53 % of the 16 measurement sites respectively having G class prevailing stabilities. In summer and spring however, neutral (D class) conditions prevail with 64 % and 57 % of mapped values respectively having this prevailing stability class. The four maps are skewed towards the centre and extreme ends of the Pasquill scale, with B, C and F classes not occurring as prevailing stabilities.

The summer map is split into three zones of differing prevailing stability. A small zone of high instability (class A) is located in the northwest of the study area. This abuts a far more extensive region of neutral stability, which extends throughout the bulk of the valley. A large unstable (class A) tract extends from the mid-East Tamar towards the southeast boundary of the study area. The Bell Bay Industrial Park has a neutral prevailing summer stability, whereas Launceston is extremely unstable.

In autumn the region closest to the mouth of the river, extending from the western shore towards the east, most frequently experiences neutral stability. A large inland belt, oriented west-northwest/east-southeast, tends to be highly stable. The region surrounding Launceston City, Site 16, has an extremely unstable prevailing stability, whereas the area to the south of that is most often neutral.

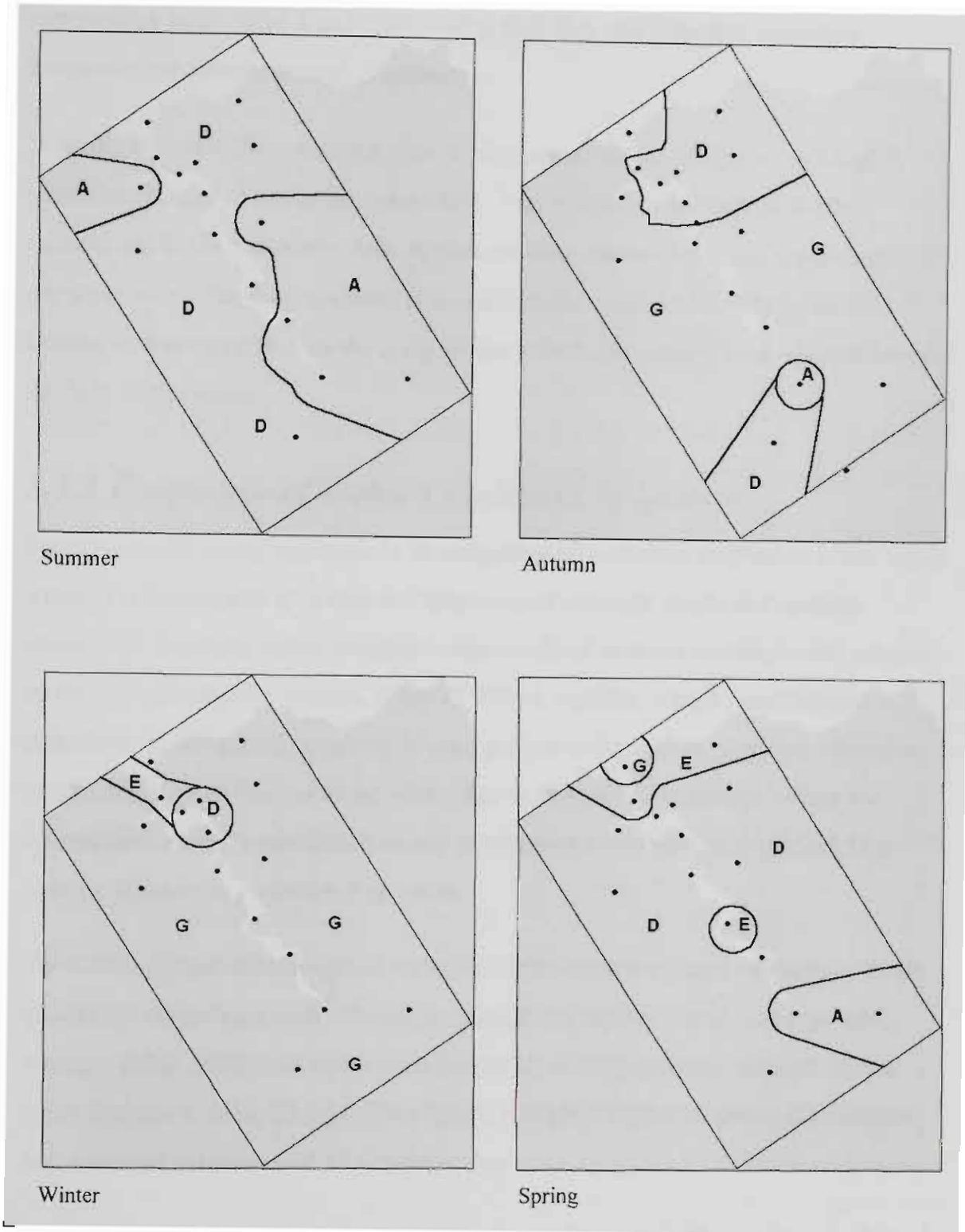

Figure 5.5 Prevailing Pasquill stability class by season (May '93 to May '96). The dots represent the location of each anemometer site and the northwest/southeast aligned rectangle shows the extent of the *TVAS* study area.

In winter, virtually the entire valley experiences extremely stable conditions most often. Departures from this are only found close to the river, near its mouth. Garden Island, Site 7, in the centre of the Tamar River, is slightly less stable than the

surrounding land. Sites 8 and 5, located at Bell Bay and Rowella, both most frequently experience neutral conditions.

In spring the prevailing stability class tends become progressively more unstable with inland distance along the valley axis. The mouth of the river most often experiences G class stability, with A class stability prevailing at the opposite end of the study area. The only anomaly is a small region of slight stability (class E), located at Windermere (Site 4), lying within a far larger neutral area which dominates the bulk of the valley.

5.3.3 Frequency of Stable Conditions by Season

Perhaps a more useful approach to investigating air pollution dispersion in the Tamar Valley via turbulence, is to map the frequency of strongly stable and unstable conditions. Strongly stable conditions were defined as those existing at the extreme of the Pasquill stability classes, F and G. When stability is high, mechanical turbulence is dampened, resulting in poor pollution dispersion. Strongly unstable conditions were defined as those with either A or B class stabilities. When the atmosphere is highly unstable then any mechanical turbulence is amplified, thus causing favourable pollution dispersion.

Table 5.5 summarises the spatial variation in the mean frequency of strongly stable conditions occurring at individual sites throughout the study area. As expected, strongly stable conditions occur least frequently during summer, with the spatial-mean frequency being 22.4 %. This figure is slightly higher in spring and autumn, and reaches a maximum of 44.6 % in winter.

The Bell Bay Industrial Park is favourably located in terms of its position in the valley. It experiences the lowest frequency of strong stability in three out of the four seasons, with summer being the exception. This value is still low however, when compared with most other sites in the study area. Despite this fact the Bell Bay site does experience significant periods of strong atmospheric stability, with the frequency ranging from 16.6 % in spring to 22.1 % in winter.

Table 5.5 Seasonal variation in site-specific and spatial-mean frequency of strongly stable (Pasquill Class F or G) conditions in the Tamar Valley study area

	Summer	*Autumn*	*Winter*	*Spring*
Minimum of the Site-Specific Strongly Stable Frequencies (%)	16.9	21.7	22.1	16.6
Location of Minimum	Site 1	Site 8	Site 8	Site 8
Spatial-Mean of all Site-Specific Strongly Stable Frequencies (%)	22.4	34.1	44.6	27.7
Maximum of the Site-Specific Strongly Stable Frequencies (%)	28.5	45.8	67.1	57.6
Location of Maximum	Site 4	Site 9	Site 1	Site 9

The location of the sites with the highest frequency of strong stability is far more variable. In summer this occurs midway along the valley, near the river at Site 4. In autumn and spring the region most likely to experience strong stability is that close to the mouth of the river, at Low Head. Winter sees the location of most frequent strong stability move to the southeast corner of the study area, at Site 1.

The spatial variation in frequency of strong stability is most easily seen in Figure 5.6. In summer the recurrent highly stable region extends throughout much of the West Tamar. As previously mentioned the Bell Bay region experiences relatively infrequent stable conditions, however the Launceston region is strongly stable between 20 and 25 % of the time.

The mid-Tamar and mouth of the river are the regions that most frequently experience strong stability during the autumn season. The Launceston region is strongly stable between 30 and 35 % of the time.

Winter sees frequent strong stability throughout the entire valley. The frequencies are highest in the southeast region of the study area, with Launceston seeing F or G stability in 35 to 55 % of cases.

A northwest/southeast aligned gradient in frequency of strongly stable conditions is seen in the spring map. This is a minimum in the southeast of the study area and rises to a local maximum at Site 4 in the mid-Tamar. It then falls to a local minimum in the Bell Bay region, before rising to a maximum at the river mouth.

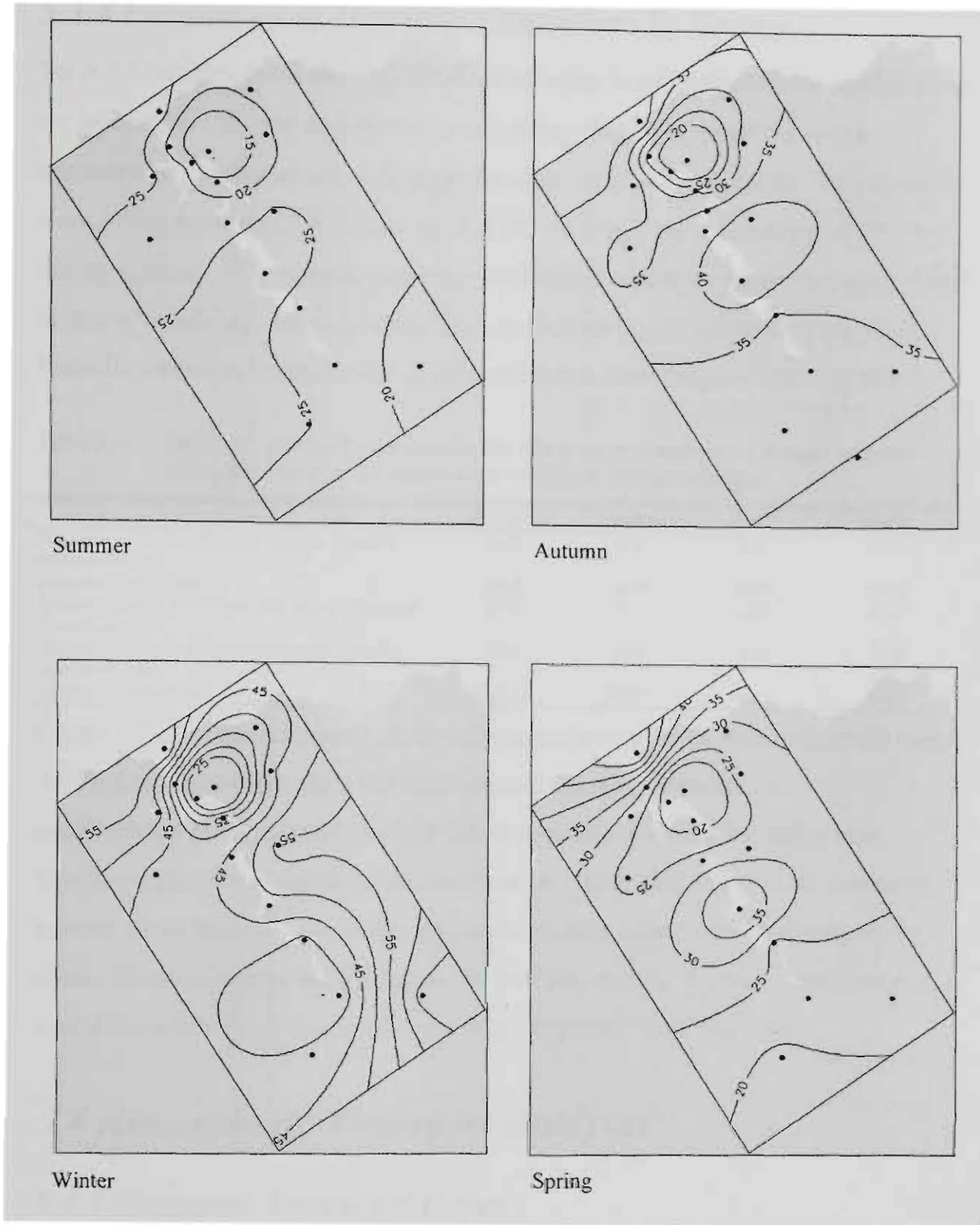

Figure 5.6 Frequency (%) of strongly stable conditions (Pasquill stability classes F and G) by season (May '93 to May '96). A 5 % contour interval is used, with index values oriented towards areas of increasing frequency. The dots represent the location of each anemometer site and the northwest/southeast aligned rectangle shows the extent of the *TVAS* study area.

5.3.4 Frequency of Unstable Conditions by Season

Table 5.6 outlines the spatial and seasonal variation in strongly unstable conditions in the study area. As is to be expected, on a valley wide basis instability is at a minimum during the winter, with a spatial-mean frequency of 12.1 %. This figure rises during autumn (17.8 %) and spring (23.9 %), reaching a maximum of 29.5 % during summer. The summer maximum and winter minimum reflect the major cause of strong instability, which is differential surface heating resulting in strong winds. Instability tends to be minimised at the coast and is most frequent inland at Site 1.

Table 5.6 Seasonal variation in site-specific and spatial-mean frequency of strongly unstable (Pasquill Class A or B) conditions in the Tamar Valley study area

	Summer	*Autumn*	*Winter*	*Spring*
Minimum of the Site-Specific Strongly Unstable Frequencies (%)	13.8	6.8	3.5	5.0
Location of Minimum	Site 4	Site 9	Site 9	Site 9
Spatial-Mean of all Site-Specific Strongly Unstable Frequencies (%)	29.5	17.8	12.1	23.9
Maximum of the Site-Specific Strongly Unstable Frequencies (%)	46.6	31.8	26.3	46.8
Location of Maximum	Site 1	Site 1	Site 1	Site 1

Figure 5.7 maps the frequency of strongly unstable conditions within the study area. All four seasonal maps show the same general trend in instability. A northwest/southeast aligned gradient exists, roughly following the valley axis. Maximum frequencies of unstable conditions are invariably found in the southeast portion of the study area, with the gradient smoothly falling with proximity to the coast. Minimums tend to be found in the Bell Bay region. As such, Launceston experiences A or B class stabilities far more frequently than Bell Bay.

5.4 Atmospheric Transport Analyses

5.4.1 Seasonal Transport Roses

The *TVAS* meteorological dataset is based around 15-minute averages. A series of rolling 'integral measures' was calculated for each 15-minute time period, based on the mean wind speed and direction time series for the following 24 hours (Allwine and Whiteman, 1994). The 24-hour wind run recorded the total wind run, in kilometres, that passed the anemometer site during the subsequent 24-hour period.

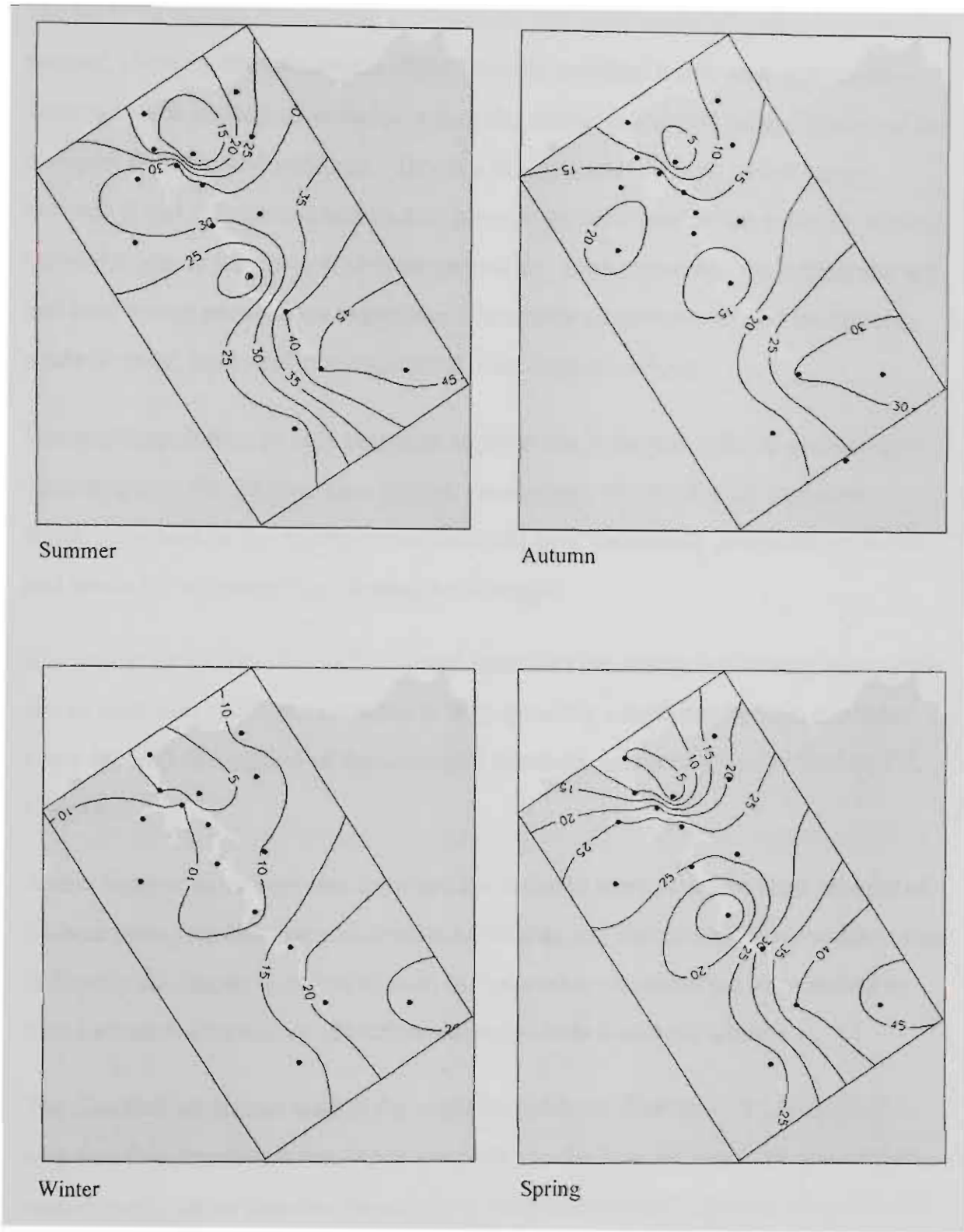

Figure 5.7 Frequency (%) of strongly unstable conditions (Pasquill stability classes A and B) by season (May '93 to May '96). A 5 % contour interval is used, with index values oriented towards areas of increasing frequency. The dots represent the location of each anemometer site and the northwest/ southeast aligned rectangle shows the extent of the *TVAS* study area.

The 96 wind vectors comprising a 24-hour period were vectorially added in a similar manner, allowing the calculation of the 24-hour resultant transport distance and direction. The recirculation factor is an index that is calculated using the ratio of the transport distance and wind run. This is a dimensionless figure, which varies between 0 and 1. Recirculation factors provide an indication of the presence of local recirculations on the chosen 24-hour time scale. Such recirculations include the sea and land breeze phenomena experienced in coastal environments, and the daytime anabatic wind, nocturnal katabatic wind cycle seen in valleys.

Recirculation factors of zero represent straight-line transport, with no recirculation occurring over the 24-hour time period. In contrast, values of unity represent situations where no net transport has occurred over the chosen 24-hour time period, and hence the air parcel has returned to its origin.

It is important to note that each measure describes the transport characteristics of the site in question, and is not intended to truly quantify actual atmospheric transport. A more detailed description of these integral measures has been given in Section 2.4, Chapter 2.

A new form of wind rose was developed in order to summarise the large amount of 24-hour transport distance and direction data that was calculated. The *transport rose* is directly analogous to the wind rose, in that vector quantities are summarised by their inclusion into various direction and magnitude frequency classes.

The direction parameter used is the resultant transport direction. It is important to note that this direction refers to the direction *in which an air parcel or contaminant would travel*, rather than the direction that it has come from. As such the northerly vane summarises the frequency of 24-hour atmospheric transport towards the north. Each vane segment displays the percentage frequency of transport distance classes associated with the vane's transport direction.

24-hour transport roses were constructed on a seasonal basis, covering seven transport distance classes for each of the eight cardinal points of the compass. A *transport calm* class was also included to categorise situations where the total daily

atmospheric transport was less than 50 km, regardless of transport direction. This frequency is printed in the hub of each transport rose. Table 5.7 summarises the transport distance thresholds selected in the construction of the transport roses.

Table 5.7 24-hour transport distance classes used in the transport rose analysis

Class	*Transport Distance (km)*	
	Lower Limit	*Upper Limit*
Transport Calm *		< 50
1	≥ 50	< 100
2	≥ 100	< 200
3	≥ 200	< 300
4	≥ 300	< 400
5	≥ 400	<500
6	≥ 500	<600
7	≥ 600	

* defined regardless of transport direction

Like wind and stability roses, transport roses are best suited to characterising the flows at a single site, rather than providing a broad view of atmospheric transport across a large area. For this reason the seasonal and year-round transport roses for all meteorological sites have been tabulated as Appendix 3a-e.

Summary tables have been appended to each seasonal transport rose table, providing the following statistics on a site-by-site basis:

- the frequency of transport distances less than 50 km, "transport calms" (%);
- the minimum transport distance (km);
- the mean transport distance (km);
- the maximum transport distance (km);
- the prevailing transport direction;
- the mean transport distance associated with this direction (km);
- the second prevailing transport direction; and
- the mean transport distance associated with this direction (km).

Each of the transport roses is oppositely skewed to the corresponding wind or stability rose. This is due to the fact that they depict the directions towards which the winds travel, whereas the wind and stability rose vanes are oriented according to the direction from which the winds have originated.

On a year-round basis, the dominant daily transport tends to be inland, with two-thirds of the sites displaying southeastward prevailing flows along the valley axis.

The presence of the westerlies is observed by the frequent occurrence of daily transport towards the east. This is most often seen in the lower reaches of the valley,

however easterly transport is still a significant feature throughout the remainder of the study area.

Far less frequent is the occurrence of atmospheric transport towards the sea. This is most readily seen at sites close to the valley axis, such as Sites 5 and 6.

As expected, inland transportation is most evident in summer, whereas seaward transport occurs more frequently during the winter months.

The seasonal variation in transport distance will be discussed in detail further on in this section.

5.4.2 Mean 24-Hour Wind Run

Table 5.8 shows that the spatial-mean 24-hour wind run varied between 244 km in winter and 330 km in spring. Autumn and summer showed spatial-mean daily wind runs of 269 and 316 km respectively. Site 11, located in the mid-Tamar region to the East of the river, experienced the lowest site-specific mean daily wind run in three out of the four seasons. In the fourth season, spring, it came second to the discontinued Site 14 located near Bell Bay. The highest site-specific mean daily wind run was found at the coastal Site 9, throughout all four seasons.

Table 5.8 Seasonal variation in site-specific and spatial-mean 24-hour wind run in the Tamar Valley study area

	Summer	*Autumn*	*Winter*	*Spring*
Minimum of the Site-Specific Mean Daily Wind Runs (km)	227.61	155.53	135.18	213.92
Location of Minimum	Site 11	Site 11	Site 11	Site 14
Spatial-Mean of all Site-Specific Mean Daily Wind Runs (km)	315.94	268.54	244.32	330.45
Maximum of the Site-Specific Mean Daily Wind Runs (km)	454.10	470.21	516.99	493.46
Location of Maximum	Site 9	Site 9	Site 9	Site 9

Figure 5.8 summarises the spatial variation in daily mean wind run for each of the four seasons. The wind runs are greatest at the coast, and diminish sharply with inland distance until the Bell Bay region is reached. The gradient in wind run decline then eases off until a minimum wind run is attained, typically covering a large region in the mid East-Tamar. Wind runs then gradually increase with distance from the coast. The Bell Bay anemometer typically experiences daily wind runs varying

between 57 % and 74 % of those experienced at the coast. In contrast the Launceston anemometer experiences 26 % to 52 % of the daily wind run experienced at the coast.

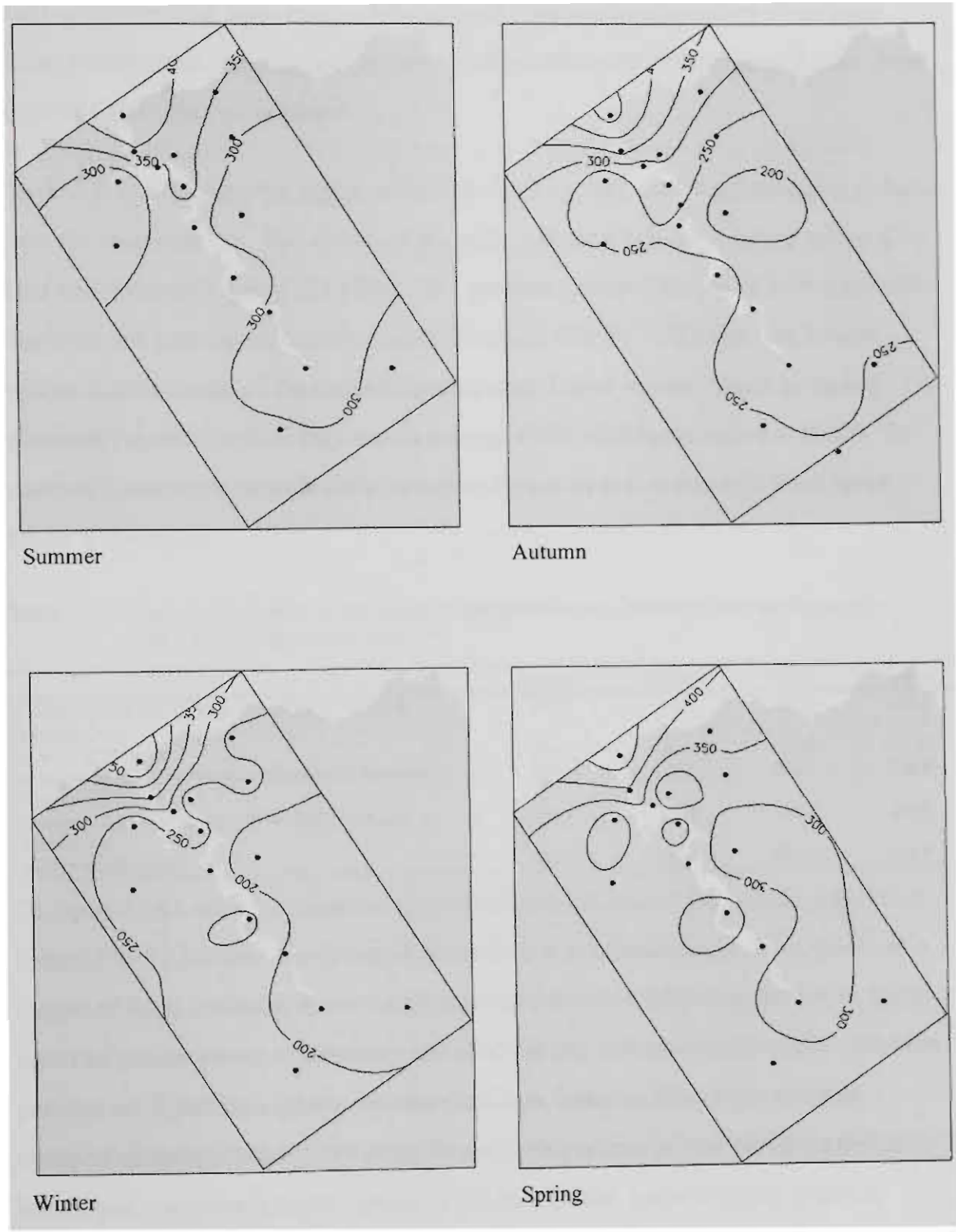

Figure 5.8 Mean daily wind run (km) by season (May '93 to May '96). A 50 km contour interval is used, with index values oriented towards areas of increasing wind runs. The dots represent the location of each anemometer site and the northwest/ southeast aligned rectangle shows the extent of the *TVAS* study area.

5.4.3 Mean 24-Hour Transport Distance

Mean daily transport distances in the study area tend to be between 70 % and 80 % of their corresponding wind runs. This suggests, that whilst on a valley wide basis some atmospheric recirculation occurs, contaminants tend to be removed from their sources rather than recirculated.

Table 5.9 summarises the spatial variability in mean daily resultant transport distance over the four seasons. The spatial-mean daily transport is lowest during winter (202 km) and highest in spring (259 km). The greatest site-specific mean daily transport distances are once again experienced at the coast (Site 9). Likewise, the lowest occurs at sites scattered throughout the mid-east Tamar region. Daily transport distances recorded at Bell Bay are on average 63 % of those recorded at Site 9. In contrast Launceston records daily transport distances that average 43 % of those found at the coast.

Table 5.9 Seasonal variation in site-specific and spatial-mean 24-hour transport distance in the Tamar Valley study area

	Summer	*Autumn*	*Winter*	*Spring*
Minimum of the Site-Specific Mean Daily Transport Distances (km)	167.0	125.6	113.0	163.4
Location of Minimum	Site 6	Site 11	Site 11	Site 14
Spatial-Mean of all Site-Specific Mean Daily Transport Distances (km)	234.5	210.1	202.0	258.5
Maximum of the Site-Specific Mean Daily Transport Distances (km)	334.2	377.5	450.8	399.9
Location of Maximum	Site 9	Site 9	Site 9	Site 9

The spatial and seasonal variation in mean 24-hour transport distance is mapped in Figure 5.9. In summer the transport distance is a maximum at the coast, however a tongue of large transport distances extends up the valley following the river. Once again minimum transport distances are found in the mid-east Tamar region. Similar patterns are found throughout the other seasons, however the tongue of large transport distances is not as evident. In addition the zone of low transport distances is enlarged, covering a large portion of the east Tamar, and extending south to include Launceston.

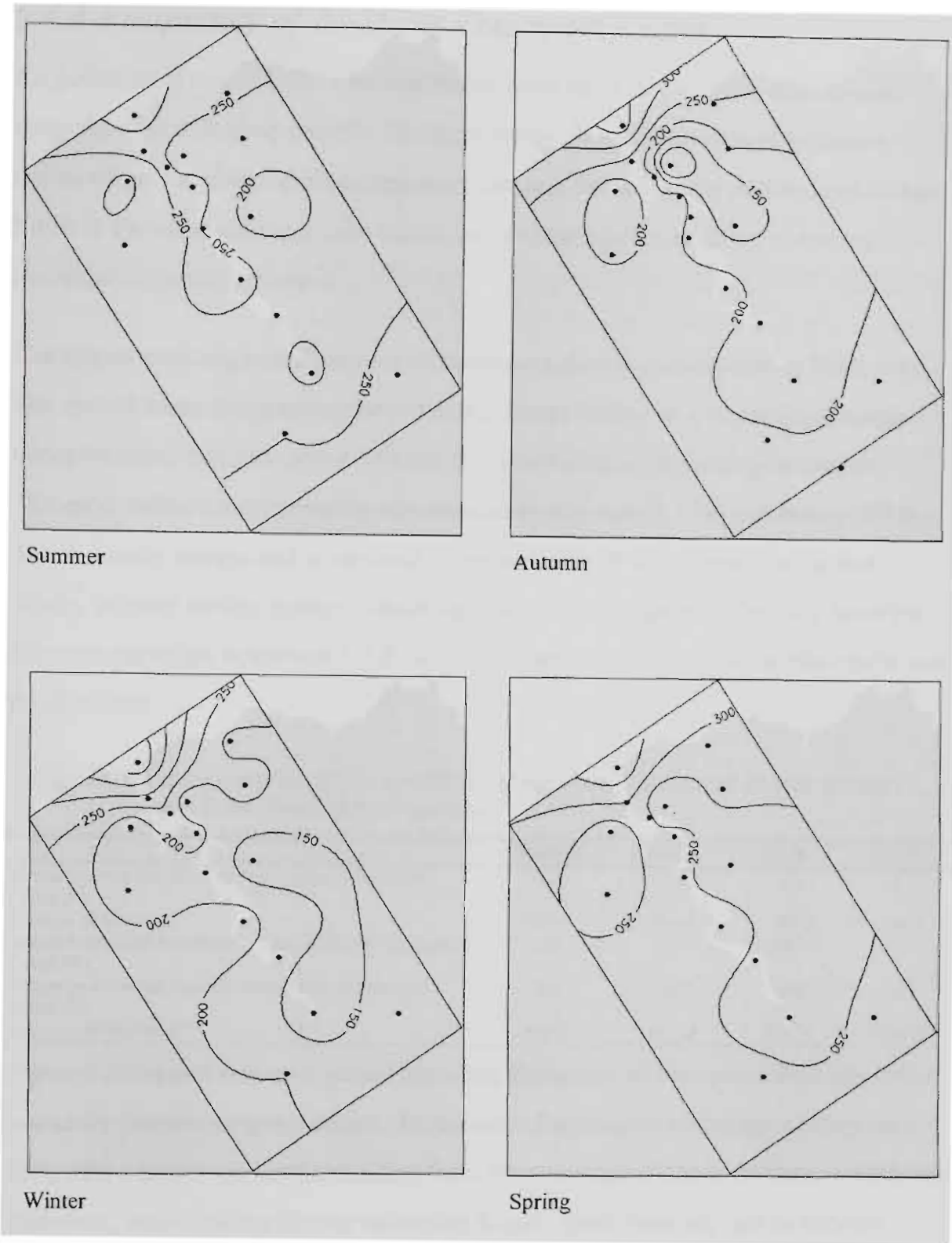

Figure 5.9 Mean daily transport distance (km) by season (May '93 to May '96). A 50 km contour interval is used, with index values oriented towards areas of increasing transport distances. The dots represent the location of each anemometer site and the northwest/ southeast aligned rectangle shows the extent of the *TVAS* study area.

5.4.4 Frequency of 24-Hour Transport Calms

Air pollution is most likely to be a problem when there is very little atmospheric transport over a 24-hour period. The term *transport calm* was coined to denote events where the daily resultant transport distance fell below the threshold of 50 km. Much in the same way that calm winds are considered directionless, so too are transport calms directionless.

The spatial and temporal frequency of transport calms is summarised as Table 5.10. The spatial-mean frequencies show that the Tamar Valley as a whole experiences transport calms between about 5 % and 20 % of the time, depending on season. Transport calms are infrequently experienced in summer (5.2 %) and spring (5.7 %). This is hardly unexpected as summer is associated with widespread convective winds, whereas strong synoptic winds regularly occur in spring. They are however far more prevalent in autumn (15.8 %) and winter (19.7 %) as more stable conditions predominate.

Table 5.10 Seasonal variation in site-specific and spatial-mean frequency of 24-hour transport calms in the Tamar Valley study area

	Summer	*Autumn*	*Winter*	*Spring*
Minimum of the Site-Specific Frequencies of Transport Calms (%)	0.9	3.2	1.0	2.2
Location of Minimum	Site 1	Site 9	Site 9	Site 9
Spatial-Mean of all Site-Specific Frequencies of Transport Calms (%)	5.2	15.8	19.7	5.7
Maximum of the Site-Specific Frequencies of Transport Calms (%)	9.1	26.2	43.0	9.9
Location of Maximum	Site 6	Site 12	Site 16	Site 16

Figure 5.10 shows that on a spatial basis, the frequency of transport calms can differ markedly from those given above. In summer, frequencies of transport calms are low, with a gentle gradient extending from the southeast of the study area towards the mid-west, where the maximum values are found. Both these regions experience similar mean daily wind runs (approximately 300 km), suggesting that this gradient may be explained in terms of recirculation. In autumn the pattern reverses, with minimum frequencies being experienced at the coast in conjunction with a large inland gradient towards the mid-Tamar region. Maximum frequencies are experienced at Site 11, East Arm. A similar pattern occurs in winter, however the inland gradient now extends inland as far as Launceston, where maximum values are

found. The spring pattern is a combination of the summer and winter patterns, with local maxima occurring in both the Launceston and mid-west Tamar regions.

5.4.5 Mean 24-Hour Recirculation Factor

The mean 24-hour recirculation factor was calculated at all anemometer sites for each season. Table 5.11 summarises the spatial-mean 24-hour recirculation factor on a seasonal basis. It lists the minimum and maximum site-specific means and identifies the locations involved.

The spatial-mean recirculation factor varies between 0.25 and 0.30, suggesting that although a diurnal reversal in the wind direction does occur, contaminants are only infrequently transported back to their source over the period of a day. The largest site-specific means are found near the valley axis, at either Site 7 on Garden Island in the middle of the river, or Site 6 on a channel marker at the edge of the river. The minimum site-specific value occurs at Site 1, the most inland site, in all four seasons.

Table 5.11 Seasonal variation in site-specific and spatial-mean 24-hour recirculation factors in the Tamar Valley study area

	Summer	*Autumn*	*Winter*	*Spring*
Minimum of the Site-Specific Mean Recirculation Factors	0.163	0.136	0.118	0.208
Location of Minimum	Site 1	Site 1	Site 1	Site 1
Spatial-Mean of all Site-Specific Recirculation Factors	0.296	0.285	0.253	0.267
Maximum of the Site-Specific Mean Recirculation Factors	0.383	0.411	0.342	0.311
Location of Maximum	Site 7	Site 7	Site 6	Site 7

A clearer view of the spatial and seasonal variation in recirculation factors is given in Figure 5.11. This shows that atmospheric recirculation events in the Tamar Valley are more closely related to inland distance than season. All four seasonal maps show the same basic pattern of minimum recirculation in the southeast of the study area, rising with proximity to the coast. The zone of maximum recirculation tends to cover large tracts of the lower to mid-west Tamar region. This is the region most affected by the diurnally-varying sea and land breezes.

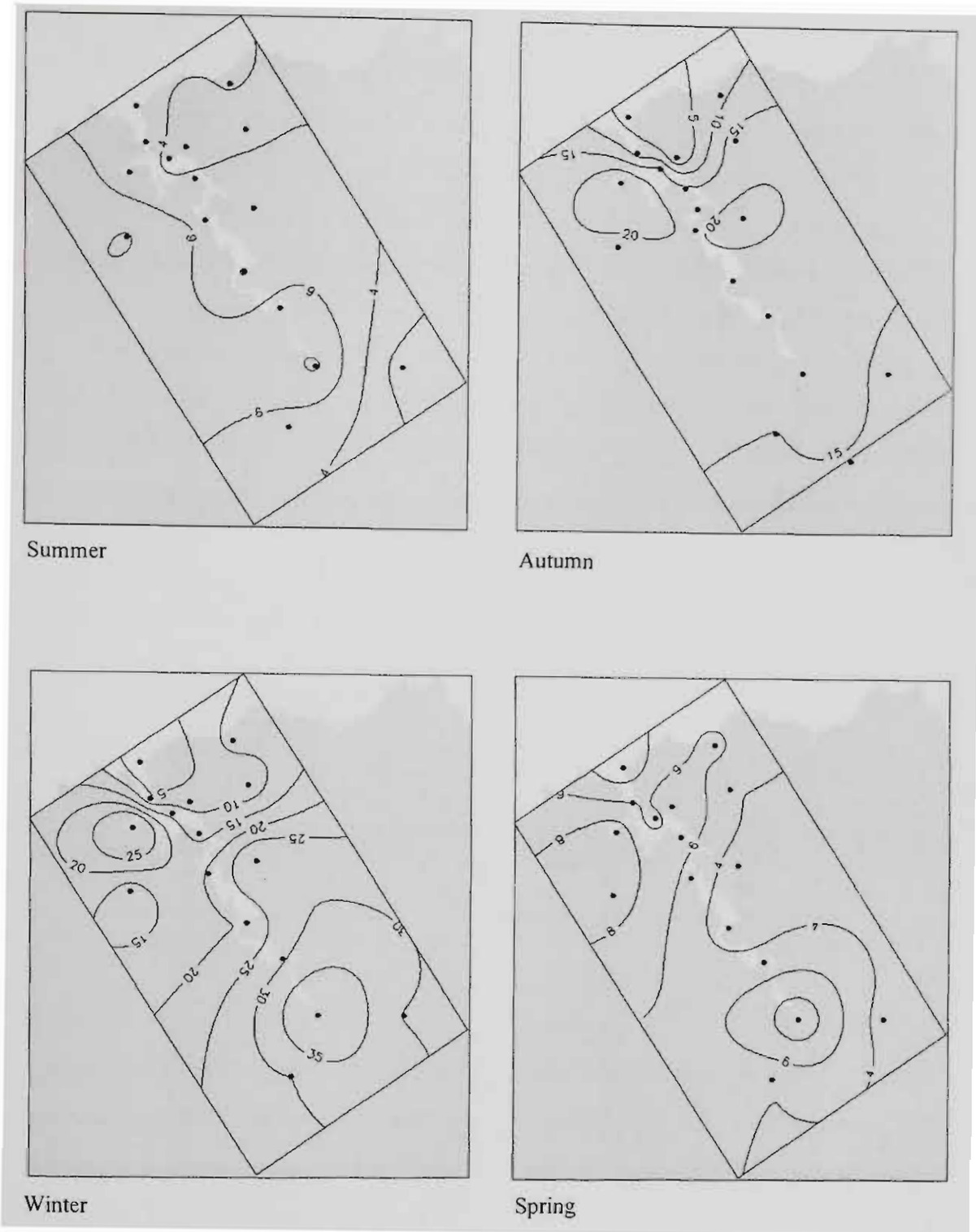

Figure 5.10 Frequency (%) of transport calms (defined as daily transport distances less than 50 km) by season (May '93 to May '96). A 2 % contour interval is used for summer and spring, with a 5% interval used otherwise. Index values are oriented towards areas of increasing frequency. The dots represent the location of each anemometer site and the northwest/southeast aligned rectangle shows the extent of the *TVAS* study area.

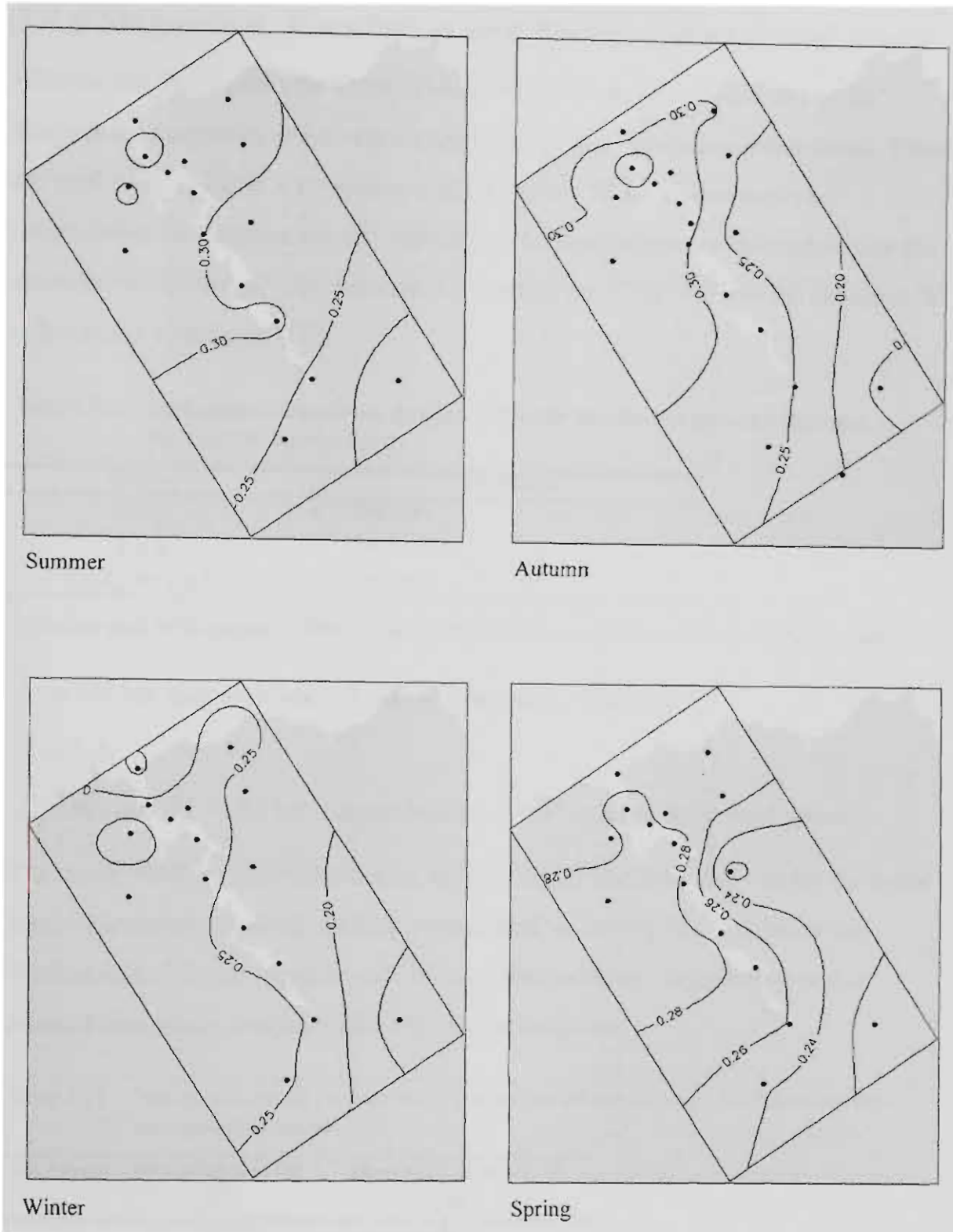

Figure 5.11 Mean daily recirculation factor by season (May '93 to May '96). A contour interval of 0.05 is used, except for spring when an interval of 0.02 is used. Index values are oriented towards areas of increasing recirculation. The dots represent the location of each anemometer site and the northwest/ southeast aligned rectangle shows the extent of the *TVAS* study area.

5.4.6 Stagnation, Ventilation and Recirculation Prone Areas

Allwine and Whiteman (1994) determined *critical transport indices* (CTIs) to characterise stagnation-prone, recirculation-prone and ventilation-prone areas. These are applied as in Table 5.12, where, S and R are the 24-hour wind runs and recirculation factors respectively, and their associated means are calculated over the entire period of record. The subscript 'c' denotes the CTIs, whereas the subscript 'v' refers to the ventilation CTIs.

Table 5.12 Application of the critical transport indices to identify sites prone to stagnation, recirculation and ventilation.

Condition	⇒	*Site Prone to ...*
$\overline{S} \le \overline{S}_c$	⇒	Stagnation
$\overline{R} \ge \overline{R}_c$	⇒	Recirculation
$\overline{R} \le \overline{R}_{cv}$ and $\overline{S} \ge \overline{S}_{cv}$	⇒	Ventilation

Allwine and Whiteman (1994) applied the following CTIs to their Arizona sites:

$\overline{S}_c$ = 170 km (approximately 2 ms^{-1} average daily wind speed);

$\overline{R}_c$ = 0.4;

$\overline{R}_{cv}$ = 0.2 and $\overline{S}_{cv}$ = 250 km (approximately 3 ms^{-1} average daily wind speed).

The mean wind run and recirculation factor was calculated at each site for the entire three-year period of record, and are summarised in Table 5.13. If Allwine and Whiteman's CTIs are applied to all 16 sites, then none are stagnation-prone or recirculation-prone, and only Site 1 is ventilation-prone.

Table 5.13 Site-specific mean 24-hour wind runs and recirculation factors for the entire three-year period of record

Site Number	*Mean Wind Run (km)* ($\overline{S}$)	*Mean Recirculation Factor* ($\overline{R}$)
1	285.9	0.16
2	285.6	0.25
3	264.1	0.28
4	333.0	0.28
5	324.2	0.31
6	218.7	0.32
7	381.3	0.33
8	309.1	0.30
9	481.1	0.27
10	288.9	0.27
11	191.6	0.24
12	222.3	0.30
13	268.1	0.30
14	226.6	0.26
15	315.7	0.30
16	197.5	0.25

This result is somewhat surprising because the Tamar Valley is so well defined. The coastal sites, especially Site 9, were expected to be well ventilated and also to be prone to daily recirculation. The diurnal reversal in winds that occurs in valleys was also expected to establish the valley axis sites as recirculation prone. Finally the dramatic reduction in wind speed with inland distance was expected to result in extensive stagnation prone regions in the upper East-Tamar and Launceston regions.

This departure from what was expected is probably due to a combination of the following factors:

- the CTIs used might only apply to the regions they were originally defined for, and as such are site-specific;
- the CTIs used are highly stringent, and only identify regions that are extreme in their proclivity to stagnation, ventilation or recirculation;
- there is a seasonality effect in stagnation-prone, ventilation-prone or recirculation-prone areas which is cancelled out by applying CTIs to means calculated over the entire period of record, covering all four seasons;
- the majority of recirculations that do occur in the Tamar Valley occur on slightly different time scales to the 24-hour transport time chosen; and
- in a similar manner stagnations may regularly occur, but on a time scale less than 24 hours.

5.4.7 Stagnation, Ventilation and Recirculation Events

Allwine and Whiteman (1994) also defined CTIs to identify stagnation, recirculation and ventilation *events*. These were applied to the *TVAS* dataset according to the definitions in Table 5.14 where:

- S_c = 130 km (approximately 1.5 ms^{-1} average daily wind speed);
- R_c = 0.6;
- R_{cv} = 0.2 and S_{cv} = 250 km (approximately 3 ms^{-1} average daily wind speed); and
- the transport time (τ) = 24 hours.

Table 5.14 Application of the critical transport indices to identify stagnation, recirculation and ventilation events occurring on a 24-hour timescale

Condition	⇒	*Event*
$S \leq S_c$	⇒	Stagnation
$R \geq R_c$	⇒	Recirculation
$R \leq R_{cv}$ and $S \geq S_{cv}$	⇒	Ventilation

Frequencies of each event class were determined on a seasonal basis at each anemometer site. The spatial-mean frequency was also calculated for each season, in order to determine valley-wide seasonal trends in stagnation, ventilation and recirculation.

Figure 5.12 shows that, of the three event classes, ventilation events are the most frequent, with spatial-mean frequencies varying between 30 % and 40 % depending on the season. Ventilation events occur 34 % of the time in summer, and fall to a minimum by winter, before then rising to a maximum in spring.

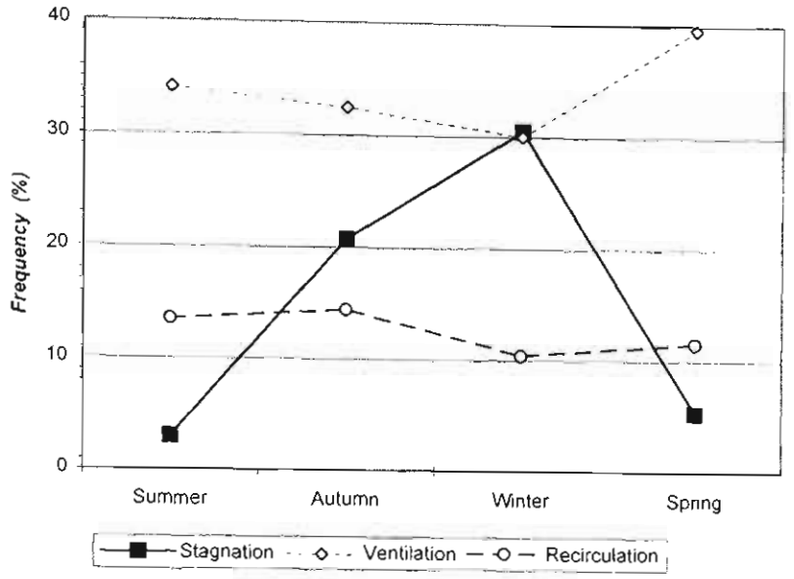

Figure 5.12 Seasonal variation in spatial-mean frequency of stagnation, ventilation and recirculation events in the Tamar Valley on a 24-hour time scale

Stagnation events are the most variable in spatial-mean frequency of the three event classes. They occur least frequently in summer (3 %), and rise in frequency during autumn (21 %) to a winter maximum (31 %). The frequency of stagnation events falls dramatically during spring (5 %).

Recirculation events are remarkably constant during all four seasons, with spatial-mean frequencies varying between 10 % and 14 %. The minimum occurs during winter, with the maximum in autumn.

The site-specific frequency of stagnation events is mapped as Figure 5.13. Stagnations occur infrequently during summer, because of the widespread surface heating resulting in convective winds. During the summer months stagnation events do not occur at the two coastal sites, Sites 9 and 15, or at Sites 4, 5 and 7, sites close to the river. Other riverside sites, such as Sites 8, 3 and 16, record low frequencies of summertime stagnation events, with frequencies of 0.1, 1.5 and 3.8 % respectively.

The frequency of stagnations gradually rises with distance from the coast, until a maximum of 15 % is reached at East Arm, Site 11. The West Arm anemometer, Site 12, also records a relatively large frequency of stagnation events during the summer. The remainder of the valley experiences stagnation events between 2 and 4 % of the time.

The autumn pattern of stagnations is similar in form to that just described for summer, however the magnitude of the frequencies is very much higher. There is a strong gradient in frequencies, ranging from 0 % at or near the coast, to over 45 % at Site 11. The West Arm anemometer, Site 12, experiences stagnations on over 35 % of occasions. The remainder of the valley, including Launceston, is stagnant between 20 % and 30 % of the time.

In winter stagnations are very much more prevalent, and the East Arm maximum has spread to include the majority of the upper East Tamar including Launceston. This region experiences stagnations, on a 24-hour timescale, over 50 % of the time.

Spring sees a dramatic reduction in the frequency of stagnations. The lower Tamar region, and the mid to upper East-Tamar experiences stagnations on just over 5 % of occasions, with the rest of the valley rarely experiencing 24-hour stagnation events. Site 14 is anomalous however, as stagnations occur 25 % of the time. When this fact was originally noted it was decided that though the anemometer station was recording accurate results and had a suitable fetch from all directions, it was poorly located in a frost hollow. The site was subsequently discontinued and the meteorological tower was relocated to Site 16.

The frequency of ventilation events is mapped for each season in Figure 5.14. The dominant spatial pattern, which is repeated to some degree in each season, is that of frequently-ventilated regions occurring at the coast, and far inland to the southeast of Launceston. The area in between is less frequently ventilated, with the mid-east Tamar experiencing slightly lower frequencies than those of the mid-west Tamar.

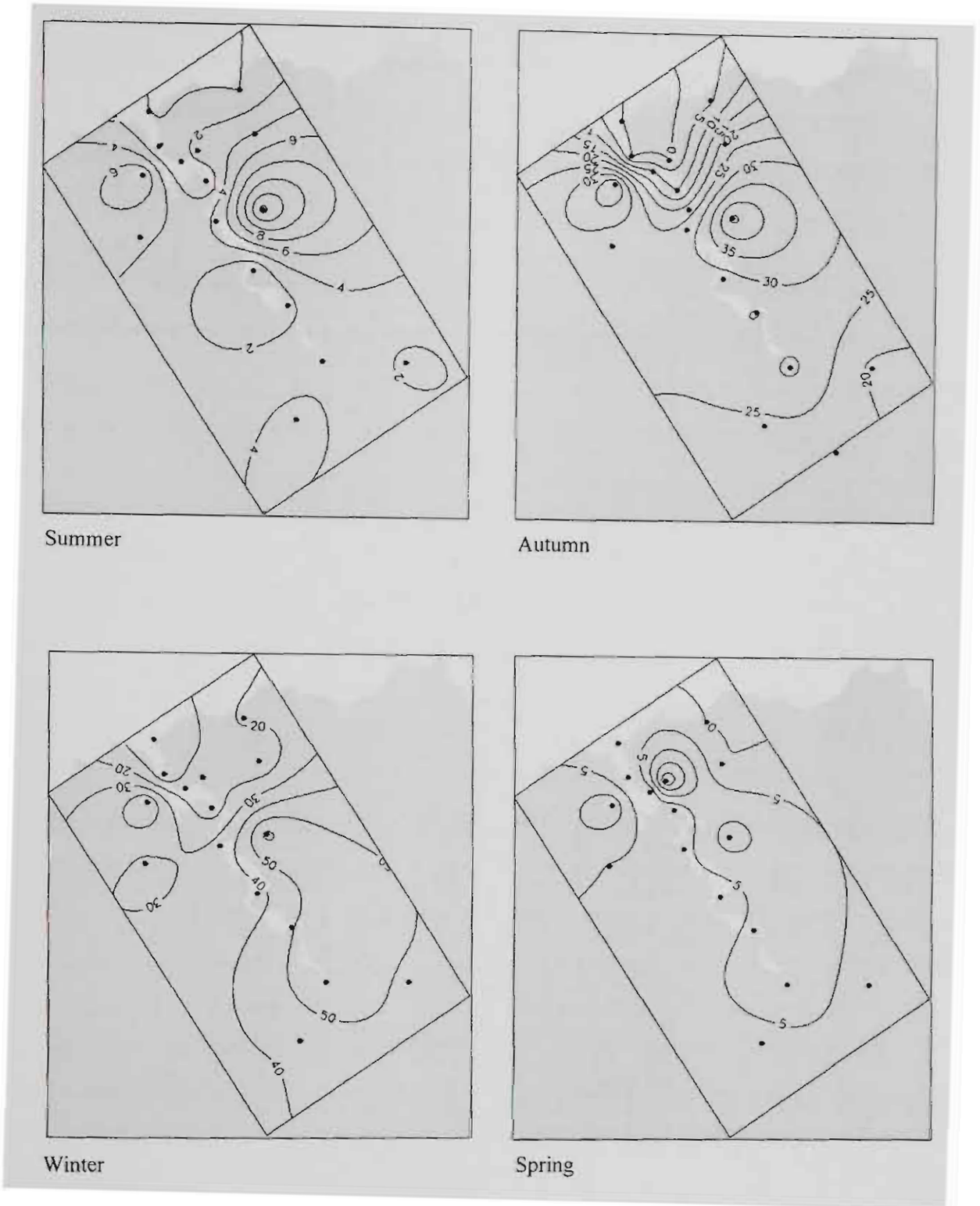

Figure 5.13 Frequency (%) of 24-hour stagnation events by season (May '93 to May '96). Index values are oriented towards areas of increasing frequency. The dots represent the location of each anemometer site and the northwest/southeast aligned rectangle shows the extent of the *TVAS* study area.

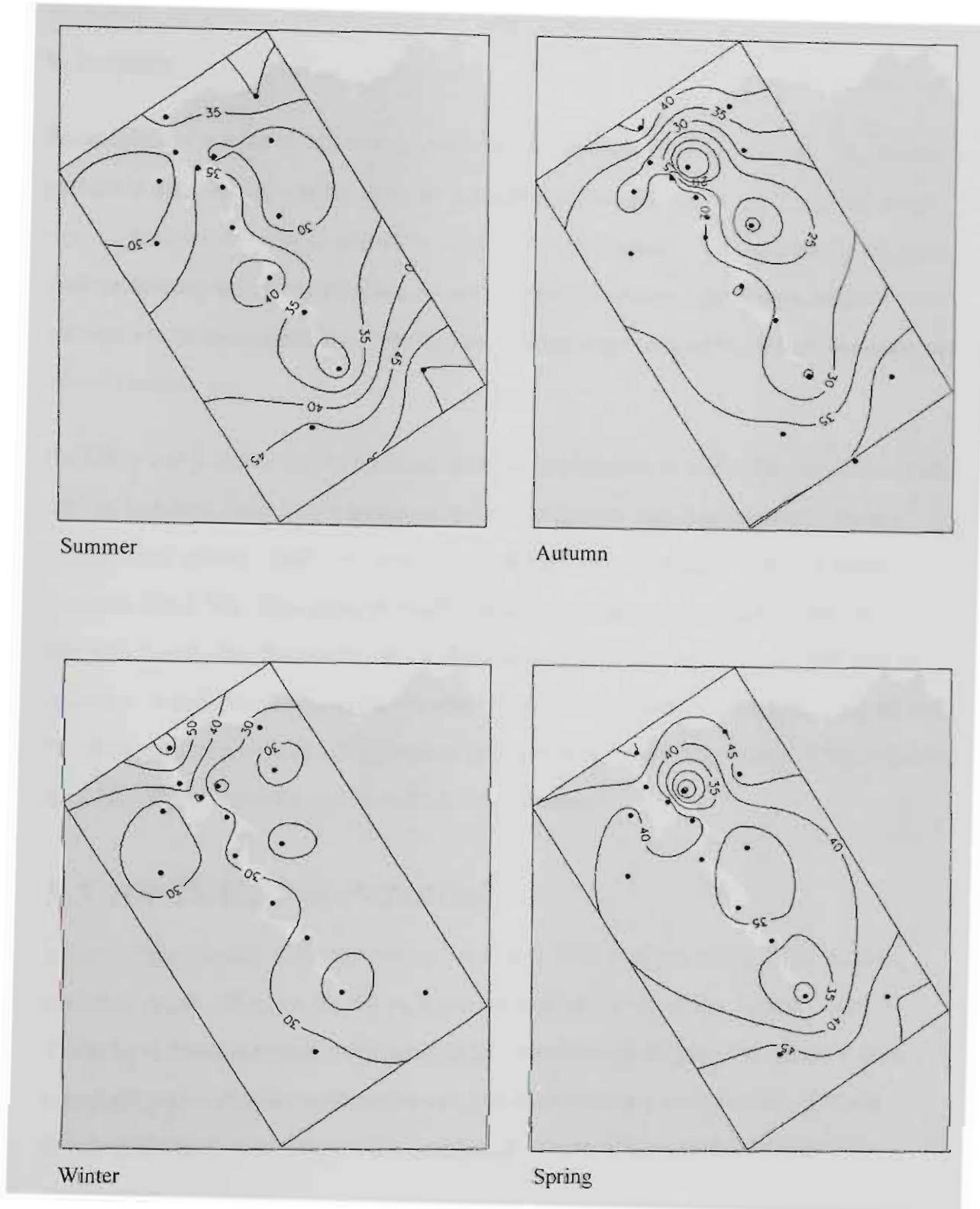

Figure 5.14 Frequency (%) of 24-hour ventilation events by season (May '93 to May '96). Index values are oriented towards areas of increasing frequency. The dots represent the location of each anemometer site and the northwest/southeast aligned rectangle shows the extent of the *TVAS* study area.

Ventilation frequencies in Launceston, (Site 16), are a minimum in winter (14.5 %) and rise to a maximum in spring (27.6 %). Bell Bay by contrast, is far more

frequently ventilated, with frequencies varying between 33.8 % in autumn and 44.5 % in spring.

Recirculation events on a 24-hour timescale are mapped in Figure 5.15. The spatial pattern is once again similar in all four seasons. Frequencies of recirculation events tend to be lowest in the southeast portion of the study area. They gradually increase with proximity to the coast, along a northwesterly bearing. The region most susceptible to recirculation events is found at the coast and up to 20 km inland on the West-Tamar.

Bell Bay and Launceston experience similar frequencies to each other in summer and spring, however Bell Bay's frequencies are far greater than Launceston's during autumn and winter. Bell Bay most frequently experiences recirculation events in Autumn (20.3 %). This most probably reflects a balance between the daytime anabatic winds and the nocturnal katabatics, which is best achieved at Bell Bay in Autumn. Launceston best achieves this balance in summer, with a frequency of 14.2 %. Recirculations occur least frequently in Launceston during winter (8 %), whilst at Bell Bay the frequencies are lowest during summer.

5.5 Air Pollution Potential

In this chapter many different parameters have been applied to the *TVAS* dataset, each having an effect on the air pollution potential (APP) of the Tamar Valley. These have been mapped, and show largely similar spatial patterns. Rather than concluding this chapter with a summary of each of these, an index of APP was developed which incorporates the combined effects of the most important parameters.

In order to standardise units, the index was based upon the frequency of occurrence of different climatological events. Six parameters were selected to form the basis of the index (at any specific location), three of which increase APP, whilst the remaining three decrease APP.

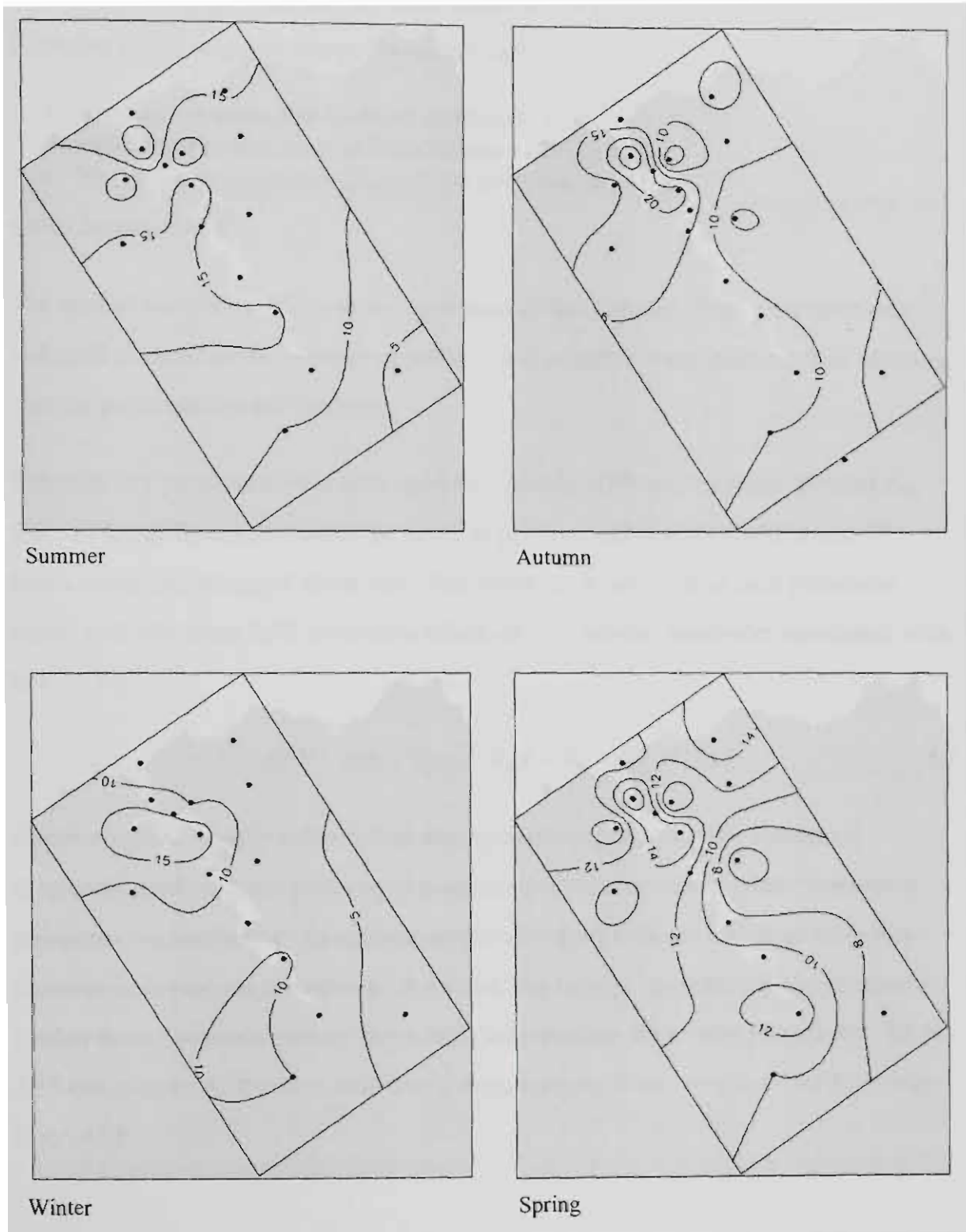

Figure 5.15 Frequency (%) of 24-hour recirculation events by season (May '93 to May '96). Index values are oriented towards areas of increasing frequency. The dots represent the location of each anemometer site and the northwest/southeast aligned rectangle shows the extent of the *TVAS* study area.

Increasing percentage frequencies of the following events act to increase APP:

- stable (F-class and G-class) conditions (Sb);
- stagnation events on a 24-hour timescale (Sg_{24}); and
- recirculation events on a 24-hour timescale (R_{24}).

Likewise increasing percentage frequencies of:

- unstable (A-class and B-class) conditions (U);
- ventilation events on a 24-hour timescale (V_{24}); and
- "fresh" or stronger (wind speed ≥ 8 ms^{-1}) breezes (U_8);

act to decrease APP.

The spatial variation of U_8 was not examined in this chapter. This parameter was included to equalise the number of positive and negative event classes, thus ensuring that the parameters were balanced.

Equation 5.1 presents the formula used to calculate APP at a location. It takes the form of the difference between the sums of positive and negative APP event frequencies (%) recorded at the site. The index is chosen so that each parameter associated with high APP is counter-balanced by a similar parameter associated with low APP.

$$APP = (Sb + Sg_{24} + R_{24}) - (U + V_{24} + U_8) \qquad 5.1$$

Positive values of APP indicate that atmospheric dispersion at the location is frequently poor, and the presence of contaminant sources would result in elevated pollutant concentrations. In contrast, negative values indicate locations subject to favourable dispersion conditions. A value close to zero suggests that the location is neither biased towards poor or favourable air pollution dispersion conditions. Table 5.15 categorises APP values into five classes ranging from 'very low' APP to 'very high' APP.

Table 5.15 Air pollution potential classes

Lower Limit	*Upper Limit*	*Designation*
	-75	Very Low APP
-75	-25	Low APP
-25	25	Medium APP
25	75	High APP
75		Very High APP

It is worth noting that the event frequencies comprising the index can all be derived from simple wind speed, wind direction and sigma-theta time-series data. These parameters are commonly recorded, thus making APP a simple and accessible measure.

APP was calculated on a seasonal basis for each *TVAS* anemometer site where all six parameters were available (Tables 5.16a-d). Seasonal APP maps were produced, with overlays showing housing densities calculated from Census96 data (Australian Bureau of Statistics, 1997). In this manner APP could be identified for all well populated regions within the study area.

Table 5.16a Spatial variation in the parameters comprising the summer APP index throughout the Tamar Valley

Site #	*Site Location*	S_h	Sg_{24}	R_{24}	U	V_{24}	U_g	*APP*
1	Nunamara	16.9	1.6	3.3	46.6	55.3	3.9	-84
2	Hadspen	25.1	4.5	9.8	21.4	46.3	5.5	-34
3	Dog Point	22.8	1.5	15.4	40.1	31.9	5.2	-37
4	Windermere	28.5	0.0	14.0	13.8	44.8	13.3	-29
5	Rowella	17.2	0.0	17.8	32.3	40.4	8.6	-46
7	Garden Island	18.7	0.0	25.9	17.6	30.8	11.2	-15
8	Bell Bay	18.5	0.1	12.5	32.6	35.4	7.4	-44
9	Low Head	27.7	0.0	18.2	18.5	36.8	20.1	-29
10	Lefroy	19.3	4.1	13.3	25.3	26.3	4.7	-20
11	East Arm	25.6	14.7	10.5	34.3	25.9	0.5	-10
12	West Arm	25.6	8.0	6.9	34.0	25.9	1.7	-21
13	Holwell	21.9	4.4	16.1	28.8	30.4	4.4	-21
15	Stony Head	21.6	0.0	15.6	22.6	40.1	7.2	-33
16	Ti Tree Bend	24.0	3.8	14.2	45.5	26.7	0.7	-31

Figure 5.16 shows that very low to medium APPs are experienced throughout the study area during summer months. APP is lowest in the southeast corner of the study area, rising with proximity to the coast along a southeast/northwest aligned gradient.

Table 5.16b Spatial variation in the parameters comprising the autumn APP index throughout the Tamar Valley

Site #	*Site Location*	S_h	Sg_{24}	R_{24}	U	V_{24}	U_8	*APP*
1	Nunamara	34.5	18.9	2.8	31.8	44.4	2.7	-23
2	Hadspen	29.9	23.8	10.0	15.7	37.2	4.7	6
3	Dog Point	34.7	24.7	11.2	22.8	29.6	3.7	14
4	Windermere	45.2	27.5	11.5	9.7	35.4	9.6	30
5	Rowella	30.0	9.9	22.7	15.4	35.1	5.6	6
6	Barrett's Point	41.3	23.2	19.1	20.0	28.5	1.2	34
7	Garden Island	22.4	0.0	31.6	11.4	28.0	7.4	7
8	Bell Bay	21.7	11.0	20.3	18.5	33.8	5.7	-5
9	Low Head	45.8	0.4	10.9	6.8	46.4	23.2	-19
10	Lefroy	32.2	22.6	13.1	12.5	32.2	3.9	19
11	East Arm	42.5	46.4	3.8	18.7	12.8	0.2	61
12	West Arm	38.5	40.4	12.6	18.9	26.9	2.0	44
13	Holwell	33.0	25.6	16.3	21.4	32.6	4.3	17
15	Stony Head	29.1	4.2	16.4	12.2	38.7	5.9	-7
16	Ti Tree Bend	30.5	31.3	13.4	30.8	24.2	0.7	20

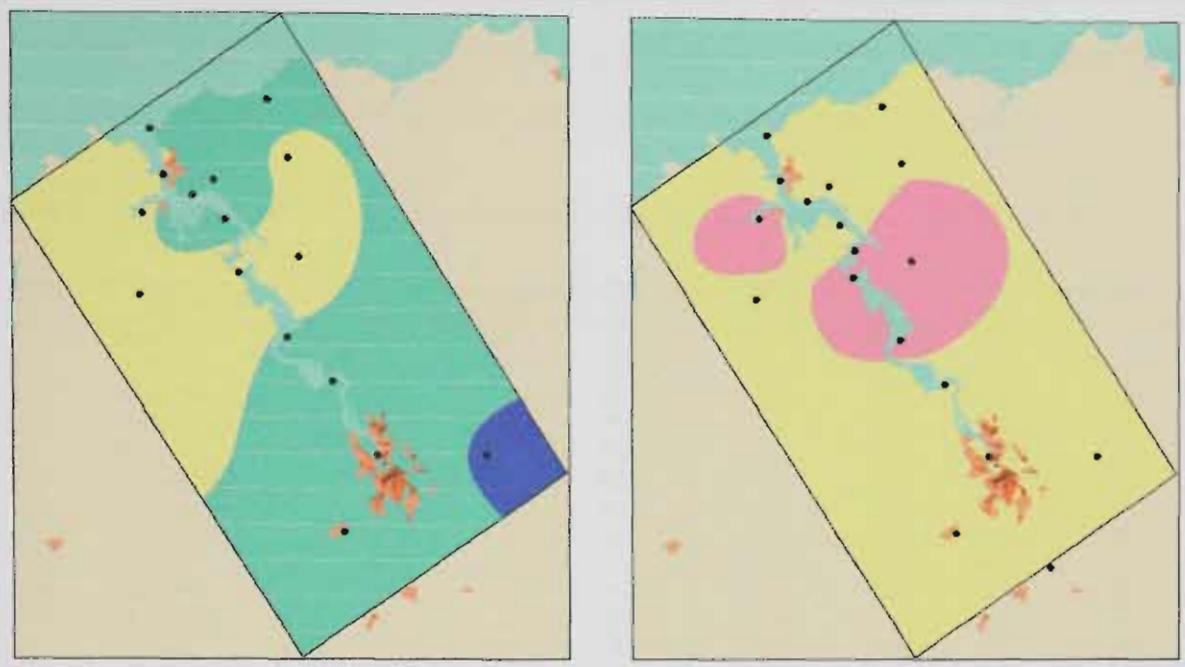

Summer

Autumn

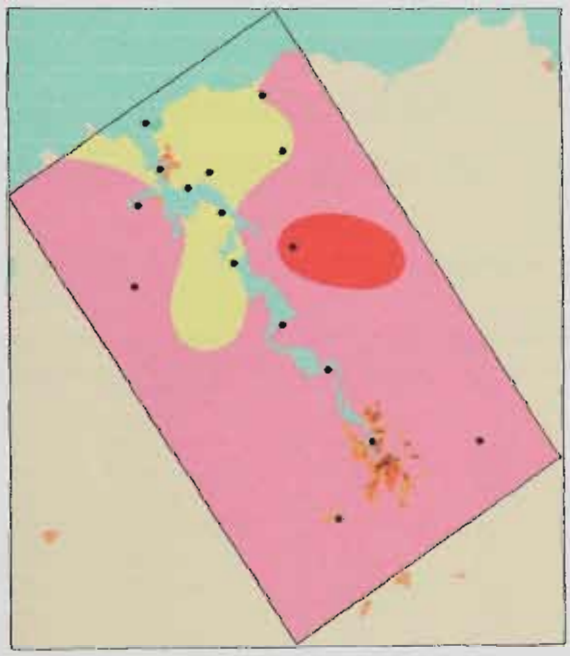

Winter

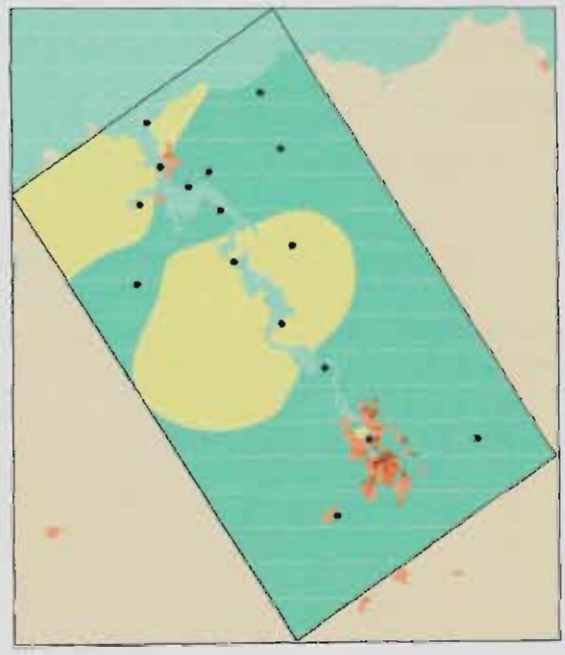

Spring

Figure 5.16 Seasonal variation in air pollution potential (May '93 to May '96) overlaid over Census 96 housing density (occupied dwellings per square kilometre). The dots represent the location of each anemometer site and the northwest/southeast-aligned rectangle shows the extent of the *TVAS* study area.

With the onset of Autumn, APP increases with either high or medium classes occurring. The high values are located in the West Arm region, and in the central to east mid-Tamar, with the remainder of the study area experiencing medium APP.

Table 5.16c Spatial variation in the parameters comprising the winter APP index throughout the Tamar Valley

Site #	Site Location	S_h	Sg_{24}	R_{24}	$\bar{U}$	V_{24}	U_g	APP
1	Nunamara	67.1	47.6	1.4	26.3	28.8	1.9	59
2	Hadspen	41.3	41.6	10.0	11.7	34.9	4.3	42
3	Dog Point	38.8	49.6	10.6	18.6	26.2	3.9	50
4	Windermere	48.6	35.3	7.9	8.3	38.9	8.4	36
5	Rowella	35.6	13.1	17.8	7.7	32.9	5.7	20
7	Garden Island	35.1	1.0	12.5	4.8	43.1	12.0	-11
8	Bell Bay	22.1	15.1	14.7	10.6	41.4	7.0	-7
9	Low Head	61.9	0.5	5.3	3.5	63.4	29.2	-29
10	Lefroy	44.0	10.3	7.5	7.0	34.9	4.0	16
11	East Arm	56.6	62.4	5.8	10.3	15.0	0.4	99
12	West Arm	52.0	50.0	20.1	14.8	22.2	1.7	84
13	Holwell	43.1	27.8	7.8	11.0	28.0	3.1	37
15	Stony Head	37.3	22.3	8.5	11.7	26.7	2.9	27
16	Ti Tree Bend	36.2	59.3	8.0	22.1	14.5	0.6	66

The greatest APP occurs during winter with values ranging between low and very high. Low index values are experienced at Low Head, with an increasing gradient extending towards East Arm (Site 11) which has a very high APP. The remainder of the study area, including the greater Launceston region, experiences high APP.

Table 5.16d Spatial variation in the parameters comprising the spring APP index throughout the Tamar Valley

Site #	Site Location	S_h	Sg_{24}	R_{24}	$\bar{U}$	V_{24}	U_g	APP
1	Nunamara	21.6	1.9	6.4	46.8	49.6	4.6	-71
2	Hadspen	18.6	2.6	10.0	21.5	47.9	8.5	-47
3	Dog Point	23.8	6.1	11.0	32.8	36.2	8.0	-36
4	Windermere	44.5	1.6	8.6	6.6	34.2	14.4	0
5	Rowella	18.0	0.3	17.0	28.7	42.7	11.4	-48
7	Garden Island	29.1	0.1	18.8	10.5	43.7	14.4	-21
8	Bell Bay	16.6	0.1	14.6	22.7	44.5	9.4	-45
9	Low Head	57.6	0.2	11.1	5.0	50.5	26.0	-13
10	Lefroy	28.1	0.3	12.7	20.6	47.9	8.0	-35
11	East Arm	27.2	12.8	4.5	26.9	29.9	0.7	-13
12	West Arm	27.4	14.4	8.2	25.0	37.9	5.1	-18
13	Holwell	23.4	4.7	14.8	29.5	39.0	6.2	-32
15	Stony Head	27.9	0.0	15.6	18.1	44.9	9.7	-29
16	Ti Tree Bend	24.6	9.8	13.3	40.2	27.6	1.8	-22

In spring APP is dramatically reduced, with regions showing either medium or low index values. Medium APP is found in the coastal regions of the study area, extending inland in the West-Tamar. A broad zone of medium APP occurs in the Mid-Tamar region, once again slightly biased towards the West-Tamar rather than East-Tamar. A final, small region of medium APP encircles the Ti Tree Bend anemometer site. The remainder of the study area experiences low APP during spring months.

5.6 Conclusion

This chapter has summarised the *TVAS* database in terms of key climatological parameters and derived variables. Wind, stability and atmospheric transport roses have been produced for each site on a seasonal basis. Maps have been produced showing the spatial variation in many additional parameters. The most important of these have been summarised into an index of air pollution potential, which is also mapped on a seasonal basis.

6 Anticyclonic Climatology of the Tamar Valley

6.1 Introduction

The Tamar Valley's air pollution problem worsens noticeably during the passage of anticyclones. Anticyclones are associated with slack pressure gradients and clear skies, thus giving rise to decoupled localised thermotopographic winds. These include weak sea breezes and valley winds which travel inland, and land breezes and katabatic winds which drain down the valley walls and axis and eventually out of the valley mouth to sea. Surface radiation inversions and elevated subsidence inversions also occur.

All of these conditions conspire to minimise the air pollution transport, thus causing poor dispersion conditions. The climatology presented in Chapter 5 will therefore be extended to include a detailed analysis for these 'worst case' conditions.

The anticyclonic climatology will be largely based upon wind speeds and directions extracted for sampling intervals when the surface pressure was at or above 1020 hPa. Vector averages will be calculated for each anemometer site, providing diurnal time series for the "average" anticyclonic day in each season. The mean anticyclonic time series will be used to produce:

- graphs depicting the diurnal variation in mean winds, at three locations situated along a transect following the valley axis;
- maps showing the spatial variation in mean wind vectors at selected times of the day; and
- an estimate of sea breeze arrival time and duration for summer and autumn.

6.2 Surface Pressure Measurements

Surface atmospheric pressure was recorded at Site 8, over a two-year period extending from early June 1994 to mid May 1996. Pressures were averaged over 15 minute time intervals. Figure 6.1 shows a seasonal breakdown of the percentage of readings equalling or exceeding 1020 hPa. This figure was chosen to represent anticyclonic, and thus poor dispersion, conditions. Spring and summer both exhibited an anticyclonicity of 17 %, well below the yearly mean of 28 %. The frequency of anticyclonic conditions rose to 30 % in autumn and then to 40 % in winter. These figures partly explain why winter and autumn are widely considered to be associated with poor pollution dispersion in the Tamar Valley.

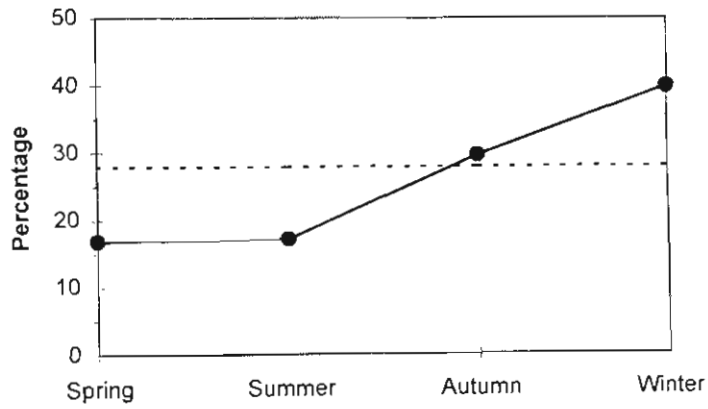

Figure 6.1 Seasonal frequency of surface pressures equalling or exceeding 1020 hPa. 15-minute means recorded at Site 8, Bell Bay, between June 1994 and May 1996. The dotted line represents the overall yearly mean of 28 %.

6.3 Methodology

The *TVAS* anemometer-network database was analysed using SQL queries. Queries were written which identified the dates and associated 15-minute time intervals when the mean atmospheric pressure, recorded at Site 8, equalled or exceeded 1020 hPa.

Wind speeds and directions from all 16 anemometer sites were then extracted on the basis of these 'anticyclonic' intervals. Seasonal means were then calculated for each 15-minute time interval, spanning the entire day, until data was built up describing the changing vector-averaged winds occurring during an "average anticyclonic day"

for each season at each measurement location. This information is summarised on both a diurnal and a spatial basis.

6.4 Diurnal and Spatial Variation in Vector Averaged Winds

Vector average winds were calculated on a seasonal basis by averaging the easterly and northerly components for each time and season, and resolving them back into wind speeds and directions. When the diurnal time series were graphed it was clear that there was a significant amount of noise present. This was removed by smoothing the easterly and northerly components of the time series prior to resolving them back into wind speeds and directions. Smoothing was conducted using running means covering the time in question, plus the two values before and the two after. On first glance this approach may seem to provide a "disjointed" dataset. Its use is defended on the grounds that after a low degree of smoothing, very clear diurnal patterns were observed.

The diurnal cycle of vector averaged winds under anticyclonic conditions was calculated on a seasonal basis for each of the 16 *TVAS* anemometer sites. For illustrative purposes, only the time series for Sites 8, 4 and 16 will be displayed.

The Tamar Valley is a coastal valley, and thus experiences thermotopographic winds common to coastlines and valleys. As such it can be difficult to determine whether the daytime winds travelling inland are caused by topographic channelling, sea breezes, or the anabatic "valley wind" experienced in most valleys regardless of proximity to the coast. In a similar manner it is difficult to determine whether the nocturnal winds travelling out of the valley towards the coast are caused by channelling, land breezes or by katabatic "mountain winds" draining down the valley axis.

In reality each situation is probably an amalgam of all three possible events. For simplicity, the daytime winds arriving from the northwest at the coast will be referred to as the sea breeze. Likewise the nocturnal flows travelling down the valley axis will be referred to as drainage or katabatic flows.

Figure 6.2 compares the 24-hour vector-averaged wind speed and direction time series, under anticyclonic conditions at Bell Bay (Site 8), for each of the four seasons. Each seasonal trace is characterised by low wind speeds overnight, with winds less than 1 ms^{-1}. Wind speeds gradually increase towards the dawn, and reach a local maximum between 09:00 and 10:00 EST. A period of calm winds then occurs prior to the onset of the sea breeze. This quickly builds up to its maximum speed during late afternoon, remaining fairly constant for three to four hours, before falling to its nocturnal levels.

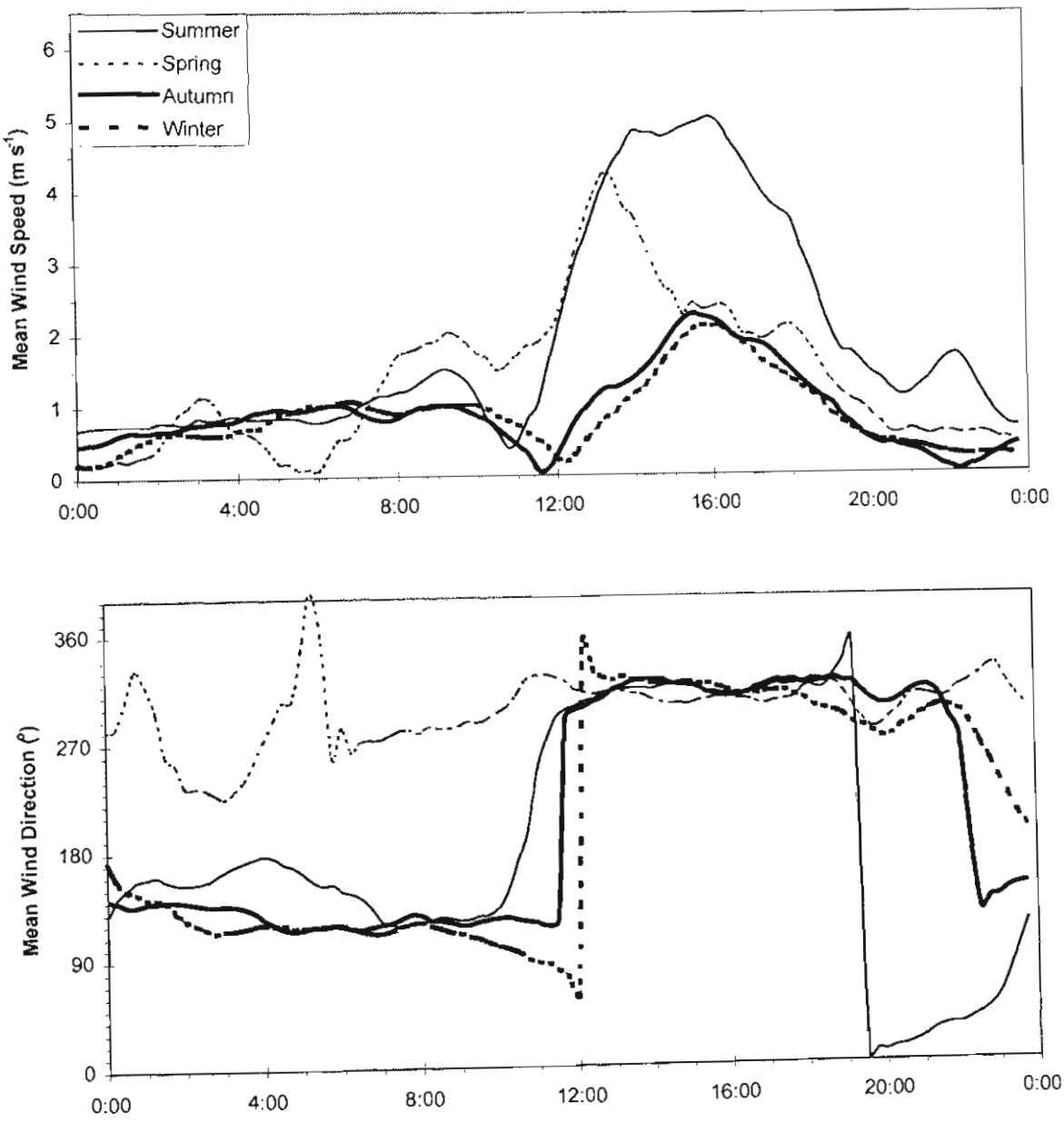

Figure 6.2 Seasonal vector averaged wind speed and direction time series recorded at Bell Bay (Site 8) under anticyclonic conditions (surface pressure ≥ 1020 hPa). Each time series has a 15-minute resolution, giving 96 consecutive time intervals spanning an entire day. Times are given as Eastern Standard Time.

Nocturnal winds tend to arrive from the southeast sector, and are the result of drainage flow down the valley axis. In summer this flow will persist from midnight to around 10:00 EST. The winds then die down in strength and gradually veer in direction from the southeast to the south, the west, then finally the northwest. This period of light, veering winds prior to the onset of the summer sea breeze has been observed many times at Site 8, and generally lasts for around one and a half hours. The northwesterly winds signal the arrival of the sea breeze and are associated with a rapid increase in wind strength. The northwesterly summer sea breeze persists for seven hours before the wind gradually dies down in speed and resumes its veering process. By midnight the wind direction has 'boxed the compass' with the winds successively arriving from the north, east, and finally southeast where it began 24 hours earlier.

During autumn the sea breeze is still evident at Site 8, however it is far lower in intensity. The diurnal change in wind directions is similar in form to that observed during summer, however, the arrival of the sea breeze is more sudden with the winds veering almost 180 ° in fifteen minutes. The northwesterly direction persists for longer than in summer. What is unusual however, is that the winds then start to back in direction from northwesterly to westerly, to southerly to southeasterly.

The winter scenario is the mirror image of that experienced in summer. Southeasterly nocturnal drainage flows still occur, gradually changing into a gentle northwesterly sea breeze. Rather than a gradual veering of the winds, as seen in the summer situation, the winds box the compass in the reverse direction.

In spring an afternoon sea breeze still occurs under anticyclonic conditions. This is evidenced by a period of stronger winds from the northwest during the early afternoon. Apart from the presence of the sea breeze, the spring trace is markedly different from those experienced during the other seasons. Nocturnal katabatic winds are absent, being replaced by light, variable winds which fluctuate between northeasterlies and southwesterlies. As the night progresses the winds settle down, becoming westerlies which gradually veer into northwesterlies. These persist all afternoon and late into the evening.

The diurnal time series for Site 4, located at Windermere, midway between Sites 8 and 16, is displayed as Figure 6.3. Representative data was not available for anticyclonic conditions during spring, so only summer, autumn and winter traces are shown. Very definite sea breezes occur during summer and autumn, with an increase in winds from the northwest occurring during the early afternoon. The development of the sea breeze at Site 4 is more gradual than that experienced at Bell Bay.

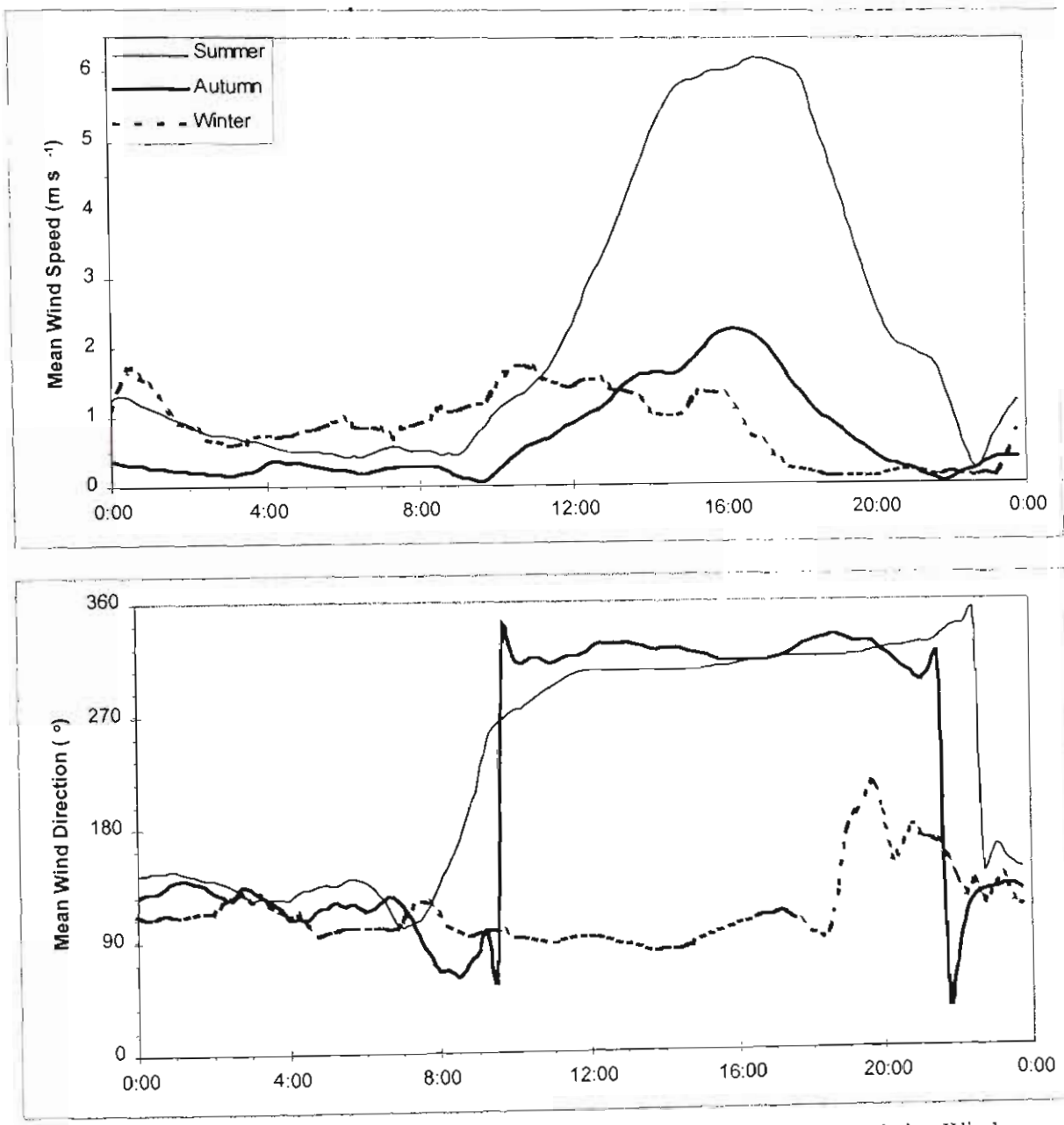

Figure 6.3 Seasonal vector-averaged wind speed and direction time series recorded at Windermere, Site 4, under anticyclonic conditions (surface pressure ≥ 1020 hPa). Data were not available for Spring. Each time series has a 15-minute resolution, giving 96 consecutive time intervals spanning an entire day. Times are given as Eastern Standard Time.

The summer sea breeze mimics that experienced at Bell Bay, with a gradual veering of the winds occurring both before and after the sea breeze. The autumn sea breeze, whilst similar in intensity to that at Bell Bay starts earlier, and occurs after a period of backing winds rather than the veering winds experienced at Bell Bay. Likewise, the departure of the sea breeze is associated with changing wind directions in the opposite manner to those simultaneously occurring at Bell Bay. These differences between the arrival and departure of the sea breeze at Bell Bay and Windermere during autumn suggest that the transitional periods are subject to localised effects, which are controlled by topography.

The weak winter sea breeze that occurs at Bell Bay during anticyclonic conditions is absent midway down the valley at Windermere. Light drainage flows prevail all day, with the winds largely remaining between the east and south.

Figure 6.4 similarly displays the mean diurnal trends in Launceston's winds using the Ti Tree Bend (Site 16) data. Again the spring trace is absent due to lack of data. While the wind speeds are slightly lower than those experienced at Sites 4 and 8, they do follow the same diurnal pattern established at these sites.

Winter anticyclonic conditions see the establishment of a gentle northerly flow at Site 16, which persists throughout the entire day. This slowly builds up in intensity during the morning, reaching its peak of 1.6 ms^{-1} around 14:30 EST before gradually falling during the afternoon.

Drainage flows, from the southeast, are seen at midnight during both summer and autumn. These persist throughout the entire night in autumn before rapidly backing into a northerly sea breeze. This transition period is far more gradual in summer, lasting from 03:00 to 10:00 EST. As expected, the summer sea breeze lasts far longer than the autumn sea breeze. After the sea breeze, the winds veer back to the southeast.

6.4.1 Spatial Variation in Vector Averaged Winds

The spatial variation in winds under anticyclonic conditions was investigated. Vector-averaged wind speeds and directions were compiled on the basis of

anemometer site, time of day and season. Winds were mapped as vectors, assigned to one of six different wind speed classes. Figures 6.5 to 6.8 map the diurnal variation in vector-averaged winds under anticyclonic conditions for summer, autumn, winter and spring respectively.

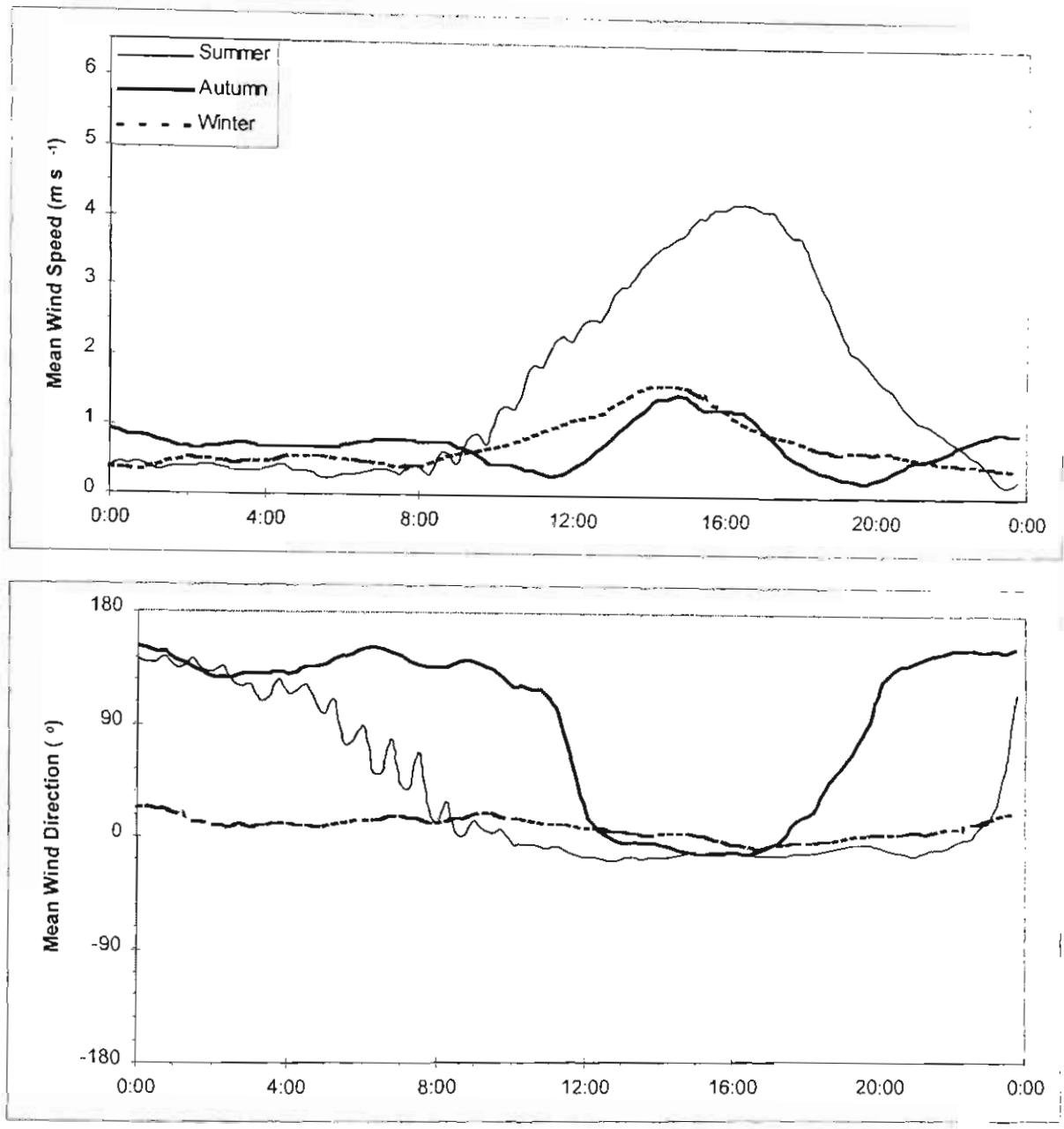

Figure 6.4 Seasonal vector-averaged wind speed and direction time series recorded at Ti Tree Bend, Launceston (Site 16) under anticyclonic conditions (surface pressure ≥ 1020 hPa). Data were not available for spring. Each time series has a 15-minute resolution, giving 96 consecutive time intervals spanning an entire day. Times are given as Eastern Standard Time. Note that the wind direction scale has been adjusted to avoid the 0/360 degree discontinuity.

During summer (Figure 6.5a-b) a weak drainage flow is evident throughout most of the valley at midnight, increasing in speed as it approaches the river mouth.

However, the flow in the upper Tamar, near the Launceston region, is more confused, often flowing up-river rather than down-river. Similar inland flows are seen at the near-coastal Sites 10 and 15 on the East-Tamar.

The inland flows in the upper Tamar are attributed to shallow localised drainage from nearby hills. The inland flow noted at Sites 10 and 15 is more problematic however, and may be a remnant sea breeze. This is feasible as the two sites are close to the coast and are separated from the valley axis by the Tippogoree Hills. The sites are therefore protected from the main axis drainage flow. This would allow localised flows to occur in the region without being swamped by more dominant valley-wide drainage patterns. The remnant sea breeze persists all night, growing weaker with inland distance and time. It is only present in summer.

This overall pattern of drainage flows throughout the valley, and a remnant sea breeze in the coastal region to the east of the study area, remains largely similar throughout the entire night. It is still evident at 09:00 the next morning. By noon the pattern has reversed, and a strong anabatic flow is present, with all sites showing an inland flow being channelled by the topography. The strongest winds are seen at the valley axis. The sea breeze builds in intensity until it reaches a maximum, which is depicted in the 18:00 map. The 21:00 map shows the beginnings of a weak drainage flow at the coast, and the remnants of the sea breeze inland.

The autumn wind vectors, shown in Figure 6.6a-b are very similar to those occurring in summer under anticyclonic conditions. The remnant nocturnal sea breeze experienced at Sites 10 and 15 is absent and is replaced with a weak drainage flow off the Tippogoree Hills.

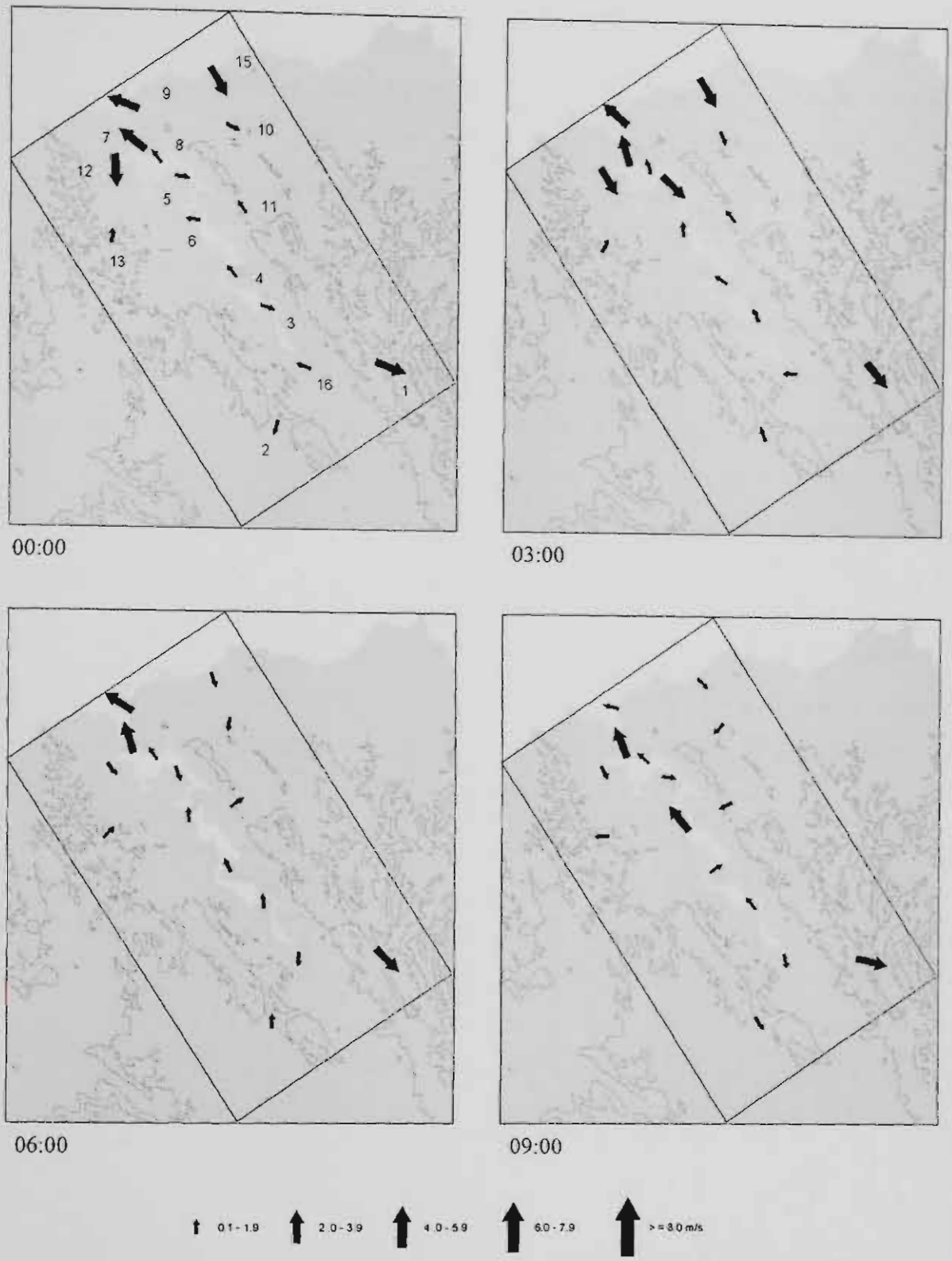

Figure 6.5a Diurnal variation in summer vector-averaged winds under anticyclonic conditions (June '94 to May '96). Anticyclonic conditions were defined whenever the surface pressure at Site 8 (Bell Bay) reached or exceeded 1020 hPa. The northwest/southeast aligned rectangle shows the extent of the *TVAS* study area. Site numbers are provided on the midnight map, and contours are drawn (using a 200 m interval) to provide an indication of topography.

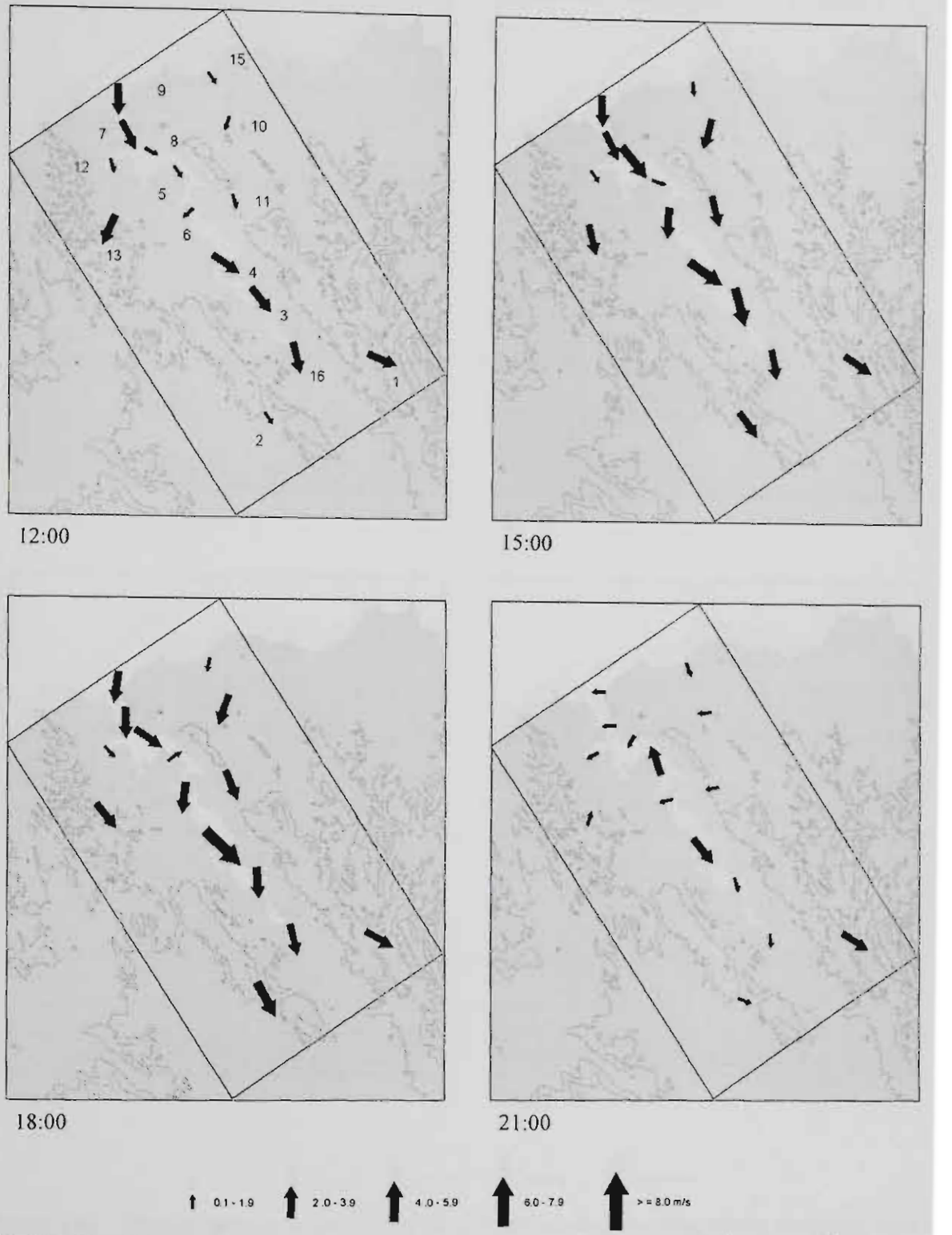

Figure 6.5b Diurnal variation in summer vector-averaged winds under anticyclonic conditions (June '94 to May '96). Anticyclonic conditions were defined whenever the surface pressure at Site 8 (Bell Bay) reached or exceeded 1020 hPa. The northwest/southeast aligned rectangle shows the extent of the *TVAS* study area. Site numbers are provided on the noon map, and contours are drawn (using a 200 m interval) to provide an indication of topography.

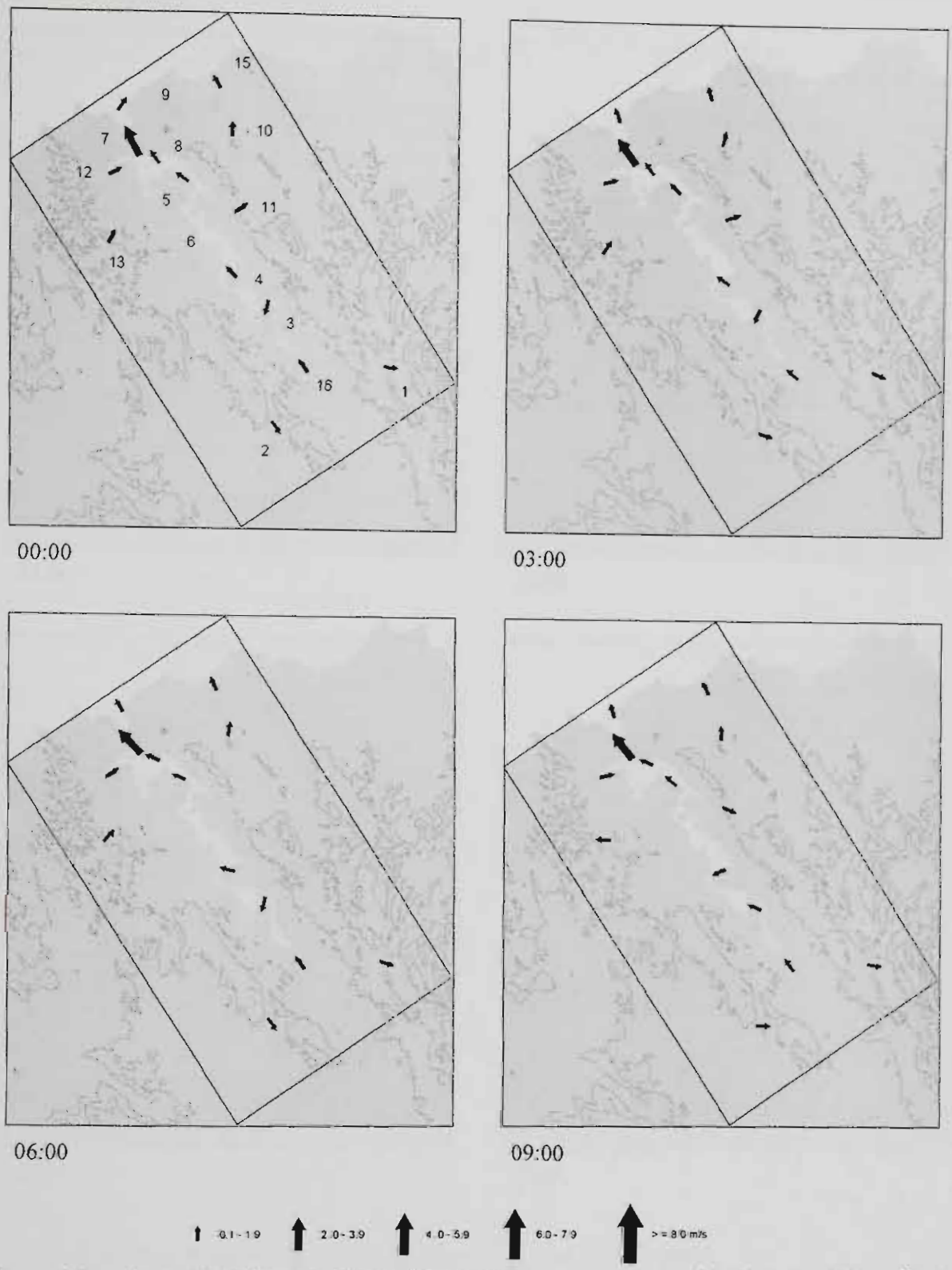

Figure 6.6a Diurnal variation in autumn vector-averaged winds under anticyclonic conditions (June '94 to May '96). Anticyclonic conditions were defined whenever the surface pressure at Site 8 (Bell Bay) reached or exceeded 1020 hPa. The northwest/southeast aligned rectangle shows the extent of the *TVAS* study area. Site numbers are provided on the midnight map, and contours are drawn (using a 200 m interval) to provide an indication of topography.

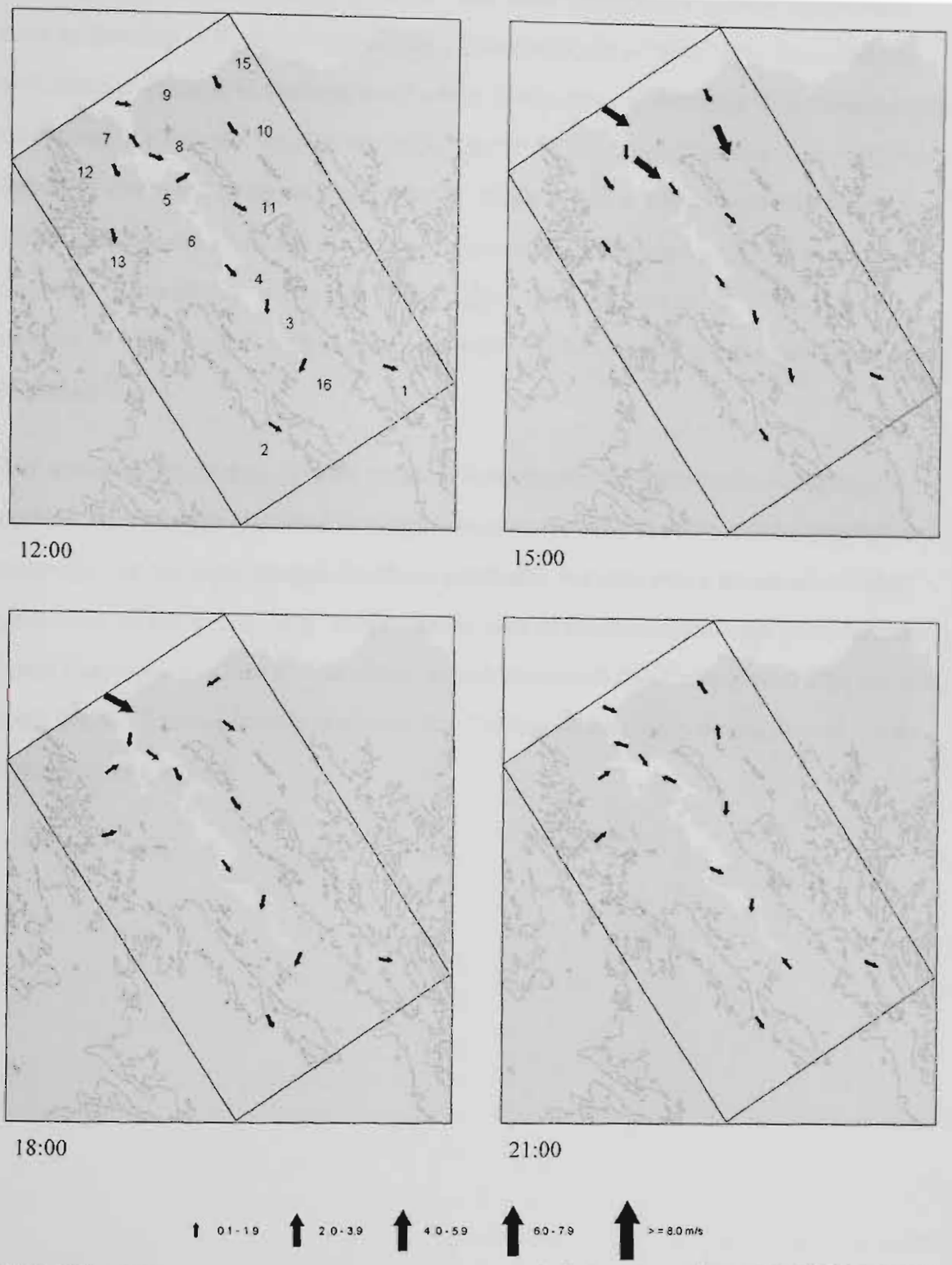

Figure 6.6b Diurnal variation in autumn vector-averaged winds under anticyclonic conditions (June '94 to May '96). Anticyclonic conditions were defined whenever the surface pressure at Site 8 (Bell Bay) reached or exceeded 1020 hPa. The northwest/southeast aligned rectangle shows the extent of the *TVAS* study area. Site numbers are provided on the noon map, and contours are drawn (using a 200 m interval) to provide an indication of topography.

During winter (Figure 6.7a-b), the midnight wind vectors show weak katabatic flows draining off local topographic features. The main mountain wind has not yet had time to develop. Of special interest are drainage flows coming from the Asbestos and Dazzler Ranges in the northwest of the study area. These flow in a northeasterly direction, skirting the Tippogoree Hills. By 03:00 the mountain wind has started to develop, and remains present until 09:00. Noon sees a confused pattern of opposing flows near the mouth of the study region associated with very light winds, and weak drainage flows appear in the rest of the valley. The sea breeze finally becomes evident at 15:00, and is still in place at 18:00. 21:00 sees the re-establishment of katabatic flows.

The spring wind vectors (Figure 6.8a-b) show similar features to those explained above. At midnight localised drainage flows occur from the dominant topographical controls. As the night progresses these gradually develop into a mountain wind at sites close to the valley axis. Of particular note is the strong drainage wind from the north that occurs at Site 5. This flow, which drains off the Tippogoree Hills, persists until 06:00. The sea breeze is present by 15:00 with relatively strong inland winds occurring until 21:00.

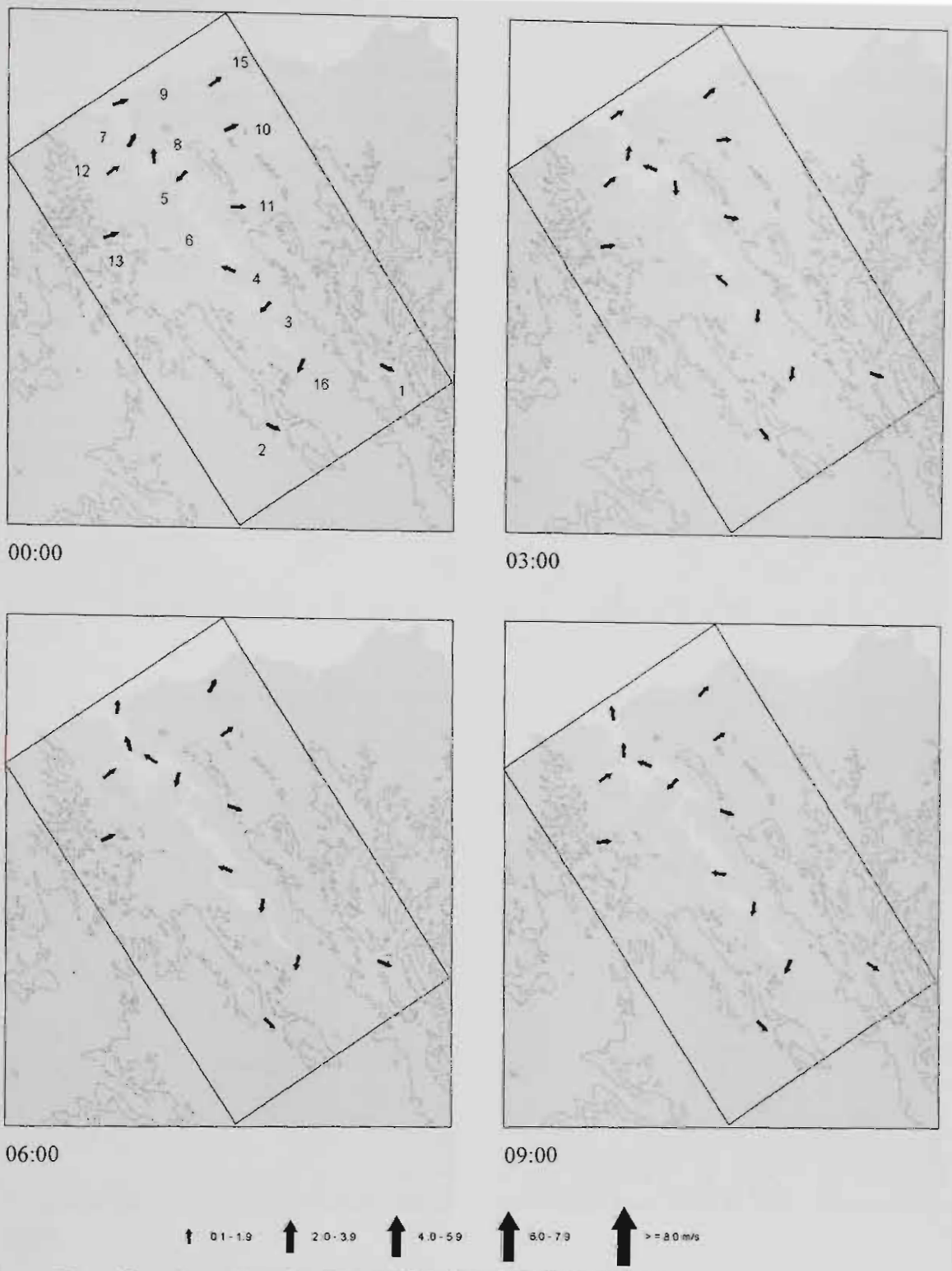

Figure 6.7a Diurnal variation in winter vector-averaged winds under anticyclonic conditions (June '94 to May '96). Anticyclonic conditions were defined whenever the surface pressure at Site 8 (Bell Bay) reached or exceeded 1020 hPa. The northwest/southeast aligned rectangle shows the extent of the *TVAS* study area. Site numbers are provided on the midnight map, and contours are drawn (using a 200 m interval) to provide an indication of topography.

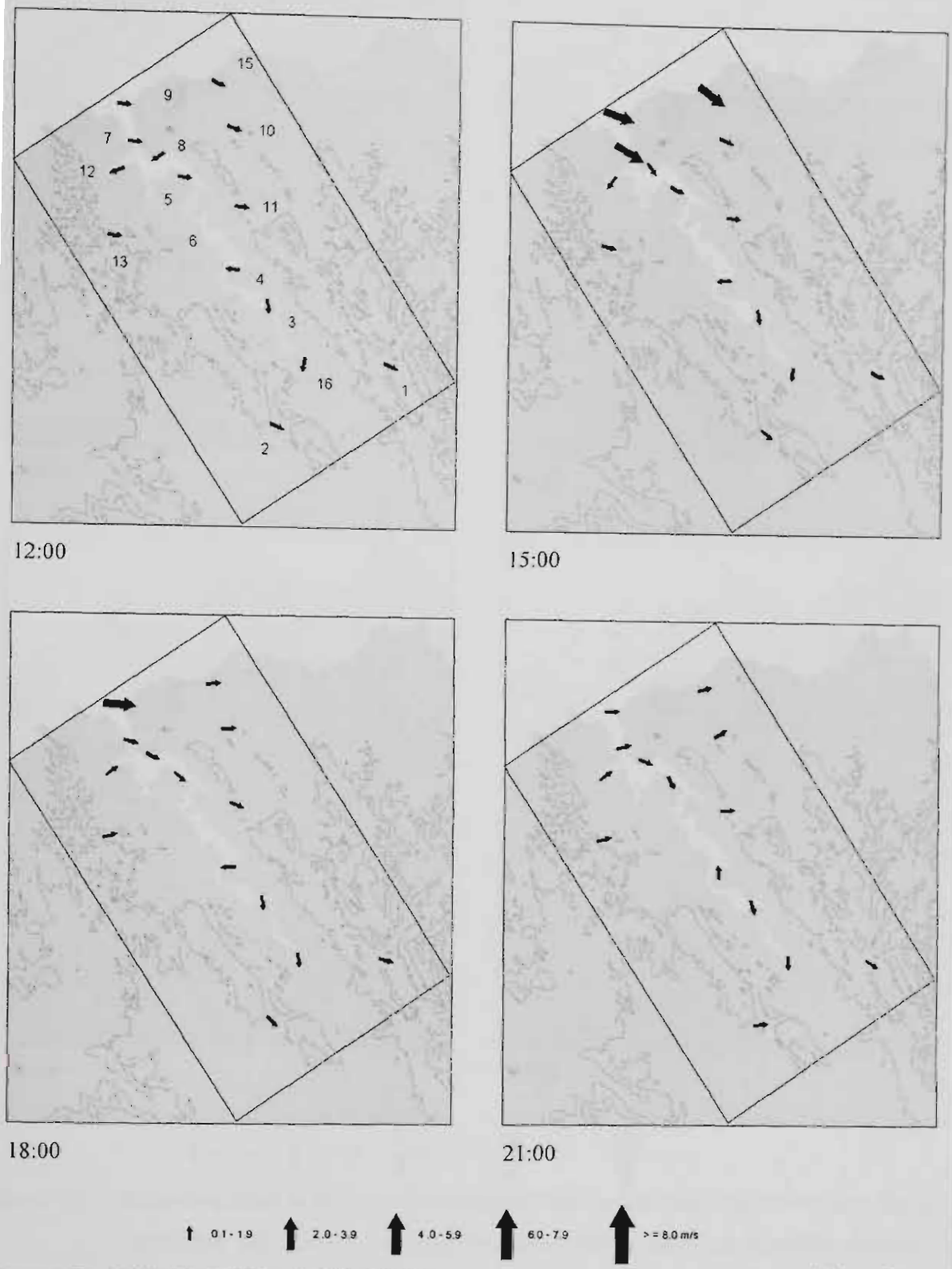

Figure 6.7b Diurnal variation in winter vector-averaged winds under anticyclonic conditions (June '94 to May '96). Anticyclonic conditions were defined whenever the surface pressure at Site 8 (Bell Bay) reached or exceeded 1020 hPa. The northwest/southeast aligned rectangle shows the extent of the *TVAS* study area. Site numbers are provided on the noon map, and contours are drawn (using a 200 m interval) to provide an indication of topography.

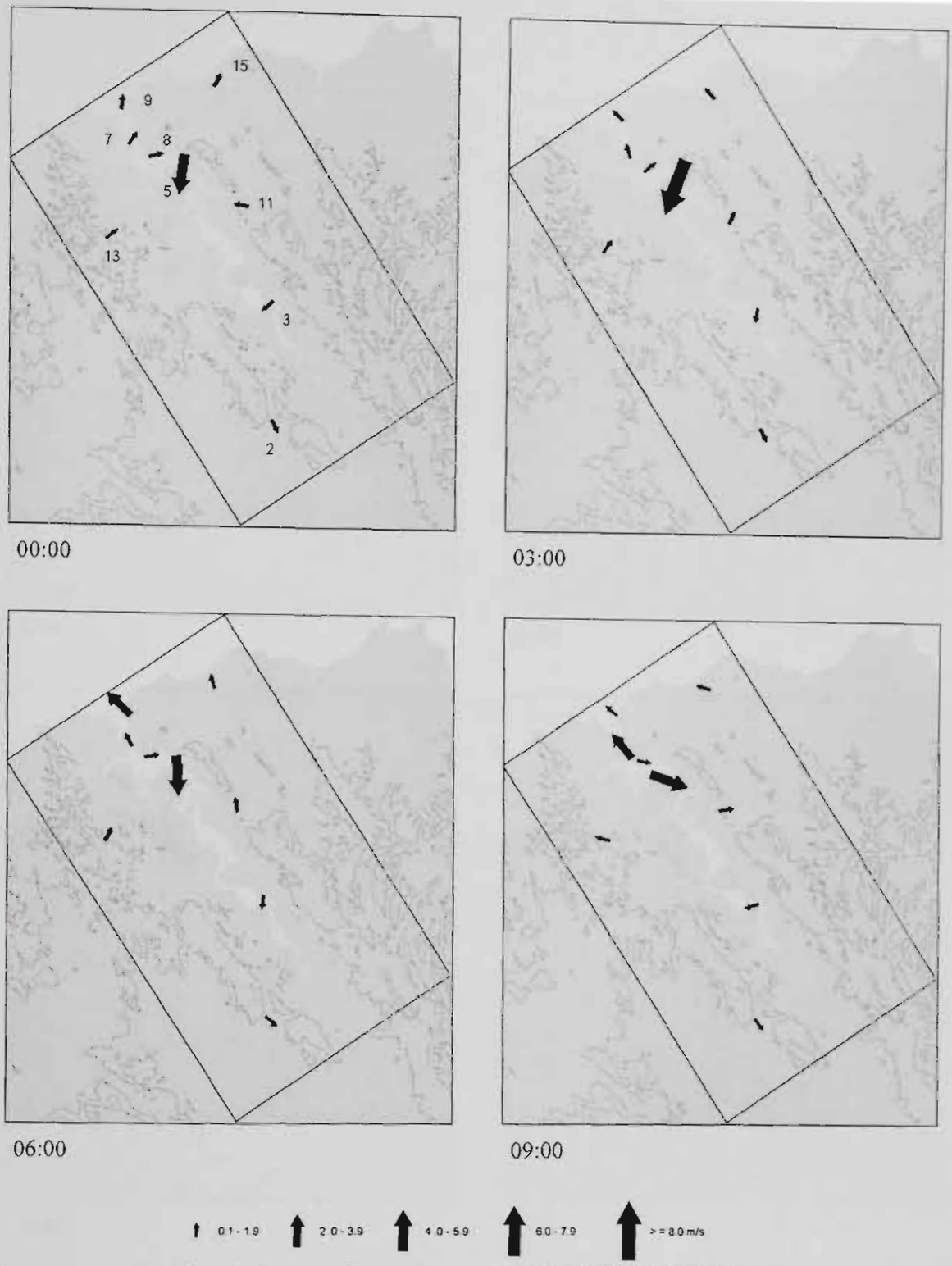

Figure 6.8a Diurnal variation in spring vector-averaged winds under anticyclonic conditions (June '94 to May '96). Anticyclonic conditions were defined whenever the surface pressure at Site 8 (Bell Bay) reached or exceeded 1020 hPa. The northwest/southeast aligned rectangle shows the extent of the *TVAS* study area. Site numbers are provided on the midnight map, and contours are drawn (using a 200 m interval) to provide an indication of topography.

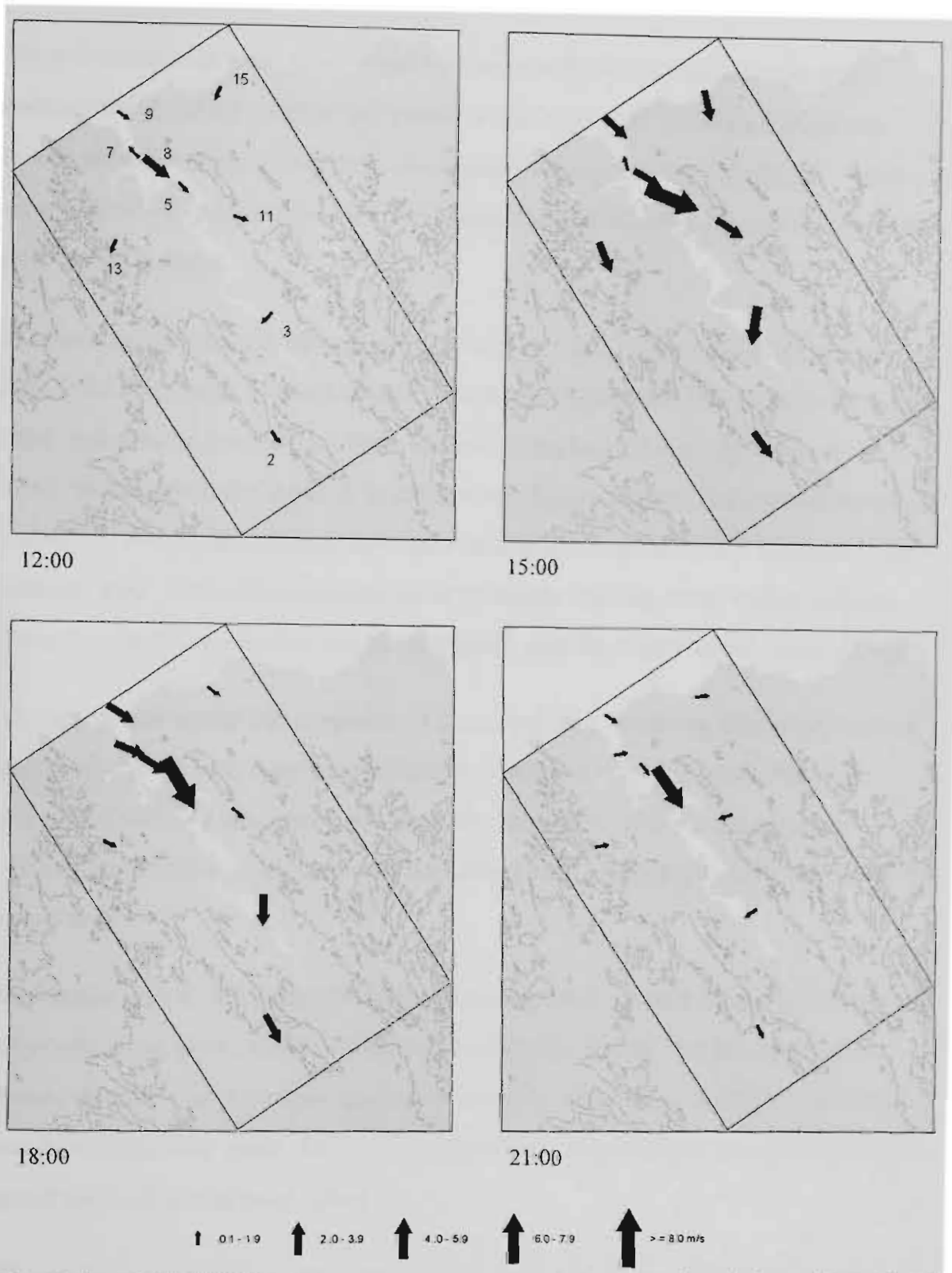

Figure 6.8b Diurnal variation in spring vector-averaged winds under anticyclonic conditions (June '94 to May '96). Anticyclonic conditions were defined whenever the surface pressure at Site 8 (Bell Bay) reached or exceeded 1020 hPa. The northwest/southeast aligned rectangle shows the extent of the *TVAS* study area. Site numbers are provided on the noon map, and contours are drawn (using a 200 m interval) to provide an indication of topography.

6.4.2 Estimating the Sea Breeze Arrival Time and Duration Throughout the Valley

The vector-average wind time series data were analysed, for each season and anemometer location, in order to provide a 'rule of thumb' indication of the sea breeze arrival and departure times under idealised anticyclonic conditions. While a clear pattern was not discovered for the winter and spring months, one was evident in summer and autumn.

Similar forms in the summer and autumn vector-averaged time series graphs were seen to be associated with sea breeze arrivals and departures. Nocturnal winds were light, and directions identified them as shallow drainage flows. After dawn, the winds would gradually increase as surface convection occurs. During midmorning a period of calm would occur as the winds shifted in direction from a drainage to an anabatic flow. This change would occur relatively quickly, often within an hour. Once the wind direction had established itself, then the winds would rise in strength.

The sea breeze would last a number of hours and then die down, frequently with an abrupt change in both speed and direction. The most common wind direction associated with the sea breeze was from the northwest, however topographic channelling of the sea breeze meant that inland sites often received the sea breeze as a northerly.

Sea breeze arrival and departure times were estimated for each location. The arrival time was given by the timing of the first significant change, towards the final sea breeze direction, in the wind direction time series. If a change was not clear in the wind direction time series, then the timing of the corresponding change in the wind speed time series was used instead.

The sea breeze departure was identified in a similar manner, using wind direction as the primary indicator of departure, with wind speed being used in the absence of a clear change in the wind direction signal. It was often difficult to determine departure times, whereas arrival times were quite distinct and easily identified. Sea breeze duration was calculated as the time difference between arrival and departure.

Four independent variables were used to model the sea breeze arrival time and duration. The first of these (X_1) was the NW/SE component of the 06:00 wind at each site, measured in ms^{-1}. This was used as a measure of the strength of the opposing drainage flow that the sea breeze had to overcome.

The remaining three independent variables were position parameters, used to identify the location of each anemometer site in terms of inland distance (km), lateral distance (km), and height (m). The inland distance (X_2) refers to the proximity of the anemometer site to the coast, measured along the valley axis. The lateral distance (X_3) is the distance of the anemometer site from the valley axis, measured normal to the axis. This parameter is not direction-dependent, and hence distances northeast or southwest of the axis are both assigned positive values. The height (X_4) is the height of the anemometer site above mean sea level. Table 6.1 summarises the positional indicator values used for each anemometer site.

Table 6.1 Position parameters for each *TVAS* anemometer site. These are used in modelling sea breeze arrival times and durations.

Site Number	*Site Location*	*Inland Distance (X_2), km*	*Lateral Distance from Valley Axis (X_3), km*	*Height (X_4), masl*
Site 9	Low Head Pilot Station	1.85	1.04	0
Site 15	The Currie - Stony Head	7.00	12.95	41
Site 7	Garden Island	7.59	2.53	2
Site 12	West Arm	9.97	7.37	10
Site 8	Bell Bay	11.67	0.89	1
Site 10	Lefroy	14.26	11.31	113
Site 5	Rowella	16.37	0.89	20
Site 13	Holwell	17.83	12.80	186
Site 11	East Arm	24.63	6.25	103
Site 4	Windermere	32.00	0.30	4
Site 3	Dog Point	39.52	1.49	2
Site 16	Ti Tree Bend STP Site	50.01	1.41	17
Site 2	Hadspen	55.40	7.07	171
Site 1	Nunamara	57.45	12.65	302

Simple multi-linear regressions were used to model sea breeze arrival time and duration. Each model took the form

$$Y = C_0 + C_1X_1 + C_2X_2 + C_3X_3 + C_4X_4 \qquad 6.1$$

where Y is the sea breeze onset time or duration, given in decimal hours, and C_0 to C_4 are the y-intercept and coefficients associated with X_1 to X_4 respectively.

Table 6.2 summarises the values taken by C_0 to C_4 for the summer and autumn commencement time and duration models. This allows the onset time and duration

to be calculated for any point in the valley, given the northwest/southeast component of the 06:00 wind at that site, and the position of the location in question.

Table 6.2 Coefficients used in modelling sea breeze onset times and durations for the summer and autumn seasons.

	Sea Breeze Onset Model		*Sea Breeze Duration Model*	
Variable	*Summer*	*Autumn*	*Summer*	*Autumn*
C_0	9.483	8.630	8.024	14.061
C_1	-0.009	1.899	0.580	-2.795
C_2	-0.094	0.029	0.162	-0.082
C_3	-0.006	-0.055	0.118	-0.411
C_4	0.399	-0.001	0.006	0.015
Multiple R	0.893	0.915	0.963	0.750
R^2	0.798	0.837	0.927	0.562
Standard Error	0.659	0.913	0.976	2.218
Observations	13	14	13	14
F	7.883	11.531	25.233	2.889
Significance F	0.007	0.001	0.000	0.086

The summer sea breeze has been well modelled in terms of onset and duration, having R^2 values of 0.80 and 0.93 respectively. This was because the arrival and departure times were distinct events and hence easily determined from the vector averaged time series for each site. Likewise the autumn onset time was clearly seen in the mean time series and hence has an R^2 value of 0.91. In contrast a poor relationship was determined for autumn sea breeze duration, as the autumn sea breeze departure is not a distinct event, and was hence difficult to determine with any degree of certainty.

These relationships have been provided as a first approximation to the sea breeze onset and duration times. They are not intended to provide an accurate representation of sea breeze characteristics, nor have they been tested against an independent dataset.

6.5 Conclusions

This chapter has extended the climatology presented in Chapter 5 by focussing solely on anticyclonic conditions. These were defined as times when the surface pressure was 1020 hPa or greater.

Vector average wind speeds and directions were calculated for all anticyclonic measurement intervals, allowing the diurnal variation in winds to be determined at each site on the "average" anticyclonic day. This process was repeated for each season. The mean anticyclonic time series were used to produce:

- graphs depicting the diurnal variation in mean winds, at three locations situated along a transect following the valley axis;
- maps showing the spatial variation in mean wind vectors at selected times of the day; and
- a model of sea breeze arrival time and duration for summer and autumn.